Koppelingsmethoden voor het numeriek modelleren
van drijvende golfenergieconvertoren

Coupling Methodologies for Numerical Modelling
of Floating Wave Energy Converters

Tim Verbrugghe

Promotor: prof. dr. ir. A. Kortenhaus
Proefschrift ingediend tot het behalen van de graad van
Doctor in de ingenieurswetenschappen: bouwkunde

UNIVERSITEIT
GENT

Vakgroep Civiele Techniek
Voorzitter: prof. dr. ir. P. Troch
Faculteit Ingenieurswetenschappen en Architectuur
Academiejaar 2018 - 2019

ISBN 978-94-6355-181-6
NUR 956, 928
Wettelijk depot: D/2018/10.500/99

Examination board

Supervisor:

prof. Andreas Kortenhaus
Coastal Engineering Research Group
Department of Civil Engineering
Faculty of Engineering and Architecture
Ghent University
Technologiepark 904
B-9052 Ghent, Belgium

Voting members:

prof. Patrick De Baets	Ghent University, Belgium	chairman
prof. Peter Troch	Ghent University, Belgium	secretary
prof. Marc Vantorre	Ghent University, Belgium	
prof. Joris Degroote	Ghent University, Belgium	
prof. Benedict Rogers	University of Manchester, UK	
dr. Alejandro J.C. Crespo	University of Vigo, Spain	
dr. Corrado Altomare	Flanders Hydraulics, Belgium	
dr. Vicky Stratigaki	Ghent University, Belgium	

Internal defence (Ghent University): 8 November 2018
Public defence (Ghent University): 12 December 2018

Funding:

This research was funded by a PhD fellowship of the Agency for Innovation by Science and Technology in Flanders (IWT), mandate number 141402

Acknowledgements

The past four years and a half have been quite the ride. Pursuing a PhD was way out of my comfort zone. It's a complex cocktail of productive days, frustrating dead-ends, successful simulations, numerous coffee breaks, panic attacks, a few rare Eureka moments, and an awful lot of time lost procrastinating. As with most thrilling rollercoaster rides, there's always sitting someone next to you whose hand you can squeeze when things get a little rough. This paragraph tries to thank all the people whose hands I was allowed to squeeze, guiding me towards this finish line.

First of all, thank you, Julien De Rouck, for calling me early 2014 and convincing me I want that extra $dr.$ in front of my $ir.$ Thank you, Andreas Kortenhaus, for taking up the roll as my supervisor, and dragging me into the rabbit hole. What our meetings maybe lacked in quantity, they made up for in quality! Thanks to Peter Troch, for letting me join a team of wonderful colleagues here at the coastal engineering research group. Thanks for the presentation tips, paper reviews, and of course the cycling conversations.

Thank you to the members of my examination board spending some of their precious time to read this dissertation and critically review it. Your feedback was very important in compiling the final version of the manuscript.

Surprisingly, it was not the asbestos filled ceilings, nor the depressingly thick concrete walls, that made my stay here at AWW worthwhile. It were the colleagues. Thank you Brecht for the impressive demonstration of 'how to do a PhD' and for all our great talks. Thank you Max for our talks, but mainly sorry that I stole 2 of your chocolates while you were on holidays. Thank you Vincent for your collegiality, Panagiotis for the excellent Raki, Minghao for helping me out in Firenze, Carlos for your enthusiasm and spontaneity, David for arranging Star Wars premieres (and I will strongly miss your imported Spanish delicacies), Ine for her delicious birthday cake, Philip for the numerous Russian gifts, Gael for your true friendship (and teaching us a plethora of Spanish curse words), Nicolas and Timothy for continuing our legacy, Ellen for our travel conversations, Lien for even more exotic travel and festival conversations, Vicky for hiring me as a photographer, Peter Devriese for introducing me to mind-mapping. Tom for being a true jack-of-all-trades, Sam for our soccer talks and free parking during the 'Ronde Van Vlaanderen', Dave

for showing us how to party after the thesis defenses and Herman for convincing me to at least once in my lifetime buy a Volvo. All jokes aside, nobody should underestimate the importance of a motivated, helpful team of colleagues.

A special thanks goes to Corrado Altomare and the DualSPHysics team. Thank you for introducing me to the wonderful world of SPH. This gave my research the definitive course it should have been following from the start. Your supervision and guidance resulted in the research output I am most proud of.

Although most of them have no utter clue what I was brooding on this past 4.5 years, my friends and family have been a huge source of support for me. Thank you mom & dad, for giving me the opportunity to study and thank you for supporting me in every choice I have made. I hope I will be able to raise my kids as well as you did, and if not, we'll just come and drop them off at your door. Thanks to my parents in law, for showing interest in what I do and regularly giving me solid advice. Last but not least, a huge thanks to my soul mate, Alexandra, who will probably laugh at this corny, melodramatic homage to her. You wanted someone smarter than you, so my only option was to pursue this $dr.$ title, because everyone knows $dr. ir. > dr.$ Love you!

Tim Verbrugghe
December 2018

Contents

Nomenclature

Latin symbols (I)

a	acceleration	m/s^2
	wave amplitude	m
	SPH particle	$-$
A	area	m^2
	amplitude	m
b_{hyd}	hydrodynamic damping coefficient	kg/s
b_{PTO}	PTO damping coefficient	kg/s
B	coefficient related to fluid compressibility	$-$
	sponge layer length	$-$
C	wave celerity	m/s
C_R	reflection coefficient	$-$
C_T	transmission coefficient	$-$
c	hydrostatic spring coefficient	N/m
c_{PTO}	added PTO spring coefficient	N/m
d	water depth	m
d_p	particle size	m
D	diameter	m
	diffracted complex wavefield	$-$
e	Euler number	$-$
E	energy	J
E_k	kinetic energy	J
E_p	potential energy	J
f_{rel}	relaxation function	$-$
F	force	N
F_h	hydrodynamic force	N
F_{rad}	radiation force	N
F_{rad}	excitation force	N
F_{res}	hydrostatic restoring force	N
F_{damp}	damping force	N
F_{tun}	tuning force	N
F_{ext}	external force	N
F_{FK}	Froude-Krylov force	N
$F_{\max}$	maximum force	N

Latin symbols (II)

F_{PTO}	force by the power take-off system	N
F_{surge}	horizontal wave-induced surge force	N
F_x	horizontal wave-induced surge force in X-direction	N
g	gravitational constant	m/s^2
h	smoothing length	m
	bed level (water depth)	m
H	wave height	m
H_s	significant wave height	m
k	wave number	$1/m$
	spring coefficient	N/m
K_D	dimensionless amplitude - disturbance coefficient	$-$
L	length	m
	wave length	m
m	mass	kg
m_a	added mass	kg
m_{PTO}	added PTO mass	kg
m_0	wave number solution of dispersion relation	$-$
M_h	hydrodynamic moment	Nm
n	normal	$-$
n_l	number of layers	$-$
N_z	number of cells in the vertical Z-direction	$-$
p	pressure	N/m^2
P	energy flux	W
q	non-dimensional particle distance	$-$
R_b	radial distance to body b	m
R_c	coupling radius	m
R	radiated complex wavefield	$-$
Re	Reynolds number	$-$
S_b	water-body interface	$-$
S	absorption function	$-$
t	time	s
T	wave period	s
	draft	m
T_d	damped natural period	s
T_m	mean wave period	s
T_R	resonance period	s
u	horizontal particle velocity	m/s
V	volume	m^3
v_x	horizontal particle velocity	m/s
v_z	vertical particle velocity	m/s
w	vertical particle velocity	m/s

Latin symbols (III)

W	width	m
	kernel function	$-$
x	horizontal space coordinate	$-$
y	second horizontal space coordinate	$-$
z	vertical space coordinate	$-$

Greek symbols

α	slope angle	$-$
γ	polytrophic constant	$-$
δ	diffusivity in SPH	$-$
Δ	difference	$-$
Δt	time step	s
Δx	grid spacing in X-direction	m
Δy	grid spacing in Y-direction	m
Δz	grid spacing in Z-direction	m
ϵ	wave steepness	$-$
	phase shift	$-$
	dimensionless wave amplitude	$-$
ζ	damping ration	$-$
η	surface elevation	m
$\eta_{\max}$	maximum surface elevation	m
θ	wave direction	$-$
	wave phase	$-$
ξ	floating body motion vector	$-$
ρ	density	kg/m^3
Σ	sum	$-$
σ	dimensionless vertical coordinate	$-$
	standard deviation	$-$
τ	wave period	s
ϕ	wave phase	$-$
Φ	velocity potential	$-$
Π	viscosity (SPH)	$-$
ϕ_R	radiation potential	$-$
ϕ_D	diffraction potential	$-$
ϕ_I	incident potential	$-$
Ω	solid boundary	$-$
ω	wave frequency	rad/s
ω_d	damped frequency	rad/s
ω_n	natural frequency	rad/s

Symbols

$^\circ$	angle	degrees
∂	partial derivative	–
d	total derivative	–

Subscripts

0	reference level
a	particle a
b	body (floating)
	particle b
bw	breakwater
B	floating body boundary
abs	absorption
d	dynamic
D	diffraction
e	experimental
exp	experimental
F	fluid boundary
gen	generation
h	sea bed boundary
i	Cartesian index
	sub iteration
	wave component
	interface
in	inlet
I	incident
j	boundary face
$\max$	maximum value
$\min$	minimum value
n	numerical
out	outlet
R	radiation
sim	simulation
w	water

Abbreviations

2-D	two-dimensional
3-D	three-dimensional
BEM	Boundary Element Method
BVP	Boundary Value Problem
CFD	Computational Fluid Dynamics
CFL	Courant-Friedrich-Lewy
CPU	Central Processing Unit
DHI	Danish Hydraulic Institute
DNS	Direct Numerical Simulation
DSPH	DualSPHysics
EMEC	European Marine Energy Centre
EU	European Union
FNPF	Fully Non-linear Potential Flow
FP	European Framework Project
FV	Finite Volumes
GEC	Golfenergieconvertor
GPU	Graphical Processing Unit
IEA	International Energy Agency
IRR	Irregular waves
ISPH	Incompressible SPH
LCOE	Levelised Cost Of Energy
LES	Large Eddy Simulations
LVDT	Linear Variable Differential Transformer
MPI	Message Passing Interface
Mtoe	Million tonnes of crude oil equivalent
NS	Navier–Stokes
OW3D	OceanWave3D
OWC	Oscillating Water Column
PTFE	Polytetrafluoroethylene
PTO	Power Take-Off
RAO	Response Amplitude Operator
REG	Regular waves
RES	Renewable Energy Share
RMSE	Root Mean Square Error
SPH	Smoothed Particle Hydrodynamics
SWL	Still Water Level
TRL	Technology Readiness Level
VOF	Volume-Of-Fluid
WCSPH	Weakly Compressible SPH
WEC	Wave Energy Converter
WG	Wave Gauge

Samenvatting

Dutch summary

Onze zeeën en oceanen bevatten een enorme voorraad aan hernieuwbare energie. Een belangrijke portie daarvan is golfenergie. Het is mogelijk om de golfbeweging om te zetten in bruikbare elektriciteit door golfenergieconvertoren (GEC) te installeren. Deze proberen op een zo efficiënt mogelijke manier de energie uit de waterdeeltjes om te zetten in mechanische energie. Een power take-off systeem zorgt vervolgens dat die mechanische energie wordt omgezet naar elektriciteit. Niettegenstaande er al onderzoek naar GEC's loopt sinds de 18^{de} eeuw, zijn er vandaag nog nauwelijks commerciële GEC-projecten die stroom voor eindgebruikers produceren. Dit is voornamelijk te wijten aan de hoge kostprijs per kilowattuur voor de eindgebruiker. Om competitief te zijn in de huidige energiemarkt, moeten GEC's qua kostprijs minstens in de buurt komen van offshore wind turbines.

Er zijn twee hoofdredenen voor de huidige hoge Levelised Cost of Energy (LCOE). Een enkele GEC produceert significant minder energie dan een enkele windturbine. Om competitief te zijn, moeten er dus veel GEC's bij elkaar geplaatst worden in zogenaamde golfenergieconverterparken (GEC-parken). Naast een hogere productiekost brengt dit ook meer logistieke problemen met zich mee zoals plaatsing en onderhoud. Ook worden GEC's veel meer onderworpen aan verwoestende stormen dan windturbines, die veilig boven het stormpeil geïnstalleerd worden. GEC's drijven op het water en worden tijdens stormen belaagd door krachtige golven. Aangezien een GEC tijdens zijn levensduur verschillende stormen moet kunnen trotseren, moeten ze zeer robuust ontworpen worden, wat de kostprijs niet ten goede komt.

Er is dus duidelijk nood aan extra onderzoek om de kost van GEC's te optimaliseren, in de hoop ze op lange termijn competitief in de hernieuwbare energiemarkt te kunnen plaatsen. Dit doctoraat probeert een steentje bij te dragen aan deze problematiek door het ontwikkelen van gekoppelde computermodellen. Het ene model is bedoeld om het golfklimaat in en rond GEC-parken te simuleren; het andere beoogt het gedetailleerd modelleren van GEC's in krachtige golven, zonder beroep te moeten doen op een supercomputer.

De eerste koppelingsmethode is ontwikkeld om golftransformaties doorheen een golfenergieconvertorpark te kunnen modelleren. Als golven invallen op een golfenergieconvertor, worden deze deels gereflecteerd en deels gediffracteerd waardoor ze van richting veranderen. Daarenboven worden drijvende GEC's geactiveerd door de golven. Door hun eigen beweging genereren ze zelf ook golven, geradieerde

golven. Deze golfinteracties binnen een GEC-park kunnen complexe vormen aannemen en leiden tot lokale hot-spots (zones met hogere golfenergie) en wakes (zones met lagere golfenergie). We noemen dit de near-field effecten. Het correct modelleren van deze near-field effecten is belangrijk om tot een optimale layout van het GEC-park te komen. Daarenboven is het belangrijk de invloed van deze near-field effecten te kennen op verder gelegen GEC-parken, of eventueel zelfs de kuststrook. Dit noemen we de far-field effecten. De ontwikkelde koppelingsmethode is in staat om zowel de near-field als far-field effecten te modelleren over een willekeurige bathymetrie, door twee bestaande computermodellen aan elkaar te koppelen: het linear golf-structuur ineractiemodel Nemoh, en de lineaire versie van het golfpropagatiemodel OceanWave3D. Eerst worden de invallende golven berekend met OceanWave3D, zonder de aanwezigheid van GEC's. Ter hoogte van de GEC-locaties worden de invallende golfhoogte en de golfperiode geregistreerd. Vervolgens worden de geradieerde en gediffracteerde golven in kleine zones rondom de GEC's berekend met Nemoh. Om dit te bekomen, dienen we de vorm van de GEC te digitaliseren en op te delen in kleine panelen. Nemoh berekent de kracht van het golfveld op elk van deze panelen aan de hand van de waterdruk, om zo de reactie van de GEC op de golven te berekenen. In een aparte simulatie, worden de geradieerde en gediffracteerde golven samen gepropageerd in OceanWave3D. Dit getransformeerd golfveld wordt opgeteld bij het originele invallend golfveld om zo het totale golfveld te bekomen, waarin zowel de near-field effecten als far-field effecten accuraat gesimuleerd worden. Deze superpositie methode is toegestaan, aangezien in beide modellen met de lineaire golftheorie wordt gerekend. De koppelingsmethode is gevalideerd door een diepgaande vergelijkingsstudie met een ander golfpropagatiemodel (MILDwave) uit te voeren, en door resultaten van het model te vergelijken met de experimentele dataset uit het WECwakes project. Hieruit blijkt dat de koppelingsmethode kan gebruikt worden voor het modelleren van GEC-parken, onderhevig aan lineaire golven.

Deze eerste koppelingsmethode is echter niet in staat om grote, krachtige golven en hun impact op GEC's te simuleren. Hiervoor zijn niet-lineaire modellen nodig. Een veelbelovende numerieke methode om niet-lineaire golfinteracties met GEC's te modelleren, is de Smoothed Particle Hydrodynamics (SPH) methode. SPH is een meshvrije, lagrangiaanse numerieke methode. Dit betekent dat er geen gestructureerd grid wordt gebruikt voor de berekeningen, maar een set numerieke deeltjes, die hun fysieke eigenschappen met zich meedragen. Dit heeft als voordeel dat SPH methodes uiterst geschikt zijn voor het modelleren van problemen met complexe randvoorwaarden, zoals het complex vrij wateroppervlak van een niet-lineaire golf. Het ontbreken van een grid resulteert in een sterk vereenvoudigde modelimplementatie en mogelijkheid tot parallellisatie. Zo kan er gebruik gemaakt worden van grafische processors (GPU) in plaats van klassieke centrale processors (CPU). Desondanks deze parallellisatie moeten miljoenen deeltjes gesimuleerd worden om accurate resultaten te bekomen, waardoor SPH steeds computationeel intensief is.

De tweede koppelingsmethode probeert het SPH-domein zo klein mogelijk te houden om de rekentijd te minimaliseren. Dit betekent echter dat er accurate randvoorwaarden opgelegd moeten worden om de gewenste golven te simuleren in het

SPH-domein. Dit wordt gerealiseerd door het SPH-model DualSPHysics met de snelle niet-lineaire potentiaalsolver OceanWave3D te koppelen. OceanWave3D kan de propagatie van niet-lineaire golven zeer snel uitrekenen over een lange afstand. Binnen dit grote domein kan een klein SPH-domein 'genest' worden. Ter hoogte van de interface tussen de twee modellen worden de nodige orbitaalsnelheden en verheffingen uitgewisseld om een naadloze overgang te verzekeren. De uitwisseling van informatie tussen beide modellen gebeurt voor en na iedere tijdstap. Een eerste versie van de koppelingsmethode maakt gebruik van dynamisch bewegende randvoorwaarden ter hoogte van de OceanWave3D-DualSPHysics interface. Het SPH-domein wordt zowel aan de golfgeneratiezijde als aan de golfabsorptiezijde begrensd door een set randpartikels, waarover de gebruiker controle heeft. De randpartikels bewegen door horizontale orbitaalsnelheden op te leggen, die berekend worden in het OceanWave3D-model. Dit resulteert in de generatie van een golf in het SPH-domein, gelijk aan de golf uit het OceanWave3D-domein. Deze propageert verder in het SPH-domein tot deze wordt geabsorbeerd door de randpartikels. In het SPH-domein wordt het vrij wateroppervlak geregistreerd. Deze waarden worden teruggestuurd naar het OceanWave3D-domein, waar de originele waarden overschreven worden. Zo wordt iedere golftransformatie uit het SPH-domein ook voortgeplant in het OceanWave3D-domein. Als we dus een drijvende GEC modelleren in het SPH-domein, zullen de gediffracteerde en geradieerde golven correct berekend worden in het SPH-domein, en zich verder voortplanten in het grotere OceanWave3D-domein. De koppelingsmethode is gevalideerd door een reeks niet-lineaire golven te simuleren en de verheffingen, orbitaalsnelheden en drukken te vergelijken met theoretische resultaten. Ook worden twee experimentele testen numeriek gemodelleerd met de koppelingsmethode. Eerst wordt een gefixeerde oscillerende waterkolom GEC gemodelleerd. Invallende golven propageren tot in een gesloten kamer waardoor de lucht gecomprimeerd wordt. Bovenaan zit een opening waardoor de lucht kan ontsnappen. Het gekoppelde model is in staat de golfverheffing binnenin de kamer correct te voorspellen. Als tweede experiment wordt een drijvende rechthoekige doos gesimuleerd. Het gekoppelde model voorspelt de beweging van de doos correct in alle vrijheidsgraden.

Het gebruik van dynamische randpartikels ter hoogte van de OceanWave3D-DualSPHysics interface heeft echter enkele nadelen. Door de natuurlijke drift in niet-lineaire golven, wordt na een bepaalde simulatietijd de ruimte tussen de verschillende randpartikels te groot waardoor de simulatie vroegtijdig kan afgebroken worden. Dit fenomeen is het meest merkbaar bij sterk niet-lineaire golven. Ook hebben dynamische randpartikels de onaangename eigenschap om niet-fysische drukpieken te introduceren wanneer een vloeistofpartikel te dicht in de buurt komt van een dynamisch randpartikel. Aangezien het gebruikte SPH-model veronderstelt dat vloeistoffen zwak samendrukbaar zijn, propageren deze drukpieken zich doorheen de vloeistof, resulterend in een lagere nauwkeurigheid van het drukveld.

De nadelen van het gebruik van dynamische randpartikels worden aangepakt door het gebruik van de recent geïntroduceerde open randvoorwaarden. In plaats van dynamische randpartikels kunnen zones met verschillende lagen bufferpartikels gedefinieerd worden. Een bufferpartikel heeft enkele eigenschappen die het uiterst geschikt maakt voor het genereren en absorberen van golven: als een bufferpartikel

het SPH-domein verlaat, wordt het automatisch vernietigd, als het partikel vanuit de bufferzone in de vloeistofzone terecht komt, wordt het automatisch omgezet in een vloeistofpartikel. Dit betekent dat er hier geen problemen met drift kunnen voorkomen. De gebruiker heeft de keuze om snelheden, verheffing en druk op te leggen aan de bufferpartikels of kan er voor kiezen om die fysische eigenschappen te laten extrapoleren uit het vloeistofdomein. Na een diepgaande studie is geconcludeerd dat deze open randvoorwaarden met bufferzones kunnen toegepast worden om nauwkeurig niet-lineaire golven te genereren en te absorberen. In de generatiezone worden horizontale orbitaalsnelheden en de verheffing opgelegd; de druk is hydrostatisch. In de absorptiezone worden eveneens de horizontale orbitaalsnelheden opgelegd. Hier worden echter de verheffing en de druk geëxtrapoleerd vanuit het vloeistofdomein. Ongewenste reflecties worden vermeden door correcties op de orbitaalsnelheden toe te passen, gebaseerd op de ondiepwatertheorie. Dit resulteert in zeer accurate golfgeneratie en absorptie in een SPH-domein dat slechts één golflengte lang is. Deze methode levert een winst tot 400 $\%$ op de normale rekentijd. Het SPH-model met open randvoorwaarden is gevalideerd door resultaten te vergelijken met theoretische oplossingen en met experimentele resultaten uit de literatuur.

Ten slotte wordt een tweede versie van de OceanWave3D - DualSPHysics koppeling voorgesteld, waarbij de open randvoorwaarden worden toegepast. Dit resulteert in een stabiele koppeling, zonder drift, waarbij het drukveld significant minder pieken vertoont. De finale koppeling wordt gedemonstreerd aan de hand van een 3D-model waarbij niet-lineaire golven inwerken op een dompende cylinder, waarbij een deel van de golf de cylinder overtopt.

Tijdens de doctoraatsperiode werd fundamenteel onderzoek verricht naar koppelingsmethodes om zowel de nauwkeurigheid als de rekentijd van numerieke modellen voor GEC's en GEC-parken te optimaliseren. De methodes werden grondig gevalideerd aan de hand van theoretische oplossingen, resultaten van andere numerieke modellen of experimentele data. De nieuwe koppelingsmethodes bewijzen performant te zijn en kunnen in een breed gamma ingenieursproblemen toegepast worden. Naar de toekomst toe is er eveneens de mogelijkheid om de methoden uit te breiden met meer functionaliteit.

Summary

The world's oceans contain an enormous amount of renewable energy. A significant portion of that energy is wave energy. It is possible to convert this wave energy into usable electricity by deploying so-called Wave Energy Converters (WECs). WECs try to capture the kinetic and potential energy within the wave and convert it to mechanical energy. Subsequently, a Power Take-Off (PTO) system is installed to convert this mechanical energy into grid-compliant electricity. Although research into wave energy started in the 18^{th} century, there are only a limited number of commercially viable WEC projects, delivering electricity to end users. This is mainly due to the high Levelised Cost of Energy (LCOE), which is still higher than other renewable sources such as offshore wind.

There are two main reasons for the high LCOE. Firstly, a single WEC produces significantly less energy than a single wind turbine. To be competitive, a lot of WECs need to be placed together in a so-called WEC farm or WEC park. This results in a higher production cost and logistical challenges such as deployment and maintenance. Secondly, WECs are more exposed to severe storms than wind turbines, which are installed safely above the storm surge. WECs are operating in the water and are subjected to heavy wave impacts. During its lifetime, a WEC needs to be able to survive a number of storms. They need to be designed robustly, driving the LCOE even further upwards.

Clearly there is a need for extra research to optimise the LCOE for wave energy, to ensure a competitive position within the global renewable energy market. This doctoral research attempts to contribute by developing new coupling methodologies for numerical modelling of wave energy converters. One type of coupling methodology aims to model the wave climate in and around WEC farms; another type is developed to accurately model WECs in a heavy wave climate, without the requirement of large supercomputers.

The first coupling methodology is developed to model wave transformations in and around wave energy converter farms. When an incident wave interacts with a WEC, a part of the wave is reflected and a part is diffracted, causing the wave to change direction. Additionally, there are WEC motions in reponse to the incident wave, which generate radiated waves. These wave interactions inside a WEC farm are a complex phenomenon, and lead to local hot-spots (regions with higher wave energy) and wakes (regions with lower wave energy). These are the so-called near-field effects, which need to be modelled accurately when studying the optimal layout of the WECs inside a WEC farm. Additionally, it is important

to know the impact of the near-field effects on WEC farms located further away, or even the impact on a nearby coastline. These are called far-field effects. The presented coupling methodology is capable of modelling both near-field and far-field effects over a variable bathymetry, by coupling two existing numerical models: the linear wave-structure interaction solver Nemoh, and a linear version of the fully non-linear potential flow (FNPF) solver OceanWave3D. First, incident waves are calculated with OceanWave3D, without the presence of any WECs. At the planned WEC locations, the incident wave height and wave period are measured. Then, the radiated and diffracted waves are calculated with Nemoh, in a restricted zone around the WECs or WEC park. Nemoh requires the WEC shape to be meshed into quadrilateral panels. It then calculates the wave forces on each panel based on the wave pressure, resulting in the response of the WEC to the incident wave. In a separate simulation, the radiated and diffracted waves are propagated into the OceanWave3D domain. This perturbed wave field is superposed on the original incident wave field to result in the total wavefield, containing both the accurate near-field and far-field effects. Superposition is allowed, since both numerical models are applying linear wave theory. The coupling methodology is validated by performing a thorough comparison study with another wave propagation solver (MILDwave), and by comparing results with experimental data obtained within the WECwakes project. This proves that the coupling methodology can be used to model WEC farms, as long as the wave conditions are linear.

However, this linear coupling methodology is not capable to model large, violent waves and their impact on WECs. This can only be done by non-linear wave-structure interaction solvers. A promising numerical method to study non-linear wave-structure interactions are Smoothed Particle Hydrodynamics (SPH). It is a meshless numerical method with a lagrangian frame of reference. This implies that the physical quantities are not calculated on a structured grid or mesh, but on a set of numerical particles, carrying the physical quantities along their path. This has the advantage that SPH methods can be applied for modelling problems with complex boundary conditions, such as the violent free surface of a non-linear wave. The absence of a structured grid also results in a simplified model and easy parallellisation. This allows for the use of a graphics processing unit (GPU) rather than the more classical central processing units (CPU). Despite this parallellisation, often millions of particles need to be simulated to reach accurate results, making SPH methods computationally expensive.

The second coupling methodology aims at minimizing the necessary SPH domain for accurate wave propagation, resulting in minimal computation time. For this to work, accurate boundary conditions are needed to generate and absorb the required waves within the SPH domain. This is obtained by coupling the SPH model DualSPHysics to the FNPF solver OceanWave3D. The latter can quickly calculate the propagation of non-linear waves in large domains. Within this large domain, a small SPH domain can be 'nested'. At the interface between both models, the necessary orbital velocities and surface elevations are exchanged to ensure a smooth transition. The information exchange is done with the Message Passing Interface (MPI) protocol and happens before and after every time step. A first version of this non-linear coupling methodology uses dynamic boundary particles

at the DualSPHysics-OceanWave3D interface. These particles are positioned at both the wave generation side and the wave absorption side of the SPH domain, and can be controlled by the user. The dynamic boundaries are move by imposing horizontal orbital velocities, measured in the OceanWave3D domain, at the interface location. This results in the generation of a non-linear wave in the SPH domain, equal to the one generated in the OceanWave3D domain. The wave propagates further into the SPH domain, only to be absorbed again by the second set of dynamic boundary particles. The free surface elevation in the SPH domain is measured and sent back to the OceanWave3D domain, where the original solution is overwritten. Like this, all wave transformations occurring in the SPH domain are also introduced and further propagated in the larger OceanWave3D domain. By introducing a floating WEC inside the SPH domain, we can accurately simulate the non-linear diffraction and radiation, and propagate these perturbances further into the OceanWave3D domain. The coupling methodology is validated by simulating a number of non-linear waves and comparing the surface elevation, orbital velocities and pressure to theoretical solutions. Also, comparison to two experimental datasets is performed. First, a fixed oscillating water column WEC is modelled. The incident waves propagated into a semi-submerged chamber, where air is compressed and released through an opening on top. The coupled model correctly predicts the surface elevation inside the chamber. Secondly, a freely floating rectangular box is simulated. All degrees of freedom are accurately predicted by the coupled model.

The application of dynamic boundary particles at the OceanWave3D - DualSPHysics interface has a couple of disadvantages. Due to the natural drift occurring in non-linear waves, the different layers of dynamic boundary particles are separated from each other after a certain amount of simulation time, resulting in a premature simulation ending. This phenomenon is most noticed with strongly non-linear waves. Additionally, dynamic boundary particles have the tendency to introduce local pressure peaks when the distance to a nearby fluid particle decreases significantly. Since the applied SPH model is weakly compressible, these pressure peaks propagate through the fluid, resulting in a lower accuracy of the pressure field.

The disadvantages of using dynamic boundary particles are mitigated by applying the recently introduced open boundaries. This allows the definition of zones with several layers of buffer particles. A buffer particle has a number of properties, making it ideal to be used for wave generation and absorption: when a buffer particle leaves the SPH domain, it is automatically removed from the simulation, and when a buffer particle crosses the interface between the buffer zone and the fluid domain, it is transformed into a fluid particle and a new buffer particle is created. Vice versa, a fluid particle is transformed into a buffer particle when it crosses the interface. Due to these properties, there are no drift issues with open boundaries. The user has the ability to impose velocity, surface elevation and pressure to the buffer particles, or to extrapolate these quantities from the fluid domain using ghost nodes. A detailed study has proven that these open boundaries can be used to accurately generate and absorb non-linear waves within an SPH domain, measuring only one wave length. In the inlet buffer zone, horizontal orbital velocities and surface elevation are imposed, while the pressure is set to be hydrostatic.

In the outlet buffer zone, horizontal orbital velocities are imposed as well, but surface elevation and pressure are extrapolated from the fluid domain. Unwanted reflections are avoided by applying a velocity correction at the inlet and outlet, based on shallow water theory. This wave generation and absorption method can result in a computational speed-up of up to 400 $\%$ with respect to a classical wave propagation simulation in DualSPHysics. The open boundary model is validated by comparing simulation results with theoretical solutions and experimental data found in literature.

A second version of the OceanWave3D-DualSPHysics coupling is presented, now applying the open boundary formulation. This results in a stable coupling, without drift problems, and with a stable pressure field without large pressure peaks. This final coupling methodology is demonstrated with a 3D simulation of non-linear waves interacting with and overtopping a heaving cylinder.

During the 4-year grant period, fundamental research was performed into coupling methodologies to improve both the accuracy and computation time of numerical models for WECs and WEC farms. The methods were thoroughly validated using theoretical solutions, results from other numerical models and experimental data. The newly developed coupling methodologies prove to have a high performance, and can be applied in a wide scale of real engineering problems. In future research, there is the possibility to even more extend the functionality of the coupling methodologies.

Chapter 1

Introduction

1.1 Background and Motivation

Global energy consumption is rising continuously. The growth of world population combined with heavy industrialization of former third world countries are major drivers of this phenomenon. In 2015 the world total primary energy supply was about 13647 Mtoe (million tonnes of crude oil equivalent) of which more than 80% are fossil fuels. Only 8.9% of the supply does not produce CO_2, of which 4.9% is nuclear (IEA, 2017). Although the European Union (EU) is working hard to reduce polluting emissions, on a world scale, CO_2 emissions are still rising significantly (see Figure 1.1). This is due to the industrialisation of former third world countries, as well as to the migration of polluting European plants towards cheap-labour countries outside of the EU.

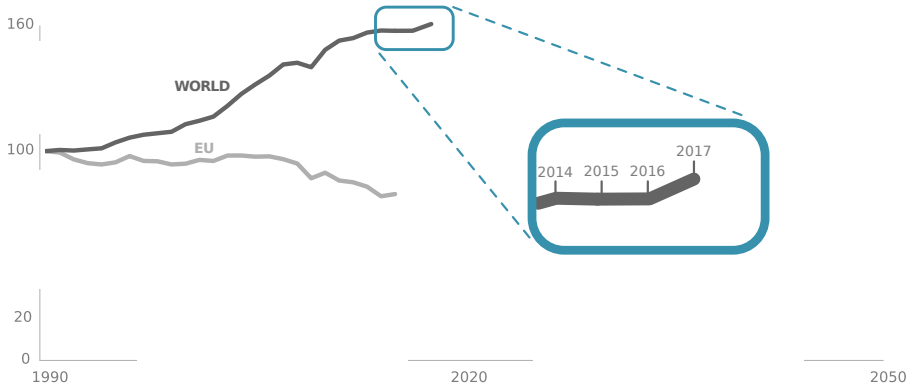

Figure 1.1: Scaled global CO_2 emissions since 1990 (iea.org)

In order to reduce global warming two important energy transitions are necessary: electrification and the introduction of more renewable energy sources (see Figure 1.2). The former indicates the need to migrate from fossil power sources to

electrical power, for example electrical cars, electric heating. However, migrating to a total energy market with mainly electrical power is not enough. It is primordial that the source of electrical power mainly comes from renewable sources. In addition to those two transitions, there is improvement now possible regarding energy efficiency.

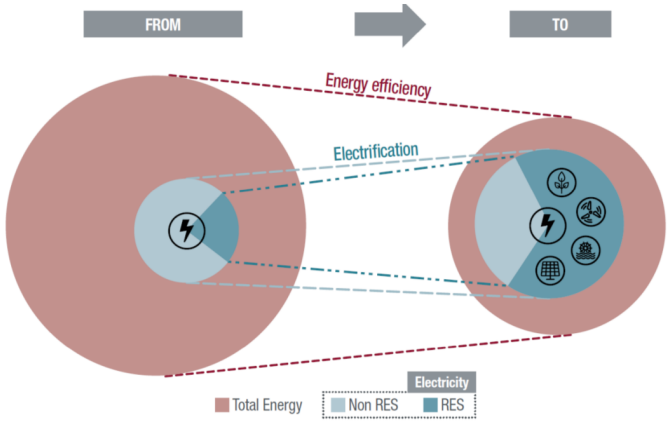

Figure 1.2: Necessary energy transition to limit global warming (elia.be). RES = Renewable Energy Share.

All sources of energies, except geothermal and nuclear, are ultimately powered by the sun (Abas et al., 2015). Much of that energy is stored as renewable energy sources within our oceans, as tidal, osmotic, thermal and wave energy. Ocean waves are efficient energy carriers transporting the sun's energy over thousands of miles. The heat of the sun creates pressure differences in the atmosphere, resulting in wind. Winds blowing across a large area of water (fetch) for a certain period transfer their energy into the water and create waves. This disturbance in the free water surface travels with the direction of the wind and continues its journey far beyond the wind swept area. Eventually the energy is dissipated when the waves reach the shoreline and break. The total worldwide wave power reaching ocean-facing shorelines is estimated at 2.1 TW (Gunn and Stock-Williams, 2012), which is about 95% of the world's electricity consumption. López et al. (2013) reports an even higher estimation of 3.7 TW. However, these numbers need to be interpreted with care. A large number of high wave energy zones are not suitable to deploy Wave Energy Converters (WECs) due to innapropriately large water depths, distance from the coast and limited accessibility. It is thus impossible for wave energy to cover the full 95% of the world's electricity need. However, in some cases, it has the potential to be a viable alternative for other renewable energy sources. Next to the power potential and transport efficiency, wave energy has more attractive benefits:

- The energy density (2-3 kW/m^2) is higher than that of wind (0.4-0.6 kW/m^2) and solar (0.1-0.2 kW/m^2).

- Electricity generation is possible up to 90% of the time.
- It has a good correlation between resource and demand, since around 44% of the global population lives within 150 km of the coast (`http://www.oceansatlas.org`).

However, wave energy also faces a number of challenges:

- Energy conversion stages are needed to convert the slowly oscillating motion (around 0.1 Hz) to a high-frequency grid-compliant electricity output (50 Hz).
- Wave power levels fluctuate continuously, while the electricity on the grid should be as smooth as possible, making energy storage systems necessary.
- Survivability in storm conditions is extremely important, but leads to expensive designs, driving the total cost upwards.
- Long-term durability proves to be a challenge, since a lot of promising prototypes have failed to operate for long periods of time, although the expected lifetime should be at least 25 years.
- Wave energy has to compete with more mature technologies like offshore wind where the investment is already done and new investors are more easily attracted.

It is clear that wave energy is worth exploring as a viable renewable energy resource. The devices which are used to extract this energy and convert it to electricity are called Wave Energy Converters (WECs). Over the years, a large number of WECs have been researched, and more than one thousand concepts have been patented (Pelc and Fujita, 2002). The European Marine Energy Center (EMEC, `www.emec.org.uk`) lists 157 known WEC concepts, characterized by a wide variety in device location, size and working principle. Despite these numbers, only a limited amount of developers reach a high technology readiness level (TRL). This is mainly due to the complexity and higher cost when testing at sea, compared to testing in tanks and flumes within a lab environment. Of the listed 157 concepts, only 5% has reached TRL5, where a large scale (100 kW) grid connected prototype is tested. Moreover, Pelc and Fujita (2002) report that Levelized Cost of Energy (LCOE) estimates for offshore wave farms are around 22-25 pence/kWh, which is significantly higher than other forms of renewable energy. The reality for wave energy is that this LCOE needs to reduce significantly before it becomes commercially viable. Within this manuscript, the research is focused on two fields where LCOE reductions are possible:

- WEC farms: a necessity to make wave energy commercially viable is by clustering a large amount of WECs together into a WEC farm. WEC farms enable costs to be reduced due to combined power lines, smoothed output, combined maintenance, etc.

- Survivability: WEC designs need to resist heavy storms, leading to expensive devices. Optimizing the design in storm conditions before construction and deployment can significantly reduce costs.

Firstly, LCOE reductions are necessary by clustering WEC devices into farms or parks. By deploying a large number of WECs at one location, a significant amount of energy can be produced. However, by placing WECs into each other's vicinity, they will have an impact on each other and on the incoming waves. It is important to note that within this research, only floating point-absorber WECs are considered. A wave traveling towards a floating WEC will interact with it in three ways (see Figure 1.3):

- Reflection: the incident wave will partly hit the WEC and reflect towards the open sea.
- Diffraction: the incident wave will partly move around the WEC and change direction.
- Radiation: the incident wave will interact with the WEC, inducing motions. This WEC motion generates waves, radiating away from the floating WEC in circular patterns.

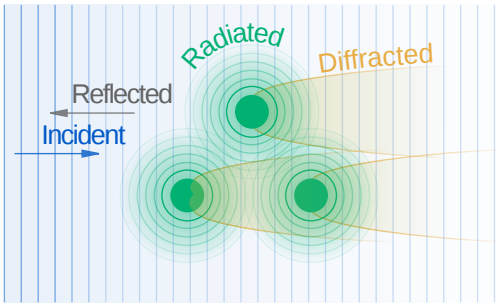

Figure 1.3: Visual representation of incident, radiated and diffracted waves around an array of 3 floating structures. The combination of these wave fields results in the total wave field around the 3 floating structures.

These wave interactions close to the structures are called "near-field" effects, while the propagation of these waves further away from the structures are called "far-field" effects. The superposition of these phenomena results in a complex perturbed wave field (Stratigaki et al., 2014b,a; Troch and Stratigaki, 2016). Simulating the wave transformations within and around a WEC array is complex; it is difficult, or in some cases impossible, to simulate both near-field and far-field effects using a single numerical model, in a time and cost-efficient way in terms of computation time and effort. This can be achieved by linear coupling of a wave-structure interaction solver for the near-field effects and a wave propagation model for the far-field effects, as illustrated in Figure 1.4.

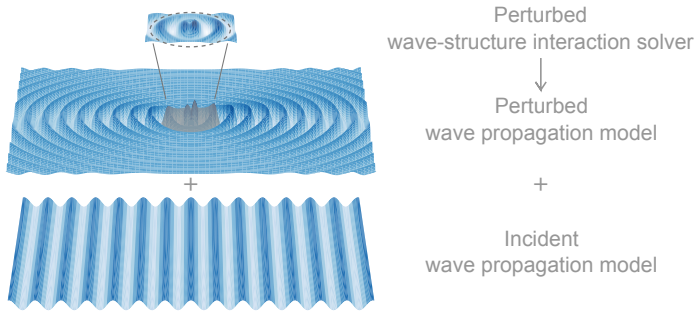

Figure 1.4: Visual representation of linear coupling methodology, where superposition is applied to achieve the total wave field

Secondly, the development of WECs can benefit significantly by improving the design in storm conditions. This is possible by performing research into the motions of the devices and forces acting on them during heavy seas and storm conditions. Specifically, numerical simulations can be performed to find the optimal WEC design in a cost-effective way. In recent years, computational power has increased significantly, allowing to numerically model wave-structure interaction with floating WECs. Specifically, Smoothed Particle Hydrodynamics (SPH, Monaghan (1992)) has proven to be an excellent method to accurately model floating objects within violent free surface flows (see Section 2.1 for the state-of-the-art). However, before SPH models can be readily applied to solve real engineering problems with reasonable computation times of hours to days, some improvements are needed, which are listed by the SPH community in the Grand Challenges (`spheric-sph.org/grand-challenges`):

1. Convergence, consistency and stability
2. Boundary conditions
3. Adaptivity
4. Coupling to other models
5. Applicability to industry

Within this research, focus is mainly put on challenges 2 and 4, by applying open boundaries and coupling the SPH model to a fully non-linear potential flow model.

1.2 Outline

The manuscript is outlined as follows. The background and motivation for the research topic has been given in Chapter 1. In Chapter 2, the state-of-the-art is given, knowledge gaps are identified and research objectives are presented. In Chapter 3, the necessary theoretical background is supplied to fully understand all

the applied numerical models. Chapter 4 presents the linear coupling methodology between the fully nonlinear potential flow (FNPF) solver OceanWave3D and the boundary element method (BEM) solver Nemoh. The methodology is explained in detail, compared to a similar coupling with a mild-slope equation solver MILDwave and compared to the WECwakes experimental dataset. Next, the 2-way non-linear coupling methodology is presented in Chapter 5. There, moving boundaries are applied on the interface between OceanWave3D and the SPH solver DualSPHysics. Validation is done with theoretical solutions and experimental data. In Chapter 6, the coupling methodology is improved by applying open boundaries for wave generation and absorption. The coupling implementation is improved as well, using both socket programming as well as using MPI protocols. A short comparison of the introduced methodologies and their applicability is given in Chapter 7. Finally, concluding remarks and suggestions for further work are given in Chapter 8.

Additionally, Appendix A presents the software package openWEC, created by the author of this manuscript. Appendix B presents the Stokes 5^{th} Order Wave Theory, while Appendix C provides the full OceanWave3D-MILDwave comparison for the linear coupling methodology and Appendix D the comparison with the WECwakes data. Finally, Appendix E presents all the code changes made to the software packages, as well as the newly created code.

Chapter 2

Scientific State-Of-The-Art

Within this chapter, a concise overview is given of the state-of-the-art for numerical modelling of WECs, available coupling methodologies, and wave generation and absorption techniques in SPH. Additional literature review is included in every chapter focusing on each particular research topic.

2.1 Numerical modelling of WECs and WEC farms

A thorough review of the state-of-the-art on available numerical models for WEC and WEC array modelling is given in the book: *Numerical modelling of wave energy converters: state-of-the-art techniques for single devices and arrays* edited by Folley (2016a). This section provides a concise review of numerical modelling of WECs and WEC farms, and is similar to the review presented in Devolder (2018).

Generally, a large number of numerical models exist to study the hydrodynamic interactions between waves and WECs. The choice for a particular model is mostly based on a trade-off between the accuracy of the results and the necessary computational time. Simple linear 1D WEC models are very fast and approximate the WEC as a mass-spring-damper system, forced by linear waves. Complex models such as computational fluid dynamics (CFD), to which SPH belongs, calculate the full 3-D flow field around the WEC and are consequently very computationally expensive. These models are thus specialised in studying the near-field effects. Additionally, selecting a numerical model strongly depends on the physics which need to be simulated and resolved. For example, some models are aimed at calculating the power absorption of a specific prototype, focusing on energy conversion and efficiency. Here, calculating the capture width ratio is often performed as a measurement of a device its performance and efficieny. It is the ratio of the mean absorbed power by the device and the incident wave energy along the device's width. It was for example used to create a database of a large number of WEC concepts in Babarit (2015). Alternatively, several models are applied to calculate the hydrodynamic flow field around the WECs as well as the motion response of the WECs (near-field zone) while other models are focussing on studying wave transformations around WEC arrays at a larger distance (far-field zone) (Folley et al., 2012).

The first numerical models were based on semi-analytical techniques and were used for modelling basic WEC geometries, such as cylinders and spheres. The first large body of research on point absorber WEC arrays was carried out by Budal (1977), Evans (1980) and Falnes (1980). Here, the maximum power absorption of the array is calculated using an analytical expression, called the point absorber method. For this method to be applicable, it is necessary that the WEC's diameter is small compared to both the wave length and the inter-WEC distance. It is thus assumed that there are now interactions between the WECs. All the available semi-analytical techniques for WEC modelling are reviewed in Child (2016). At that time (seventies and eighties), computational power was limited, limiting the techniques to use linear theory. However, over the past decades, computational power has increased significantly, enabling reduction of model assumptions and resulting in the use of more complex WEC modelling methods. Despite this increase in computational power, semi-analytical models are still used for preliminary design studies of large WEC arrays and for array layout optimizations. Due to their performance, they allow for a large set of configurations to be tested.

Still assuming linear potential flow theory, more advanced techniques were developed to model complex WEC geometries. Specifically, a panel method called the Boundary Element Method (BEM) was developed in order to numerically calculate hydrodynamic properties such as added mass, hydrodynamic damping, wave diffraction, radiation and excitation forces. These coefficients are explained in detail in Chapter 3. Examples of software packages are Aquaplus (Delhommeau, 1987), ANSYS Aqwa (2018), WAMIT (2016) and Nemoh (Babarit and Delhommeau, 2015). The latter has been used in the creation of openWEC, an open-source WEC modelling tool created by the author of this manuscript, and further explained in Appendix A. These models are applied to calculated the hydrodynamic response of a WEC to an incident wave field in the frequency domain. An overview of these frequency-domain models is given in Alves (2016). These models can also be used to perform simulations of large WEC arrays because of increased available computational power. In Balitsky et al. (2017b) an optimisation algorithm for WEC array layouts was developed. Similarly, the power production of a heterogeneous array of heaving bodies was optimized using a BEM solver in Bellew et al. (2009). Comparison with experimental data and second-order models was performed in Bellew and Stallard (2010). The floater response within an array was numerically modeled and response amplitude operators (RAO) were compared to experimental data in Thomas et al. (2008). A similar approach is used to model the optimal configuration of a multi-body WEC line absorber system in Moreno (2015). Next to frequency-domain modelling, also time-domain modelling is often applied (Ricci, 2016). In certain cases, it is necessary to study the motion of a WEC in the time domain, for example when the effect of a realistic non-linear power take-off (PTO) system or when the influence of mooring lines is studied. PTO control algorithms and mooring forces are often non-linear. According to Folley et al. (2012), this makes time-domain modelling very powerful, but compared to frequency domain models, more computation time is required. Another modelling technique is the use of probabilistic models, for example spectral-domain models. Here, a statistical representation of the sea state is used and the WEC's response is predicted by a

transformation function (Folley, 2016b). A disadvantage of the time and spectral domain models is that they are restricted to linear hydrodynamics and are only valid for small amplitude waves and small motions of the WECs. Note that some time domain models allow the implementation of weakly non-linear terms such as non-linear buoyancy or viscous forces and non-linear PTO or mooring forces.

Due to the rapid increase of computational power more advanced, non-linear models could be applied for WEC modelling. A thorough review of non-linear methods used for WEC modelling can be consulted in Penalba et al. (2017). Here, the focus is put mainly on fully non-linear potential flow (FNPF) models and computational fluid dynamics (CFD) models, to which both mesh-based solvers such as finite-volume (FV) methods and mesh-free solver such as smoothed particle hydrodynamics (SPH) belong. FNPF models are more efficient in terms of computation time than CFD models. FNPF models assume an inviscid flow and are able to model steep waves and large device motions for non-breaking wave conditions (Fitzgerald, 2016). However, it is impossible for FNPF models to simulate phyiscal processes such as overturning and breaking waves, wave slamming, air entrainment, water exit or entry problems and turbulence. Furthermore, the inclusion of viscous damping forces are important to predict realistic WEC motions, especially near resonance (Li et al., 2012). Additionally, research is still lacking on the importance of non-linear potential flow effects in relation to viscous flow effects, specifically for prototype-scale WECs (Fitzgerald, 2016; Penalba et al., 2017). The WEC physics are best reproduced using a non-linear viscous computational fluid dynamics solver. An extensive review on CFD-based numerical wave tanks for high-fidelity numerical modelling of ocean wave energy systems is given in Windt et al. (2018). CFD solves the Navier–Stokes equations, representing the hydrodynamics with a very high accuracy. CFD is necessary to model complex physical processes for WEC modelling, such as wave breaking, extreme wave conditions and wave-by-wave control algorithms. In these conditions, and specifically close to resonance, viscous and non-linear effects need to be captured by the numerical model. In addition, turbulence modelling is necessary when flow separation and vortex shedding occur. Turbulent flows can be modelled using several approaches. In a direct numerical simulation (DNS), the model resolution is increased to resolve the turbulent flows. In large eddy simulations (LES), only part of the vortices is resolved by the mesh, while the other part is calculated by a turbulence model. In a Reynolds-averaged Navier–Stokes (RANS) simulation, all turbulent effects are modelled and none are resolved. For example, the drag coefficients on heaving point-absorbers were estimated using a RANS model in Gu et al. (2018). In Wolgamot et al. (2015), the use of CFD for WECs is reviewed and a comparison between CFD and experimental results has been performed for various studies, demonstrating the feasibility of CFD simulations for wave energy applications. While array modelling in CFD is very computationally expensive, it has been performed in Devolder (2018).

The above described CFD models are all mesh-based Eulerian solvers. However, Lagrangian mesh-less methods can be successfully applied for WEC modelling as well. One of these methods is the Smoothed Particle Hydrodynamics (SPH) method. Instead of grid cells, SPH uses particles which are moving inside the computational domain and estimate physical properties as a weighted average of the

neighboring particles (see Section 3.6 for a detailed theoretical background). The Lagrangian reference frame of SPH makes it useful in solving problems with large deformations and distorted free surfaces. The feasibility of using SPH for WEC modelling is reported in Verbrugghe et al. (2017a). Floating bodies in waves have been successfully studied in 2-D in Manenti et al. (2008). Monaghan et al. (2003) and (2005) have shown that their SPH method conserves both linear and angular momentum. Bouscasse et al. (2013a) has succesfully validated nonlinear water wave interaction with floating bodies in SPH, comparing results with experimental data from Hadžić et al. (2005), which include free-surface deformations due to the motion (heave, surge and pitch) and presence of floating boxes. Canelas et al. (2015) has performed several validations, analysing the buoyancy-driven motion with solid objects which are larger than the smallest flow scales and have various densities. This was done using DualSPHysics, an open-source code based on the SPH methodology. Wave generation by a heaving cylinder and incident waves interacting with a fixed cylinder were studied in Omidvar et al. (2012). 3-D problems of wave generation by a heaving cone and a floating body in waves undergoing predominantly heave motion are investigated in Omidvar et al. (2013). Specific modelling of WECs has been performed in Altomare et al. (2016b) and Chen et al. (2014) while both fixed and floating Oscillating Water Columns (OWC) have been modelled in Crespo et al. (2017) and (2018b).

2.2 Coupling methodologies for wave-structure interaction solvers

In order to study both the near-field and far-field effects, different numerical models can be merged into a coupled model. A coupled model uses the best features of each individual model to accelerate the numerical simulation and improve the total accuracy. Typically, a wave propagation model is coupled to a wave-structure interaction solver. The first is applied to calculate the incident waves and propagate the wave transformations in a large domain (far-field zone) at a low computational cost. The latter is used to calculate the hydrodynamic flow field around a WEC and its response in a relatively small domain (near-field zone) and is typically more computationally expensive.

Weakly coupled models, where one model is run before the other (1-way information transfer), have been applied to connect a Boundary Element Method (BEM) solver with a Volume-Of-Fluid (VOF) solver in Lachaume et al. (2003) and Biausser et al. (2004). Similarly, a fully non-linear potential flow (FNPF) model has been used to initialize a VOF model in Hildebrandt et al. (2013). A similar coupling is realised in Janssen et al. (2010), where a particle-based Lattice-Boltzman model is nested within the FNPF model. For linear simulation over variable bathymetry, there have been studies coupling a wave propagation model (shallow water equations or potential flow theory) and a BEM wave-structure interaction solver. This coupling methodology, applying a circular coupling zone, has been first introduced by Stratigaki et al. (2014a) and Troch and Stratigaki (2016), and was adapted and applied in Verbrugghe et al. (2017b). Recently, improvements have been made to

optimize performance and accuracy, as demonstrated by Balitsky et al. (2017a) and Verao Fernandez et al. (2017). Similar methodologies have been applied by Charrayre et al. (2014b) and Tomey-Bozo et al. (2016). The latter applies a rectangular coupling zone rather than a circular one.

Strong coupling is also evident in the literature, for example BEM-level set methods (Colicchio et al., 2006) and models where BEM is coupled to VOF (Kim et al., 2010; Guo et al., 2012). Fully nonlinear potential flow theory solvers and particle methods hybrid algorithms have also been tested with success, demonstrated by Sriram et al. (2014). Recently, the creation of hybrid models with SPH has also become popular, specifically with the adoption of Finite Volumes (FV). In Marrone et al. (2016) and Altomare et al. (2016a) a weakly compressible SPH formalism has been used, while incompressible SPH (ISPH) has been employed in a previous study by Napoli et al. (2016), where a coupling with FV was realised.

Coupling SPH solvers to other models is one of the SPHERIC Grand Challenges (`spheric-sph.org/grand-challenges`). A general algorithm for one-way coupling of SPH with an external solution has been proposed in Bouscasse et al. (2013b). The interaction between the SPH solver and the external solution is achieved through an interface region containing a ghost fluid, used to impose any external boundary condition. In Fourtakas et al. (2018), A hybrid Eulerian-Lagrangian incompressible SPH formulation is introduced, where two different SPH formulations are coupled rather than two completely different solvers. The SPH solver DualSPHyics has been coupled in Altomare et al. (2016a) and (2018a), where a one-way coupling was realized with the wave propagation model SWASH. A numerical wave flume has been created to simulate wave impact and run-up on a breakwater. The first part of the numerical flume is simulated using the faster SWASH model, while the wave impact and run-up are calculated using DualSPHysics. Here, a one-way coupling is sufficient, since there is only interest in the impact of waves on the breakwater. In Kassiotis et al. (2011), a similar approach has been adopted, where a 1D Boussinesq-type wave model is applied for wave propagation in most of the spatial domain, and SPH computations focus on the shoreline or close to off-shore structures, where a complex description of the free-surface is required. In Narayanaswamy et al. (2010), the Boussinesq model FUNWAVE was coupled to DualSPHysics, where the key development was the definition of boundary conditions for both models in the overlap zone. A wave generator in SPH moved according to the velocities from the adjacent Boussinesq nodes. Similarly, an incompressible SPH solver has been coupled to a non-linear potential flow solver QALE-FEM in Fourtakas et al. (2017). In Chicheportiche et al. (2016), a one-way coupling between an potential Eulerian model and an SPH solver is realised, applying a non-overlapping method using the unsteady Bernoulli equation at the interface. In Chang et al. (2018), both a 1-D and 2-D coupling between SPH and a shallow water equation (SWE) model was realised to simulate open channel flows. These studies applied coupling to speed up the simulation time by minimizing the computationally intensive SPH domain. Other studies apply coupling to combine both the benefits of mesh-based and mesh-free CFD methods. In Didier et al. (2013), the wave propagation model FLUINCO is coupled to an SPH code, and validated with experimental data of wave impact on

a porous breakwater. A hybrid multiphase OpenFOAM-SPH model is presented in Kumar et al. (2015), where the SPH method is used on free surfaces or near deformable boundaries whereas OpenFOAM is used for the larger fluid domain. A similar coupling is used, where breaking waves are modelled with SPH and the deeper wave kinematics are modelled with a FV method. This has been demonstrated in Marrone et al. (2016) for a weakly-compressible SPH (WCSPH) solver and in Napoli et al. (2016) for an incompressible SPH (ISPH) solver.

2.3 Wave generation and absorption in SPH

To date, in SPH modelling, two main approaches have been used (Altomare et al., 2017):

- moving boundary generation;
- internal generation;

Internal wave generation with a non-reflective internal wavemaker algorithm has been proposed by Lin and Liu (1999). Thre, the Boussinesq equations are used to derive a momentum source term, which is added into an Incompressible SPH model using the Lagrangian Navier–Stokes equations. The most common wave generation method in SPH is the moving boundary generation. This mechanism tries to translate the mechanical wave generation techniques of experimental facilities directly into the numerical model. A moving boundary is implemented as a numerical wavemaker that generates and absorbs waves. Examples of this generation method can be found in Didier and Neves (2012); Manenti et al. (2008); Meringolo et al. (2015); Altomare et al. (2017). A 2-D numerical wave tank was presented in Ni and Feng (2013). This wave tank was based on the open-source SPH-based DualSPHysics model (Crespo et al., 2015). Source generation was applied and wave absorption was performed using analytical relaxation approach. In this study, instead of moving boundaries, water particles inside the source generation zone move according to periodical velocities calculate with Stokes wave theory. However, only regular wave cases were validated using this approach. Neither irregular waves nor second-order bound long waves were simulated. Additionally, this type of wave generation technique has a higher computational cost than wave generation with moving boundaries. This is due to the large number of water particles needed in both the generation zone and the sponge layers (Ni et al., 2014). In Altomare et al. (2018b), the relaxation zone method was successfully implemented into DualSPHysics, acting as an internal wave maker and allowing coupling to other models or analytical solutions. An absorbing wavemaker was implemented in the SPHysics model (Gomez-Gesteira et al., 2012) by Wen et al. (2016). However, only linear wave theory was applied to generate the waves and only regular wave tests were considered. Omidvar et al. (2013) used an irregular wave generation based on the linear wave theory to generate focused waves. Neither super nor subharmonic components were considered in their approach. Recently, Ni et al. (2018) presented a wave generation and absorption technique with non-reflective open boundaries, very similar to the method introduced in this work. However, there are some key

differences rendering the method described in this work more flexible than the one introduced by Ni et al. (2018), which will be discussed in section 6.2.2.

In addition to wave generation, wave absorption is equally important in any physical or numerical model within coastal engineering. Wave absorption is specifically necessary to damp the wave energy and reduce the reflections generated by the domain boundaries. This can be done using passive wave absorber systems, which can be established by placing a gentle slope, porous material or screens in front of the boundaries. Like this, a large amount of the incident wave energy can be dissipated. Dimensions of passive wave absorption systems typically depend on the specific wave conditions. An exponential wave damping zone was applied in Lind et al. (2012). In DualSPHysics, a similar algorithm is implemented and introduces a damping region in the fluid domain (Altomare et al., 2017). The numerical algorithm is very similar to application of sponge areas or porous materials in physical model tests.

Passive absorption is not sufficient when waves interact with structures; active wave absorption system is then needed. In active absorption, the wave generation method is corrected in order to remove the reflected waves present in the domain and to damp the re-reflection phenomenon. With moving wave generators, such as paddles and flaps, the corrected wavemaker displacement in function of time is obtained by transforming the original wave signal, to which an appropriate filter is applied. This filter can be a time-domain or frequency-domain filter. In literature, there are differences noticeable in the type of feedback correction signal used. In Schäffer and Klopman (2000); Altomare et al. (2017), the free-surface elevation at the wavemaker is used, while free-surface elevation and/or orbital velocities at a fixed position in the fluid domain were used by Frigaard and Christensen (1995). In Salter (1981), forces acting on the wavemaker were measured and used to calculate the correction signal. The active wave absorption algorithm developed in this work applies velocity corrections to the wave generator and wave absorber, based on the measured surface elevations within the fluid domain, and thus relates the most to Schäffer and Klopman (2000) and Altomare et al. (2017).

2.4 Knowledge gaps

Based on the literature review, the following knowledge gaps can be identified:

- There is a lack of numerical tools to model both near-field and far-field effects of floating WECs over variable bathymetry.
- No coupling has been performed yet between a BEM solver and a FNPF solver.
- There are no SPH models which have been coupled to a FNPF solver using moving boundaries at the interface.
- A 2-way coupling between SPH models and wave propagation models has never been done.

- Open boundaries have not been applied yet to generate and absorb waves in DualSPHysics.
- There are no SPH models which have been coupled to a FNPF solver using open boundaries at the interface.

2.5 Objectives and methodology

In this work, fundamental research is performed to fill the knowledge gaps defined in section 2.4. The connection between the identified gaps, the pursued objectives and the applied methodology to achieve the objectives is illustrated in Figure 2.1. The following objectives have been set to fill the knowledge gaps:

1. Development of a linear coupling methodology between a BEM solver and FNPF solver;
   A linear coupling methodology between the BEM solver Nemoh and the FNPF solver OceanWave3D is developed. This allows to model linear wave-structure interactions of WECs and WEC arrays and propagate the resulting wave transformations over a large domain with variable bathymetry.
2. Development of a 2-way non-linear coupling between an SPH solver and a FNPF solver;
   A non-linear coupling methodology between the SPH solver DualSPHysics and the FNPF solver OceanWave3D. The coupling is developed in two versions: one with moving boundaries and one with the recently introduced open boundaries.
3. Wave generation and absorption in DualSPHysics with open boundaries;
   The recently introduced open boundaries allow for flows to freely enter and exit the DualSPHysics domain. In this work, these boundaries are applied to generate, propagate and absorb waves using an inlet and outlet zone with buffer particles, and impose a corrected velocity profile to those particles.

To achieve these objectives, both a linear and non-linear coupling methodology are developed. First, a linear coupling between the BEM solver Nemoh and the FNPF solver OceanWave3D is realised. Since linear theory is applicable, the coupling can apply the superposition principle: the total wavefield around a WEC array is obtained by superposing incident and perturbed wavefields. The incident wavefield is propagated over a large OceanWave3D domain, with an optional variable bathymetry. The perturbed wavefield can be calculated by Nemoh, in a small domain around the WEC array, and propagated further in the large OceanWave3D domain. Both resulting wavefields are summed to obtain the total wavefield. The methodology is validated by comparing the results to an alternative wave propagation model MILDwave and by comparing results to experimental data from the WECwakes project. The non-linear coupling methodology cannot apply the superposition principle, thus an online non-linear coupling is needed. The SPH solver DualSPHysics is nested into the FNPF solver OceanWave3D. At the coupling interfaces, surface elevations and orbital velocities are measured in OceanWave3D

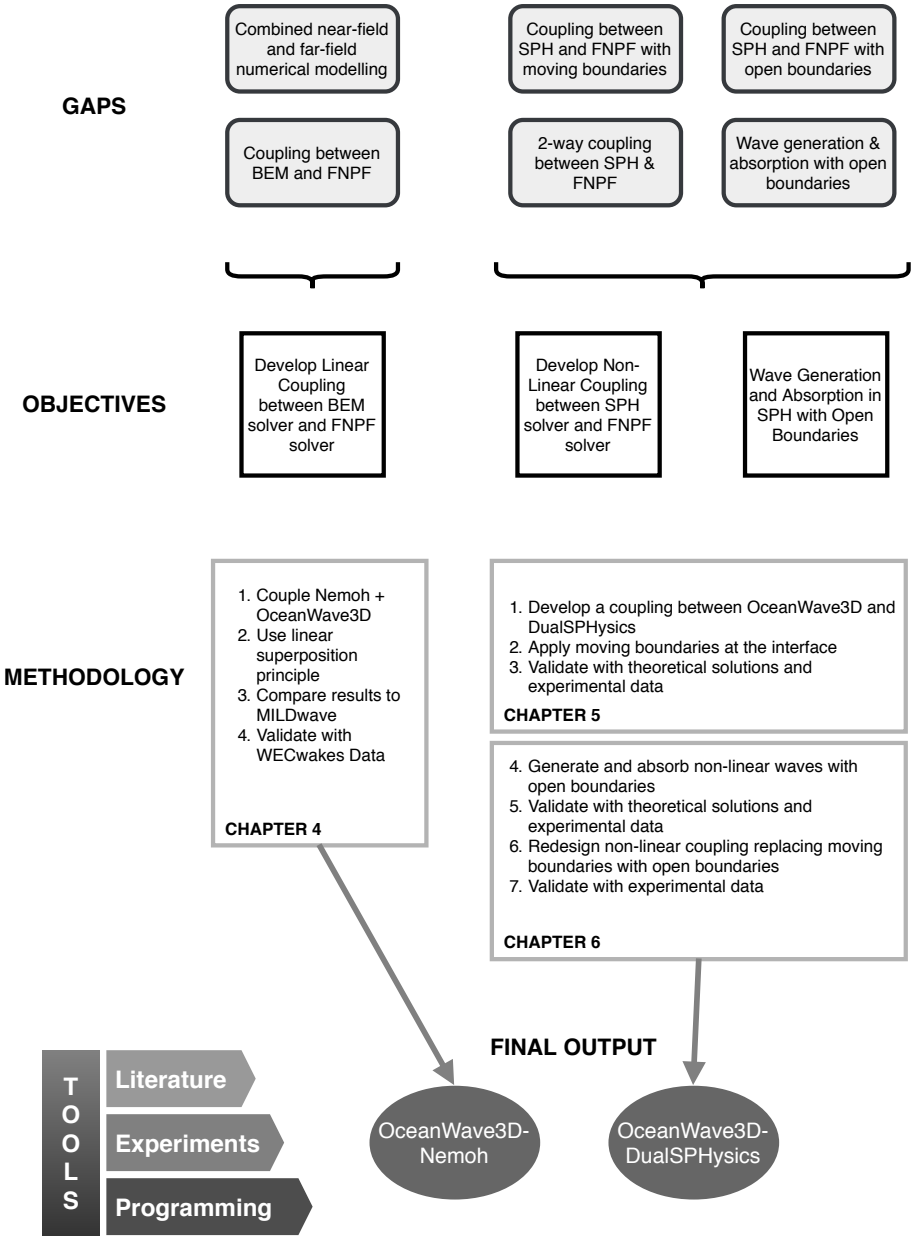

Figure 2.1: Flowchart of the identified knowledge gaps, pursued objectives and the applied methodology to achieve them.

and imposed on the SPH particles. In a first coupling version, moving boundaries with dynamic boundary particles are used to transfer the orbital velocities. A second version applies open boundaries where buffer particles are used to generate and absorb the waves. However, the validity of using open boundaries for wave generation and absorption in DualSPHysics is first studied. Validation is done with theoretical solutions and experimental data. The DualSPHysics surface elevations can be sent back to OceanWave3D, overwriting the original solution, resulting in a 2-way coupling. Like this, wave transformations occurring in the DualSPHysics domain can propagate further in the OceanWave3D domain. All coupling methodologies are validated with experimental data or theoretical solutions. A final 3D coupling is demonstrated in a proof-of-concept where a comparison is made with experimental tests performed in the large wave flume at Ghent University.

Chapter 3

Theoretical Background

In this chapter, a detailed theoretical background is provided for readers who are not familiar with the topics discussed in this manuscript. It starts with an elementary introduction of the linear wave theory, but gradually gets more complex explaining the radiation problem, setting up the motion equation for floating bodies and providing the theoretical background for the software packages used.

3.1 Introduction to water waves

The response of a WEC to specified sea states requires knowledge of the physics of water waves. When people talk about waves, they mostly think about nice sinusoidal movement of the water surface. Although similar patterns are found in nature in the form of swell or regular waves, mostly the sea surface is characterised by a chaotic three dimensional wave pattern, called irregular waves. The response of the WEC will thus also be irregular and three-dimensional. It is challenging to comprehend the full complexity of this time-varying surface. The irregularity of waves can however be approximated through the superposition of multiple regular wave layers, each with different wavelengths, amplitudes, wave periods, angles and phases. In 2-D the surface elevation of the ocean can be described by equation 3.1. Figure 3.1 shows the principle for 3-D waves.

$$\eta(x,t) = \sum_{i=1}^{n} a_i \cdot \sin\left(k_i x - \omega t\right) \tag{3.1}$$

Here, η is called the surface elevation, depending on the position x and time t. The wave amplitude of component i is denoted a_i, while k_i is the wave number and ω the wave frequency. Underneath the surface of the waves, the water particles move along circular and elliptical paths. These orbital motions are the greatest near the free surface and their motion is restricted towards the sea bottom. They are very important in the interaction with floating and submerged bodies.

Once the wave theory is established, the response of the WEC can be studied

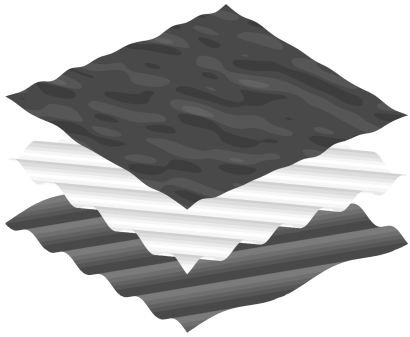

Figure 3.1: Irregular waves superposition principle

by determining all acting and counteracting forces. The motion equation is then derived as a classical spring-mass-damper system. Lastly it is investigated how the energy absorption of a WEC can be optimised.

3.2 The Linear Wave Theory

3.2.1 Introduction

In the 19^{th} century George B. AIRY published the linear wave theory, a first-order small-amplitude theory which up to this day is still used as a basis for many theories in ocean and coastal engineering (Airy, 1841). It describes all characteristics of a regular sinusoidal wave in a vertical two dimensional space-time coordinate system. In what follows the theory will be discussed step by step, using the Coastal Engineering Manual (of Engineers, 2002) as a guideline.

Ocean waves with periods ranging from 3 to 25 seconds are primarily wind-generated. Other waves like tidal waves and internal waves are not within the scope of this study. The linear wave theory aims at developing an understanding of surface gravity wave mechanics through the examination of waves with constant amplitudes and periods.

The AIRY theory builds on a number of assumptions in order to obtain a first-order mathematical expression. The theory proves to be very useful providing the assumptions are not strongly violated:

- The fluid is homogeneous and incompressible (ρ is constant)
- Surface tension can be neglected
- The Coriolis effect can be neglected
- The pressure at the free surface is constant and uniform

- The fluid is ideal or inviscid
- There is no interaction with other water motions, the flow is irrotational (only normal forces, shear forces are neglected)
- The bed is a flat, fixed, impermeable boundary (the vertical velocity at the bottom is zero)
- The wave amplitude is small in relation to the wavelength and the waveform is invariant in time and space
- Waves are plane or long-crested (2-D)

3.2.2 Wave parameters

Waves are characterised by a number of parameters. Figure 3.2 illustrates the different wave parameters. A regular wave is represented by the spatial variable x ,the temporal variable t or the combination of both, the phase $\theta = kx - \omega t$. The value of θ varies between 0 and 2π.

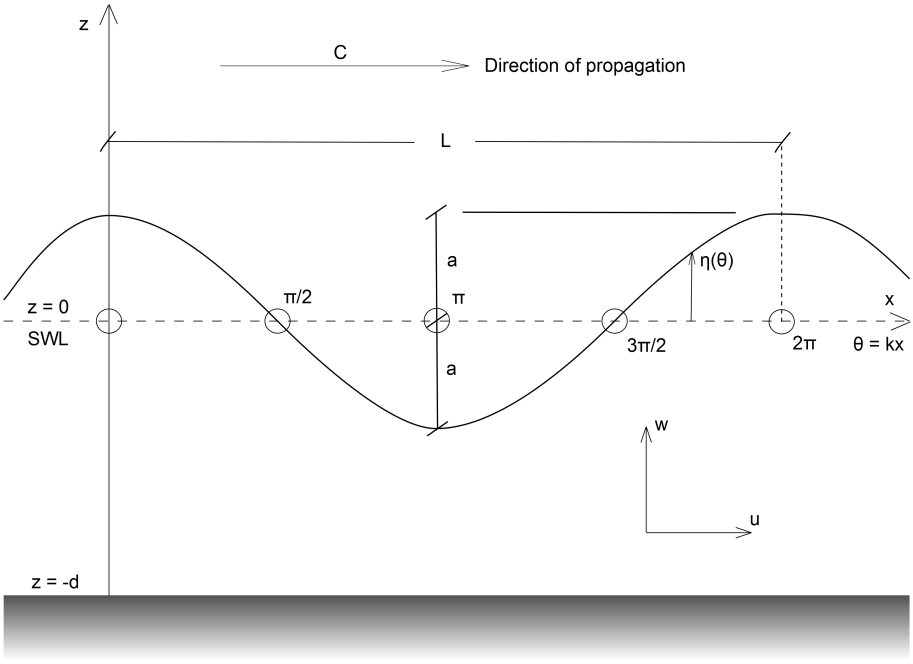

Figure 3.2: Wave parameters

The characterisation of a linear wave is completed by the wave height $H = 2a$, the wavelength L and the water depth d. The highest point of the wave is called the crest, while the lowest point is the trough. The height of the crest above the still water level (SWL) is the wave amplitude a. The time interval between

two crest (or trough) passages is called the wave period T. The wave length L is the distance between two wave crests if a snapshot of the moving wave is taken. Other parameters can be deduced from these. the angular frequency ω is defined as $\omega = 2\pi/T$, the wave number is $k = 2\pi/L$, the wave celerity is $C = L/T$ and the wave steepness is $\epsilon = H/L$.

3.2.3 Velocity Potential

Previously the assumption of irrotationality was made, neglecting all shear forces on the water particles. This assumption allows introducing the velocity potential $\phi(x, z, t)$, a scalar function of which its partial derivatives are the horizontal and vertical particle velocities u and w (see equation 3.2 and 3.3).

$$u = \frac{\partial \phi}{\partial x} \tag{3.2}$$

$$w = \frac{\partial \phi}{\partial z} \tag{3.3}$$

Due to the inviscid and incompressible behaviour of the ideal fluid, the velocity at each point will satisfy equation 3.4, the continuity equation. Replacing the velocities with equations 3.2 and 3.3, the well known Laplace Equation in ϕ is found (equation 3.5).

$$\frac{\partial u}{\partial x} + \frac{\partial w}{\partial z} = 0 \tag{3.4}$$

$$\frac{\partial^2 \phi}{\partial x^2} + \frac{\partial^2 \phi}{\partial z^2} = 0 \tag{3.5}$$

3.2.4 Boundary conditions

In order to solve the partial differential equation, boundary conditions need to be defined. Firstly the bottom is considered impermeable, thus the vertical velocity should be zero at all time (equation 3.6). Secondly a fluid particle at the free surface should remain at the surface at all times. This kinematic boundary condition is expressed in equation 3.7. Another boundary condition at the free surface dictates that the pressure p at the surface must be equal to the atmospheric pressure, which we assume to be constant. This dynamic boundary condition is formulated in equation 3.8 and is derived from the Bernoulli Equation.

$$w(x, z = -d, t) = \frac{\partial \phi}{\partial z}(x, z = -d, t) = 0 \tag{3.6}$$

$$\frac{\partial \eta}{\partial t} + u\frac{\partial \eta}{\partial x} = w \tag{3.7}$$

$$\frac{p}{\rho} + \frac{\partial \phi}{\partial t} + \frac{1}{2}(u^2 + w^2) + g\eta = 0 \tag{3.8}$$

No complete solution is known for this mathematical problem, although it can be found for some special cases. Assuming the free surface elevation $\eta(x,t)$ is very small relative to the wavelength L, a solution can be found by linearizing the equations through scaling and dimensional analysis.

3.2.5 Solutions of the Linear Wave Theory

The solution of the differential problem delivers the three core aspects of the linear wave theory: the velocity potential ϕ, the free surface elevation η and the dispersion relation. The latter describes the fixed relation between the wave frequency and the wave number. From these three base equations all characteristics of the regular wave can be deduced. Due to the asymptotic behaviour of hyperbolic functions, simplifications are possible. Mostly the factor kd, with k the wave number and d the water depth, is found inside the hyperbolic functions, which mean there are alternate formulations available for deep (kd is large) and shallow (kd is small) water, relative to the wavelength L. The most important deduced wave parameters are listed in table 3.1.

$$\phi(x,z,t) = \frac{ag}{\omega}\frac{\cosh(k(z+d))}{\cosh(kd)}\cos(\omega t - kx) \tag{3.9}$$

$$\eta(x,t) = a\sin(\omega t - kx) \tag{3.10}$$

$$\omega^2 = gk\tanh(kd) \tag{3.11}$$

The hyperbolic functions dictate the depth-related behaviour of the water particles. The motion of the particles is negligible deeper than half a wavelength under the free surface. Also in deep water the particles describe circular motions, while the trajectories become more and more elliptical. In shallow water the particle motion is not negligible at the bottom. The particle ellipses gradually flatten from the free surface to the bottom, where a pure horizontal oscillating motion is retained (see figure 3.3).

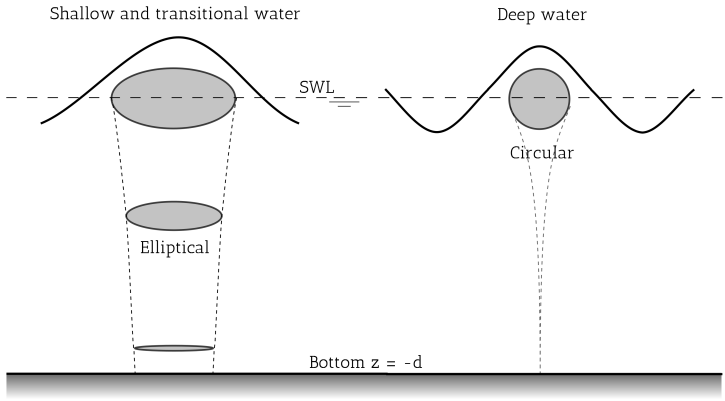

Figure 3.3: Wave orbital motions

		Water depth		
Quantity	**Symbol**	**Deep**	**Shallow**	**Intermediate**
	kd	$\geq \pi$	$0 - \pi/10$	$\pi/10 - \pi$
Dispersion Relation	ω	$\sqrt{gk}$	$k\sqrt{gk}$	$\sqrt{gk\tanh(kd)}$
Celerity	C	$\frac{gT}{2\pi}$	$\sqrt{gd}$	$\frac{gT^2}{2\pi}\tanh(kd)$
Group Speed ratio	n	$\frac{1}{2}$	1	$\frac{1}{2}\left(1 + kd\frac{1-\tanh^2(kd)}{\tanh(kd)}\right)$
Horizontal velocity	$u(x,z,t)$	$a\frac{gT}{L}e^{kz}\cos(\theta)$	$\sqrt{\frac{g}{d}}a\cos(\theta)$	$a\frac{gT}{L}\frac{\cosh(k(z+d))}{\sinh(kd)}\cos(\theta)$
Vertical velocity	$w(x,z,t)$	$a\frac{gT}{L}e^{kz}\sin(\theta)$	$\frac{gT}{L}a\frac{z+d}{d}\sin(\theta)$	$a\frac{gT}{L}\frac{\sinh(k(z+d))}{\sinh(kd)}\sin(\theta)$
Horizontal excursion	$\xi(x,z,t)$	$-ae^{kz}\sin(\theta)$	$\frac{1}{kd}a\sin(\theta)$	$-a\frac{\cosh(k(z+d))}{\sinh(kd)}\sin(\theta)$
Vertical excursion	$\zeta(x,z,t)$	$ae^{kz}\cos(\theta)$	$\frac{z+d}{d}a\cos(\theta)$	$a\frac{\sinh(k(z+d))}{\sinh(kd)}\cos(\theta)$
Pressure oscillation	$p(x,z,t)$	$pga\, e^{kz}\cos(\theta)$	$pga\ \cos(\theta)$	$pga\ \frac{\cosh(k(z+d))}{\cosh(kd)}\cos(\theta)$

Table 3.1: Linear Wave Theory quantities

3.2.6 Wave Energy

An important quantity to be studied is the amount of wave energy transported within a wave. The total energy of the wave system is calculated by taking the sum of the potential energy E_p and kinetic energy E_k. The latter is the energy carried by the moving water particles, while the first originates from the part of the fluid mass above the SWL, the wave crest. The kinetic energy is calculated in equation 3.12, while the potential energy is formulated as equation 3.13. According to the AIRY theory the potential equals the kinetic energy and their sum is equation 3.14. The total energy per unit surface area, the specific energy or energy density, is shown in equation 3.15.

$$\bar{E_k} = \int_x^{x+L} \int_{-d}^{\eta} \rho \frac{u^2 + w^2}{2} dz\, dx = \frac{1}{16} \rho g H^2 L \tag{3.12}$$

$$\bar{E_p} = \int_x^{x+L} \rho g \left[\frac{(\eta + d)^2}{2} - \frac{d^2}{2} \right] dx = \frac{1}{16} \rho g H^2 L \tag{3.13}$$

$$E = \frac{1}{8} \rho g H^2 L \tag{3.14}$$

$$\bar{E} = \frac{E}{L} = \frac{1}{8} \rho g H^2 \tag{3.15}$$

The wave energy flux is the rate of energy transport in the direction of wave propagation. It is calculated across a vertical plan perpendicular to the direction of wave direction and integrated over the entire depth. Equation 3.16 describes the energy flux and shows that wave energy is transported with the group velocity rather than the phase velocity.

$$\bar{P} = \frac{1}{T} \int_t^{t+r} \int_{-d}^{\eta} p\, u\, dz\, dt = \bar{E} n C = \bar{E} C_g \tag{3.16}$$

3.3 Free-floating body

A body freely floating on the ocean waves has 6 degrees of freedom: 3 translations and 3 rotations (see figure 3.4). Some bodies are restricted to one or more degrees of freedom. For example, the point-absorber WEC described in Chapter 4 of this PhD is restricted to the heaving motion. However for this theoretical background all degrees of freedom are used. The displacement is formulated by a six-dimensional vector ξ while the velocities are presented by the vector $\mathbf{v}$.

As with linear wave theory, a velocity potential is needed. The function not only has to satisfy the boundary conditions for a regular wave, also an extra boundary

condition is required at the interface between the free floating body and the water as well as a boundary at infinity. To obtain these conditions the problem is split up in 2 sub problems. The radiation problem describes the forced motion of a body in originally still water. The diffraction problem studies the forces on a fixed body in a regular wave field (see figure 3.5). The steps followed in this section are mainly based on the work of De Backer (2009).

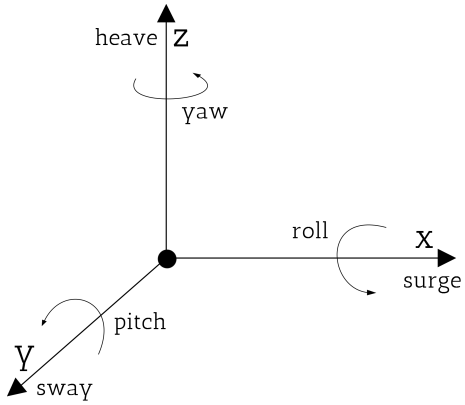

Figure 3.4: 6 degrees of freedom of a free floating body

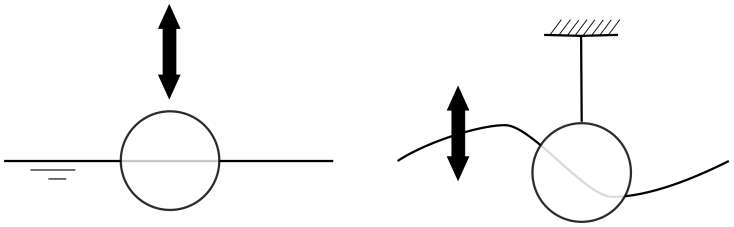

Figure 3.5: Radiation (left) and Diffraction (right) sub problems

3.3.1 Radiation Problem

The first sub problem assumes an initial still water level. A sinusoidal motion is then forced on the free floating body. This motion will radiate waves resulting in a flow described by the radiation potential function ϕ_R. In equation 3.17 $\phi_i^{(1)}$ is the potential per unit displacement amplitude in mode i.

$$\phi_R = \sum_{i=1}^{6} \xi_i \phi_i^{(1)} \tag{3.17}$$

The radiation potential must satisfy the previous boundary conditions and the boundary conditions at the water-body interface. The vector $\mathbf{n}$ is a unit vector with direction normal to the ξ vector. Secondly a radiation condition at infinity must

be satisfied, called the 'far field radiation condition'. It expresses the conservation of energy principle in equation 3.19. Here R_b is the distance to the body and C_f is a constant. The conservation principle is expressed through dividing by $\sqrt{R_b}$.

$$\frac{\partial \phi_i}{\partial n} = v_i n_i \tag{3.18}$$

$$\phi_i = jC_f \frac{e^{jkR_b}}{\sqrt{R_b}} \ for\ R_b \rightarrow \infty \tag{3.19}$$

3.3.2 Diffraction problem

Secondly the device is fixed in all degrees of freedom within a regular wave field. Waves hitting the body will be diffracted and a flow is induced described by the diffraction potential ϕ_D. This diffraction potential must fulfill the laplace equation (3.5), the boundary condition on the bottom (3.6) and the ones on the free surface (3.7 and 3.8). An extra boundary condition is necessary on the water-body interface S_b. There the continuity of the incident (ϕ_I) and diffracted potential must be satisfied leading to equation 3.20.

$$\frac{\partial \phi_D}{\partial n} = -\frac{\partial \phi_I}{\partial n} \ on\ S_b \tag{3.20}$$

The same far-field boundary condition (equation 3.19) as in the radiation problem applies here. Thus only the boundary condition at the body surface differs from the boundary conditions of the radiation potential. Here the body has a predefined velocity normal to the body surface.

3.3.3 Forces and pressure

Now that the radiation and diffraction potential functions are defined together with their boundary conditions, they can be combined into a total velocity potential ϕ. Assuming all three functions are harmonic with a frequency ω, ϕ can be expressed as in equation 3.21. The hat symbols indicate the complex nature of the amplitude of the velocity potential and body displacement vector.

$$\begin{aligned} \phi &= \phi_I + \phi_R + \phi_D \\ &= \mathrm{Re}\left[\left(\sum_{i=1}^{6} \hat{\xi}_i \hat{\phi}_i + \hat{\phi}_I + \hat{\phi}_D\right) e^{j\omega t}\right] \end{aligned} \tag{3.21}$$

Using the BERNOULLI equation, the pressure can be obtained from the total velocity potential. For this we assume the reference (atmospheric) pressure to be $p_0 = 0$.

$$\begin{aligned} p &= -\rho \frac{\partial \phi}{\partial t} - \rho g z \\ &= -\rho \mathrm{Re}\left[j\omega \left(\sum_{i=1}^{6} \hat{\xi}_i \hat{\phi}_i + \hat{\phi}_I + \hat{\phi}_D\right) e^{j\omega t}\right] - \rho g z \end{aligned} \tag{3.22}$$

By integrating the pressure acting on the body surface S_b , the hydrodynamic forces F_h and moments M_h can be found. In equations 3.23 and 3.24 $\mathbf{n}$ is the normal vector and $\mathbf{r}$ is the position vector. The total force vector is described as $\mathbf{F}$.

$$F_h = \iint_{S_b} p\mathbf{n}\,\mathrm{d}\mathbf{S} \tag{3.23}$$

$$M_h = \iint_{S_b} p(\mathbf{r}\times\mathbf{n})\,\mathrm{d}\mathbf{S} \tag{3.24}$$

In equation 3.22 the integration over S_b of the three terms inside the brackets is now discussed. The force resulting from integration of the first term is called the radiation Force F_{rad} . It consists of a part proportional to the body's acceleration and of a part proportional to the velocity. The first is multiplied by the constant $m_{a_{ji}}$, called the added mass/inertia and the latter one is multiplied by the constant $b_{hyd_{ji}}$, called the hydrodynamic damping coefficient. The index i denotes the direction of oscillation and j is the direction of the force acting upon the body.

$$F_{rad,j} = \sum_{i=1}^{6} -m_{a_{ji}}\frac{\mathrm{d}^2\xi_i}{\mathrm{d}t^2} - b_{hyd_{ji}}\frac{\mathrm{d}\xi_i}{\mathrm{d}t} \tag{3.25}$$

Integrating the second term results in the force contained by the incident wave potential. This force is called the FROUDE-KRYLOV force. It is the force acting on the body as if the body itself does not disturb the wave field. Integration of the third term results in the diffraction force. Mostly the sum of the FROUDE-KRYLOV force and the diffraction force is referred to as the exciting force F_{ex} . Lastly integrating the last term (outside the brackets) of equation 3.22 and subtracting gravity forces results in the hydrostatic restoring force F_{res} .

Setting up the motion equation always starts with the NEWTONś second law of motion. It dictates that the force acting on a body is proportional to thre rate of change of momentum. It means that in order to change the state of motion of an object, there has to be an internal or external force acting on the body (see equation 3.26).

$$m\cdot\mathbf{a} = \sum\mathbf{F} \tag{3.26}$$

Applying the second law of motion to the free floating body results in:

$$\sum_{i=1}^{6}\left[(m_{ji}+m_{a_{ji}})\frac{\mathrm{d}^2\xi_i}{\mathrm{d}t^2} + b_{hyd_{ji}}\frac{\mathrm{d}\xi_i}{\mathrm{d}t} + c_{ji}\xi_i\right] = \hat{F}_{ex_j}e^{j\omega t} \tag{3.27}$$

If all degrees of freedom are considered, then m_{ji} , $m_{a_{ji}}$, $b_{hyd_{ji}}$ and c_{ji} are all 6×6 matrices housing the coefficients for their specific degree of freedom.

Equation 3.27 is a set of coupled differential equations. This set simplifies to a single differential equation when only one degree of freedom is chosen. In the next section the solution of the motion equation is discussed for the heaving motion of a floating body.

3.4 Solving the Point-absorber Motion Equation

In this section the motion equation for the heaving motion of a point-absorber WEC is solved. First the system is assumed to be a classic spring-mass-damper system with an external harmonic force. In this way the dynamic behaviour of the body itself is studied. Secondly the hydrodynamic forces are added and the total response of a point-absorber WEC to a harmonic exciting force is studied.

$$(m + m_a)\frac{\mathrm{d}^2 z}{\mathrm{d}t^2} + b_{hyd}\frac{\mathrm{d}z}{\mathrm{d}t} + cz = F_{ex} \cdot e^{j\omega t} \tag{3.28}$$

3.4.1 Spring-mass-damper system

First a classic forced spring-mass-damper system is studied. The external force is harmonic with amplitude F_A and frequency ω (see figure 3.6).

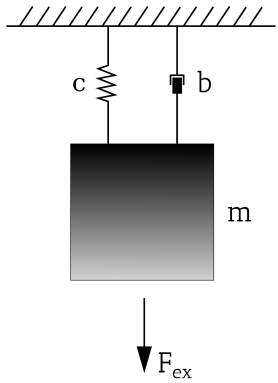

Figure 3.6: Classic forced mass-spring-damper system

The system is solved for its complementary function which arises solely due to the system itself (no external force applied). The equation of motion simplifies to:

$$m\frac{\mathrm{d}^2 z}{\mathrm{d}t^2} + b\frac{\mathrm{d}z}{\mathrm{d}t} + cz = 0 \tag{3.29}$$

It is easily seen that the solution to this partial differential equation is of the form $a \cdot e^{\lambda t}$. Substituting this into equation 3.29 results in a simple quadratic equation in λ.

$$\begin{aligned} \left(m\lambda^2 + b\lambda + c\right) \cdot ae^{\lambda t} &= 0 \\ m\lambda^2 + b\lambda + c &= 0 \end{aligned} \tag{3.30}$$

The solution to equation 3.30 is given in equation 3.30 and depends on the value of $b^2 - 4cm$. Depending on its sign the roots will either be real or complex. If the value is zero the system is critically damped. In this state the system returns to its equilibrium position in the fastest manner without any oscillations.

$$\lambda_{1,2} = \frac{-b \pm \sqrt{b^2 - 4cm}}{2m} \tag{3.31}$$

The roots can be rewritten into equation 3.34 with the introduction of two widely used variables: the natural frequency ω_n and the damping ratio ζ.

$$\omega_n = \sqrt{\frac{c}{m}} \tag{3.32}$$

$$\zeta = \frac{b}{2m\omega_n} \tag{3.33}$$

$$\lambda_{1,2} = -\zeta\omega_n \pm \omega_n\sqrt{\zeta^2 - 1} \tag{3.34}$$

The damping behaviour of the system now depends on the value of $\zeta^2 - 1$. Three different states are defined and visualised in figure 3.7.

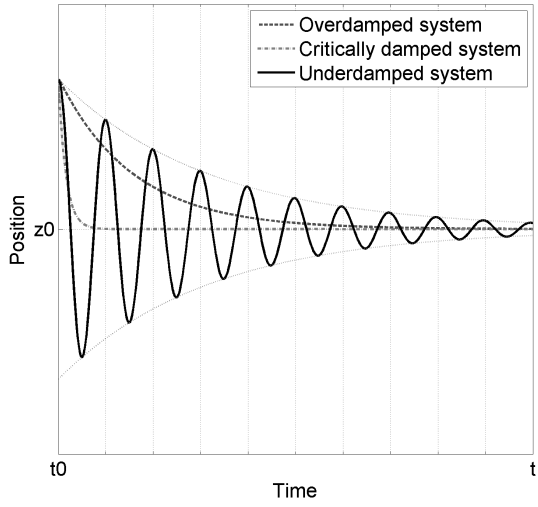

Figure 3.7: Damping modes of an unforced mass-spring-damper system

- $0 < \zeta < 1$: The roots of the equation are a pair of complex conjugates. The response of the system is sinusoidal with an exponential decaying amplitude. The system is underdamped.
- $\zeta > 1$: The roots of the equation are a pair of real numbers. Their are no complex variables, thus the response is non-oscillatory with exponential decay. The system is overdamped.

- $\zeta = 1$: There is one real solution to the problem. The system is critically damped and returns to its equilibrium in the fastest way without oscillating.

The heaving motion of a point-absorber WEC is a typical example of an underdamped system. In this mode the body makes oscillations around its equilibrium position with exponentially decreasing amplitudes. The roots in equation 3.34 are substituted in the general solution $a \cdot e^{\lambda t}$, resulting in equation 3.35. For this the damped natural frequency is introduced, calculated as $\omega_d = \sqrt{1-\zeta^2} \cdot \omega_n$. Using the Euler identity, equation 3.35 can be rewritten in a more simplified form.

$$z(t) = e^{-\zeta\omega_n t} \cdot \left(a_1 e^{i\omega_d t} + a_2 e^{-i\omega_d t}\right) \tag{3.35}$$

$$z(t) = A \cdot e^{-\zeta\omega_n t} \cdot \sin\left(\omega_d t + \phi\right) \tag{3.36}$$

In equation 3.36 A and ϕ are constants, depending on the initial conditions of the system. The initial position and the initial velocity are needed to determine both constants. The first one is easily found by setting $t = 0$ in equation 3.36. For the latter the equation must be derived to t and then $t = 0$ should be substituted. The constants are then found as:

$$A = \sqrt{\frac{\omega_d^2 x_0^2 + (v_0 + \zeta\omega_n x_0)^2}{\omega_d^2}} \tag{3.37}$$

$$\phi = \tan^{-1}\left(\frac{\omega_d x_0}{v_0 + \zeta\omega_n x_0}\right) \tag{3.38}$$

Now the complementary function is known, the external force can be applied. The reaction of the system solely due to the applied force is called the particular solution. The total solution is then found as a superposition of the complementary function and particular solution.

Due to the fact that the external force has a sinusoidal profile and the system described is a linear system, the response will also be a steady-state sinusoidal motion. The particular solution is thus of the form:

$$z(t) = z_A \cdot \sin\left(\omega t + \epsilon\right) \tag{3.39}$$

Here z_A is the amplitude of the steady-state motion and ϵ is the phase shift relative to the applied force. By substituting equation 3.39 into the main motion equation, the two constants can be calculated.

$$z_A = \frac{F_A}{\left[(c - m\omega^2)^2 + (b\omega)^2\right]^{1/2}} \tag{3.40}$$

$$\tan\epsilon = \frac{-b\omega}{c - m\omega^2} \tag{3.41}$$

The total response of a spring-mass-damper system to a sinusoidal exciting force is finally calculated as the sum of the complementary function and the particular solution:

$$z(t) = A \cdot e^{-\zeta\omega_n t} \cdot \sin\left(\omega_d t + \phi\right) + z_A \cdot \sin\left(\omega t + \epsilon\right) \tag{3.42}$$

3.4.2 Point-absorber motion equation

Although the dynamic behaviour of a point-absorber WEC shows large resemblances with a classic spring-mass-damper system, it is a little bit more complex. An important difference is the introduction of the damping force F_{damp}, the PTO force applied to absorb the energy, and the tuning force F_{tun}, an invested force to perform phase-control on the device. The complete motion equation is given in equation 3.43.

$$m\frac{\mathrm{d}^2 z}{\mathrm{d}t^2} = F_{ex} + F_{rad} + F_{res} + F_{damp} + F_{tun} \tag{3.43}$$

The exciting wave force is given by F_{ex}. The radiation force has already been discussed in section 3.3.1. It is characterised by a part proportional to the acceleration and a part proportional to the velocity. In the first term the parameter m_a is called the added mass, while b_{hyd} is the hydrodynamic damping coefficient.

$$F_{rad} = -m_a(\omega)\frac{\mathrm{d}^2 z}{\mathrm{d}t^2} - b_{hyd}(\omega)\frac{\mathrm{d}z}{\mathrm{d}t} \tag{3.44}$$

F_{res} is the hydrostatic restoring force. It is the vector sum of the upward ARCHIMEDES force F_{arch} and the downward gravity pull F_g . The force is proportional to the position of the buoy. The hydrostatic behaviour can be represented by a spring constant c, the hydrostatic restoring coefficient. It is expressed as $c = \rho g A_w$, with A_w the waterline area of the heaving body.

$$F_{res} = F_{arch} - F_g = \rho g V(t) - mg = -cz \tag{3.45}$$

The damping force is the force applied by the PTO to absorb the wave energy. The force is proportional to the body's velocity and is characterised by the external damping coefficient b_{PTO}. The force is assumed linear although in practice it mostly is not. The same applies for the tuning force, which is proportional to the acceleration and can be seen as a supplementary mass (see equation 3.46). It is a force which requires reinvestment of the energy. However due to the supplementary mass, the natural frequency of the system is manipulated to bring it closer to the frequency ω_w of the incoming wave train (see equation 3.47). In this way the response of the body can be maximised through the resonance principle.

$$F_{tun} = m_{PTO}\frac{\mathrm{d}^2 z}{\mathrm{d}t^2} \tag{3.46}$$

$$\omega_n = \sqrt{\frac{c}{m + m_a + m_{PTO}}} \approx \omega_w \tag{3.47}$$

Having defined all force terms adding to the inertia of the device, the total motion equation can be rewritten as follows (visual representation in figure 3.8):

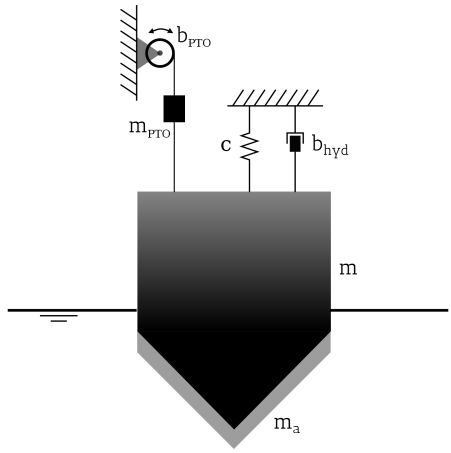

Figure 3.8: Point-absorber WEC system diagram

$$(m+m_a(\omega)+m_{PTO})\frac{\mathrm{d}^2z(t)}{\mathrm{d}t^2}+(b_{hyd}(\omega)+b_{PTO})\frac{\mathrm{d}z(t)}{\mathrm{d}t}+cz(t)=F_{ex}(\omega,t) \quad (3.48)$$

An important remark to make is the frequency dependency of the hydrodynamic damping coefficient and the added mass. Both of these parameters can be calculated using BEM solvers such as Wamit (2016) and Nemoh (Babarit and Delhommeau, 2015). The parameters b_{PTO} and m_{PTO} are controllable and can be optimised for every incoming wave train. Although maximum response is desired, extra restrictions will be introduced to avoid unrealistic motion of the buoy (for example submerging of the buoy, too high cable velocity, ...).

The steady state solution of equation 3.48 has already been determined (see equation 3.39: $z = z_A \sin(\omega t + \epsilon)$). This time the amplitude z_A and phase angle ϵ are given by:

$$z_A(\omega) = \frac{F_{ex,A}}{\sqrt{\left[c-(m+m_{PTO}+m_a(\omega))\cdot\omega^2\right]^2+\left[(b_{hyd}(\omega)+b_{PTO})\omega\right]^2}} \quad (3.49)$$

$$\epsilon = \phi_{ex} - \tan^{-1}\left(\frac{(b_{hyd}(\omega)+b_{PTO})\omega}{c-(m+m_a(\omega)+m_{PTO})\omega^2}\right) \quad (3.50)$$

3.5 BEM solver Nemoh

The linear wave-structure interaction solver used in this research is the open-source software package Nemoh, developed at Ecole Centrale de Nantes (Babarit and Delhommeau, 2015). The current Version v2.03 is based on linear potential flow theory and thus makes the following assumptions:

1. The fluid is inviscid;
2. The fluid is incompressible ;
3. The flow is irrotational;
4. The wave amplitude is small w.r.t. the wavelength;
5. The amplitude of the body motion is small w.r.t. its dimension;
6. The sea bottom is flat;

The flow is described by a velocity potential ϕ, as a function of time and space. The flow field $\vec{\nu}$ is expressed as the gradient of the velocity potential:

$$\vec{\nu} = \nabla\phi \tag{3.51}$$

Combining Equation (3.51) with Assumption 2 leads to the well-known Laplace equation:

$$\Delta\phi = 0 \tag{3.52}$$

This equation is valid in the entire fluid domain, denoted Ω. The whole velocity potential problem becomes then a linear Boundary Value Problem (BVP), visually represented in Figure 3.9. The boundary conditions are given in the set of Equation (3.53).

$$\begin{cases} \frac{\partial\phi(M)}{\partial z} = \frac{\omega^2}{g}\phi(M) & \forall M \in \partial\Omega_F \\ \frac{\partial\phi(M)}{\partial z} = 0 & \forall M \in \partial\Omega_h \\ \frac{\partial\phi(M)}{\partial z} = f(M) & \forall M \in \partial\Omega_B \\ \sqrt{R}(\frac{\partial\phi(M)}{\partial R} - im_0)(\phi - \phi_0) \to 0 & R \to 0 \end{cases} \tag{3.53}$$

Here, $M(x, y, z)$ is a given point in the fluid domain, $f(M)$ is a scalar function, m_0 is the wave number solution of the dispersion relation and ϕ_0 is the incident wave potential at infinity. The boundary conditions are expressed over the different boundary surfaces, where the indices stand for:

- F: fluid domain boundary
- h: sea bed boundary
- B: floating body boundary
- i: interface of floating body with the free surface

This 3-D problem can be transformed into the 2-D problem of a source distribution on the body surface using Green's second identity and the appropriate Green function (Delhommeau, 1987, 1989). The mathematical problem is then discretized using a constant panel method, leading to a linear matrix problem whose coefficients are the influence coefficients. The BVP is numerically solved in the frequency domain; leading to the full flow field underneath the body. From the flow field, several other quantities are calculated:

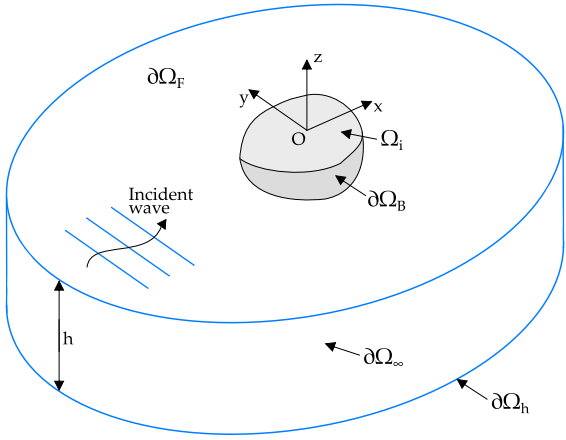

Figure 3.9: Linear boundary value problem, numerically solved in Nemoh. (Figure adapted from Babarit and Delhommeau (2015))

- The hydrodynamic coefficients: added mass m_A and hydrodynamic damping b_{hyd};
- The pressure field p on the body surface and the Froude–Krylov forces F_{FK};
- Far-field diffracted and radiated velocity potential in the form of Kochin functions;
- Near-field diffracted and radiated surface elevation $|D| \exp(i\phi_D)$ and $|R| \exp(i\phi_R)$;

These quantities are necessary for the coupling with each of the wave propagation models, which are discussed in the next section.

3.6 SPH solver DualSPHysics

Within this work, the software used for the detailed non-linear modelling of the wave-structure interactions is DualSPHysics (Crespo et al., 2015). It applies the Smoothed Particle Hydrodynamics (SPH) formulation, a mesh-less method that interprets a continuous fluid as a set of discrete elements, named particles. This section, which is strongly based on the DualSPHysics User Guide v4.2 (Crespo et al., 2018a), explains the theory behind the SPH method and some of the algorithms available within DualSPHysics.

Within SPH, the physical properties of a particle a, determined by the Navier–Stokes equations, can be calculated by interpolation of the values of the nearest neighbouring particles. The contribution of the neighbouring particles is weighted, based on their distance to particle a, using a Kernel function with a characteristic length h (see Figure 3.10). When a particle is at a distance larger than $s \cdot h$ away

from particle a, the interaction can be neglected. The parameter s depends on the choice of the Kernel and is set to be equal to 2 in this work.

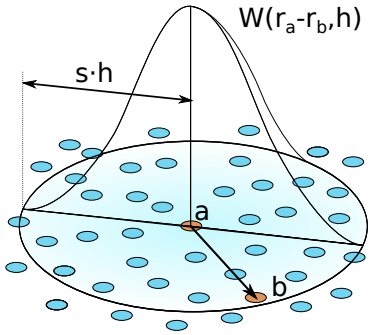

Figure 3.10: Visualisation of Kernel function W with smoothing length h

Fundamentally, any function $F(\mathbf{r})$, defined in **r'**, is estimated by integral approximation:

$$F(\mathbf{r}) = \int F(\mathbf{r'})W(\mathbf{r}-\mathbf{r'},h)d\mathbf{r} \tag{3.54}$$

In order to solve equation 3.54 numerically, discretisation is necessary. In its discrete form, the integral approximation transforms into an interpolation at a given location (or particle a) and a summation over all the particles within the region of compact support of the kernel:

$$F(\mathbf{r}_a) \approx \sum_b F(\mathbf{r}_b)W(\mathbf{r}_a-\mathbf{r}_b,h)\Delta v_b \tag{3.55}$$

Here, Δv_b is the volume of the neighbouring particle b. If $\Delta v_b = m_b/\rho_b$, with m and ρ being the mass and density of particle b, then equation 3.55 becomes:

$$F(\mathbf{r}_a) \approx \sum_b F(\mathbf{r}_b)\frac{m_b}{\rho_b}W(\mathbf{r}_a-\mathbf{r}_b,h) \tag{3.56}$$

The choice of the smoothing kernel has a large influence on the performance of the SPH model. The kernel is expressed as a function of the non-dimensional distance between particles $q = r/h$. Here, r is the distance between a certain particle a and a particle b, while h is the smoothing length, controlling the area around particle a in which neighbouring particles are considered. In this research, a Quintic kernel is applied (Wendland, 1995) with an influence domain of $2h$ ($s = 2$), defined as:

$$W(r,h) = \alpha_D\left(1-\frac{q}{2}\right)^4(2q+1) \qquad 0 \le q \le 2 \tag{3.57}$$

Here, α_D is equal to $7/4\pi h^2$ (2-D).

3.6.1 Governing equations

The governing equations in SPH are the Navier–Stokes equations, of which the momentum equation is expressed as follows:

$$\frac{d\mathbf{v}}{dt} = -\frac{1}{g}\nabla P + \mathbf{g} + \mathbf{\Gamma} \tag{3.58}$$

Where $\mathbf{g}$ is the gravitational acceleration and $\mathbf{\Gamma}$ are dissipative terms. In its SPH formulation, the momentum conservation is expressed as:

$$\frac{d\mathbf{v}_a}{dt} = -\sum_b m_b \left(\frac{P_b}{\rho_b^2} + \frac{P_a}{\rho_a^2} + \Pi_{ab}\right) \nabla_a W_{ab} + \mathbf{g} \tag{3.59}$$

In equation 3.59, P_k is the pressure of particle k, while ρ_k is the density. The viscosity term Π_{ab} is based on the artificial viscosity scheme, as proposed by Monaghan (1992). It is a common method used in SPH to introduce viscosity, mainly due to its simplicity. It is defined as:

$$\Pi_{ab} = \begin{cases} \frac{-\alpha \overline{c_{ab}} \mu_{ab}}{\overline{\rho_{ab}}} & \mathbf{v}_{ab} \cdot \mathbf{r}_{ab} < 0 \\ 0 & \mathbf{v}_{ab} \cdot \mathbf{r}_{ab} > 0 \end{cases} \tag{3.60}$$

With $\overline{\rho_{ab}} = 0.5(\rho_a + \rho_b)$, $r_{ab} = r_a - r_b$ and $\mathbf{v}_{ab} = \mathbf{v}_a - \mathbf{v}_b$, in which r_k is the particle position and v_k the velocity. $\overline{c_{ab}}$ is the mean speed of sound and α is a coefficient that needs to be set by the user to ensure a proper dissipation. In this research, the value of α is set to 0.01, based on Altomare et al. (2015a), where wave propagation and wave loadings on coastal structures were studied.

This research applies a weakly-compressible SPH formulation (WCSPH). This means that the mass of every particle is kept constant, while only their density fluctuates. These fluctuations are calculated by solving the continuity equation, expressing the conservation of mass. In SPH formulation, this is defined by:

$$\frac{d\rho_a}{dt} = \sum_b m_b \mathbf{v}_{ab} \cdot \nabla_a W_{ab} \tag{3.61}$$

Using a weighted summation of the mass terms would result in a density decrease in the interface between fluids, near the free surface and close to the boundaries. For this reason, a time differential is used, as suggested in Monaghan (1992).

One of the main reasons of large computation times in compressible SPH models is the necessity for a very small time step due to the inclusion of the speed of sound. However, the compressibility can be adapted by artificially setting the speed of sound to a lower value, resulting in a reasonable time step. This enables the use of an equation of state to determine the pressure of the fluid. This method is considerably faster than solving the Poisson's equation, appearing in an incompressible approach. According to Monaghan (1994) and Batchelor (2000), the relationship between density and pressure follows Tait's equation of state; a small density oscillation will lead to large pressure variations:

$$P = B\left[\left(\frac{\rho}{\rho_0}\right)^{\gamma} - 1\right] \tag{3.62}$$

Here, B is related to the compressibility of the fluid, while ρ_0 is the reference density, which is set to $1000\ kg/m^3$ in this research. The parameter γ is the polytrophic constant, ranging between 1 and 7. The maximum limit for the density is set for $B = c^2\rho_0/\gamma$, with c the speed of sound. Consequently, the choice of B is of high importance, since it determines the value of the speed of sound. As mentioned before, the speed of sound can be artificially lowered to ensure a reasonable time step (Monaghan, 1994). However it is advised to keep the speed of sound at least 10 times faster than the maximum expected flow velocity.

The time integration of the equations can be performed using a Verlet scheme or a two-stage Symplectic method. The latter is time reversible in the absence of friction or viscous effects (Leimkuhler et al., 1996). In this work, both schemes are applied, where the explicit second-order Symplectic scheme has an accuracy in time of $\mathcal{O}(\Delta t^2)$ and involves a predictor and corrector stage. An explicit time integration scheme is applied, depending on the CFL number, the force terms and the viscous diffusion term. This enables use of a variable time step Δt, calculated according to Monaghan and Kos (1999).

3.6.2 Initial inter-particle distance

The initial inter-particle distance, d_p , is the grid size that is initially used in SPH to distribute each particle within the computational domain at the start of the simulation, at $t = t_0$. As soon as the calculation starts, the fluid particles can move freely. However, the selected d_p determines the mass of the particle and the total amount of fluid and boundary particles, thus being an expression of the model resolution. In this work, convergence studies are carried out to analyze the influence of the model resolution on the results.

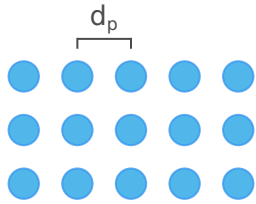

Figure 3.11: Visualisation of the inter-particle distance d_p at start time $t = t_0$.

3.6.3 Delta-SPH formulation

The state equation mentioned in Section 3.6.1 describes a very stiff density field. Unfortunately, this can lead to high-frequency low-amplitude oscillations in the density scalar field (Molteni and Colagrossi, 2009). This effect is enlarged by the natural disordering of the lagrangian particles. In order to mitigate these pressure fluctuations, DualSPHysics allows the user to apply a delta-SPH formulation. This is performed by adding a diffusive term to the continuity equation 3.61, which was

originally introduced by Molteni and Colagrossi (2009):

$$\frac{d\rho_a}{dt} = \sum_b m_b \mathbf{v}_{ab} \cdot \nabla_a W_{ab} + 2\delta_\Phi h c_0 \sum_b (\rho_b - \rho_a) \frac{r_{ab} \cdot \nabla_a W_{ab}}{r_{ab}^2} \frac{m_b}{\rho_b} \quad (3.63)$$

Here, δ_Φ is the free parameter which needs to be selected appropriately. Physically, the delta-SPH formulation can be defined as adding the Laplacian of the density field to the continuity equation. The influence of this added term in the continuity equation has been carefully studied by Antuono et al. (2012). There, the convergence of the operators was analysed by decomposing the Laplacian operator, together with a linear stability analysis to investigate the influence of δ_Φ. Within the fluid domain bulk, equation 3.63 represents an exact diffusive term. However, close to open boundaries such as the free surface, the behaviour changes. There, the kernel is truncated (there are no particles sampled outside of an open boundary), which results in a net first-order contribution (Antuono et al., 2012). Consequently, a net force is applied to the particles. For non-hydrostatic situations, this force is not considered relevant, since the magnitude is negligible with respect to any other involved forces. Antuono et al. (2012) did propose corrections to this effect, but they require a large computational cost since the correction involves the solution of a renormalization problem for the density gradient. Within this work, the recommended delta-SPH (δ_Φ) coefficient of 0.1 (Crespo et al., 2015) is applied.

3.6.4 Floating Objects

In this work, DualSPHysics will be used to model floating WECs in non-linear wave conditions. Within SPH, the motion of a floating object is determined by calculating the interaction forces between fluid particles and floating boundary particles. By summing up all calculated force contributions, the accelerations, velocities and consequently the translations and rotations of the floating object can be determined. The floating body is assumed to be rigid, and the net force on each floating boundary particle is computed as a weighted sum of the surrounding fluid particles, based on the selected kernel function W and the smoothing length h. A floating boundary particle k thus experiences a force per unit mass described by:

$$\mathbf{f}_k = \sum_{a \in WPs} \mathbf{f}_{ka} \quad (3.64)$$

Here, $\mathbf{f}_{ka}$ is the force per unit mass exerted by the fluid particle a within the kernel W on the boundary particle k. This force is found by applying Newton's law:

$$m_k \mathbf{f}_{ka} = -m_a \mathbf{f}_{ak} \quad (3.65)$$

For the calculation of the motions of the floating body, the standard equations of rigid body dynamics can be applied:

$$M \frac{d\mathbf{v}}{dt} = \sum_{k \in BPs} m_k \mathbf{f}_k \quad (3.66)$$

$$I \frac{d\mathbf{\Omega}}{dt} = \sum_{k \in BPs} m_k \left(\mathbf{r}_k - \mathbf{R}_0\right) \times \mathbf{f}_k \quad (3.67)$$

Here, M is the total mass of the floating object, while I is the moment of inertia, $\mathbf{v}$ the translational velocity, $\mathbf{\Omega}$ the rotational velocity and $\mathbf{R}_0$ the center of mass. Time integration of equations 3.66 and 3.67 is applied to predict the values of $\mathbf{v}$ and $\mathbf{\Omega}$ for the beginning of the next time step. Every boundary particle in the floating body consequently has a velocity given by:

$$\mathbf{u}_k = \mathbf{v} + \mathbf{\Omega} \times (\mathbf{r}_k - \mathbf{R}_0) \tag{3.68}$$

All boundary particles within the floating body are finally moved by time integration of Equation 3.68.

3.6.5 Practical implementation

As described above, solving the SPH formulation of the Navier–Stokes equations requires a lot of computation time. This is due to the compressibility of the fluid, requiring a small time step, and the number of neighbouring particles within the kernel. Consequently, powerful computing hardware is necessary to perform SPH modelling.

Table 3.2: Computing power employed for the present research

	CPU	**GPU**
Brand	Intel	Nvidia
Type	i7 6700	GTX 1070
Cores	4	1920
Memory	32 GB	8 GB
Clock Speed	3.4 GHz	1.5 GHz

DualSPHysics, the software applied in this research was originally written in Fortran and only available to compute on Central Processing Units (CPUs) (SPHysics). However, in recent years Graphics Processing Units (GPUs) have appeared as a low-cost alternative to accelerate numerical models. GPUs are specifically designed to manage large amounts of data. Their computing power has developed to be much larger and faster than conventional CPUs in certain cases. Since SPH solvers have an algorithmic structure, very open to parallelism, the computing power of GPUs can be also applied to SPH methods. DualSPHyiscs is created specifically with GPUs in mind, giving the user the choice to calculate on either a CUDA-enabled GPU or a CPU. Several optimizations was implemented to obtain the maximum performance in both architectures (Domínguez et al., 2013). Within the present research, both the CPU and GPU version of DualSPHysics are used to run the two-way coupled wave propagation model. In Table 3.2, the specific hardware is detailed.

3.7 Wave Propagation

3.7.1 OceanWave3D

Throughout this research, the wave propagation model OceanWave3D was used extensively for generating and propagating incident waves over a fixed or variable bathymetry. OceanWave3D is an open-source, fully non-linear potential flow solver (Engsig-Karup et al., 2009, 2013). It is aimed at closing the performance gap between traditional Boussinesq-type models and volume-based solvers such as the fully non-linear potential flow model, and enables fast (near) real-time hydrodynamics calculations. Within this research, it has been used both in its linear mode and its fully non-linear mode. The following section explains the physics behind the software, and is a summary of the full mathematical background, described in Engsig-Karup et al. (2009).

3.7.1.1 Governing Equations

The fully non-linear potential flow problem for waves on a fluid of variable depth is applied to calculate the free surface elevations on a 3-D grid. As typical for potential flow problems, kinematic and dynamic boundary conditions govern the evolution of the free surface:

$$\partial_t \eta = -\nabla\eta \cdot \nabla\tilde{\phi} + \tilde{w}(1 + \nabla\eta \cdot \nabla\eta) \tag{3.69}$$

$$\partial_t \tilde{\phi} = -g\eta - \frac{1}{2}\left(\nabla\tilde{\phi} \cdot \nabla\tilde{\phi} - \tilde{w}^2(1 + \nabla\eta \cdot \nabla\eta)\right) \tag{3.70}$$

These are defined in function of the free surface quantities $\tilde{\phi} = \phi(x, y, \eta, t)$ and $\tilde{w} = \partial_z \phi|_{z=\eta}$. The Laplace equation needs to be solved in the fluid domain in order to find $\tilde{w}$ and develop equations 3.69 and 3.70 in time. For this, it is required that $\tilde{\phi}$ and η are known, together with the kinematic bottom boundary condition:

$$\phi = \tilde{\phi}, \quad z = \eta \tag{3.71}$$

$$\nabla^2\phi + \partial_z z\phi = 0, \quad -h \leq z < \eta \tag{3.72}$$

$$\partial_z\phi + \nabla h \cdot \nabla\phi = 0, \quad z = -h \tag{3.73}$$

There is no flow allowed through solid boundaries. This means the flow field needs to be parallel to those boundaries, which implies that the velocity potential ϕ must obey a no-normal flow condition:

$$\mathbf{n} \cdot (\nabla, \partial_z)\phi = 0, \quad (\mathbf{x}, z) \in \partial\Omega \tag{3.74}$$

Here, $\mathbf{n} = (n_x, n_y, n_z)$ is a normal vector, pointing outward from the structural boundary surfaces $\partial\Omega$. The version of OceanWave3D used in this work, assumes all solid boundaries to be vertical and aligned with the x- or y-direction, with the exception of the fluid bottom.

Due to the oscillatory nature of waves, the free surface boundary is time-dependent and moves with a position, unknown in advance. Therefore, a convenient transformation of the vertical coordinate is applied, mapping the free surface

solution to a time-invariant domain. This is done by using a non-conformal σ-coordinate transformation:

$$\sigma \equiv \frac{z + h(\mathbf{x})}{\eta(\mathbf{x}, t) + h(\mathbf{x})} \equiv \frac{z + h(\mathbf{x})}{d(\mathbf{x}, t)} \tag{3.75}$$

In the transformed domain, the Laplace problem evolves to:

$$\Phi = \tilde{\phi}, \quad \sigma = 1 \tag{3.76}$$

$$\nabla^2\Phi + \nabla^2\sigma(\partial_\sigma\Phi) + 2\nabla\sigma \cdot \nabla(\partial_\sigma\Phi) + (\nabla\sigma \cdot \nabla\sigma + (\partial_\sigma)^2)\partial_{\sigma\sigma}\Phi = 0, \quad 0 \leq \sigma < 1 \tag{3.77}$$

$$(\partial_z\sigma + \nabla h \cdot \nabla\sigma)(\partial_\sigma\Phi) + \nabla h \cdot \nabla\Phi = 0, \quad \sigma = 0 \tag{3.78}$$

Here, $\Phi(\mathbf{x}, \sigma, t) = \phi(\mathbf{x}, z, t)$. All of the non-linear coefficients can be calculated from the known bottom positions and free surface.

In the σ-coordinates, the no-normal flow condition at the structural boundaries is written as:

$$\mathbf{n} \cdot (\nabla, \partial_z\sigma\partial_\sigma)\phi = 0, \quad (\mathbf{x}, \sigma) \in \partial\Omega \tag{3.79}$$

Starting from the solution for the wave potential Φ in the σ-domain, the real physical flow variables u and w in the (x, z)-domain can be obtained using the chain rule:

$$\mathbf{u}(\mathbf{x}, z) = \nabla\phi(\mathbf{x}, z) = \nabla\Phi(\mathbf{x}, \sigma) + \nabla\sigma\partial_\sigma\Phi(\mathbf{x}, \sigma) \tag{3.80}$$

$$w(\mathbf{x}, z) = \partial_z\phi(\mathbf{x}, z) = \partial_\sigma\Phi(\mathbf{x}, \sigma)\partial_z\sigma \tag{3.81}$$

The continuous problem is discretized using a method of lines approach. The time-integration of the free-surface conditions is performed using a classical explicit four-stage, fourth-order Runge-Kutta scheme. Spatial derivatives are replaced by their discrete versions using the high-order finite difference method and non-linear terms are treated by direct product approximations at the collocation points. At the structural boundaries of the domain, i.e. at the bottom and wall sides, Neumann conditions are imposed.

3.7.2 MILDwave

In simulating the far-field effects, the wave propagation model MILDwave is employed (Troch, 1998; Troch and Stratigaki, 2016). MILDwave, developed at the Coastal Engineering Research Group of Ghent University, Belgium, is a phase-resolving model based on the depth-integrated mild-slope Equations (3.82) and (3.83) by Radder and Dingemans (1985). This particular model has been used also in modelling WEC arrays in a number of recent studies (Troch and Stratigaki, 2016; Beels, 2009; Beels et al., 2008, 2010, 2011; Stratigaki et al., 2014a).

3.7.2.1 Governing Equations

The depth-integrated mild-slope Equations (3.82) and (3.83) by Radder and Dingemans (1985) are solved, which describe the transformation of linear irregular waves with a narrow frequency band over a mildly varying bathymetry (bed steepness up to 1/3):

$$\frac{\partial \eta}{\partial t} = B\phi - \nabla \cdot (A \nabla \phi) \tag{3.82}$$

$$\frac{\partial \phi}{\partial t} = -g\eta \tag{3.83}$$

Here, η and ϕ are, respectively, the surface elevation and the velocity potential at the free water surface, g is the gravitational acceleration and the values of B and A are calculated as:

$$B = \frac{\omega^2 - k^2 \cdot C \cdot C_g}{g} \tag{3.84}$$

$$A = \frac{C \cdot C_g}{g} \tag{3.85}$$

with C the phase velocity and C_g the group velocity for a wave with wave number k and angular frequency ω.

A finite difference scheme on a two-step space-centered, time-staggered computational grid is used to discretize and solve equations 3.82 and 3.83. The domain is uniformly divided in grid cells with dimensions Δx and Δy and central differences are used for spatial as well as time derivatives. Both η and ϕ are calculated in the center of each grid cell at different time levels, $(n+\frac{1}{2})\Delta t$ and $(n+1)\Delta t$, respectively, leading to the following discretized equations (Brorsen and Helm-Petersen, 1999):

$$\begin{aligned} n_{i,j}^{n+\frac{1}{2}} \cong\ & n_{i,j}^{n-\frac{1}{2}} + B_{i,j}\phi_{i,j}^{n}\Delta t \\ & - \frac{A_{i+1,j} - A_{i-1,j}}{2\Delta x}\frac{\phi_{i+1,j}^{n} - \phi_{i-1,j}^{n}}{2\Delta x}\Delta t \\ & - A_{i,j}\frac{\phi_{i-1,j}^{n} - 2\phi_{i,j}^{n} + \phi_{i+1,j}^{n}}{(\Delta x)^2}\Delta t \\ & - \frac{A_{i,j+1} - A_{i,j-1}}{2\Delta y}\frac{\phi_{i,j+1}^{n} - \phi_{i,j+1}^{n}}{2\Delta y}\Delta t \\ & - A_{i,j}\frac{\phi_{i,j-1}^{n} - 2\phi_{i,j}^{n} + \phi_{i,j+1}^{n}}{(\Delta y)^2}\Delta t \end{aligned} \tag{3.86}$$

Internal wave generation techniques are used in combination with absorbing sponge layers at the open boundaries. Waves are generated at an offshore boundary

using the source term addition method, adding an additional surface elevation η^* to the calculated value on a wave generation line for each time step. The wave generation line can be straight, an arc or a circle. The numerical absorption of the waves in sponge layers is obtained by multiplying the calculated surface elevations on each new time step with an absorption function $S(b)$ that has a value of 1 at the start of the sponge layer and smoothly decreases till a value of 0 at the end. 2 absorption functions are available in MILDwave:

$$S_1(b) = \sqrt{1 - (\frac{b}{B_s})^2} \tag{3.87}$$

$$S_2(b) = \frac{1}{2}\left(1 + \cos\left(\pi \frac{b}{B_s}\right)\right) \tag{3.88}$$

with B_s the length of the sponge layer and b the distance from the outside boundary, both expressed in number of grid cells.

Chapter 4

Linear Coupling Methodology

In Chapter 2, a number of knowledge gaps were introduced, one of them being the lack of numerical tools to model both near-field and far-field effects of floating WECs and WEC arrays over variable bathymetry. In this fourth chapter of the thesis, a linear coupling methodology is introduced to perform fast numerical simulations of floating WECs or WEC farms. With the development of a linear methodology, the superposition principle is applied to simulate a total wave field in large domains. The research presented is based on the following articles:

originally published as:
Verbrugghe, T., Stratigaki, V., Troch, P., Rabussier, R. and Kortenhaus, A. (2017). A comparison study of a generic coupling methodology for modeling wake effects of wave energy converter arrays. *ENERGIES*, 10:11. doi:10.3390/en10111697.

Verbrugghe, Tim, Peter Troch, Andreas Kortenhaus, Vicky Stratigaki, and AP Engsig-Karup. 2016. "Development of a Numerical Modelling Tool for Combined Near Field and Far Field Wave Transformations Using a Coupling of Potential Flow Solvers." In 2nd International Conference on Renewable Energies Offshore, 61-68.

4.1 Introduction

The success of the WEC technology strongly depends on its economic competitiveness and efficiency with regard to other renewable energy resources, like wind and solar energy. To achieve competitive WEC technologies, a large number of devices is needed in a park or farm configuration, composed of WEC arrays (Troch et al., 2010). Deploying a large number of WECs in the sea has a significant impact on the propagation of the incident waves, through the WEC array (Stratigaki et al., 2014b). Due to the interaction of the WECs with the incident waves, the following wave field physical processes, called "near-field effects", take place:

- Reflection: the incident wave encounters the WEC. A part of its energy is absorbed by the WEC; a part is transmitted past the WEC; and the remaining

part is reflected, back to the open sea, with a smaller wave height and a different phase.

- Diffraction: the waves undergo a change in direction as they pass around the WEC, as a result of the lateral yield of momentum flux, resulting in a concentric pattern, superimposed on the incident waves.
- Radiation: as a response to the incident wave field, a WEC that is not fixed and has at least one degree of freedom will be put in motion, resulting in the creation of radiated waves.

The combination of the above physical phenomena results in a complex total wave field (see Figure 4.1, conveniently duplicated from Figure 1.3). At specific locations, the superposition of the waves leads to a higher energy content, called "hot spots". In other locations, mostly in the lee of the WEC, there are wake effects, leading to a lower energy content. Consequently, it is important to have an understanding of the location of hot spots and wakes in order to efficiently position a large number of WECs in an array layout. Moreover, this complex near-field wave field will propagate further outwards and have an effect on the far-field wave field, the so-called "far-field effects". It has been shown that the maximum absorbed energy of point-absorbers is directly linked to the interaction of the radiated wave field with the incident wave field (Todalshaug, 2013). Although this study mainly focuses on wave interactions with heaving point-absorber WECs, the described modeling methodology is applicable to any floating/fixed offshore structure/device.

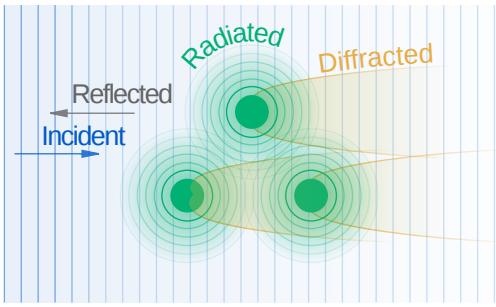

Figure 4.1: Visual representation of incident, reflected, radiated and diffracted waves around an array of three floating structures. The combination of these wave fields results in the total wave field around the three floating structures.

The research presented in this chapter focuses on the numerical modelling of wave-structure and wave-wave interactions within closely-spaced clusters of floating or fixed structures. Currently, there is no numerical model readily available to perform fast simulations of wave propagation in a large domain, over variable bathymetry, through closely-spaced structures; a choice has to be made between the use of accurate wave-structure interaction models with limited domain sizes

and large domain wave propagation models, which lack the ability of accurately modeling complex wave fields. This research aims at overcoming these limitations by combining a wave-structure interaction solver and a wave propagation model to simulate wave propagation through closely-spaced clusters of floating or fixed structures, such as WECs or floating wind turbines.

Next, an overview of the numerical modelling of WEC arrays is given. Many different models exist and are based on various theoretical or applied approaches. Previous work (Wolgamot et al., 2015; Folley et al., 2012; Folley, 2016a) has given an interesting overview of the different types of numerical models, and these studies concluded that all models have specific advantages and disadvantages and often result in making a decision between either computational speed or accuracy. In addition, the modeling can be performed in the frequency domain or the time domain. The first is typically known for fast computation times, but often leads to overestimation of absorbed power (Rahmati and Aggidis, 2016). The latter is necessary when combined wave-structure and wave-wave interaction are studied.

First, the wave-structure interaction models in the near-field are discussed. The most commonly-used models are the Boundary Element Method (BEM) potential flow solvers (for example Aquaplus (Delhommeau, 1987), ANSYS Aqwa (Aqwa, 2018), WAMIT (Hill, 2018), Nemoh (Babarit and Delhommeau, 2015)). These calculate the frequency-dependent hydrodynamic properties of a single or multiple WEC devices. These tools allow one to study the near-field effects such as radiation and diffraction for a linear, regular incident wave over a flat sea bottom. Secondly, due to a better description of the related physics as presented in Yu and Li (2013), the use of codes resolving the Navier–Stokes equations (for example Computational Fluid Dynamics (CFD) models (Agamloh et al., 2008; Finnegan and Goggins, 2012; Devolder et al., 2016; Mccallum, 2017) and Smoothed Particle Hydrodynamics (SPH) (Crespo et al., 2015; Omidvar et al., 2012; Manenti et al., 2008; Omidvar et al., 2013)) for modelling WECs is growing nowadays. The governing equations are solved in the time domain; this means the physical variables do not have to be constant per frequency, but can vary in a non-linear manner over time (for example slack-lined mooring forces, non-linear PTO forces). The BEM and the Navier–Stokes-based solvers will be hereafter referred to as "wave-structure interaction solvers".

The second group of numerical modelling tools focuses on wave propagation models, mainly applied to study far-field effects. Within these, a WEC or floating device is represented in a simplified way, for example by a porous structure that extracts a specific quantity of wave power from the incoming waves. The simulated WEC exhibits a specific amount of reflection, transmission and absorption of the incident waves. Firstly, there are the spectral propagation models. They consider a complete WEC array as a spatially-uniform energy sink (Millar et al., 2007; Alexandre et al., 2009; Carballo and Iglesias, 2013). Often, these models are used to study the impact of a WEC farm on the coastal wave climate. The downsides of these type of models are the omission of the wave interactions in between WEC devices and the parametrized power absorption by the WEC. The most important drawback is the inaccurate representation of wave diffraction by the WECs. The whole WEC array is approximated as one giant structure absorbing a part of the

incident wave energy. Secondly, there are time domain wave propagation models; a distinction can be made between wave propagation models based on mild-slope equations (Troch et al., 2010; Charrayre et al., 2014a; Stratigaki et al., 2014a; Troch and Stratigaki, 2016) and Boussinesq-type or FNPF models (Venugopal and Smith, 2007; Engsig-Karup et al., 2009; Verbrugghe et al., 2016).

All of the above-mentioned models suffer from a common problem: they cannot be used to model both near-field interactions and far-field effects, as recently reviewed in Folley et al. (2012); Li et al. (2012). Models based on the Boundary Element Method (BEM) approach of potential flow theory or on the approach of Navier–Stokes equations suffer from a high computational cost, when simulating power absorption and the wave field alteration due to large WEC arrays. Simulation domains of non-constant water depth are prohibitive, which results also in restrictions on the number of the simulated WECs (typically less than 10 WECs). However, in order to investigate far-field effects, for example to study coastal impact, much larger computational domains are required.

On the other hand, the approach of wave propagation models enables simulation of these far-field effects. Large WEC arrays installed in large domains (several tens of kilometers) are modelled at a reasonable computational cost. As a result, the changes in wave field and the associated environmental impacts can be studied at the regional scale. However, the WECs are approximated up to now by using parametrized energy sinks and empirically tuned energy absorption coefficients. This method only partially addresses the underlying physics, which may lead to erroneous model conclusions. Moreover, when it comes to the modelling of oscillating WECs, the radiated wave field induced by the WEC's motion is not considered in wave propagation models such as in Vidal et al. (2007); Mendes et al. (2008); Le Crom et al. (2008).

The present research focuses on introducing a generic coupling methodology, combining the near-field accuracy of wave-structure interaction models with time-efficient far-field wave propagation models. An application of this methodology has resulted in two "in-house" developed modelling tools; both of them combining the BEM wave-structure interaction model, Nemoh, with a fast wave propagation model. The first tool uses a depth-averaged mild-slope equation model called MILDwave (Troch, 1998; Troch and Stratigaki, 2016), while the second one is a 3-D, fully-non-linear potential flow solver called OceanWave3D (Engsig-Karup et al., 2009). The latter model has the extra advantage of being able to calculate non-depth averaged wave kinematics. Near-field effects such as radiation and diffraction are calculated by the BEM solver, and the interaction with the incident waves and further propagation in the far-field over variable bathymetry are handled by the wave propagation model.

In Section 4.2 of this chapter, the coupling methodology is introduced. Next, the methodology is applied to a wave-structure interaction solver and two wave propagation models, to model the near-field and far-field effects in and around a WEC array, as presented in Section 4.3. A sensitivity analysis on the grid size and coupling radius is given in Section 4.4. In Section 4.5, the results of the numerical models are compared to each other, covering a wide spectrum of wave conditions and WEC array layouts. In addition, the OceanWave3D-Nemoh model is compared

to an experimental dataset. The results of the present study are discussed in Section 4.6 together with the concluding remarks.

4.2 Coupling Methodology

A numerical coupling methodology for predicting the wave field around devices or structures (single or in a park layout) is presented and is inspired by the work of Stratigaki et al. (2014a); Troch and Stratigaki (2016), where an internal circular wave generation boundary around floating structures was applied to pass information from WAMIT (Hill, 2018) to MILDwave and propagate the waves within the wave propagation domain. The present coupling methodology has been developed to combine:

1. the advantages of the approach of wave-structure interaction solvers, which accurately formulate and efficiently resolve the physical processes in wave energy absorption and floating structures;
2. and the benefits of the approach of wave propagation models, which efficiently resolve the propagation and transformation of waves over large distances, including bathymetric variability and wave transformation processes when approaching the coastline.

4.2.1 General Concept

The goal of the coupling methodology is to predict the total wave field, by superposing the perturbed (reflected + diffracted + radiated) wave field and the incident wave field. For the perturbed waves, a frequency domain wave-structure interaction solver is used within a restricted zone around the floating or fixed devices. The propagation and transformation of the incident waves in a large domain is calculated by employing a wave propagation model. The coupling methodology is applicable to both floating and fixed offshore devices. However, in this research, the focus is put on floating devices or structures, which is the most complex and computationally demanding case. The general concept is sketched in Figure 4.2.

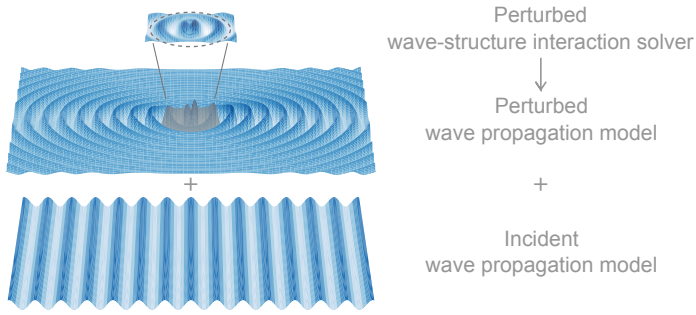

Figure 4.2: General concept of the coupling methodology between the numerical models.

The main coupling mechanism is a superposition of two separate simulations: one for the perturbed wave field and another for the incident wave field. The perturbed wave field is a combination of the radiation and diffraction (including wave reflection) and is calculated during a first run in the frequency domain by the wave-structure interaction solver, within a restricted zone around the device/structure, indicated by the dashed circle in Figure 4.2. Note that this zone can be used either around a single device/structure or around a cluster of devices/structures. Within the wave propagation model, the perturbed field is propagated outwards from the center of the domain. In a separate run, the incident waves are propagated over the entire domain in the wave propagation model. It is only after both runs have finished that the wave fields are superposed to result in the total wave field. This superposition principle is possible, since the linear wave theory is applicable.

4.2.2 Calculating the Perturbed Wave Field

The perturbed wave field is the superposition of the radiated and diffracted field and is calculated in two steps. First, a frequency domain simulation is performed in the wave-structure interaction domain with a flat bathymetry; here, we use a linear BEM solver, where the static and dynamic pressure are integrated over the floating body resulting in radiation and diffraction forces. These quantities depend on the body shape, the degrees of freedom, the wave period and the local water depth. Many different body shapes are possible, ranging from axisymmetric shapes to WEC devices, barges, ships and offshore platforms.

The wave-structure interaction calculation results in the complex, frequency-dependent radiated and diffracted wave fields (including the wave reflection), which are calculated on a rectangular grid. This grid is chosen to be smaller and finer than the wave propagation grid, which offers higher accuracy.

In the next step, the diffracted and radiated waves, as calculated in the previous step, are propagated in the wave propagation model with varying bathymetry. Specifically, they are imposed on a circular wave generation zone and are propagated towards the outside of the domain. At this point, it is to be noted that this internal wave propagation zone should not necessarily be circular and can be otherwise defined. In order to impose the perturbed wave field in the wave propagation model, it is necessary to transform both the radiated and diffracted wave field to the time domain within that coupling zone:

$$\begin{aligned}\eta_R(x,y,t) = \sum_{j=1}^{n_b} \mathrm{Re}\{&A \cdot (-i\omega) \cdot |\mathbf{RAO}_j| \cdot \exp(i\phi_{\mathbf{RAO}_j}) \\ &\cdot |\mathbf{R}_j| \cdot \exp(i\phi_{\mathbf{R}_j}) \exp(-i\omega t)\}\end{aligned} \tag{4.1}$$

$$\eta_D(x,y,t) = \mathrm{Re}\{A \cdot |\mathbf{D}| \cdot \exp(i\phi_{\mathbf{D}}) \exp(-i\omega t)\} \tag{4.2}$$

Within Equations (4.1) and (4.2), η_R is the radiated wave field in the time domain. This is a summation of the radiated wave field for each device/structure in the array. η_D is the diffracted wave field for the complete array. A is the wave

amplitude. $|\mathbf{RAO}_j|$ is the amplitude of the complex response amplitude operator for the corresponding device/structure j, defined by Equation (4.3) (Babarit et al., 2013), while $\phi_{\mathbf{RAO}_j}$ is the phase angle. $|\mathbf{R}_j|$ is the amplitude of the complex radiated wave field for device/structure j and a specific frequency, coming directly from the wave-structure interaction model, while $\phi_{\mathbf{R}_j}$ is the phase angle. $|\mathbf{D}|$ is the amplitude of the diffracted wave field, while ϕ_D is the phase angle. The parameters calculated with the BEM solver are indicated with bold font.

$$\mathbf{RAO_j} = \frac{\mathbf{F_{ex,j}}}{-(\mathbf{m_j} + \mathbf{m_{a,j}} + m_{PTO})\omega^2 + i\omega(\mathbf{b_{hyd,j}} + b_{PTO}) + (\mathbf{c_j} + c_{PTO})} \quad (4.3)$$

In Equation (4.3), $\mathbf{F_{ex,j}}$ is the complex wave excitation force, $\mathbf{M_j}$ the mass of device/structure $\mathbf{j}$, $\mathbf{m_{A,j}}$ the added mass, $\mathbf{b_{hyd,j}}$ the hydrodynamic damping coefficient and $\mathbf{c_j}$ the hydrostatic stiffness. The effect of a linear Power Take-Off (PTO) system on the radiated wave field is taken into account by adding external mass m_{PTO}, damping b_{PTO} or spring coefficient c_{PTO}. The parameters calculated with the BEM solver are indicated with bold font.

The perturbed (radiation + diffracted) wave field is propagated using the wave propagation model from within a circular zone around the device/structure (see Figure 4.3). The circular area (light gray gradient) is a wave generation zone defined by a radius R_c, termed as the "coupling radius". Within that circular zone, the surface elevation is imposed, so waves are forced to propagate away from the device/structure. At the interface between the wave generation zone and the wave propagation domain, the waves are released and propagate across the domain. From that point onwards, the governing wave propagation equations take over and take into account the (variable) bathymetry. At the left and right side of the wave propagation domain, wave absorbing boundary conditions such as relaxation zones or sponge layers are applied (dark gray zones).

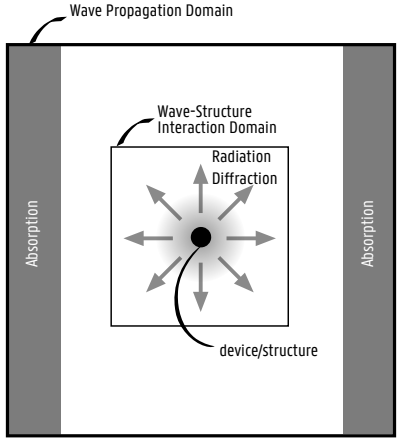

Figure 4.3: Scheme for introducing information from the wave-structure interaction solver to the wave propagation model. Gray gradient zones are generation zones, and dark gray zones are absorption zones.

4.2.3 Calculating the Incident Wave Field

The incident wave field is directly calculated in the time domain within the wave propagation model. However, special attention is needed for the phase angle of the incident wave. It is important that at the center of the circular coupling zone, the phase angle is always equal to $-\omega t$. This is necessary since the perturbed wave field is coming from the frequency domain, where the phase is referenced with respect to the center of the device/structure. This phase matching is ensured by calculating the phase angle in the incident wave run, at the center of the coupling zone, and subtracting this value from the perturbed wave field phase angle. The numerical setup is illustrated in Figure 4.4. The wave propagation models are able to simulate shoaling and refraction of incident waves over complex bathymetries. In the case of mild-slope equation models, the slopes need to remain within a gradient of $1/3$, while Boussinesq-type models and fully non-linear potential flow models can handle any type of bathymetry, however with a certain pre-processing and numerical instability cost (Stratigaki et al., 2011). At the left, boundary conditions of the generation of regular linear waves are applied:

$$\eta_I(x,y,t) = \mathrm{Re}\{A \cdot \exp(-i(\omega t - k(x\cos\theta - y\sin\theta)))\} \tag{4.4}$$

In Equation (4.4), η_I is the incident surface elevation, A is the wave amplitude, ω is the wave frequency (in rad/s), k is the wave number and θ is the wave direction. Waves propagate towards the right side, where the waves are absorbed by a relaxation boundary condition or a sponge layer. The top and bottom boundaries can be reflective (no-flux boundary condition) or absorbing, depending on the selected wave propagation model. When reflective boundaries are applied, it is advised to extend the wave propagation domain, perpendicular to the incident wave direction.

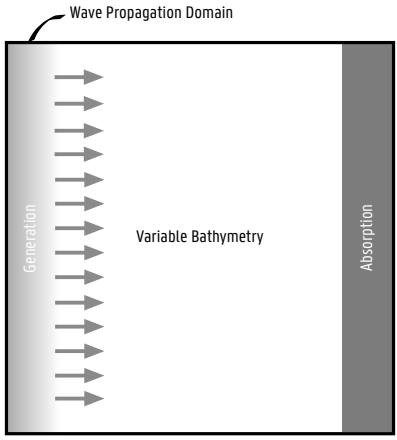

Figure 4.4: Scheme for propagation of incident waves in the wave propagation model. The gray gradient zone is a wave generation zone, and the dark gray zone is a wave absorption zone. No structure/device is present.

In the case of irregular incident waves, the superposition principle can be applied. A linear, irregular wave can be represented as a sum of a finite number of regular wave components, each with a characteristic wave height and wave period derived from the wave spectrum. In order to avoid local attenuation of the surface elevation η_I, each regular wave component should be shifted with a random phase angle ϕ_i:

$$\eta_I = \sum_{i=1}^{n} \mathrm{Re}\{A_i \cdot \exp(-i(\omega t - k(x\cos\theta - y\sin\theta) - \phi_i))\} \tag{4.5}$$

Modelling the wave propagation of irregular waves through a closely-spaced cluster of floating/fixed offshore devices requires performing multiple coupled simulations with regular waves, each shifted with a random phase angle, and finally superposing all individual regular wave fields.

4.2.4 Implementation

The implementation of the coupling methodology into OceanWave3D (OW3D) and Nemoh is illustrated in Figure 4.5. Here, it is shown that the incident run and radiation/diffraction run are separate processes, each containing their own input variables. The incident run depends on the selected wave height, period, (variable) bathymetry and the computational OW3D grid. The incident waves are simulated in the time domain, resulting in the incident wave field over the selected bathymetry. The radiation/diffraction run only depends on the wave period, since the results are calculated for a wave height of 1 m, and scaled afterwards depending on the incident wave height. Other input variables are the shape of the WEC, the local water depth and a second computational grid, concentrated around the WEC device. The radiated and diffracted surface elevations are calculated in the frequency domain, resulting in a complex wavefield containing the amplitude and phase. These wavefields are scaled with the incident wave amplitude and converted to the time domain, as defined with equations 4.1 and 4.2. Next, they are superposed to the incident wave field, resulting in the total wavefield in the time domain.

4.3 Application of the Coupling Methodology

In this section, the coupling methodology, described in Section 4.2, will be demonstrated for predicting WEC array effects. Moreover, it will be demonstrated for two different wave propagation models: MILDwave and OceanWave3D.The results obtained by the coupling methodology implemented in these two wave propagation models will be compared to each other and to experimental data, obtained within the WECwakes research project.

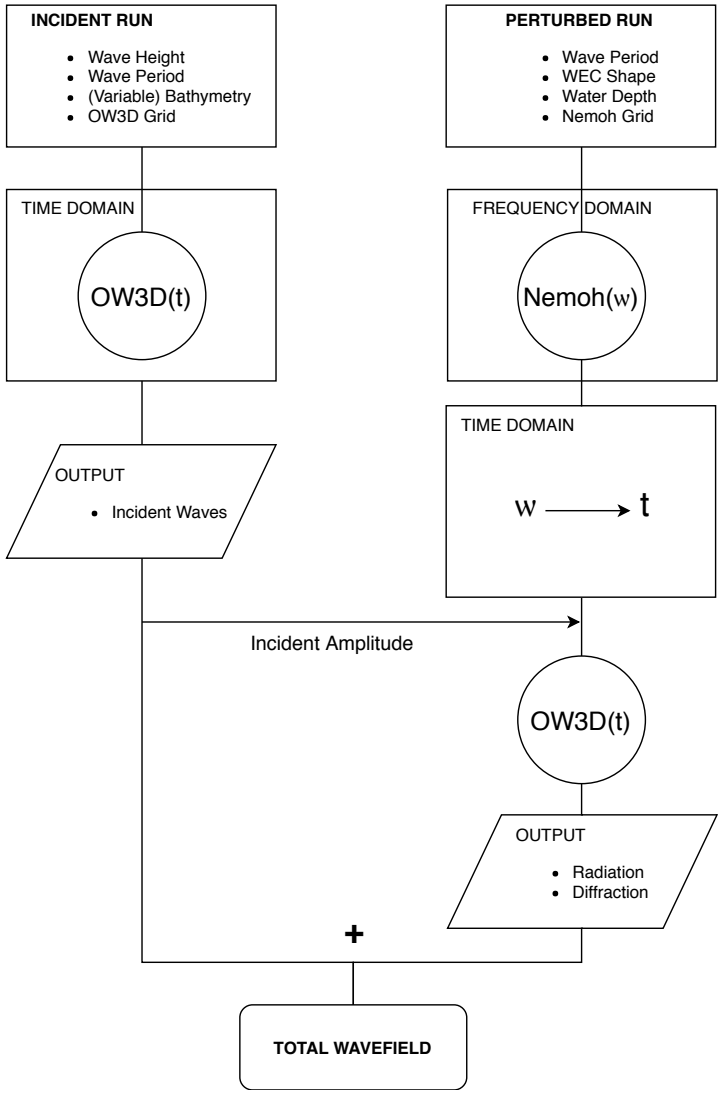

Figure 4.5: Scheme for implementation of linear coupling algorithm

4.3.1 Wave-Structure Interaction Model

The wave-structure interaction solver used in this research is the open-source software package Nemoh, developed at Ecole Centrale de Nantes by Babarit and Delhommeau (2015). The current Version v2.03 is based on linear potential flow theory, of which the details have been discussed in Section 3.5.

4.3.2 Wave Propagation Models

The second part of the coupling methodology is the wave propagation model. This model propagates the incident waves and predicts their interaction with the diffracted and radiated waves as predicted by Nemoh. For this, two separate software packages are applied: MILDwave, a 2-D model based on mild-slope equations, and OceanWave3D, a 3-D model based on fully non-linear potential flow equations. We will denote the coupled models as the MILDwave-Nemoh model and the OceanWave3D-Nemoh model, respectively.

4.3.2.1 MILDwave

In simulating the far-field effects, the wave propagation model MILDwave is employed (Troch, 1998; Troch and Stratigaki, 2016). MILDwave, developed at the Coastal Engineering Research Group of Ghent University, Belgium, is a phase-resolving model based on the depth-integrated mild-slope equations by Radder and Dingemans (Radder and Dingemans, 1985) (see Section 3.7.2). This particular model has been used also in modelling WEC arrays in a number of recent studies (Troch and Stratigaki, 2016; Beels, 2009; Beels et al., 2008, 2010, 2011; Stratigaki et al., 2014a). The mild-slope Equations (3.82) and (3.83) are solved using a finite difference scheme that consists of a two-step space-centered, time-staggered computational grid, as detailed in Brorsen and Helm-Petersen (1999).

4.3.2.2 OceanWave3D

The second applied wave propagation model is called OceanWave3D. The software is open-source and applies a fully-non-linear potential flow solver (Engsig-Karup et al., 2009, 2013). It is aimed at closing the performance gap between traditional Boussinesq-type models and volume-based solvers and enables fast (near) real-time hydrodynamics calculations. The fully-non-linear potential flow problem for waves on a fluid of variable depth is applied to find the free surface elevations on a 3-D grid, with vertical sigma layers. This allows for the prediction of velocity profiles, in contrast to MILDwave, which only supports depth-averaged velocities. When applying the coupling method to OceanWave3D, the non-linear effects are omitted. Consequently, the linear superposition method can be applied and the total transformed wave field can be created by summation of the independent surface elevations and potentials. A detailed theoretical background can be found in Section 3.7.1.

4.3.3 Experimental Dataset

In 2013, as part of the WECwakes research project funded by the EU FP7 HYDRALAB IV program, experiments have been conducted in the Shallow Water Wave Basin of the Danish Hydraulic Institute (DHI) in Hørsholm, Denmark (Stratigaki et al., 2014b). A large number of tests was performed on large arrays of point absorber-type WECs (up to 25 units, see Figure 4.6). The research performed within the WECwakes project focuses on generic heaving WECs, intended for validation purposes of numerical models.

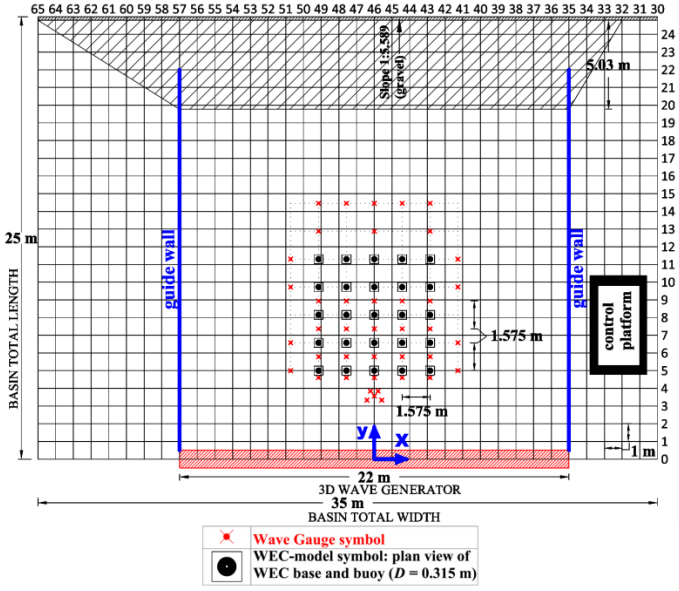

Figure 4.6: Plan view of the WECwakes experimental arrangement in the DHI wave basin and 5×5-WEC rectilinear array. Grid at 1.0-m increments, wave gauge arrangement (×) and WEC positions (•) are indicated. The hatched region along the x-axis at the bottom of the figure denotes the extent of the wave paddles, while at the opposite end, the wave absorbing beach is shown. At the sides, plywood guide walls are used.

A range of WEC array geometric configurations and wave conditions have been tested. Each WEC unit is composed of a buoy, designed to heave along a vertical shaft only, and can thus be modeled as a single degree of freedom system (see Figure 4.7). The WEC consists of a cylindrical body and a spherical bottom. The diameter is 0.3150 m, while the draft is 0.3232 m. The water depth is fixed at 0.7000 m. Energy absorption through the WECs' PTO system, is modelled by realizing energy dissipation through friction-based damping of the WECs' heave motion. Wave gauges are used to measure the wave field within and around the arrays. Displacement meters are mounted on each WEC unit for the measurement of the heave displacement. The wave-induced surge force is measured on five WECs along the central line of the array.

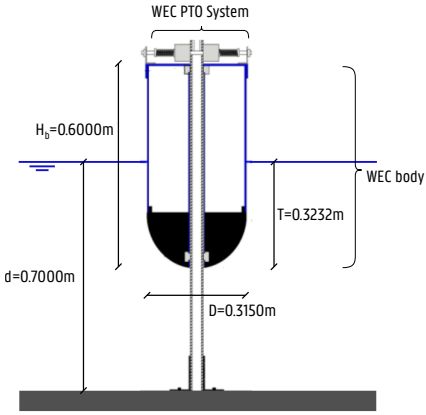

Figure 4.7: Sketch of the WECwakes WEC unit. D is the WEC diameter; d is the water depth; T is the draft of the WEC; while H_b is the total height of the device.

The experimental setup of 25 individual WEC units in an array layout, placed in the large wave tank, is at present the largest setup of its kind, studying the important impacts on power absorption and wave conditions of WEC array effects. Most importantly, the WECwakes database is comprehensive and is applicable not only to WEC arrays, but also to floating structures/platforms, stationary cylinders under wave action, etc., for understanding of, for example wave impact on the cylinders and wave field modifications around them. The WECwakes database is accessible to the research community as specified under the HYDRALAB rules.

4.3.4 Test Program

4.3.4.1 Comparison between Wave Propagation Models Using the Coupling Methodology

The first objective of this research is to compare the results obtained by the application of the introduced coupling methodology to both wave propagation models. For this reason, a test program based on long-crested regular and irregular waves is set up, as presented in Table 4.1. The WEC-WEC distance L_{W-W} is fixed at $3D$ with D the diameter of the WEC. A cylindrical device is chosen with $D = 20$ m and a draft of $T = 5$ m. The following characteristics are varied during the tests:

- Wave type: regular (REG) and irregular waves (IRR)
- Water depth d: deep and transitional water
- Number of WECs: ranging from one to five
- Array geometrical layout: several configurations
- Bathymetry: fixed bottom; two beach profiles (Beach_1, Beach_2); one sea bottom

Table 4.1: Test program for the comparison of the coupling methodology. (H = Wave Height, T = Wave Period, d = Water Depth, L_{W-W} = WEC-WEC distance)

Test Number #	**Wave Type**	**H (m)**	**T (s)**	**d (m)**	**Layout**	L_{W-W} **(m)**
1	REG	0.5	8	50		-
2	REG	0.5	8	25		-
3	REG	0.5	8	25		3D
4	REG	0.5	8	25		3D
5	REG	0.5	8	25		3D
6	REG	0.5	8	25		3D
7	REG	0.5	8	Beach_1		3D
8	REG	0.5	8	Beach_2		3D
9	REG	0.5	8	Sea Bottom		3D
10	IRR	0.5	8	Sea Bottom		3D

Tests 3 to 10 are performed with multiple WECs. It is important to mention that the coupling methodology is applied by coupling the complete array of WECs, instead of coupling each WEC individually. Tests 7 to 9 and 10 are performed with varying bathymetry. Test 7 refers to wave propagation over a gradual beach slope (Beach_1) with a gradient of $1/12$ going from 50 m depth to 25 m over a length of 300 m. The bathymetry of Test 8 (Beach_2) consists of two consecutive beach slopes with a gradient of around $1/10$ with water depths from 50 m to 25 m to 1 m. Finally, Tests 9 and 10 are based on a sea bottom bathymetry with an average depth of 37 m. All bottom profiles are illustrated in Figure 4.8.

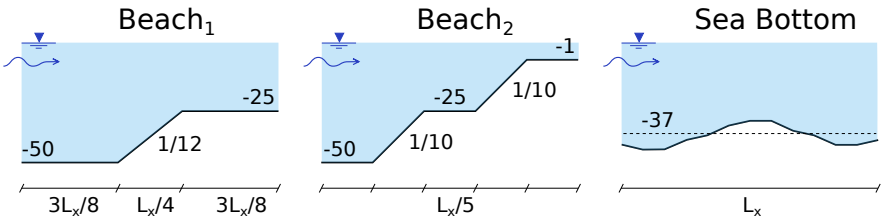

Figure 4.8: Varying bathymetry profiles as used in the numerical simulations. L_x is the wave propagation domain length.

The accuracy of the results will be assessed by calculating the K_D value, over a specific time window Δt, as defined in Equation (4.6). It is the ratio of the numerically-calculated disturbed wave height $H_{s,d}$ to the incident wave height $H_{i,d}$. The surface elevation η is squared and summed up over all n time steps within the time window Δt. It is multiplied with the relative time step, which is the ration of the time step dt to the time window Δt: $\frac{dt}{\Delta t}$ and a factor of eight. From this value, the square root is taken and finally divided by the incident wave height H_i (for regular waves) or significant wave height $H_{s,i}$ (for irregular waves).

$$K_D = \frac{H_{s,d}}{H_{s,i}} = \frac{\sqrt{8 \cdot (\sum_i^n \eta_i^2) \cdot \frac{dt}{\Delta t}}}{H_{s,i}} \tag{4.6}$$

The K_D value summarizes the wave interactions during the entire simulation duration in one value per grid cell. When $K_D > 1$, it indicates a local increase of wave height or "hot spot", while a value $K_D < 1$ indicates a local decrease of wave height or "wake".

Within the comparison study, results from both wave propagation models are compared with each other. Additionally, the results are compared to a pure BEM solution where possible (regular waves with constant water depth). The accuracy of the models is estimated based on the following outputs:

- Contour plots of the K_D values throughout the entire domain
- Line cross-sections of the K_D values along the wave direction

- Contour plots of the relative differences between the results obtained by the wave propagation models
- Calculation of relative K_D error values

the numerical domain measures 1200 m long and 1800 m wide, with a 300 m-long wave generation zone and a 300 m-long wave absorption boundary. The grid size is set to $dx = 5.0$ m, which corresponds to the suggested value of $L/20$, as explained in Section 4.4.1. The time step is set to $dt = 0.4$ s, and the coupling radius is $R_c = 10dx = 50m$ (see Section 4.4.2).

4.3.4.2 Comparison to Experimental Data

The WECwakes experiments consisted of 591 tests in total. Out of these tests, one geometrical array configuration is selected for a detailed comparison with the results of the coupling methodology. Additionally, 12 more test cases are studied, of which the results can be found in Appendix D. There are two sets of regular incident wave conditions with wave height $H = 0.074$ m and wave period T, either 1.18 s (close to the resonance period T_R of the device) or 1.26 s. These wave conditions, combined with a constant water depth of $d = 0.7$ m, result in non-linear Stokes second order waves. Although the numerical model is only valid for linear waves, the incident waves are only weakly non-linear. The wave propagation model OceanWave3D will be run in non-linear mode, in contrast to what was advised in Section 4.3.2.2, to ensure maximum accuracy of incident waves. Superposing the weakly non-linear incident and perturbed waves will lead to an error smaller than 0.1% on the wave trough in comparison to linear wave theory, justifying the application of the superposition principle. The comparison is performed for a configuration of nine WEC units, arranged in a 3 $\times$ 3 layout (see Figure 4.9). The WEC units have an equal spacing of five WEC diameters $5D = 1.575$ m.

The DHI wave basin has a wave generation width of 22 m, while the waves propagate over a length of 25 m. Side walls are installed in the basin to guide the incident waves and reflect the perturbed waves. This is mainly done to simplify the comparison to numerical models, where it is difficult to absorb waves from different directions.

Each WEC unit is equipped with a friction-based PTO system. The effect of this PTO is included in the simulations by adding an external numerical damping term b_{PTO} to the RAO, as previously demonstrated in Equation (4.3). In order to identify the correct value for this added damping, the RAO is calculated for several values of b_{PTO}. When the peak of the RAO curve is located exactly on the natural frequency $\omega_R = 2\pi/T_R = 5.32$ rad/s, the external damping is considered correct. As illustrated in Figure 4.10, the correct value of b_{PTO} lies between 20 and 25 kg/s. Further iterations lead to a value of $b_{PTO} = 23.5$ kg/s.

The comparison of the results is based on the surface elevation, registered by 19 resistive wave gauges, distributed over the domain as illustrated in Figure 4.9. For each wave gauge, the surface elevation is compared to the signal obtained by the numerical model. The location of the wave gauges is not perfectly aligned

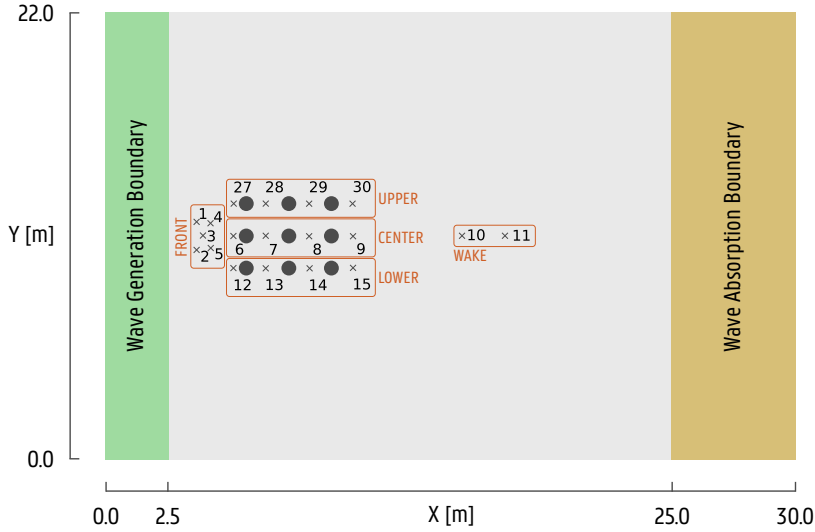

Figure 4.9: Setup of both the experimental and computational domain; WEC array layout (•) and wave gauge distribution (×) used for the comparison with experimental tests. The code numbers of the used wave gauges are also shown, together with their zone name.

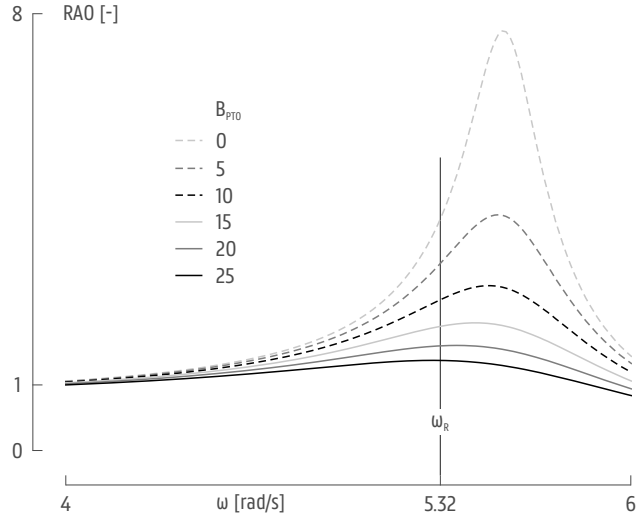

Figure 4.10: Iterative method to identify the correct external damping coefficient.

Table 4.2: Sensitivity analysis on grid size dx.

Test	a	b	c	d	e
dx	$L/40$	$L/30$	$L/20$	$L/10$	$L/5$

with the computational grid, so results are interpolated. The accuracy of the numerical model is quantified by calculating the normalized RMSE between the surface elevation of the numerical model and the experimental data:

$$RMSE_a = \frac{\sqrt{\frac{1}{n}\sum_{i=1}^{n}(\eta_{n,i} - \eta_{e,i})^2}}{H/2} \tag{4.7}$$

Additionally, the domain shown in Figure 4.9, measures 30 m long and 22 m wide, with a 2.5 m-long wave generation zone and a 5 m-long wave absorption boundary. The grid size is set to $dx = 0.1$ m, which corresponds to the suggested value of $L/20$, as explained in Section 4.4.1. The time step is set to $dt = 0.05$ s, and the coupling radius is $R_c = 10dx = 1m$ (see Section 4.4.2).

4.4 Sensitivity Analysis

Before diving into the comparison study, a good base setup is required for the numerical simulations. The aim is to apply both numerical models on the same computational grid. This grid should be chosen carefully to ensure converging results, whilst maintaining an acceptable computational time. For this reason, a sensitivity analysis is performed based on two grid characteristics. The first is the grid spacing dx in the x-direction. In this study, $dx = dy$, where dy is the grid spacing in the y-direction. The spacing has a direct impact on the computational time and the resolution of the output files. Here, the objective is to have the coarsest grid leading to a converged result, in order to minimize the computational time. The second characteristic is the coupling radius R_c. Ideally, this zone is kept as small as possible, in order to retain a large zone for the wave interactions in the wave propagation model.

4.4.1 Grid Spacing

First, a sensitivity analysis is performed based on the grid spacing of the wave propagation model. The computational grid consists of square cells with size $dx = dy$. This size is varied, based on the wave length L of the incident waves, in order to achieve a convergent solution (see Figure 4.11). The largest grid size resulting in an accurate solution will be selected. The accuracy is determined by comparing the solution of the coupling methodology (applied to OceanWave3D) to a single BEM solution. The grid spacing dx is varied from $L/40$ to $L/5$, as denoted in Table 4.2.

The sensitivity analysis is performed using the case of "Test 1" from Table 4.1. The K_D value is calculated over a longitudinal section going through the center

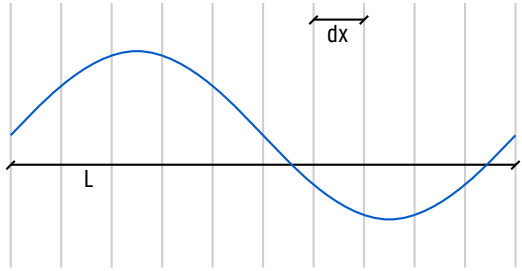

Figure 4.11: Illustration of grid size sensitivity analysis (here, $dx = L/10$).

of the domain. The results are illustrated in Figure 4.12. Here, all five different grid spacings are plotted together with the BEM frequency domain result. In front of the device, there is a clear zone where wave reflection is observed. In the lee of the device, there is a wake that gradually disappears along the x-axis. At the beginning and at the end of the domain, there are wave relaxation zones where all energy is absorbed.

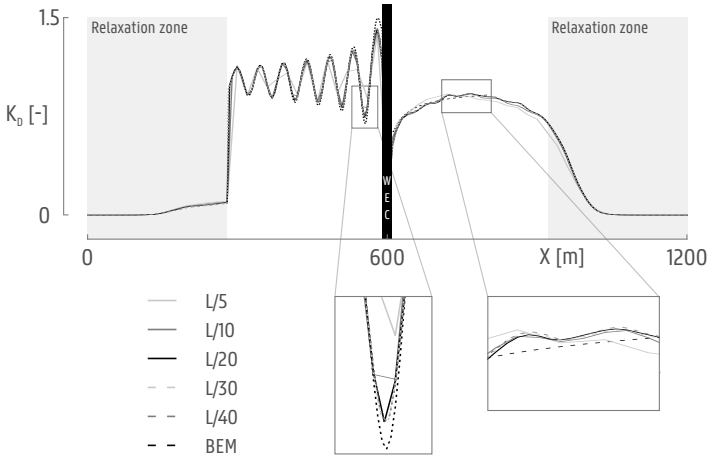

Figure 4.12: Sensitivity analysis for grid spacing, dx. Results from the coupling methodology applied to OceanWave3D, showing K_D results along a longitudinal section in the middle of the domain. A coupling radius $R_c = 10dx$ was applied.

In Figure 4.12, it is difficult to assess the convergence of the results. For this reason, two regions of interest are enlarged for more detailed comparison. It becomes immediately clear that the grid spacings equal to $L/5$ and $L/10$ are too coarse. The peaks of the wave reflection are not reproduced, and the wake region is not accurately defined. The three finest resolutions $(L/20, L/30, L/40)$ are all within a 0.5% difference between each other. In order to better quantify the results, the L_2 error norm is calculated, assuming the Nemoh solution is the correct one.

This error is defined as:

$$L_2 = \sqrt{\sum_{i=1}^{n} |K_{D,O} - K_{D,O}|^2} \tag{4.8}$$

With $K_{D,O}$ the OceanWave3D dimensionless amplitude and $K_{D,O}$ the one calculated by Nemoh. The errors are summarized in Table 4.3. It is clear that the rate of convergence is sublinear. However, it is seen that the result is converged for a grid spacing $dx = L/20$. This value will be used within this study, since it also leads to reasonable computational time of around 30 min.

Table 4.3: L_2 error norm for different grid sizes dx.

dx	$L/5$	$L/10$	$L/20$	$L/30$	$L/40$
L_2	0.96	0.41	0.39	0.41	0.4

4.4.2 Coupling Radius

For the second sensitivity analysis, the value of the coupling radius R_c is varied. Around the WEC device/array, a circular coupling zone is defined. Within this zone, the surface elevation values are forced into the wave propagation model, as resulted from the BEM simulation. The smaller this coupling zone is, the more space is available to freely propagate the waves and interact with other wave components. In order to identify the ideal coupling radius, the coupled model is run several times using each time a different coupling radius (see Figure 4.13). The results are compared to a solution obtained with the BEM model on the same computational grid. The coupling radius R_c is varied from 3 to 20 dx (see Table 4.4).

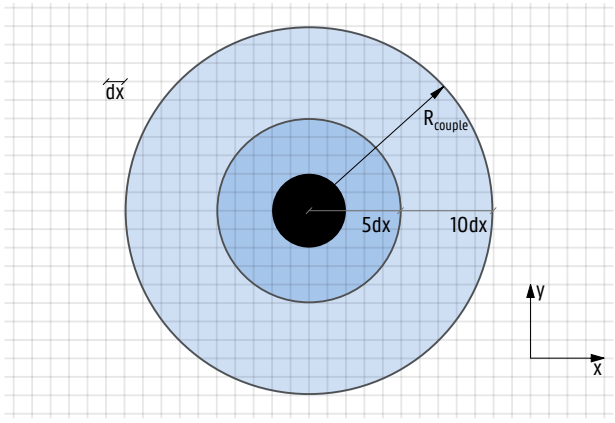

Figure 4.13: Illustration of coupling radius R_c sensitivity analysis. The WEC is illustrated as a solid black circle.

Table 4.4: Sensitivity analysis on coupling radius R_c.

Test	i	ii	iii	iv	v
R_c	3 dx	5 dx	10 dx	15 dx	20 dx

The sensitivity analysis is again performed using "Test 1" from Table 4.1. The K_D value is calculated over a longitudinal section going through the center of the WEC. The results are illustrated in Figure 4.14. Here, all five different radii are plotted together with the frequency domain result.

In the figure, it is difficult to assess the convergence of the results. For this reason, the same two regions as in Figure 4.12 are enlarged in more detail. The results obtained for all tested coupling radii are close to each other, but in the enlarged zone to the right, it is immediately clear that the coupling radii equal to three dx and five dx are too small to provide a sufficiently accurate result. The K_D value of those radii differs from the one with the largest coupling radius up to 5%. The three largest coupling radii all indicate the same converged result. For the completion of the test program, a coupling radius equal to 10 dx will be retained. In combination with the selected grid size of $dx = L/20$, this leads to a coupling radius of $L/2$.

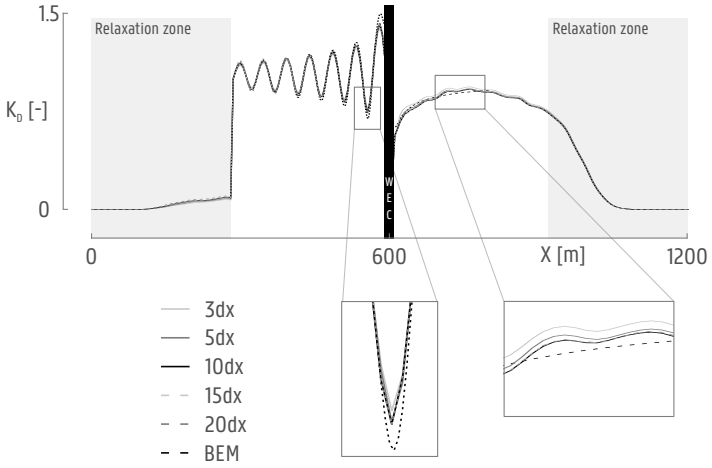

Figure 4.14: Sensitivity analysis for coupling radius, R_c. Results from coupling methodology applied to OceanWave3D, showing K_D results along a longitudinal section in the middle of the domain.

4.5 Validation

4.5.1 Comparison of Numerical Models

In this section, the results of the comparison study between MILDwave and OceanWave3D, using the coupling methodology, are discussed. For each test described in Table 4.1, the K_D results are compared. An extensive comparison will be performed for Test 1, while the results of the remaining tests will be condensed in RMSE values.

4.5.1.1 Test 1

As defined in Table 4.1, "Test 1" consists of simulating the wave field around one single WEC in deep water. Each simulation is run for 150 s, allowing the wave field to completely develop a steady state. Firstly, the K_D values for both the MILDwave-Nemoh coupled models and the OceanWave3D-Nemoh coupled models are illustrated in Figure 4.15. Qualitatively, both figures correspond very well. The coupling zone is masked out (see central white area) since the implementation technique for each coupled model is slightly different. In front of the coupling zone, a clear reflection pattern with higher K_D values is observed, while in the lee of the coupling zone there is a wake with reduced K_D values.

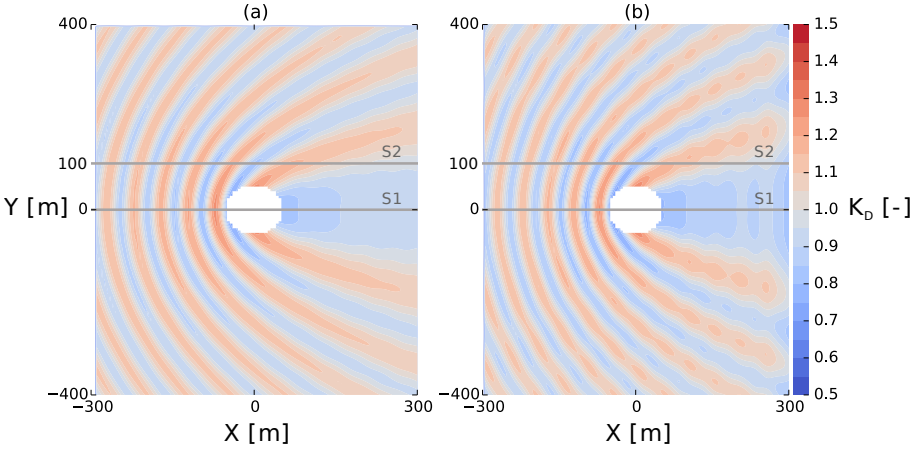

Figure 4.15: Contour plots of K_D results for the coupled models: (**a**) MILDwave-Nemoh and (**b**) OceanWave3D-Nemoh.

A closer look is taken at two longitudinal sections in Figure 4.16. Section S1 is crossing the domain center, while Section S2 is taken at a location of $y = 100$ m. Again, the coupling zone is masked out for Section S1. Since Test 1 is performed with regular, linear waves over a constant water depth, the K_D results can be compared to the Nemoh solution, as well. Both coupled models MILDwave-Nemoh and OceanWave3D-Nemoh achieve a very good correspondence with the Nemoh result and are very close to each other.

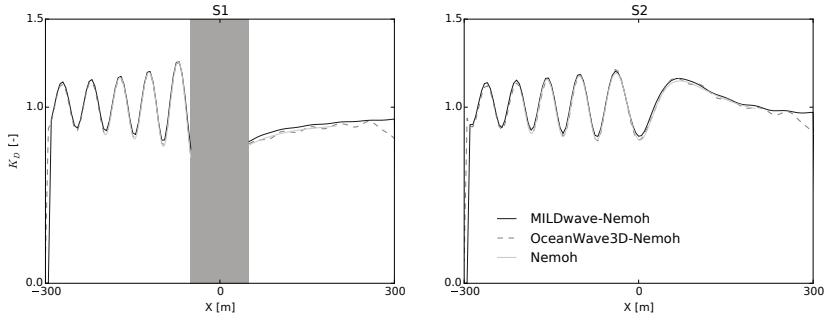

Figure 4.16: K_D results along the two longitudinal sections indicated in Figure 4.15 (Section 1 (S1): left; S2: right) for MILDwave-Nemoh, OceanWave3D-Nemoh and Nemoh.

In Figure 4.17, the relative K_D differences, $(K_{D,1} - K_{D,2})/K_{D,1} \times 100\%$, between the MILDwave-Nemoh, OceanWave3D-Nemoh and Nemoh models are quantified. Three plots show the difference between MILDwave-Nemoh and Nemoh, OceanWave3D-Nemoh and Nemoh and MILDwave-Nemoh and OceanWave3D-Nemoh, respectively. The MILDwave-Nemoh model maximally differs 5% from the Nemoh result in the reflection zone in front of the WEC. This relative difference with Nemoh remains below 2% for the OceanWave3D-Nemoh model. Comparing both coupled models to each other results in a maximum K_D difference of 5%, very locally in the diffraction zone.

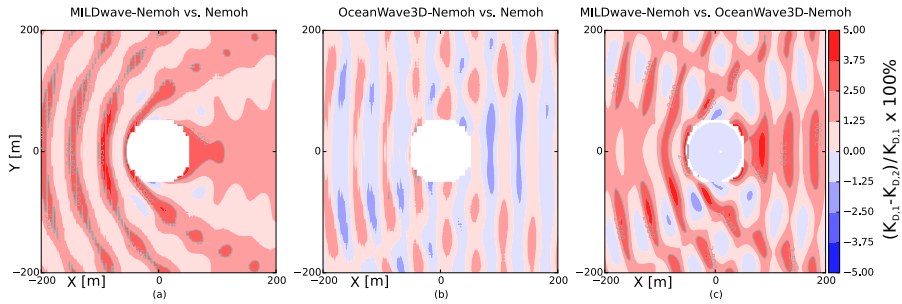

Figure 4.17: Contour plots of relative K_D errors comparing: (**a**) MILDwave-Nemoh and Nemoh; (**b**) OceanWave3D-Nemoh and Nemoh; (**c**) MILDwave-Nemoh and OceanWave3D-Nemoh.

As a final quantification of the comparison between the coupled models MILDwave-Nemoh, OceanWave3D-Nemoh and the wave-structure interaction solver Nemoh, one RMSE value can be calculated for the whole domain, based on the K_D results. This is obtained by calculating the RMSE for each grid cell and averaging the result over the whole domain. For Test 1 from Table 4.1, this results in an error of RMSE $= 1.7\%$ for the MILDwave-Nemoh coupled model compared to Nemoh, an error RMSE $= 1.0\%$ for OceanWave3D-Nemoh compared to Nemoh and RMSE $= 1.7\%$ comparing both coupled wave propagation models MILDwave-Nemoh and OceanWave3D-Nemoh.

4.5.1.2 Comparison Summary

For each test of Table 4.1, the same comparison method is applied as the one presented in Section 4.5.1.1. However, for practical simplicity reasons, the remaining tests are summarized by calculating one RMSE value over the whole domain. For the tests performed with a flat bottom, there are three RMSE values: an error value comparing the MILDwave-Nemoh coupled model to Nemoh, one comparing the OceanWave3D-Nemoh model with Nemoh and an error value comparing both coupled models MILDwave-Nemoh and OceanWave3D-Nemoh. In the tests performed with a variable bathymetry, only the wave propagation models can be directly compared, since Nemoh is not applicable there. The summary for Tests 1 to 10 of Table 4.1 is given in Figure 4.18. It is clear that the coupling methodology succeeds in accurately propagating a total wave field, according to linear wave theory. For Tests 1 to 6, a direct comparison with Nemoh can be made since there is a flat bottom. Error values of K_D remain below 3%. When looking in more detail, it is clear that the largest errors are occurring at the border of the coupling zone. However, at a distance of only a couple of grid cells, the results are excellent. Due to the comparison with Nemoh, it can be concluded that the coupling methodology is able to extend the domain limitations of the wave-structure interaction model and accurately propagate a complex wave field over a larger domain. An assumption is then made that the accuracy of the wave field will remain high with variable bathymetries. The simulations with variable bathymetry show a very good agreement between MILDwave-Nemoh and OceanWave3D-Nemoh, as well, with RMSE values remaining below 5%. The simulation with irregular waves is the least accurate. The choice of which wave propagation model to use is easily made based on the following guideline. Since MILDwave calculates significantly faster, the only reasons to apply OceanWave3D are when: the bathymetry has slopes larger than $1/3$ and there is a need for calculating velocity profiles or simulations with weakly non-linear waves. If these conditions or requirements are not applicable, then the use of MILDwave-Nemoh is strongly recommended, as this robust model provides quick and accurate results.

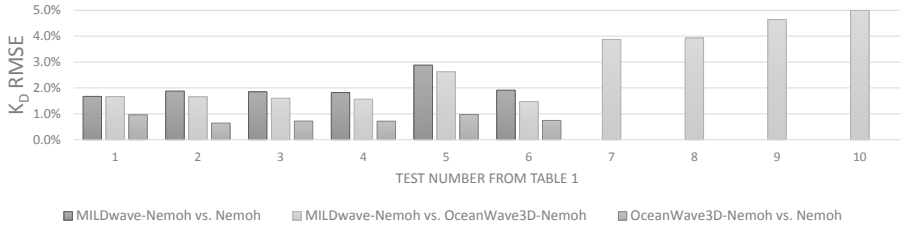

Figure 4.18: RMSE values for whole domain between coupled wave propagation models MILDwave-Nemoh and OceanWave3D-Nemoh and the wave-structure interaction solver Nemoh.

4.5.2 Comparison to the Experimental Dataset

The comparison of the K_D results obtained with the OceanWave3D-Nemoh model with the experimental WECwakes data is performed based on the surface elevations at the 19 selected wave gauges, shown in Figure 4.9. First, the results for the test with a wave period of 1.18 s are discussed and, then, the results for the test with a wave period of 1.26 s.

4.5.2.1 Regular Waves with Wave Period $T = 1.18$ s

The first tested waves have a wave period of $T = 1.18$ s, which is close to the natural period T_R of the WEC. In Figure 4.19, the surface elevations within a selected time window of the simulation are illustrated. All signals are displayed at the same scale. Overall, there is a good agreement with the experimental data. In some locations (for example Wave Gauges (WG) 6, 9, 12, 13, 28, 29), the experimental surface elevation has some clear non-linear behavior, which is logically not reproduced in the numerical results. These non-linearities possibly originate from both viscous effects, as well as non-linear wave radiation, as discussed in Mccallum (2017). When the spherical bottom part of the WEC device is partly emerging above the free surface, the wave radiation becomes non-linear. The superposition of this non-linear radiated wave with the quasi-linear wave results in a non-linear combined wave. Since the WEC devices are heaving in resonance, this phenomenon is strongly present. A quantitative comparison between the data will be given in Section 4.5.2.3.

4.5.2.2 Regular Wave with Wave Period $T = 1.26$ s

The second wave has a period of $T = 1.26$ s. In Figure 4.20, the surface elevations within a selected time window of the simulation are illustrated. Again, there is a good agreement with the experimental data. In some locations (for example WG 4, 6, 8), the experimental surface elevation has some clear non-linear behavior (see Section 4.5.2.1), which is logically not reproduced in the numerical results. However, in general, the surface elevation looks more linear than in the first test. This can be due to the incident wave period, which is outside the natural period T_R of the WEC. A more quantitative comparison between the data will be given in Section 4.5.2.3.

4.5.2.3 Comparison Summary

The error between the numerical and experimental data is expressed as RMSE values and maximum error values. In Figure 4.21, the error on the surface elevation for each wave gauge of Figure 4.9 is given for both test cases of $T = 1.18$ s and $T = 1.26$ s, respectively. At the top of the figure, the location zone of the wave gauges is given. On average, the surface elevation differs 10% from the experimental data, with slightly better results for the first test ($T = 1.18$ s). The RMSE error values range from 4% to 17% while the maximum errors range from 11% to 34%. The wave gauges in the front and upper zone have the best

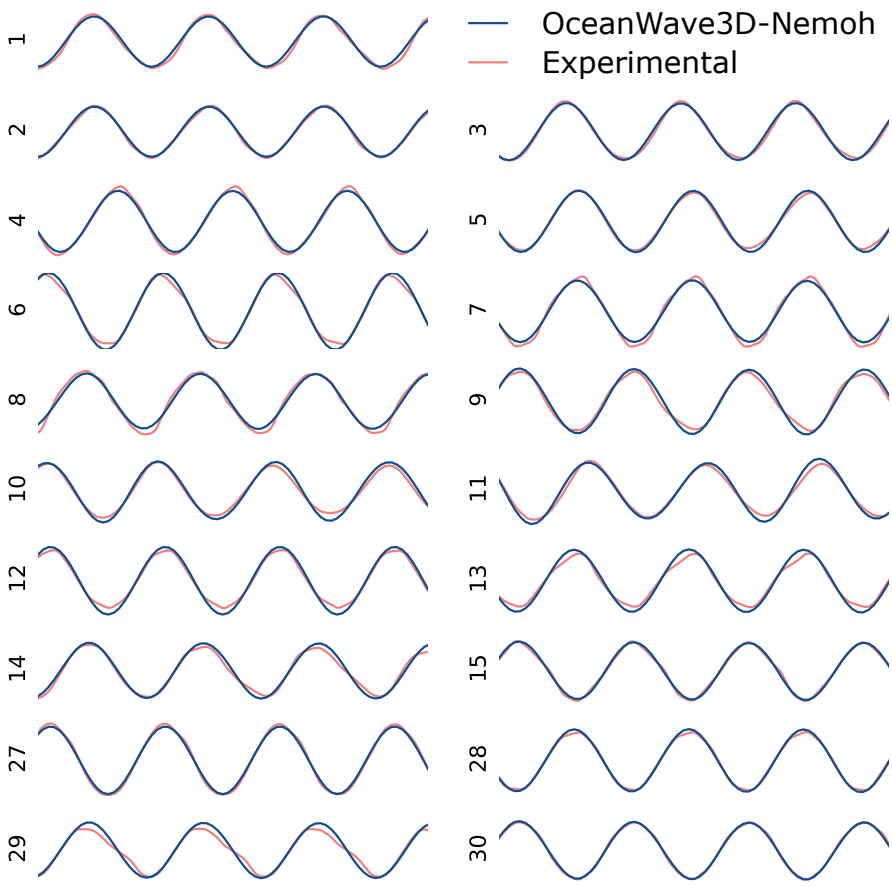

Figure 4.19: Comparison of the wave signal between the OceanWave3D-Nemoh model and the experimental data for all 19 wave gauges in the experimental dataset for incident waves with period $T = 1.18$ s. The WG number (see Figure 4.9) is indicated at the left of each wave signal.

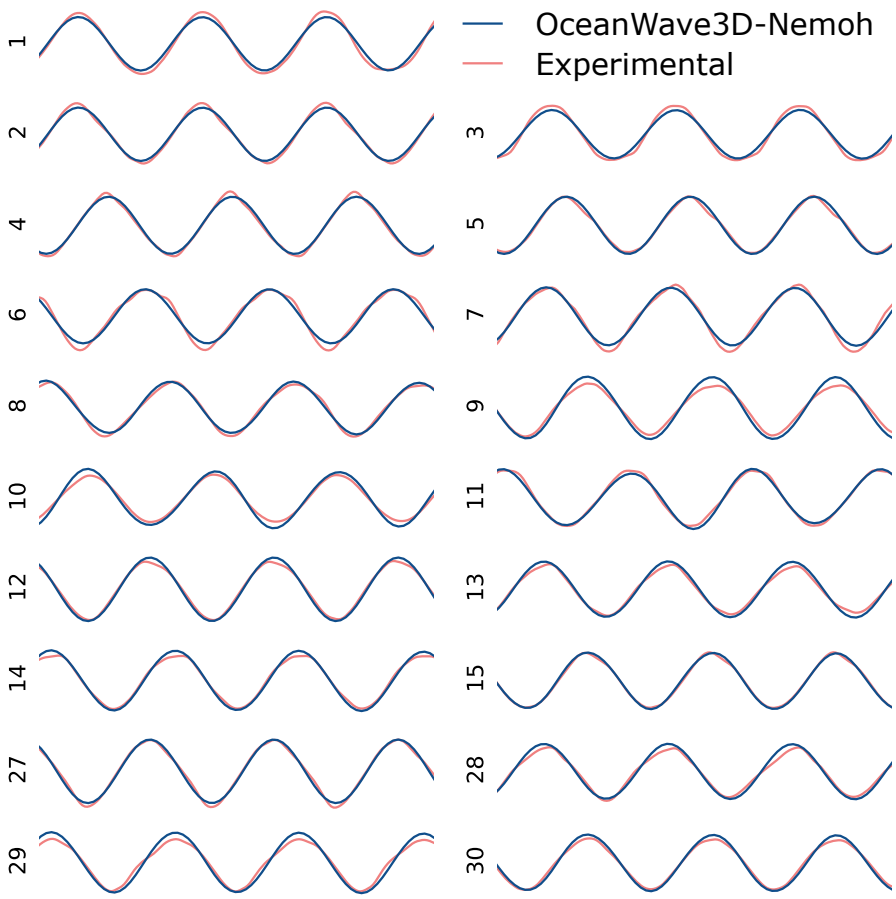

Figure 4.20: Comparison of the wave signal between the OceanWave3D-Nemoh model and the experimental data for all 19 wave gauges in the experimental dataset for incident waves with period $T = 1.26$ s. The WG number (see Figure 4.9) is indicated at the left of each wave signal.

correspondence with the experimental data (9% error), while the center zone has the largest error (12% error). Caution is necessary with interpreting these results, since the experimental data are inherently non-linear. The incident wave is a weakly non-linear Stokes second order wave. Additionally, the applied PTO system is a linear damper in theory, but behaves more like a non-linear Coulomb damper in practice. Nevertheless, this is the only dataset available for large WEC arrays, and the conditions are close enough to linear. While the comparison of this particular test gives a good agreement, this is not the case for all WECwakes tests. 12 more test cases have been studied, some with very good agreement, others with lesser agreement. All these additional test results can be explored in Appendix D.

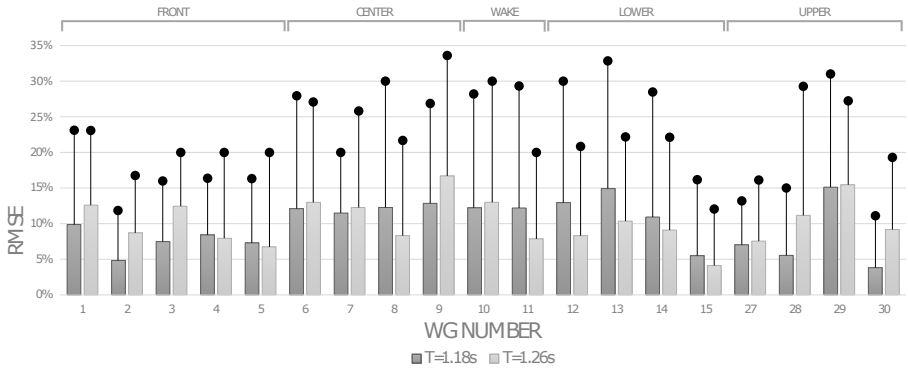

Figure 4.21: Comparison of RMSE and maximum error values for $T = 1.18$ s and $T = 1.26$ s for all 19 wave gauges of Figure 4.9 in the experimental dataset.

4.6 Conclusions

In this chapter, a generic coupling methodology is introduced to perform numerical modelling of (closely-spaced) offshore floating or fixed structures. By combining the accurate near-field wave-structure interaction solver with fast far-field wave propagation models, it is possible to model regular and irregular waves propagating through offshore device clusters over a variable bathymetry. This was demonstrated by employing two different wave propagation models, MILDwave and OceanWave3D, to model wave propagation through floating wave energy converter arrays. The numerical comparison proved that both MILDwave-Nemoh and OceanWave3D-Nemoh are capable of providing accurate surface elevations for a range of different test cases. In general, it is advised to apply MILDwave-Nemoh, since it calculates reasonably faster. However, OceanWave3D-Nemoh can be applied for bathymetries with steep slopes, for the calculation of non-depth averaged 3D simulations and weakly non-linear simulations. This development fills the first two identified knowledge gaps of Section 2.4.

The introduced coupling methodology has limitations, as well. Firstly, since the methodology uses the superposition principle for obtaining a total wave field, only linear waves conditions lead to correct results. However, applying the methodology

to weakly non-linear wave conditions only introduces a small error, as demonstrated in Section 4.5.2. Secondly, within the coupling zone, the solution is coming solely from the wave-structure interaction solver. It is thus necessary to have a flat bottom within that zone. Thirdly, typical BEM wave-structure interaction solvers are limited to a maximum number of fixed or floating bodies (for example Nemoh allows up to 25 bodies). However, in practice, they are sufficient for typical device farm applications. This limitation can be solved by applying a different type of wave-structure interaction solver. Fourthly, the coupling methodology does not allow direct simulation of irregular waves. Only a summation of several regular waves can be applied, which leads to an increase of the computational time.

In conclusion, despite some limitations, the coupling methodology has proven to be a valuable tool that is applicable in the following fields:

- Far-field simulations of fixed/floating offshore devices, such as assessment of coastal impact, with significant higher accuracy than previously applied spectral methods;
- Generic wave-wave and wave-structure interactions;
- Assessing energy production of large WEC arrays;
- Assessing wave propagation through large floating or fixed structure arrays, for example floating wind farms;
- Optimization of floating or fixed structure array layout, based on the local wave climate and bathymetry.

Continuation of this work, improving the linear coupling methodology and optimizing it for irregular short-crested waves is done in-house, as detailed in Verao Fernandez et al. (2018).

Chapter 5

Non-Linear Coupling Methodology with Moving Boundaries

In this fifth chapter of the thesis, a non-linear coupling methodology is introduced to perform accurate numerical simulations of wave-structure interactions of for example floating WECs. The non-linear wave structure interaction solver DualSPHysics is coupled to the wave propagation solver OceanWave3D in a 2-way method. The research presented is based on the following articles:

originally published as:
Verbrugghe, T., Domìnguez, J. M., Crespo, A. J. C., Altomare, C., Stratigaki, V., Troch, P. and Kortenhaus, A. (2018). Coupling methodology for smoothed particle hydrodynamics modelling of non-linear wave-structure interactions. *Coastal Engineering*, 138:184–198. 10.1016/j.coastaleng.2018.04.021.

Verbrugghe, Tim, Brecht Devolder, J.M. Domìnguez, Andreas Kortenhaus, and Peter Troch. 2017. "Feasibility Study of Applying SPH in a Coupled Simulation Tool for Wave Energy Converter Arrays." In Proceedings of the 12th Wave and Tidal Energy Conference, 679-689.

Verbrugghe, Tim, Andreas Kortenhaus, Peter Troch, and JM Domìnguez. 2017. "A Non-linear 2-way Coupling Between DualSPHysics and a Wave Propagation Model." In Proceedings of Spheric2017, 1-7.

5.1 Introduction

The previous Chapter introduced in a linear coupling methodology, capable of simulating near-field and far-field effects around WEC arrays, over a variable bathymetry. This methodology is useful for linear and even weakly non-linear wave conditions,

corresponding to the operating conditions of a WEC array. However, often more severe sea states are occurring at these offshore locations, with strongly non-linear waves acting on the WEC devices. Studying the response of floating WECs or any floating structure in strongly non-linear wave conditions is not possible with the formerly introduced linear coupling methodology. Hence, this chapter introduces a non-linear coupling methodology, allowing simulations of non-linear wave structure interactions.

During the past decades, construction of offshore and nearshore structures has seen a steady increase. Next to traditional oil platforms, offshore and nearshore areas are suited for the installation of fixed and floating wind turbines, artificial islands, tidal turbines and wave energy converters. These structures, fixed or floating, have a significant influence on the local wave field. Within coastal engineering it is of great interest to be able to accurately identify the near-field and far-field wave transformations influenced by these structures. The superposition of these phenomena results in a complex perturbed wave field (Stratigaki et al., 2014b,a; Troch and Stratigaki, 2016). Simulating the wave transformations within and around a WEC array is complex; it is difficult, or in some cases impossible, to simulate both near-field and far-field effects using a single numerical model, in a time and cost-efficient way in terms of computation time and effort. This can be achieved by coupling of a wave-structure interaction solver for the near-field effects and a wave propagation model for the far-field effects. This strategy is well documented in literature, for weak and strong coupling methods (see Section 2.2).

In this research, focus is put on coupling of a fully non-linear 3-D potential flow solver (OceanWave3D (Engsig-Karup et al., 2009)) with a weakly-compressible SPH (WCSPH) wave-structure interaction solver DualSPHysics (Crespo et al., 2015). The objective is to simulate wave impacts on floating and fixed structures in real sea and storm conditions, characterized by irregular, 3-D waves with the occurrence of non-linear effects. The coupling is performed in a two-way manner, allowing the disturbed wave field around the structure to be propagated towards the far-field. The coupled model allows for simulation of offshore structures in higher order irregular waves and more extreme wave conditions. This coupling methodology has been developed to combine:

1. the advantages of the approach of wave-structure interaction solvers based on smoothed particle hydrodynamics, which accurately formulate and efficiently resolve the physical processes, specifically for quantification of wave forces (Altomare et al., 2015a).

2. the benefits of the approach of wave propagation models, which resolve the propagation and transformation of waves over large distances, with a fast computation time, including bathymetric variability over the domain and wave transformation processes when approaching the coastline.

Smoothed particle hydrodynamics are a flexible Lagrangian and mesh-less technique for Computational Fluid Dynamics (CFD). The Lagrangian reference frame of SPH makes it useful in solving problems with large deformations and distorted free surfaces. In comparison with other numerical methods, the SPH formulation

is simple and robust (Monaghan, 2005). SPH has been successfully applied to a number of free-surface problems that involve wave breaking and splashing (Monaghan and Kos, 1999; Dalrymple and Rogers, 2006). The impact between a rigid body and water has been studied in Monaghan et al. (2003). A fixed cylinder in a wave train and forced motion of cylinders generating waves is mentioned in Omidvar et al. (2012), while floating bodies in waves have been successfully studied in 2-D (Manenti et al., 2008). The feasibility of applying SPH for modelling of wave energy converters has been studied in Verbrugghe et al. (2017a). 3-D problems of wave generation by a heaving cone and a floating body in waves undergoing predominantly heave motion are investigated in Omidvar et al. (2013). The latter has also indicated that there is a computational benefit of calculating with a variable particle mass distribution.
Coupling SPH solvers to other models is one of the SPHERIC Grand Challenges (`spheric-sph.org/grand-challenges`). A general algorithm for one-way coupling of SPH with an external solution has been proposed in Bouscasse et al. (2013b). The interaction between the SPH solver and the external solution is achieved through an interface region containing a ghost fluid, used to impose any external boundary condition. In Fourtakas et al. (2018), A hybrid Eulerian-Lagrangian incompressible SPH formulation is introduced, where two different SPH formulations are coupled rather than two completely different solvers. The SPH solver DualSPHyics has been coupled in Altomare et al. (2016a), where a one-way coupling was realized with the wave propagation model SWASH. A numerical wave flume has been created to simulate wave impact and run-up on a breakwater. The first part of the numerical flume is simulated using the faster SWASH model, while the wave impact and run-up are calculated using DualSPHysics. Here, a one-way coupling is sufficient, since there is only interest in the impact of waves on the breakwater. In Kassiotis et al. (2011), a similar approach has been adopted, where a 1D Boussinesq-type wave model is applied for wave propagation in most of the spatial domain, and SPH computations focus on the shoreline or close to off-shore structures, where a complex description of the free-surface is required. Similarly, an incompressible SPH solver has been coupled to a non-linear potential flow solver QALE-FEM in Fourtakas et al. (2017). In Chicheportiche et al. (2016), a one-way coupling between an potential Eulerian model and an SPH solver is realised, applying a non-overlapping method using the unsteady Bernoulli equation at the interface. These studies applied coupling to speed up the simulation time by minimizing the computationally intensive SPH domain. Other studies apply coupling to combine both the benefits of mesh-based and mesh-free CFD methods. In Didier et al. (2013), the wave propagation model FLUINCO is coupled to an SPH code, and validated with experimental data of wave impact on a porous breakwater. A hybrid multiphase OpenFOAM-SPH model is presented in Kumar et al. (2015), where the SPH method is used on free surfaces or near deformable boundaries whereas OpenFOAM is used for the larger fluid domain. A similar coupling is used, where breaking waves are modelled with SPH and the deeper wave kinematics are modelled with a Finite volume method. This has been demonstrated in Marrone et al. (2016) for a weakly-compressible SPH (WCSPH) solver and in Napoli et al. (2016) for an incompressible SPH (ISPH) solver.

In the present research, the main reasons for developing coupling is to save computation time and to achieve fully non-linear wave generation. Compared to all the coupling methodologies described above, the coupling methodology presented herein differentiates itself based on the following novel features:

- The coupling methodology contains two coupling interfaces: one 'upwave' of the SPH domain and one 'downwave' of the SPH domain;
- The individual models are coupled at every time step using a Message Passing Interface (MPI) implementation;
- The coupling information is shared between the coupled models based on a two-way principle;

The SPH solver receives detailed information on the wave kinematics from the wave propagation model, while the transformed surface elevations (reflection, diffraction and radiation) resulting from the wave-structure interaction are transferred back to the wave propagation model. This is necessary for two reasons. Firstly, the interest is to study the motions of offshore and near-shore floating structures. Extending the SPH domain until the coastline, would lead to an unnecessarily large computational cost. For this, boundary conditions are needed upwave and in the lee of the floating structure. A two-way coupling ensures the most accurate implementation of these boundary conditions. Secondly, apart from the floater motions, the main interest is to study the effects of the floating structures on the wave field and the propagation of that disturbed wave field further away from the device. For this reason a two-way coupling where the surface elevation is coupled back to the wave propagation model, is mandatory.

In Section 5.3 of this chapter, the principles of the coupling methodology are presented. A detailed description of the models, employed to demonstrate the proposed coupling, is provided, followed by an explanation of the coupling algorithm. Next, the results of a number of tests performed with the coupling methodology are discussed in Section 5.5. The focus is put on simulations of linear and non-linear waves, as well as comparing simulation results to those obtained from two experimental datasets. Finally, concluding remarks are made in Section 5.8.

5.2 DualSPHysics as WEC modelling tool

Before presenting the coupling methodology, it is necessary to check if SPH and specifically DualSPHysics are capable of reproducing the perturbed wavefield around a WEC. For this reason, a feasibility study is performed, where a number of basic test cases are simulated to check the applicability of DualSPHysics to model floating WECs. First, the radiated waves of a heaving cylindrical body are studied. Next, the diffraction pattern around the same body is discussed. Then, the free decay of a heaving sideways cylinder is compared to results from literature. Finally, results from the response of a heaving WEC are compared to experimental data.

5.2.1 Wave radiation

5.2.1.1 Methodology

The set-up of the radiation test is illustrated in Fig. 5.1. A flat, cylindrical body is forced with a heaving motion in the center of a circular water tank. The sidewalls are sloped to absorb radiated waves and avoid reflection. The specific parameters for the model of radiated waves of a heaving cylindrical body are given in Table 5.1.

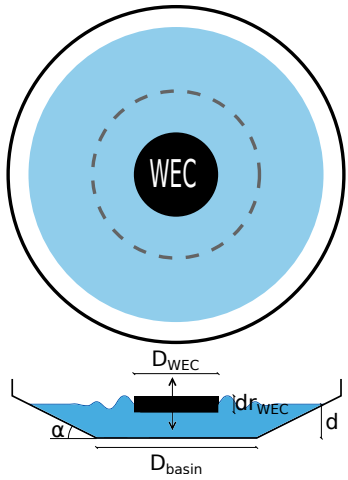

Figure 5.1: Set-up of numerical radiation test.

Table 5.1: Radiation test parameters

Parameter	Symbol	Value
WEC diameter	D_{WEC}	$10\ m$
WEC draft	dr_{WEC}	$1\ m$
Basin Diameter, bottom	D_{basin}	$20\ m$
Slope, side walls	α	$23°$
Water depth	d	$4\ m$
Heave amplitude	A	$0.5\ m$
Heave period	T	$5\ s$
Particle size	d_p	$10/5\ cm$
Simulation time	t_{sim}	$10\ s$

The conditions are selected in order to make sure the radiated waves are as close to linear as possible. The flat cylindrical shape is specifically selected to have a large radiating potential. According to Nemoh, the radiated waves should have a

maximum amplitude of around $0.2m$. The recommendation is to have at least 4-5 fluid particles per wave amplitude (Altomare et al., 2015a; Padova et al., 2014), hence the particle size of $0.05m$. For comparison purposes, a coarser model with $d_p = 0.1m$ is also run. In order to have perfect linear waves with this amplitude, the water depth should be at least $15m$. This would lead to an amount of fluid particles the GPU memory can not handle. For this reason the radiated waves are just outside the linear range (stokes 2^{nd} order). However, the 2^{nd} order effects will remain small justifying the comparison with a linear potential flow solver. This set-up results in a domain with 23.4 million particles, calculating on a GTX1070 GPU with 1920 CUDA® cores for $42h$.

In order to check the accuracy of the radiated waves, a comparison is made with a boundary element method (BEM) solver, called Nemoh. The solver treats the boundary value problem in the frequency domain; leading to the full flow field underneath the body. From this flow field several other quantities are calculated:

- The hydrodynamic coefficients: added mass and hydrodynamic damping;
- The pressure field on the body surface and the Froude-Krylov forces;
- Far field diffracted and radiated velocity potential in the form of Kochin functions;
- Near field diffracted and radiated surface elevation in a complex form.

Here, the last quantity is used for the comparison, from which the instantaneous radiated field can be calculated with equation 5.1:

$$\eta_{rad}(t) = \mathrm{Re}\left\{A \cdot (-i\omega) \cdot |RAO|\, e^{i\varphi_{RAO}} \cdot |R| \cdot e^{i\varphi_R} e^{-i\omega t}\right\} \tag{5.1}$$

with A the heave amplitude, RAO the response amplitude operator, ω the angular frequency and R the complex radiated wave field coming from Nemoh.

5.2.1.2 Results

The forcing of radiated waves is compared to a linear solution obtained by Nemoh. The surface elevation is compared in the time domain at two locations: one is $3\ m$ away from the edge of the cylinder, while the other is close at $0.1\ m$. Secondly the free surface elevation is compared at a fixed time step of $4.5\ s$, in function of the distance from the cylinder.

5.2.1.2a Comparison at 3 m The comparison between the linear Nemoh results and the SPH results for two different d_p values is illustrated in Fig. 5.2. It is clear that the overall shape of the radiated wave is similar to the linear solution. However, there are some differences noticeable. The coarse model overestimates the wave trough, which can be explained by the limited accuracy due to a particle size of $d_p = 0.1\ m$. The finer SPH model coincides more with the linear solution. There is a slight asymmetry to the wave profile, which can be explained by shallow

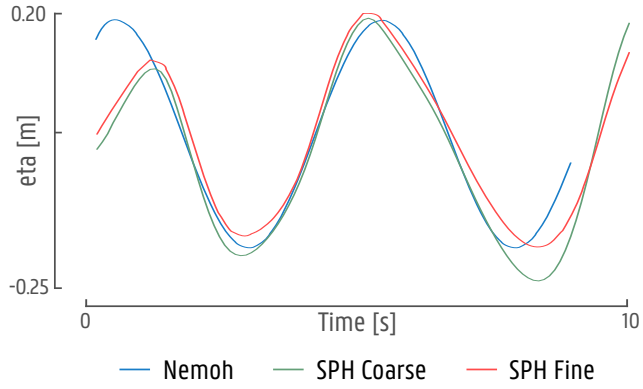

Figure 5.2: Comparison of free surface elevation at $\Delta r = 3.0\ m$

water principles where the wave crest is propagating faster than the wave trough. Important is to notice that the amplitude of the radiated wave is within 5% of the Nemoh solution. Applying a finer resolution could lead to more accurate results but computational power was insufficient for this case. Additionally, Rogers and Dalrymple (2008) have shown that comparing non-linear SPH to linear solutions strongly benefits from removing the nonlinear terms.

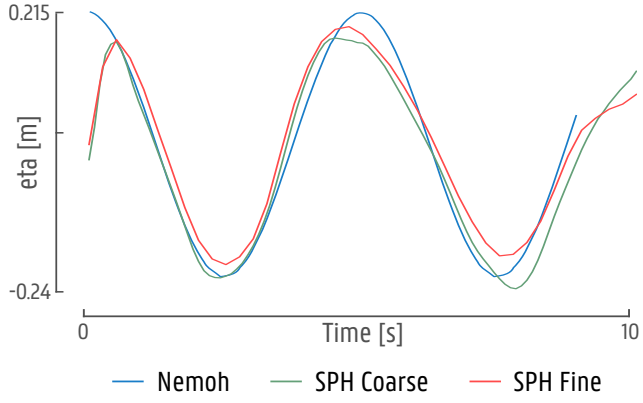

Figure 5.3: Comparison of free surface elevation at $\Delta r = 0.1\ m$

5.2.1.2b Comparison at 0.1 m Looking at the radiated field closer to the heaving cylinder, the comparison is illustrated in Fig. 5.3. A similar conclusion can be made as with the comparison further away from the cylinder. Overall there is a good correspondence between the linear solution and the SPH solution, with better results for the finer particle size. Here, the wave trough of the fine SPH solution is slightly higher than the linear solution. However, the difference is smaller than one particle size d_p. Alternatively, the difference can be explained by the occurrence of second order effects due to the shallow water depth.

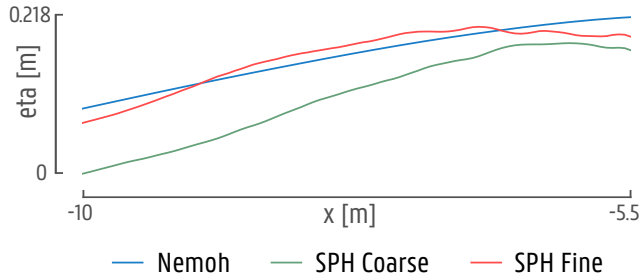

Figure 5.4: Comparison of radiated free surface elevation at $t = 4.5\ s$

5.2.1.2c Comparison at 4.5 s Lastly, a comparison is made at a fixed time step, where the wave profile is studied for all 3 models. The time step is selected based on the occurrence of a wave crest directly next to the heaving cylinder. In Fig. 5.4, it is clear that the finer SPH solution corresponds significantly better to the linear Nemoh solution. There are some fluctuations around the linear solution, but all are smaller than $0.03\ m$, which is well below the particle size.

5.2.1.2d Conclusion DualSPHysics is capable of modelling wave radiation caused by a heaving WEC. Selection of a fine particle size leads to an accurate solution, where the variations with respect to a linear solution remain below $0.6d_p$.

5.2.2 Wave diffraction

5.2.2.1 Methodology

The set-up of the diffraction test is illustrated in Fig. 5.5. The WECwakes buoy, a cylindrical body with spherical bottom, introduced in Section 4.3.3, is kept stationary. A wave paddle generates regular waves coming from the left boundary, hitting the stationary WEC. Waves are reflected back to the paddle and diffracted to the sides of the domain. The right part has an upwards slope, in order to avoid reflection at the end of the flume. The side walls are modelled with a so-called periodic boundary condition, implicating that there is a symmetry around the x-axis. In this manner, there is no reflection coming from the side walls. The specific parameters for the model of diffracted waves around a fixed WEC are given in Table 5.2.

Again, the results are compared to a BEM solution coming from Nemoh. The instantaneous diffracted field and incident wave field can be calculated with the equations 4.2 and 4.4 from Chapter 4.

5.2.2.2 Results

Incident waves are hitting a fixed WEC device and are diffracted and reflected. The free surface elevation is compared in the time domain to a linear solution obtained by Nemoh at two locations: one is $1\ m$ in front of the WEC device, while the other is $1\ m$ behind it. Secondly, the free surface elevation is compared at a fixed time step of $14\ s$, as a function of the distance of the numerical wave flume.

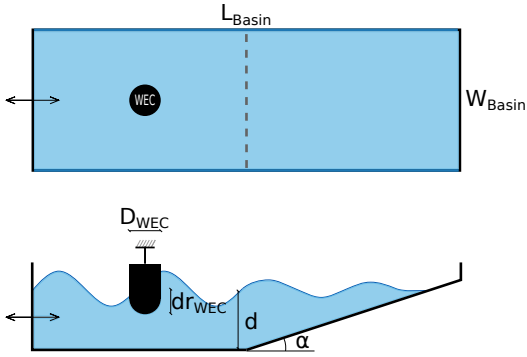

Figure 5.5: Set-up of numerical diffraction test.

Table 5.2: Diffraction test parameters

Parameter	Symbol	Value
WEC diameter	D_{WEC}	$0.315\ m$
WEC draft	dr_{WEC}	$0.3232\ m$
Basin Length	L_{basin}	$12\ m$
Basin Width	W_{basin}	$4\ m$
Slope, beach	α	$20°$
Water depth	d	$1\ m$
Wave Height	H	$0.2\ m$
Wave Period	T	$2.0\ s$
Particle size	d_p	$0.02\ m$
Simulation time	t_{sim}	$15\ s$

5.2.2.2a Comparison at 1 m in front of the WEC The comparison between the linear Nemoh results and the SPH result is illustrated in Fig. 5.6. It is clear that the agreement of the diffracted wave is similar to the linear solution. However, the wave crest of the SPH solution is 7% higher than the Nemoh solution. The difference is smaller than the particle size $d_p = 0.02\ m$. In front of the WEC, slight reflection is expected. Analysis of the SPH results leads to a result of 5% reflection immediately in front of the device, which is close to the 3%, predicted by Nemoh.

5.2.2.2b Comparison at 1 m behind the WEC Looking at the diffracted field behind the fixed WEC device, the comparison is illustrated in Fig. 5.7. A similar conclusion can be made as with the comparison in front of the WEC device. Overall there is a good agreement between the linear solution and the SPH solution. Again, all differences are smaller than one particle size d_p. Behind the WEC, a

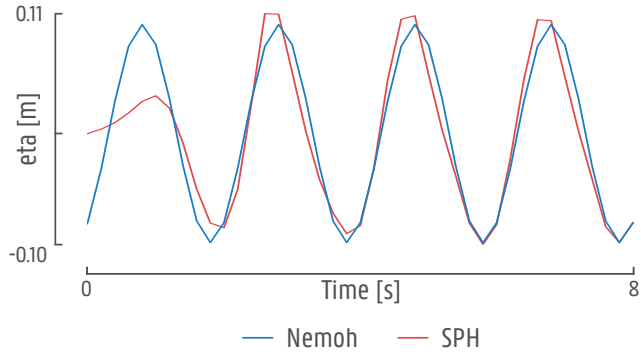

Figure 5.6: Comparison of free surface elevation at $\Delta r = -1.0\ m$ (in front of the WEC)

reduction of wave amplitude is expected. Analysis of the SPH results leads to a result of 10% wave reduction immediately behind the device, while Nemoh predicts a reduction of 6%.

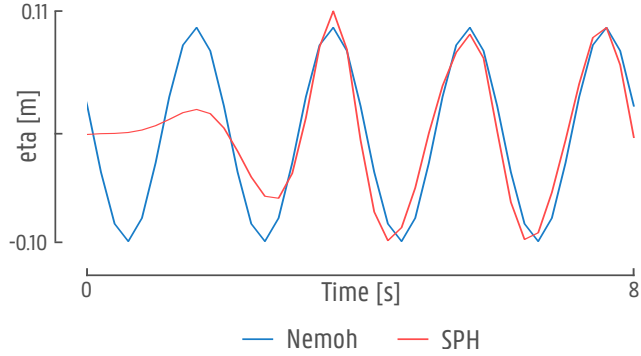

Figure 5.7: Comparison of free surface elevation at $\Delta r = 1.0\ m$ (behind the WEC)

5.2.2.2c Comparison at 14 s Lastly, a comparison is made at a fixed time step, where the wave profile is studied for both SPH and Nemoh. The time step is selected based on the occurrence of a wave trough in front of the WEC and a crest directly behind the WEC. In Fig. 5.8, it is clear that the SPH solution corresponds to the linear Nemoh solution with variations smaller than d_p, at a certain distance from the WEC. There are larger errors close to the WEC, exceeding the particle size d_p.

5.2.2.2d Conclusion DualSPHysics is capable of modelling wave diffraction around a fixed WEC. In front and behind the device, at some distance, the variations with respect to a linear solution remain below $0.8d_p$. Close to the device, variations are larger up to a maximum difference of $2.5d_p$. However, the real water surface close to a fixed device is characterized by non-linear effects like wave

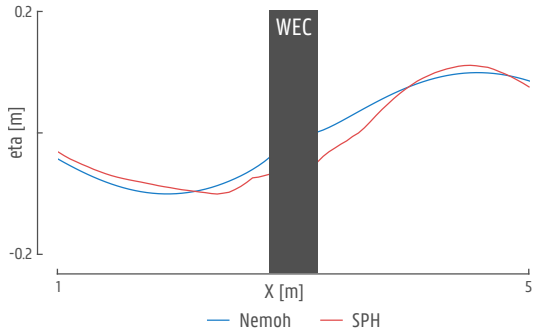

Figure 5.8: Comparison of diffracted free surface elevation at $t = 14\ s$

run-up, viscosity and turbulence. In this aspect, the linear Nemoh solution will be less accurate than the SPH model.

5.2.3 Comparison with experimental results: free decay

5.2.3.1 Methodology

In this section a free-decay test is performed and compared to experimental data. A free-decay test is a simple experiment allowing to discover the resonance period of a device and the hydrodynamic damping. These parameters strongly depend on the mass of the device, the water surface area and the shape. The experimental data originates from Ito (2018) and has previously been used to validate an OpenFOAM CFD model in Simscale (2018). Since the floating device is a long cylinder, lying on its side, the $3-D$ experiment can be simplified to a $2-D$ numerical simulation. The heaving cylinder has a diameter of $0.1524\ m$. The device is positioned in a wave flume with a length of $4\ m$ and a water depth of $1.2446\ m$. The device is pushed down over a distance of $0.0254\ m$ and released. The decay motion is registered with a linear variable differential transformer (LVDT). In the numerical model, at the flume boundaries, a periodic boundary condition is applied to avoid reflection of the radiated waves. The SPH simulation is performed at 3 different particle sizes. The specific parameters used in the SPH model are given in Table 5.3.

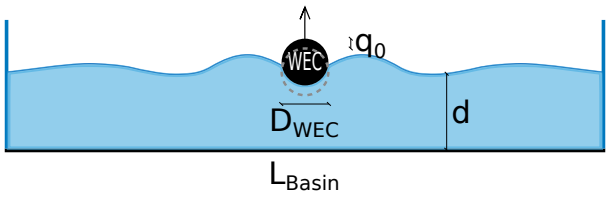

Figure 5.9: Set-up of numerical decay test.

Table 5.3: Free-decay test parameters

Parameter	Symbol	Value
WEC diameter	D_{WEC}	$0.1524\ m$
WEC draft	dr_{WEC}	$0.0762\ m$
Initial deflection	q_0	$-0.0254\ m$
Basin Length	L_{basin}	$4\ m$
Water depth	d	$1.2446\ m$
Particle size	d_p	$1/0.5/0.25\,mm$
Simulation time	t_{sim}	$2.5\ s$

5.2.3.2 Results

The decay motion is simulated with the SPH model at three different particles sizes: $d_p = 0.001\ m$, $d_p = 0.0005\ m$ and $d_p = 0.00025\ m$ as illustrated in Fig. 5.10. Both axes are normalized, in order to compare directly to the results of Simscale (2018). The y-axis is normalized by dividing with the initial position z_0, while the x-asis is the normalized time, defined as $t * \sqrt{g/r}$ with t the real time, r the WEC radius and g the gravitational acceleration. The coarse SPH model already has a good correlation with the experimental data, but there is some discrepancy at the extremes. However, going to a medium or fine particle size drastically improves the correspondence to the experiment: variations for the coarse size are around $2d_p$ while the finer sizes have variations lower than $1d_p$. The fine SPH simulation is only marginally better than the medium simulation: variations remain just below $1d_p$. In practice, the medium grid size would be used, since it results in a 4 times faster computation time.

5.2.4 Comparison with experimental results: regular waves

5.2.4.1 Methodology

In addition to the free-decay test, a test in regular waves is performed. The regular wave train has a wave height of $0.04\ m$ and a wave period of $1.6\ s$. The purpose of this test is to verify that the device's response to incident waves is accurate. The wave flume and WEC device are the same as described in Devolder et al. (2016). The WEC device is restricted to the heave motion by a vertical rod with a square cross section. The WEC is guided over the rod by teflon bearings. In the numerical simulation, the WEC is restricted to the heave motion by setting the linear accelerations in the X-direction to zero as well as all rotational accelerations. The simulation is performed in $2 - D$, since there is no interest here in diffracted wave patterns.

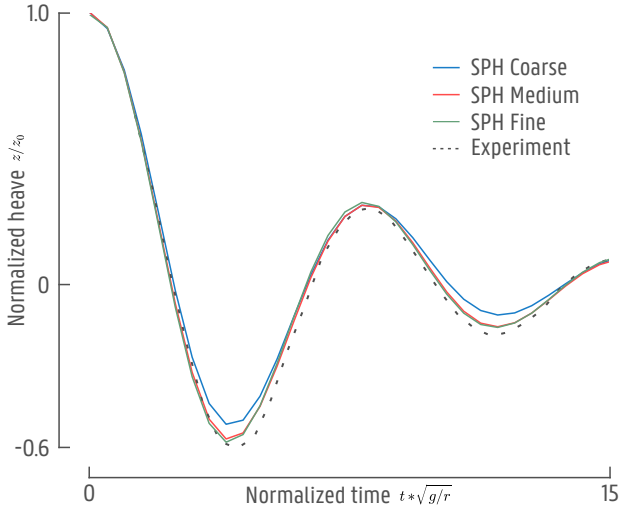

Figure 5.10: Comparison of decay motion of a heaving cylinder.

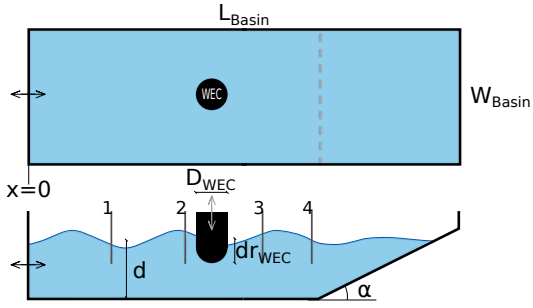

Figure 5.11: Set-up of regular wave response test.

5.2.4.2 Results

The heaving motion of the WEC is compared to the experimental results in Fig. 5.12. The results shows the WEC is heaving with a slightly larger amplitude in the SPH model (up to 15%) as in the experimental data. This can be explained by the extra friction caused in the experiment by the Teflon bearings on the vertical shaft.

The perturbed wave field, a combination of incident, radiated and diffracted waves is compared to the experiment on 4 locations (Fig. 5.11), as illustrated in Fig. 5.13. The wave generation in the experiment is characterised by a gradual build-up. In the numerical experiment, the full wave height is reached reasonably fast to minimize the simulation time. Consequently, there is a bad agreement at the beginning of the simulation. The first comparison is at $3\ m$ in front of the wave paddle, where the incident wave is compared. Here, it is seen that in both the

Table 5.4: Regular wave test parameters

Parameter	Symbol	Value
WEC diameter	D_{WEC}	$0.315\ m$
WEC draft	dr_{WEC}	$0.3232\ m$
Basin Length	L_{basin}	$10\ m$
Basin Width	W_{basin}	$1\ m$
Slope, beach	α	$11°$
Water depth	d	$0.7\ m$
Wave height	H	$0.04\ m$
Wave period	T	$1.6\ s$
Particle size	d_p	$0.001\ m$
Simulation time	t_{sim}	$25\ s$

SPH model and the experiment there is a good agreement of the surface elevation. The second graph shows the surface elevation at $x = 4.6\ m$, or $0.35\ m$ in front of the floating WEC. Here, the results are almost identical between the SPH model and the experimental data, proving that the WEC device in both the experiment and the model are excited by the same wave.

The third measuring point is at $x = 6.25\ m$, or $1.35\ m$ behind the WEC device. Here, there is a significant difference of up to 50% between the SPH model and the experimental data. In the SPH simulation, there is a significant decrease in wave amplitude of 45% behind the WEC, while this is not the case in the experiments. Additionally, there is a clear asymmetry in the wave signal. This can be an effect of performing the simulation in 2-D. Finally, the surface elevation is compared at $x_4 = 7.8\ m$, where the wave amplitude of the SPH model is still smaller than the experimental data, but the effect is much less pronounced (only 30% difference vs. 50% at location 3).

From this study, it can be concluded that SPH is a viable method to model the basic linear wave transformations within WEC modelling. However, due to the high computational effort, it should mostly be applied in situations where non-

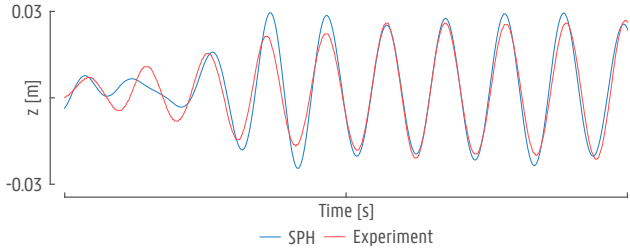

Figure 5.12: Comparison of the heaving motion of the WEC, positioned at $x = 4.95\ m$.

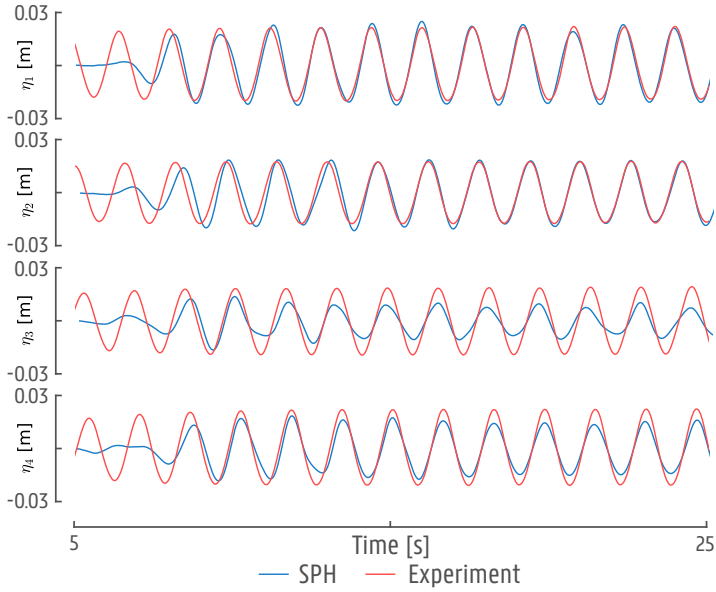

Figure 5.13: Comparison of the perturbed wavefield at several locations: $x_1 = 3.0\ m$, $x_2 = 4.6\ m$, $x_3 = 6.25\ m$, $x_4 = 7.8\ m$

linear effects are important, such as shallow water, extreme waves or even breaking waves.

5.3 Coupling Methodology

5.3.1 Generic Description

The ideal strategy for a 3-D coupling methodology can be realised as illustrated in Figure 5.14. It is inspired by the work by Troch and Stratigaki (2016) who first presented coupling between the wave propagation model MILDwave (Troch, 1998) and the BEM wave-structure interaction solver WAMIT (Hill, 2018), using an internal circular wave generation boundary around floating structures to pass information from WAMIT to MILDwave and propagate the waves within the wave propagation domain. In the present work, a large wave propagation domain is set up for propagating fully non-linear, short-crested 3-D waves. Within the large domain, a number of fixed or floating structures is installed. The wave-structure interactions of each of these structures is modelled within a circular zone, closely spaced around the structure with a custom designed interface for exchanging information between the two models. Within the circular zone, the interaction of the floating structure with the incident waves is calculated, resulting in a combination of diffracted and radiated waves. Within the wave propagation domain, these diffracted and radiated waves can propagate further away from the floating

structure. Although this generic description suggests a 3-D coupling methodology, the proposed coupling methodology has only been applied here in 2-D, and is validated with 2-D test cases. For the application of the coupling methodology, the wave propagation model OceanWave3D is coupled to the SPH wave-structure interaction solver DualSPHysics.

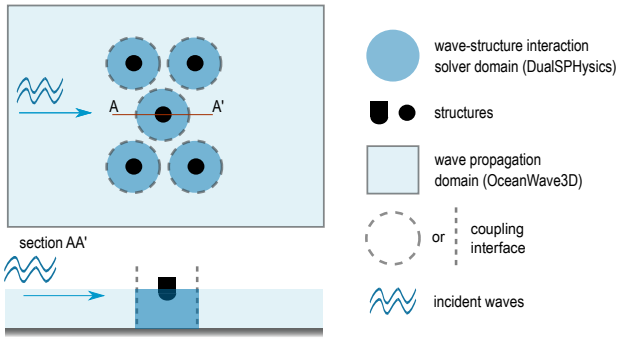

Figure 5.14: Plan view (top) and longitudinal section along section AA'(bottom), illustrating the proposed coupling principle. Circular wave-structure interaction zones (SPH) with a fixed or floating structure in the center are coupled to a wave propagation model. Information is transferred at the interfaces upwave and in the lee of the structure.

5.3.2 SPH solver DualSPHysics

The theoretical background of the applied wave-structure interaction solver, DualSPHysics, has been detailed in Chapter 3. Specific for this chapter, the focus is put on applying moving boundaries at the coupling interface.

5.3.2.1 Boundary conditions

Within this research, the boundary conditions in the SPH model are described by a set of particles that are considered separate from the fluid particles. The method is called Dynamic Boundary Conditions (DBC), and is available within the DualSPHysics software. These boundary conditions are presented and validated in Crespo et al. (2007). The boundary particles have the same properties as the fluid particles, but they do not move according to the forces exerted on them. They remain either in a fixed position or move according to a prescribed motion. When a fluid particle approaches a boundary and the distance between the boundary particles and the fluid particles becomes smaller than twice the smoothing length h, the density of the affected boundary particles increases, resulting in a pressure increase. In turn, this results in a repulsive force being exerted on the fluid particle due to the pressure term in the momentum equation. Stability of this method relies on the length of time step taken being suitably short in order to handle the highest present velocity of any fluid particles currently interacting with boundary particles and it is therefore an important issue when considering how the variable

time step is calculated. Validations with dam-break flows and sloshing tanks have been published with good results and also comparing these boundary conditions with other approaches (Domínguez et al., 2015). In addition, DBC have also been shown to be suitable to reproduce complex geometries in Altomare et al. (2014) and can be used for wave generation, as shown in Altomare et al. (2017).

5.3.3 Coupling methodology

5.3.3.1 Principle of the coupling methodology

As mentioned before, SPH simulations are computationally demanding. Consequently, the computational domain size in an SPH model is often limited to a zone closely spaced around the area of interest. However, for accurate wave propagation, there is a spatial need for wave generation and wave absorption, around $3-4$ wavelengths long. This leads to a significant increase in water particles, and thus higher computation times. Wave generation techniques available in DualSPHysics are first and second order wave generation by using piston-type or flap-type wave paddles (Altomare et al., 2017). This wave generation method requires a certain wave propagation length before the full kinematics and surface elevation are developed. By coupling DualSPHysics to the fully non-linear potential flow solver OceanWave3D, the objective is to simulate higher-order irregular short-crested waves in a domain which is as small as possible.

In an attempt to treat both the problem of computational effort and the problem of wave generation, a 2-D coupling methodology as illustrated in Figure 5.15 is developed. Although both OceanWave3D and DualSPHysics can be run in 3-D, currently only a 2-D coupling has been implemented, which is described here. A numerical wave flume is created where waves are propagated within a two-way coupled model. In the large wave propagation domain, fully non-linear waves are generated by a 2-D implementation of OceanWave3D. This model calculates both the surface elevation and horizontal and vertical wave kinematics over a varying bathymetry. The fully non-linear potential flow equations are solved over a rectangular grid, which is split up in vertical layers. Waves are generated at the left side and absorbed at the right side, by using relaxation zones as described in Engsig-Karup et al. (2009); Larsen and Dancy (1983).

OceanWave3D is coupled to DualSPHysics v4 by implementing two internal coupling interfaces within the OceanWave3D domain: one for SPH wave generation (interface 1 in Figure 5.15) and one for SPH wave absorption (interface 2 in Figure 5.15). At the interfaces, the horizontal orbital velocities are registered at every time step and sent to the DualSPHysics simulation. Here, the orbital velocities are imposed on the dynamic boundary conditions. These are implemented as a stack of rectangular moving boundary blocks, with a height equal to the particle size, d_p. The dynamic boundary particles are generating waves at the left side, and absorbing waves at the right side. The horizontal position of every moving boundary block can be calculated at every time step, by integrating the horizontal orbital velocity profile using Equation 5.2:

$$x_{b,i+1} = x_{b,i} + u_i \cdot \Delta t \tag{5.2}$$

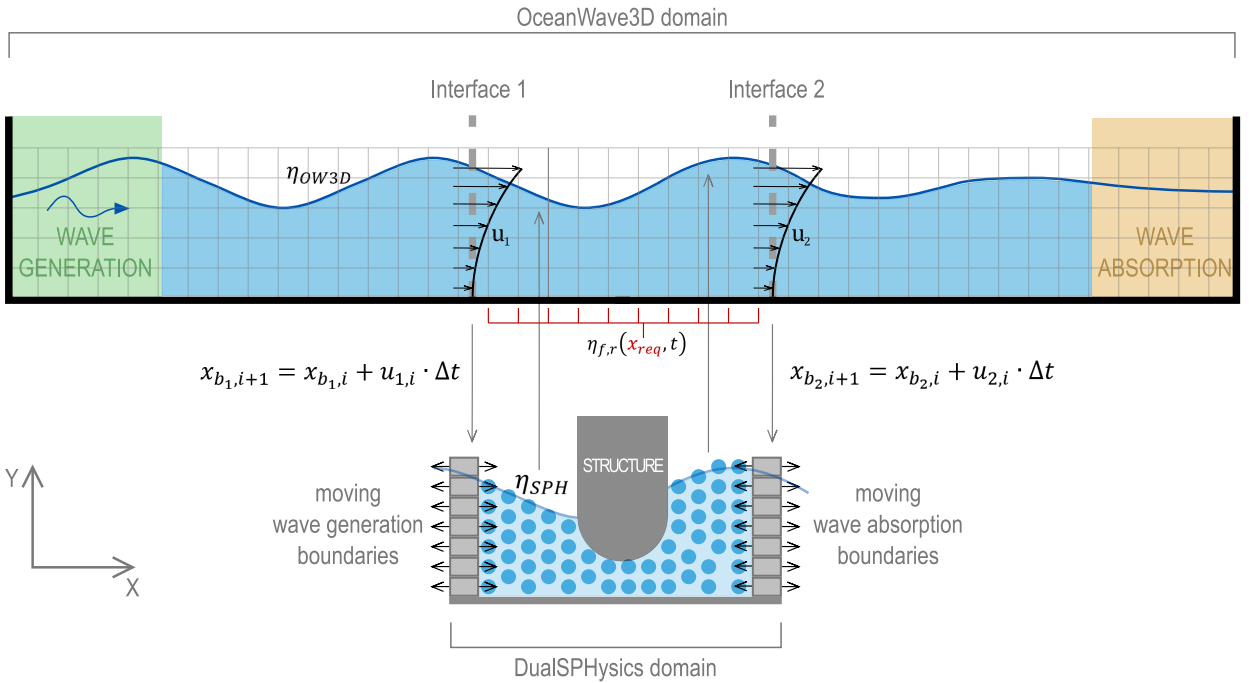

Figure 5.15: Principle of 2-D coupling between OceanWave3D and DualSPHysics around a structure under wave action. The top part shows the complete domain in OceanWave3D. The bottom part illustrates the DualSPHysics zone.

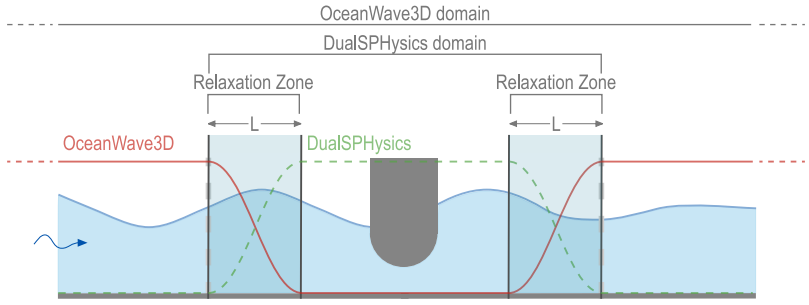

Figure 5.16: Sketch of 'relaxation zones' providing a smooth transition between the OceanWave3D domain and the DualSPHysics domain.

Both models are running simultaneously, albeit DualSPHysics with a significantly smaller time step. At the end of each OceanWave3D time step, Δt_{OW3D}, both models are synchronised. DualSPHysics transfers information back to OceanWave3D, specifically surface elevation information. To ensure a smooth transition between the DualSPHysics free surface and the OceanWave3D free surface, a 'relaxation function' is applied (see Figure 5.16). The applied function f_{rel} is the same as is applied within OceanWave3D's generation and 'absorption relaxation' zones and is given in Equation 5.3, with L the length of the zone.

$$f_{rel} = \left(\frac{x - x_0}{L}\right)^{3.5} \tag{5.3}$$

5.3.3.2 Coupling implementation

The implementation of the coupling methodology consists of 4 coupling elements (see Figure 5.17):

1. Python Main Script
2. OceanWave3D process
3. Python Interface
4. DualSPHysics process

The first element is the Python main script. it is a preprocessor, used to configure the coupled simulation. It creates input files for both DualSPHysics and OceanWave3D, based on the user input. It launches the parallel execution of DualSPHysics, OceanWave3D and the Python communication script. OpenMPI is used to interconnect these three processes. It applies the widespread MPI standard, implemented by all platforms (here, Fortran, C++ and Python are connected), minimizes the necessary changes in the code, and allows the distributed execution of programs.

The second element is the wave propagation model (OceanWave3D process); it generates and propagates the waves in a large domain. It provides the velocity data for the coupling interface and receives the surface elevation information from DualSPHysics.

The third element is the Python Interface: a communication process, which takes care of the communication between the DualSPHysics process and the OceanWave3D process. Although a direct communication between these processes is possible with MPI, the use of a dedicated Python process is justified because of the following reasons:

- Each model uses a different coding language, so a high-level language like Python simplifies the coupling tasks.
- Both models are in constant evolution with regular source code updates. It is thus beneficial to minimize the necessary changes in the models.
- Using Python as the communicator allows to easily monitor intermediate results and find errors in the transferred data.

The fourth element is the DualSPHysics process, where the wave-structure interaction is simulated in a small domain. It applies the velocity information from OceanWave3D to generate and absorb the waves, while sending back the surface elevation information.

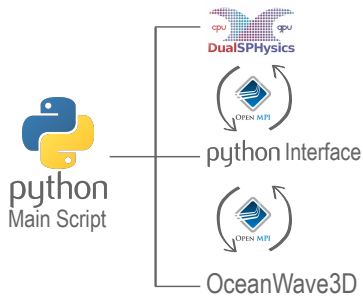

Figure 5.17: Program scheme of 2-D coupling between Oceanwave3D and DualSPHysics. Three processes are initiated and connected via an OpenMPI implementation.

5.3.3.3 Code Alterations

The coupling implementation from Figure 5.17 requires source code changes in OceanWave3D, DualSPHysics and the creation of Python scripts. This section summarizes the code alterations for each software package.

5.3.3.3a OceanWave3D Code Changes In order to enable an online two-way coupling with OceanWave3D, a number of code changes need to be made. The following files were adapted to allow the coupling methodology to work:

1. Input file `OW3D.inp`;
   An extra line was added to the input file, indicating coupling should be applied, and specifying the coordinates of the coupling zone.

2. file `globalvariables.f90`;
   Global variables are created for the coupling file, coupling zone coordinates and indices and the received SPH free surface.

3. file `ReadinputFileParameters.f90`;
   The extra line added to the input file is read into its corresponding global variables, to be used by the coupling routine.

4. file `OceanWave3DTakeATimeStep.f90`;
   At every time step, the coupling routine is called, after a check if coupling is enabled.

5. file `CoupleRoutine.f90`;
   This subroutine initializes the MPI communication, calculates the indices for the coupling interface locations and calculates the horizontal orbital velocities from the wave potential. It sends the velocities and the surface elevation to the Python script, and receives the filtered SPH surface elevation, which it uses to overwrite the original surface elevations.

5.3.3.3b Python Code Python is used to connect the different coupling pieces together. Although a direct coupling between OceanWave3D and DualSPHysics is technically possible, using Python as an intermediate station allows for a much higher flexibility and allows the user to perform easy accuracy checks and simplifies the debugging process. The following files have been developed:

1. main file `main_MPI.py`;
   This file loads in the set-up parameters, writes away the input files for OceanWave3D and DualSPHysics, and executes the simulations. For a two-way simulation, an MPI-run is started where the OceanWave3D simulation is assigned to the first process, the script `run_2way.py` is assigned to the second process and DualSPHysics is assigned to the third process.

2. communication file `run_2way.py`;
   this file manages the two-way communication between OceanWave3D, Python and DualSPHysics, using the MPI protocol. Several MPI commands are issued to receive and send data from and to OceanWave3D and DualSPHysics.

3. functions file `functions.py`;
   This file contains functions for interpolating the orbital velocities in the sigma coordinates to the moving SPH boundary blocks, functions to apply the relaxation and functions to create the necessary input files and to post-process the results.

5.3.3.3c DualSPHysics Code Changes A number of code changes and additions are performed on the DualSPHysics source code. The following files were altered:

1. main files `JSphGpuSingle.cpp` and `JSphCpuSingle.cpp`;
   This is the main simulation file for a GPU or CPU run. Here, the MPI communication with Python is performed. The MPI connection is initialized at the start of the simulation and terminated after the final time step. During the time-stepping, the moving boundary positions received from Python are stored in arrays and sent to the function `RunMotion()`, while the free surface elevation is calculated and sent back to Python. For the CPU code, in the function `FtCalcForces()` the motion of the floating object can be restricted to a specific degree of freedom.

2. file `JSphGpu.cpp` and `JSphCpu.cpp`;
   Here, the function `RunMotion()` is altered, respectively for the GPU and CPU calculations. The function is altered to accept the old and new boundary block positions, and linearly interpolate between these two according to the current time step.

3. file `JSphGpu_ker.cu`;
   Here, in the function `KerFtCalcForcesRes()`, the motion of floating objects can be restricted to a specific degree of freedom, for example the heave motion.

5.3.3.4 Coupling algorithm

In practice, the coupling algorithm is coded as follows. In step 1, the main Python script is run to set up the computation. The following variables are initialized:

- Flume parameters: length, depth, coupling zone, mesh size, particle size
- Wave parameters: wave height, wave period, wave type
- Structure parameters: shape, size, floating/fixed
- Simulation parameters: duration, time step

Both the input files for OceanWave3D and DualSPHysics are created based on the selected input parameters. A dedicated simulation folder is created and the SPH run is initialized by running a preprocessing tool.

In step 2, the main coupled model is initiated by issuing an MPI run where three tasks are divided over three processes:

- Process 0: OceanWave3D simulation
- Process 1: Python interface (data processing, communication hub)
- Process 2: DualSPHysics simulation

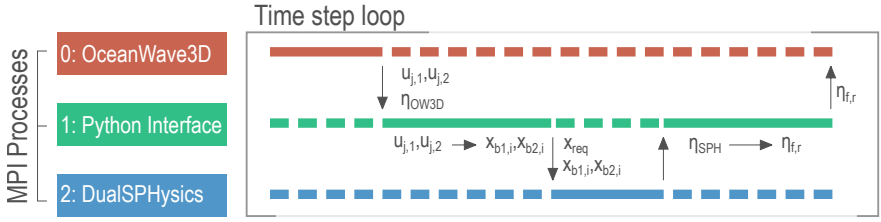

Figure 5.18: Coding algorithm of coupling between Oceanwave3D and DualSPHysics. Data is transferred from one process to another during one time step. Visual representation of the symbols can be found in Figure 5.15

The coupling algorithm is illustrated in Figure 5.18. The OceanWave3D wave propagation model is run for one time step. At the end of the time step, the horizontal water velocities at the coupling zone boundaries $u_{j,1}, u_{j,2}$ with $j = 1 : m$ and m the number of vertical layers in OceanWave3D, and the surface elevation η_{OW3D} are sent to the Python process with the "MPI Send" command. Since the DualSPHysics simulation has much more dynamic boundary particles in the vertical direction than OceanWave3D has vertical layers, the velocities need to be integrated and interpolated to the boundary block positions $x_{b_1,i}, x_{b_2,i}$ with $i = 1 : n$ and n the number of the boundary blocks for the DualSPHysics simulation. These boundary block positions are sent to the DualSPHysics process, together with the x-coordinates, x_{req}, of the OceanWave3D grid points which lie within the coupling zone. Next, DualSPHysics is run with a duration, equal to the OceanWave3D time step. Within DualSPHysics, the surface elevation at the x_{req} locations is calculated with the built-in interpolation routine. When DualSPHysics has run for a duration equal to the OceanWave3D time step, the free surface elevation, η_{SPH}, is sent back to the Python process. Here, the relaxation function given in equation 5.3 is applied to the head and tail of the free surface array, to ensure a smooth transition between the OceanWave3D and DualSPHysics solution (see Figure 5.16 for relaxation zones). Additionally, a Savitzky-Golay filter (Savitzky and Golay, 1964) is applied to η_{SPH} to mitigate the irregularities with sizes smaller than the smoothing length $h = 1.2 \cdot d_p \cdot \sqrt{2}$, caused by the interpolation routine. This filtered signal, $\eta_{f,r}$, is finally sent back to OceanWave3D, where its original solution η_{OW3D} is overwritten with the new free surface received by DualSPHysics. In this version of the coupled model, only the surface elevation is transferred back to OceanWave3D. Although this is not a complete coupling of all physical parameters, it does result in accurate results for the proposed purposes. The main focus of the research is on wave transformations within and around WEC arrays. This focus on surface elevation and floater response mainly requires a good representation of the wave profile and accurate floater dynamics. For the interests of the topics with which the present research deals, the applied coupling principle leads to highly satisfactory results when investigating the surface elevation and floater response. Moreover, by not coupling back the velocity field, the SPH velocity fields which are prone to noise, depending on the applied diffusion scheme, will not be introduced

into the wave propagation model. Additionally, externally added noise would lead to numerical instabilities.

5.4 Convergence Analysis

For each of the 3 test cases, a particle size is selected which leads to a result that is as close as possible to a converged result, without sacrificing too much computation time. The convergence study is demonstrated here for Wave Type II of Test Case 1, but has been performed for all test cases to ensure proper convergence.

The convergence is checked by applying the coupled model to the wave propagation of a Stokes 2^{nd} order wave with wave height $H = 0.08\ m$, wave period $T = 2.0\ s$ in a water depth of $d = 1.0\ m$. The simulation is performed for four different particle sizes d_p, with a refinement factor of 2.0. The surface elevation in the center of the domain is presented in Figure 5.19. A closer look at the wave trough reveals that the result is practically converged for the two finest particle sizes $d_{p,3}$ and $d_{p,4}$. In order to estimate the relative convergence error, the exact solution of the surface elevation at the wave trough, $\eta_{t,exact}$, is estimated based on the Richardson's extrapolation (Richardson, 1911; Richardson and Gaunt, 1927), using the surface elevation at the wave trough from the three finest particle sizes ($\eta_{t,2}$ from $d_{p,2}$, $\eta_{t,3}$ from $d_{p,3}$, $\eta_{t,4}$ from $d_{p,4}$). The exact solution $\eta_{t,exact}$ is given in Table 5.5, and is calculated as follows:

$$\eta_{t,exact} = \eta_{t,3} + \frac{\eta_{t,4} - \eta_{t,3}}{1 - 2^{-\alpha}} \tag{5.4}$$

$$\text{with } \alpha = \frac{\ln \frac{\eta_{t,2} - \eta_{t,3}}{\eta_{t,3} - \eta_{t,4}}}{\ln 2} \tag{5.5}$$

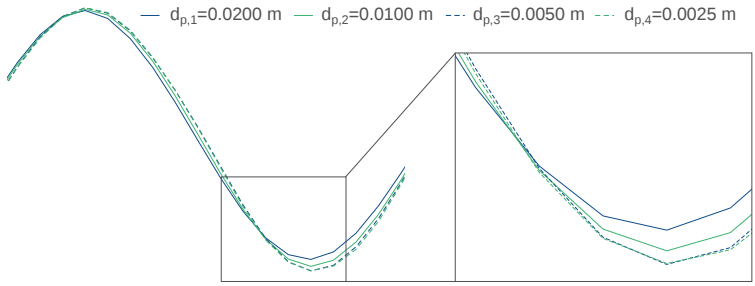

Figure 5.19: Convergence of the surface elevation of a Stokes 2^{nd} order wave using four particle refinements ($d_{p,1}$, $d_{p,2}$,$d_{p,3}$ and $d_{p,4}$). A closer look is taken at the wave trough to show the convergence.

The results in Table 5.5 show that already for the particle size refinement with $d_{p,3} = 0.005$ the error is low enough at 0.61%. For all the tests performed in this research, a similar refinement is performed to ensure a converged result.

Table 5.5: Particle size convergence and Richardson's extrapolation

	Particle Size d_p **[m]**	**Surface Elevation at Trough** $\eta_{t,i}$ **[m]**	**error**
$d_{p,2}$	0.0100	-0.03509	2.72%
$d_{p,3}$	0.0050	-0.03589	0.50%
$d_{p,4}$	0.0025	-0.03604	0.08%
		Exact:	
-	-	-0.03607	-

The order of convergence can be estimated by calculating the L_2 error norm for each resolution and plotting these errors in function of the particle size. The L_2 error norm is calculated as follows:

$$L_2 = \sqrt{\sum_{i=1}^{n} |\eta_{SPH} - \eta_{exact}|^2} \tag{5.6}$$

The L_2 error norm for the free surface elevation is plotted in function of the particle size d_p in Figure 5.20. It is noticed that the L_2 error reduces for smaller d_p values. The order of convergence lies between first-order and second-order. Typically, Lagrangian SPH formulations have several sources. There are mollification errors since the quantities are smoothed within a kernel. There is a discretisation error by replacing continuum properties with locally smoothed quantities. There are summation errors when the kernel does not have full support. The integral interpolant gives at least a second-order interpolation. However, this is before the continuum is discretised and the simulation is run. This means that the order of convergence for Lagrangian SPH is typically lower than 2.

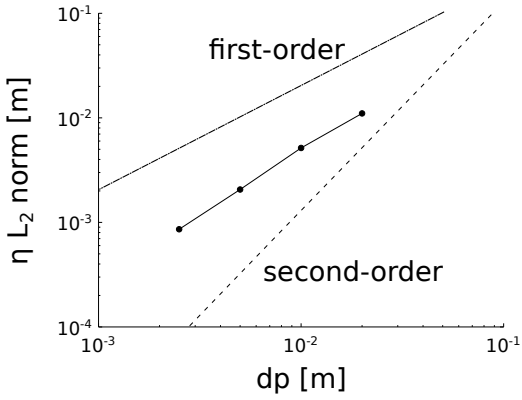

Figure 5.20: L_2 Norm Error for SPH results at different resolutions

5.5 Validation

A series of test cases is performed for validating the proposed coupling methodology. In Test Case 1, a range of linear and non-linear waves are propagated over a flat sea bottom, with no presence of structure in the computational domain. Here, the focus lies on demonstrating the ability of the coupling methodology to propagate waves in between two moving boundaries. In Test Case 2, the coupled model is compared to experimental data from a fixed Oscillating Water Column (OWC) wave energy converter. In Test Case 3, a freely floating box is simulated using the coupled model, and is compared to experimental data. In each test case, the initial condition is a zero condition with a steady water level and no particle motion.

5.5.1 Test Case 1: Regular wave propagation

In this section, the described two-way coupled model is applied to simulate a series of propagating waves. The waves are selected based on their linear or non-linear characteristics, as described by the diagram of Le Méhauté (1969). A selection of four wave types is made, which encompasses a wide range of non-linear and linear theories. The specific characteristics such as wave height H, wave period T, water depth d and particle size d_p are listed in Table 5.6). The particle size is selected based on the refinement method described in section 5.4. The validity of each wave theory is illustrated in Figure 5.21.

Table 5.6: Wave Conditions

Wave Type Test	Wave Theory	Wave Height H [m]	Wave Period T [s]	Water Depth d [m]	Wave Length L [m]	Particle Size d_p [m]
I	Linear	0.02	1.5	1.0	3.35	0.0020
II	Stokes 2^{nd}	0.08	2.0	1.0	5.22	0.0050
III	Stokes 3^{rd}	0.15	2.0	0.7	4.62	0.0050
IV	Stream function	0.06	2.0	0.3	3.26	0.0025

The numerical domain and test set-up is illustrated in Figure 5.22. It consists of a $2-D$ wave flume with a total length of $50.0\ m$ and a varying water depth according to the applied wave conditions. The waves are generated within OceanWave3D in a wave generation zone with a length of $20.0\ m$. At the other end of the OceanWave3D domain, a wave absorption zone is installed with the same length. The DualSPHysics zone is located between $x_1 = 20.0\ m$ and $x_2 = 25.0\ m$.

For each selected wave type test from Table 5.6, a time-series is shown where three wave signals are compared:

- Theoretical wave signal, generated using WaveLab (Frigaard and Andersen, 2014)
- Simulated wave signal using OceanWave3D
- Simulated wave signal using the two-way coupled model

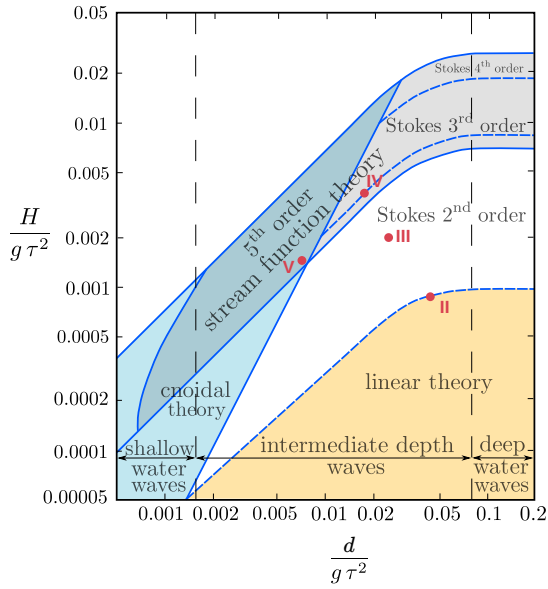

Figure 5.21: Selection of waves tested with the two-way coupled model. Tests I-IV are indicated on the graph (adapted from Le Méhauté (1969)). $\frac{d}{g\tau^2}$ is the normalized water depth while $\frac{H}{g\tau^2}$ is the normalized wave height.

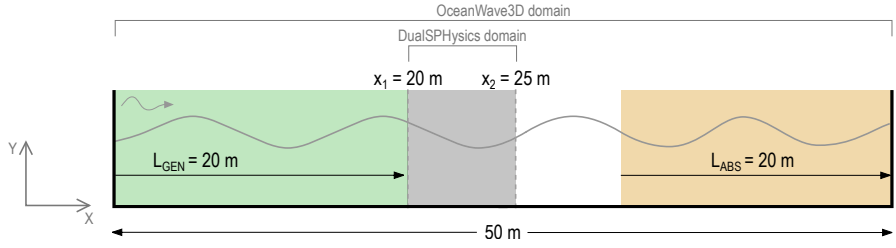

Figure 5.22: Test set-up in the numerical domain. L_{gen} is the wave generation zone, L_{abs} is the wave absorption zone.

By analyzing the wave signal in the time-domain, typical non-linear wave characteristics such as wave steepness, asymmetry and higher wave troughs are checked for accurate reproduction.

5.5.1.1 DualSPHysics Parameters

The efficiency and accuracy of DualSPHysics was investigated in Altomare et al. (2015b) for wave propagation and absorption showing good agreement between numerical results and experimental data. Accordingly, similar SPH options used for that work will be used here to perform the numerical simulations. Table 5.11 summarises the SPH formulation and some parameters used.

Table 5.7: SPH formulation and parameters.

Time Integration Scheme	Verlet
Time Step	Variable (including CFL and viscosity)
Kernel	Wendland
Smoothing Length	$1.2 \cdot d_p \cdot \sqrt{2}$
Viscosity Treatment	Artificial ($\alpha = 0.01$)
Equation of State	Tait equation
Boundary Conditions	Dynamic Boundary Particles
δ-SPH	Yes (δ-SPH = 0.1)

5.5.1.2 Wave Type Test I - Linear Wave

The first wave type test includes a linear wave with a wave height of $H = 0.02\ m$, wave period of $T = 1.5\ s$ in a water depth of $d = 1.0\ m$. Since this wave type lies within the linear theory zone (see Figure 5.21), the surface elevation should match the theoretical profile, defined in Equation 5.7:

$$\eta(t) \quad = \quad \frac{H}{2} \cos\left(\frac{2\pi}{T} \cdot t\right) \tag{5.7}$$

5.5.1.3 Wave Type Test II - Stokes 2^{nd} Order Wave

The second wave type test is based on a non-linear wave with a wave height of $H = 0.08\ m$, wave period of $T = 2.0\ s$ in a water depth of $d = 1.0\ m$. This results in a wave profile described by the Stokes 2^{nd} order wave theory (see Figure 5.21), as defined by Equations 5.8 and 5.9.

$$\eta(t) = a\left[\cos\theta + ka\frac{3-\sigma^2}{4\sigma^3}\cos 2\theta\right] + \mathcal{O}\left((ka)^3\right) \quad (5.8)$$

$$H = 2a\left(1 + \frac{3}{8}k^2a^2\right) \quad (5.9)$$

$$\text{with } \sigma = \tanh kd \quad (5.10)$$

$$\text{and with } \theta = \frac{2\pi}{T}\cdot t \quad (5.11)$$

5.5.1.4 Wave Type Test III - Stokes 3^{rd} Order Wave

The third wave type test is based on a non-linear wave with a wave height of $H = 0.15\ m$, wave period of $T = 2.0\ s$ in a water depth of $d = 0.7\ m$. This results in a wave profile described by the Stokes 3^{rd} order wave theory (see Figure 5.21), defined in Equation 5.12.

$$\eta(t) = a\left[\cos\theta + \frac{ka}{2}\cos 2\theta + \frac{3(ka)^2}{8}\cos 3\theta\right] + \mathcal{O}\left((ka)^4\right) \quad (5.12)$$

5.5.1.5 Wave Type Test IV - Stream Function Wave

The last wave type test is based on a stream function wave with a wave height of $H = 0.06\ m$, wave period of $T = 2.0\ s$ in a water depth of $d = 0.3\ m$. The Stream function wave theory was developed by Dean and Dalrymple (Dean and Dalrymple, 1991b). The method involves computing a series solution to the fully non-linear water wave problem, involving the Laplace equation with two non-linear free surface boundary conditions (constant pressure and a wave height constraint).

5.5.1.6 Comparison of surface elevations

The results by the comparison of surface elevations, calculated at the center of the coupling zone, are summarized in Figure 5.23 and in Table 5.8. In Figure 5.23, the surface elevations for all 4 simulated wave types are compared between theoretical solution, a stand-alone OceanWave3D run and the coupled model. In general, the simulation results show a very good correspondence with the theoretical solutions. Both the wave crest and wave trough are very close to the theoretical results. The asymmetry of the wave profile in the non-linear wave types (II-IV) is also reproduced. The accuracy of the results is quantified by analysing the surface elevation at the wave crests and the wave troughs. The two-way coupled model is compared to the theoretical solution by calculating the ratio of the wave amplitudes $err_{\%}$ (equation 5.13) and the relative difference err_h expressed in the smoothing length $h = 1.2 \cdot d_p \cdot \sqrt{2}$ (equation 5.14). Here, a_{SPH} is the wave amplitude of the coupled model results, where a_{Theory} is the wave amplitude of the theoretical solution. Additionally, the maximum error and its location are calculated as well and are defined as the L_∞ error.

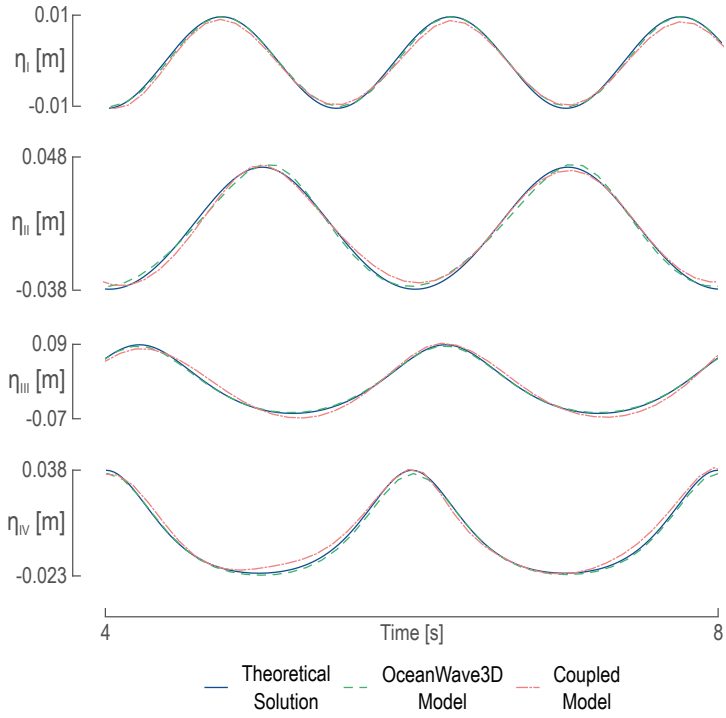

Figure 5.23: Comparison of the surface elevations in the center of the domain for all 4 simulated wave types, between the theoretical solution, a stand-alone OceanWave3D run and a two-way coupled model run.

$$err_{\%} = |1 - \frac{a_{SPH}}{a_{Theory}}| \cdot 100 \tag{5.13}$$

$$err_{h} = \frac{|a_{SPH} - a_{Theory}|}{h} \tag{5.14}$$

$$L_{\infty,h} = \frac{\max|\eta_{SPH} - \eta_{Theory}|}{h} \tag{5.15}$$

The results indicate that the propagated waves are very close to the theoretical values. The relative errors range from 1% to 14% (see Table 5.8), while the errors expressed in smoothing length h range from $0.03h$ to $0.53h$. The maximum error of 14% is registered at the wave trough of the third-order Stokes wave. This error is equivalent to $0.53h$, which is still within the acceptable error of $1h$ for an SPH simulation. However, the maximum error values indicate errors higher than the smoothing length h for the third-order Stokes wave and the Stream function wave. The location of these errors is each time close to the wave trough. In general, the wave crest is better reproduced than the wave trough, with the wave trough being more frequently underestimated than overestimated. Similar results are noticeable for a stand-alone DualSPHysics model (Altomare et al., 2017).

Table 5.8: Relative and maximum errors of coupled model results with respect to theoretical surface elevation

	Wave Crest		Wave Trough		Maximum	
Wave Test	$err_{\%}$	err_h	$err_{\%}$	err_h	$L_{\infty,h}$	t_∞
I	7%	0.21	6%	0.18	0.42	5.8
II	1%	0.03	11%	0.24	0.73	5.3
III	3%	0.18	14%	0.53	1.31	7.3
IV	3%	0.12	9%	0.24	1.16	4.3

5.5.1.7 Comparison of orbital velocities

A wave is fully characterised by its surface elevation and by the horizontal and vertical orbital velocities. First, a series of contour plots is presented where the velocity field is compared between the two-way coupled model and an OceanWave3D simulation. The results are given in Figure 5.24. Here, four sets of two contour plots are given; one set for each simulated wave type (I-IV). In each set, the left plot is the result from a stand-alone OceanWave3D model, while the right one is the coupled model solution. Figure 5.24 is aimed at a qualitative comparison between the Eulerian OceanWave3D model and the Lagrangian DualSPHysics model. For each set, the same colour range is used for easier comparison. The velocity range is very comparable between both models, but some differences are seen in the overall shape of the velocity field. Where OceanWave3D gives a smooth result with a clear transition between negative and positive orbital velocities, the coupled model result is significantly less smooth. At a first glance, the coupled model result of Wave Type Test I, has the least smooth solution. This is however a result of the limited velocity range ($\pm 0.05\ m/s$). The visible noise can be attributed to two sources.

- The use of a weakly-compressible SPH (WCSPH) solver leads to pressure and velocity noise (Crespo et al., 2015). Within WCSPH, the speed of sound is artificially lowered to keep the necessary time step reasonably high. However, this leads to non-physical pressure waves propagating through the fluid which result in noisy pressure and velocity values.

- The use of dynamic boundary conditions leads to pressure peaks close to the boundary particles. Here, the boundary particles satisfy the same equations as the fluid particles, however they do not move according to the forces exerted on them. Instead, they move according to the orbital velocities received from OceanWave3D. Using this boundary condition, when a fluid particle approaches a boundary particle and the distance between them decreases beyond the kernel range, the density of the boundary particles increases giving rise to an increase in pressure. This results in a repulsive force being exerted on the fluid particle due to the pressure term in the momentum equation. This locally enlarged pressure leads to noise in pressure waves

and consequently noise in velocity profiles within the fluid. A more detailed explanation can be found in Crespo et al. (2007).

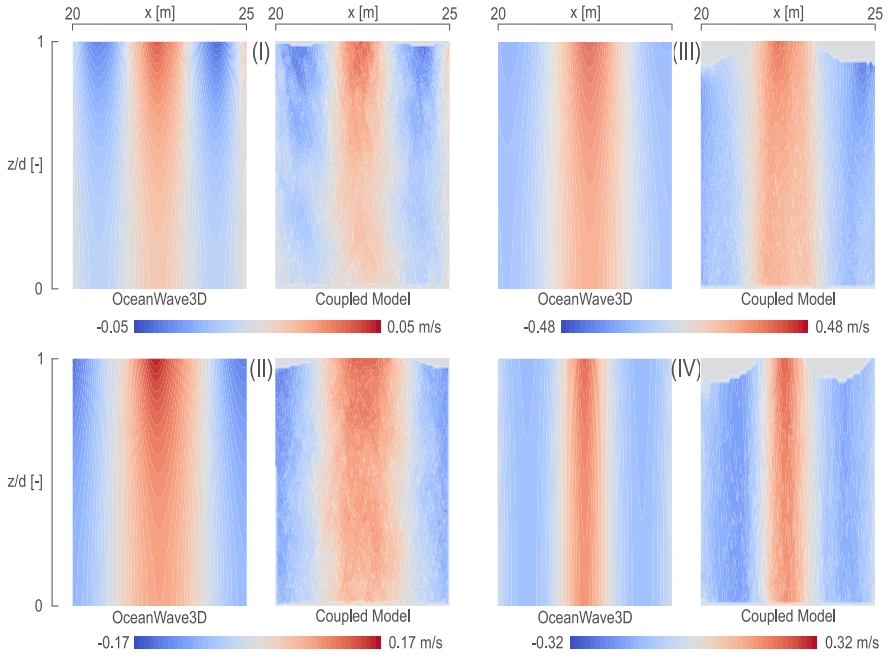

Figure 5.24: Four sets of contour plots of the horizontal orbital velocities under a wave crest for all 4 simulated wave types. Each set contains two contour plots: one for a stand-alone OceanWave3D model, and one for the coupled model. The horizontal orbital velocities are plotted in function of the normalized water depth z/d. The gray zones have no data due to the free surface being lower than the still water level.

It can be concluded, that using WCSPH is inherently sensitive to noise in pressure and velocity fields. However, some measures can be taken to try to mitigate the noise:

- Using incompressible SPH (ISPH) would lead to much smoother velocity and pressure fields, but at a huge computational cost. However, the added value of the proposed coupling is aimed to be applied for practical engineering problems, where computational speed combined with the required level of accuracy, is of high importance. A comparison between WCSPH and SPH can be found in Lee et al. (2010).
- Applying a correction term to the dynamic boundary particles, which results in slightly less pressure noise, as demonstrated in Ren et al. (2015). However, a free parameter needs to be tuned for each problem and here we want to present a general approach.

- Applying filtering of the noise in the pressure field in post-processing, using for example a filtering technique based on Wavelet Transform, as presented in Meringolo et al. (2017). For the purposes of the present study, this is not necessary. However, in the future, this method will be investigated to see if it can be valuable to this coupling methodology.

- Using a diffusive numerical scheme, which is available in DualSPHysics as the delta-SPH formulation, as described in Molteni and Colagrossi (2009)

Of these measures, the last is are applied to the performed simulations in this study. Overall, there is a good qualitative agreement between both the standalone OceanWave3D model and the coupled model, especially concerning the main objective of this coupling methodology is to use it for modelling of the free surface and WEC response within WEC arrays. Regarding the surface elevations, which is the focus of the present study, the coupling methodology does perform well.

Next, the horizontal and vertical orbital velocities at location $x = 22.5\ m$, in the center of the coupled model, are compared in more detail to the solution obtained with a stand-alone OceanWave3D model and to the theoretical solution as well. In Figures 5.25 and **??**, the velocity profiles of all 4 waves at the center of the DualSPHysics domain are given. There is a good correspondence between the three solutions, with the coupled model solution having a less continuous profile. However, the values are close to the theoretical and OceanWave3D solutions. In order to quantify the accuracy of the simulated profiles, the normalized root mean square error $RMSE = \sqrt{\frac{1}{n}\sum_{i=1}^{n}(u_{x,sim} - u_{x,theory})^2}/max(u_{x,theory})$ with respect to the theoretical solution is given in Table 5.9. The error between OceanWave3D and the theoretical solution is denoted with $RMSE_{T-O}$, while the error between the coupled model and the theoretical solution is denoted with $RMSE_{T-S}$. Since an RMSE value is an indication of an average error, also the $L_\infty = \max|u_{x,sim} - u_{x,theory}|/max(u_{x,theory})$ errors are calculated, also normalized with the maximum theoretical orbital velocity. Here it is clear that OceanWave3D is highly capable of producing an accurate velocity profile with very low errors ranging from 0.003 to 0.04. The coupled model solution is slightly further away from the theoretical solution with $RMSE_{T-S}$ ranging from 0.041 to 0.113. The maximum errors range from 0.081 to 0.134 for the horizontal orbital velocities, while for the vertical orbital velocities they range from 0.077 to 0.177. The locations of these maximum errors vary from close to the sea bottom to close to the free surface.

Finally, the pressure distribution is compared to a theoretical profile in Figure 5.27. The mean total pressure is illustrated by a line together with the standard deviation as a shaded area. The standard deviation is directly related to the added dynamic pressure due to the wave action. Good results are obtained. The wave tests I, II and IV have excellent agreement, while wave test III has a good correspondence for the mean pressure, but has a significantly higher standard deviation. Wave test III has the highest wave height of $0.15m$, leading to higher pressure fluctuations and higher velocities of the moving boundaries. Again, the RMSE values are calculated for the mean total pressure as $RMSE = \sqrt{\frac{1}{n}\sum_{i=1}^{n}(p_{sim} - p_{theory})^2}/max(p_{theory})$, see Table 5.10. The RMSE

Table 5.9: RMSE and L_∞ values of velocity profiles

	Wave Type Test			
Error	I	II	III	IV
$RMSE_{u,T-O}$	0.028	0.04	0.029	0.011
$RMSE_{u,T-S}$	0.041	0.056	0.041	0.044
$L_{\infty,u,T-S}$	0.081	0.134	0.091	0.101
$RMSE_{w,T-O}$	0.005	0.028	0.003	0.006
$RMSE_{w,T-S}$	0.113	0.050	0.072	0.064
$L_{\infty,w,T-S}$	0.177	0.077	0.152	0.116

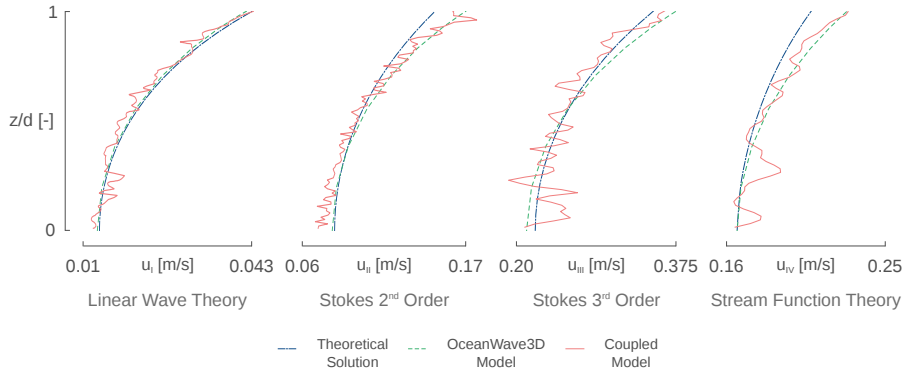

Figure 5.25: Comparison of the horizontal velocity profile $u_{x,i}$ in function of the normalized water depth z/d for all 4 simulated wave types, between the theoretical solution, a stand-alone OceanWave3D run and a two-way coupled model run.

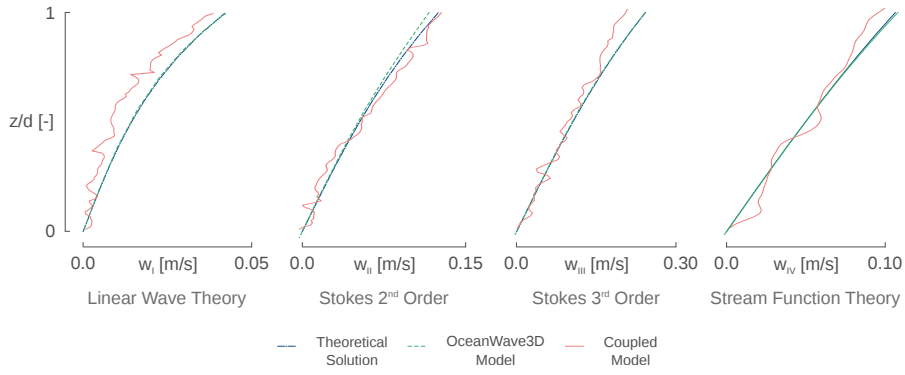

Figure 5.26: Comparison of the vertical velocity profile w_i in function of the normalized water depth z/d for all 4 simulated wave types, between the theoretical solution, a stand-alone OceanWave3D run and a two-way coupled model run.

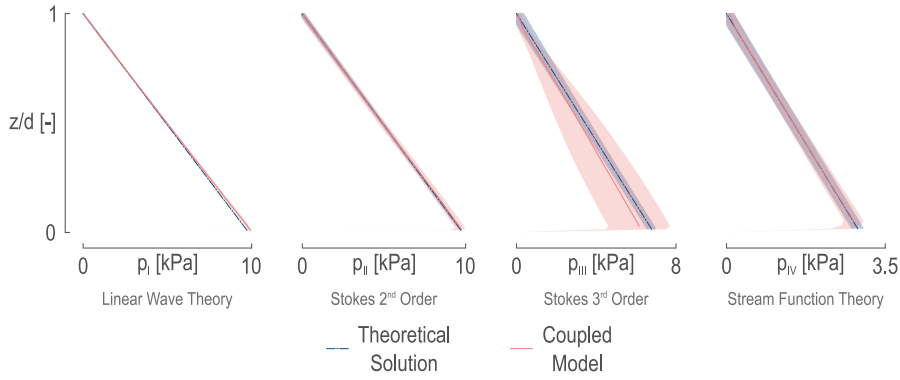

Figure 5.27: Comparison of the mean total pressure and the corresponding standard deviation in function of the normalized water depth z/d for all 4 simulated wave types, between the theoretical solution and a two-way coupled model run.

Table 5.10: RMSE values of mean total pressure profiles

Wave Type Test	$RMSE_{T-S}$ **[-]**
I	0.010
II	0.0049
III	0.0469
IV	0.0055

values for all 4 waves are low, ranging from 0.0049 to 0.0469, with the best performance for wave type II and the worst performance for wave type III.

5.5.2 Test Case 2: fixed OWC

Next, the coupled model is applied to model the surface elevations around a fixed Oscillating Water Column (OWC) wave energy converter. The experiment details are discussed in Iturrioz et al. (2014); Crespo et al. (2017), and the results have been compared to a volume-based solver, and to a stand-alone DualSPHysics model (Crespo et al., 2017) as well. In this section, the aim is to obtain results employing the coupled model, with high correspondence to the stand-alone DualSPHysics model. The experimental and numerical test set-up is illustrated in Figure 5.28. The fixed OWC device is positioned in the center of the coupled model zone, which is chosen to be $5\ m$ wide. The OWC has a submerged opening of $0.3\ m$, while the square air opening at the top measures $0.05\ m$. The draft of the device is $0.2\ m$ and the water depth is $0.6\ m$. The incident wave has a wave height of $H = 0.08\ m$ and a wave period $T = 3.2\ s$, resulting in a Stokes 2^{nd} order wave. A particle size of $d_p = 0.0050\ m$ is used, which leads to a converged result after testing several particle sizes.

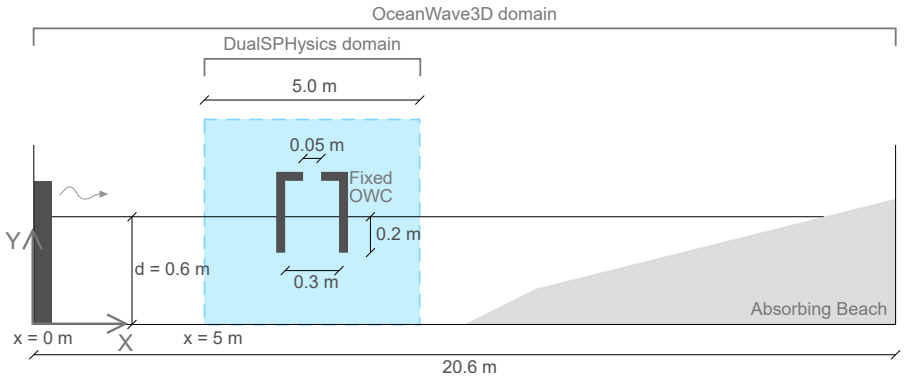

Figure 5.28: Experimental and numerical test set-up for modelling the surface elevation inside an OWC device. The DualSPHysics domain and OceanWave3D domain are indicated.

5.5.2.1 DualSPHysics Parameters

The efficiency and accuracy of DualSPHysics was investigated in Crespo et al. (2017) for a fixed OWC device showing good agreement between numerical results and experimental data (water elevation inside the chamber). Accordingly, the same SPH options used for that work will be used here to perform the numerical simulations. Table 5.11 summarises the SPH formulation and some parameters used to reproduce numerically the wave interaction with fixed OWC device.

Table 5.11: SPH formulation and parameters.

Time Integration Scheme	Symplectic
Time Step	Variable (including CFL and viscosity)
Kernel	Wendland
Smoothing Length	$1.2 \cdot d_p \cdot \sqrt{2}$
Viscosity Treatment	Artificial ($\alpha = 0.01$)
Equation of State	Tait equation
Boundary Conditions	Dynamic Boundary Particles
δ-SPH	No

5.5.2.2 Results

The surface elevation is registered in the center of the OWC device and compared to the experimental data in Figure 5.29. The stand-alone DualSPHysics simulation results from Crespo et al. (2017) are added to the comparison. There is a quali-

tative and quantitative agreement between the result from the coupled model, the stand-alone DualSPHysics simulation and the experimental data. The non-linear behaviour when the water level is dropping inside the OWC is nicely reproduced. However this behaviour is not visible during the rising of the water level, although it is present in the experimental data. Quantitatively the correspondence for the surface elevation is excellent with a RMSE value of less than half the smoothing length h.

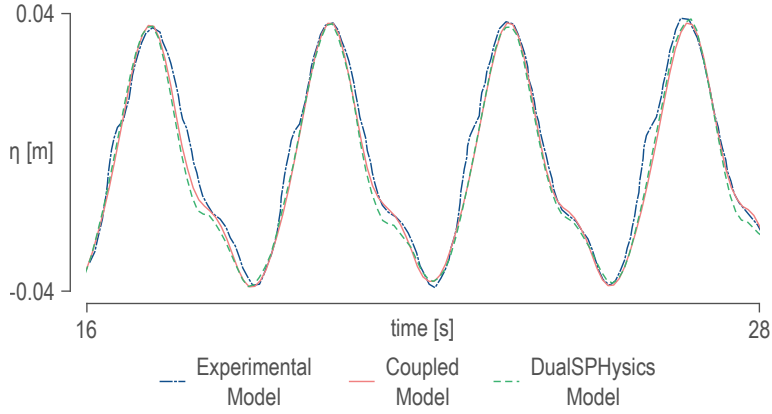

Figure 5.29: Surface elevation in the center of the OWC device compared to experimental data and a stand-alone DualSPHysics model.

Additionally, Figure 5.30 shows the velocity magnitude around the OWC device within the DualSPHysics domain. Upwave and in the lee of the OWC, there are locally higher velocities up to $0.25\ m/s$, due to the disturbance of the orbital velocities.

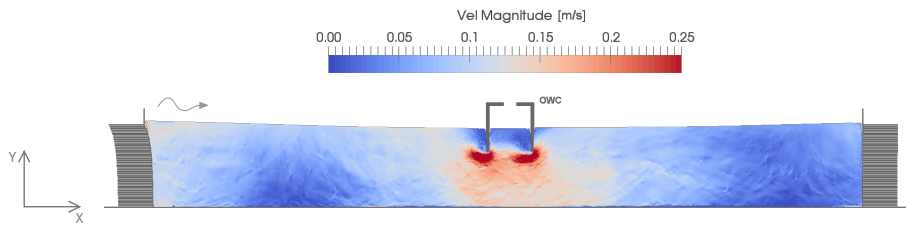

Figure 5.30: Velocity magnitude of water particles around the OWC at $t = 19\ s$ within the DualSPHysics domain of the coupled model.

5.5.3 Test Case 3: floating box

In a third simulation, the coupled model is applied to compare the response of a floating box to experimental data, as described in Ren et al. (2015). The experimental and numerical test set-up is illustrated in Figure 5.31. The full wave

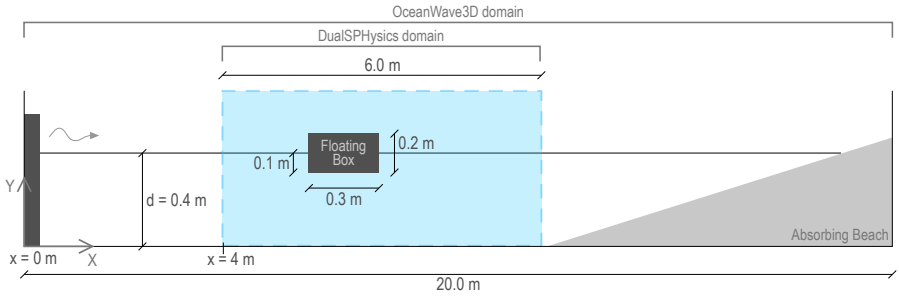

Figure 5.31: Experimental and numerical test set-up for simulation of the response of a floating box to a custom wave signal. The DualSPHysics domain and OceanWave3D domain are indicated.

propagation domain has a length of $20.0\ m$. The floating box is positioned at $x = 5.5\ m$ and has the dimensions $0.3\ m$ x $0.2\ m$ (LxH) with a draft of $0.1\ m$. The water depth is $0.4\ m$, while the DualSPHysics domain is $6.0\ m$ wide and starts at $x = 4.0\ m$. A regular wave with wave height $H = 0.1\ m$ and wave period $T = 1.2\ s$ is generated, characterised as a Stokes 3^{rd} order wave. A particle size of $d_p = 0.005\ m$ is used.

5.5.3.1 DualSPHysics Parameters

Here, the same DualSPHysics settings are used as in Test Case 2.

Table 5.12: SPH formulation and parameters.

Time Integration Scheme	Symplectic
Time Step	Variable (including CFL and viscosity)
Kernel	Wendland
Smoothing Length	$1.2 \cdot d_p \cdot \sqrt{2}$
Viscosity Treatment	Artificial ($\alpha = 0.01$)
Equation of State	Tait equation
Boundary Conditions	Dynamic Boundary Particles
δ-SPH	No

5.5.3.2 Results

Since the simulation is performed in 2-D, the motion of the floating box is characterised by three degrees of freedom: heave, pitch and surge. These motions are compared to the experimental data and a stand-alone SPH simulation in Figure 5.32. "Graph 1" of Figure 5.32 shows the heaving motion of the box. A good

correspondence is found with a maximum error of $1.37h$. In "Graph 2", the pitch motion is accurately reproduced as well, with a maximum error of $1.32h$. "Graph 3" illustrates the drifting nature within the surge motion. The largest error is found at the end of the simulation and is equal to $4.7h$. This error is logically larger than the error on the other motions since there is a net drift in the x-direction. The slightest difference in drift velocity will lead to larger errors over time. Overall, the stand-alone DualSPHysics result still gives slightly more accurate results than the coupled model. This is probably due to the larger domain and the difference between the paddle wave generation and the coupled wave generation.

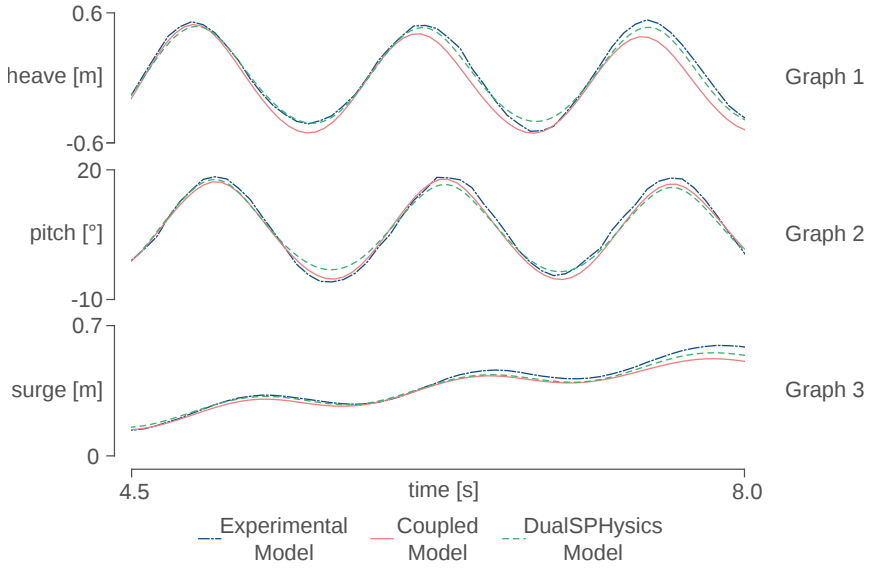

Figure 5.32: Time series of the 3 degrees of freedom of the box with heave, pitch and surge responses.

Lastly, the velocity field in the DualSPHysics domain of the coupled model is given in Figure 5.33, with maximum velocity magnitude of $0.4\ m/s$ close to the floating box. The velocity is shown at time $t = 7.5\ s$, when a wave crest is passing underneath the floating box.

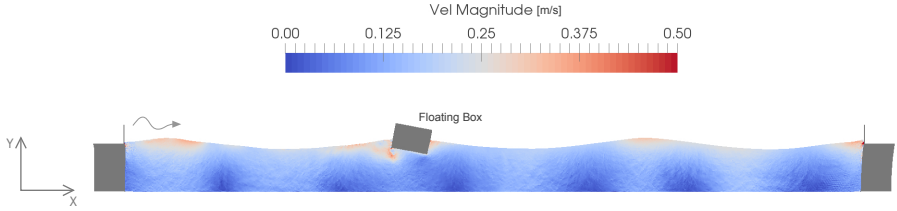

Figure 5.33: Velocity magnitude of water particles around the floating box at $t = 5\ s$ within the DualSPHysics domain of the coupled model.

5.6 Computational speed-up

One of the main benefits of applying the present two-way coupling methodology, is to keep the DualSPHysics domain as small as possible. This leads to a significant reduction of computational effort and cost. In order to quantify the achievable computational speed-up, the number of particles and the simulation runtime is compared between the coupled model and a stand-alone DualSPHysics model. As described in Figure 5.22, the OceanWave3D domain has a length of $50.0\ m$, while the DualSPHysics domain measures $5.0\ m$. Theoretically this would lead to a computational speed-up of 10. However, this result is too optimistic since DualSPHysics is capable of doing stand-alone wave propagation simulations with a shorter numerical wave flume length. The recommendation is to have a flume length of 3-4 wavelengths long (In Altomare et al. (2016a) a flume length of around 3.6 wave lengths was used). Based on this, the stand-alone DualSPHysics simulations are run and compared to the coupled model in Table 5.14. The comparison between the number of particles results in a theoretical speed-up. However, the runtime comparison indicates that there can be a difference between theoretical speed-up and effective computational speed-up. Nevertheless, it is clear that a significant computational speed-up is possible by applying the coupling methodology. The effective computational speed-up ranges from 134% to 420%.

In order to estimate how much overhead time is lost due to the MPI communications, one of the test cases (Test Case 2: fixed OWC) is run and the computation time dedicated to the individual processes is monitored (see Table 5.13). The simulation is divided in 4 timings: Initialisation, OceanWave3D, DualSPHysics and Overhead time. The latter includes the integration and interpolation of orbital velocities to boundary block positions and the filtering of the surface elevation. From Table 5.13, it is clear that almost all the computation time in the coupled model is taken up by the DualSPHysics process taking 99.598% of the total load. The second most demanding process with 0.273% is the OceanWave3D process while the overhead is responsible for only 0.125% of the computational effort.

Table 5.13: Duration of different sub-processes during OWC test case

Task	Duration [s]	Load [%]
Initialisation	0.12	0.004
OceanWave3D	8.32	0.273
DualSPHysics	3036.86	99.598
Overhead	3.81	0.125
Total	3049.11	100

It has to be noted that a more thorough analysis of timings is advised. The test case could be repeated with several resolutions, and dedicated profiling software could be used to provide more insight into the real computational impact of a coupling algorithm. Here, this was not performed since the communication processes only account for 0.125% of the total computational effort. However, it is advised to perform this analysis in future work.

Table 5.14: Computational speed-up for all performed tests

Test	Time [hr]			# Particles		
	DualSPHysics	Coupled Model	Computational Speed-up	DualSPHysics	Coupled Model	Theoretical Speed-up
Wave I	39.33	15.53	253%	2442k	1277k	191%
Wave II	14.97	3.57	420%	1734k	463k	374%
Wave III	3.30	1.08	305%	1041k	329k	316%
Wave IV	1.30	0.97	134%	301k	212k	142%
OWC	1.86	0.85	219%	350k	129k	273%
Box	2.63	1.51	174%	676k	330k	205%

5.7 Two-way or not two-way, that's the question

The presented coupling methodology allows for a two-way coupling between OceanWave3D and DualSPHysics. The two-way principle is obtained by sending the surface elevation from DualSPHysics back to OceanWave3D and overwriting the original solution. One of the research objectives is to focus on wave transformations within and around WEC devices and WEC arrays. This focus on surface elevation and floater response mainly requires a good representation of the wave profile and accurate floater dynamics. If the wave transformations around a WEC are correctly reproduced in DualSPHysics, they can be propagated further away in OceanWave3D due to the two-way coupling.

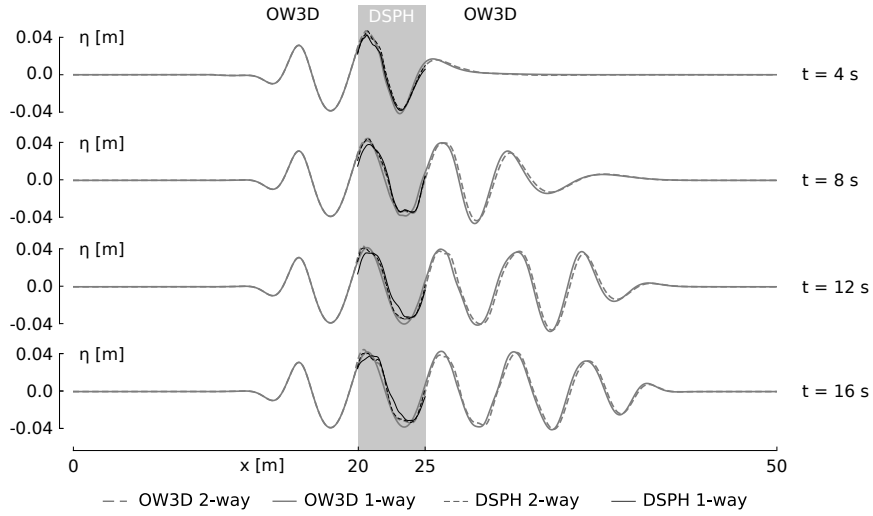

Figure 5.34: Surface elevation in function of horizontal flume position for both the OceanWave3D and DualSPHysics results, comparing one-way solutions to two-way solutions. The SPH zone is situated from x = 20.0 m to x = 25.0 m.

A comparison between a one-way coupled and two-way coupled simulation is shown in Figure 5.34. There, 4 snapshots of the full OceanWave3D (OW3D) domain are given at 4 different moments in time. The total flume is 50 m long with a 5 m long DualSPHysics (DSPH) zone ranging from x = 20 m to x = 25 m. Since the two-way coupling applies relaxation zones, only the center $1/3$ part of the DSPH solution exactly overlaps the OW3D solution. It can be noticed that there is not a big difference between one-way or two-way coupling for the OW3D simulation. However, for DSPH, there is a significant difference in the wave trough. When coupling one-way, the wave trough is higher than when a two-way coupling is applied. The difference is however around one particle size d_p, which is an acceptable error. Although the wave through is better reproduced in a two-way coupling, there is a non-linear bump visible in the DSPH results, which is

not physical. Also, the one-way coupled simulation can run for longer simulation times, since the OW3D surface elevations are not overwritten, and no numerical instabilities can occur.

As a guideline, two-way coupling should only be used when the research objective is to study both near- and far-field effects around floating devices. A one-way coupling without overwriting the original OW3D surface elevation is advised for regular simulations where the focus is on the wave-structure interactions, since it leads to a slightly more stable simulation. Additionally, in the next Chapter, it will be shown that very accurate results are obtained by applying one-way coupling with open boundaries.

5.8 Conclusions

In this chapter, a two-way coupling methodology between a fully non-linear potential flow wave propagation model and an SPH wave-structure interaction solver was introduced. The coupled model consists of a nested SPH zone within a larger wave propagation domain. At both boundaries of the SPH zone, there is an interface with the wave propagation model. Here, boundary blocks are moved horizontally, matching the horizontal orbital velocities underneath the wave field calculated with the wave propagation model. This results in wave generating blocks at the left side of the SPH zone and wave absorbing blocks on the right side. Within the SPH zone, the surface elevation is registered and sent back to the wave propagation model. This development fills the third and fourth knowledge gap, defined in Section 2.4.

In the present research, the introduced coupling methodology is applied to the wave propagation model OceanWave3D and the wave-structure interaction solver DualSPHysics. The two-way coupled model is programmed within an OpenMPI environment, where 3 subprocesses are transferring and processing data. Next to an OceanWave3D and DualSPHysics process, there is a Python process, directing the information transfer and processing the data before sending it to the dedicated process. The code is compiled to run on both CPUs and GPUs.

A proof-of-concept 2-D coupled model is introduced to demonstrate the capabilities of the two-way coupling. Firstly, wave propagation of 4 different wave types (linear and non-linear) is performed, resulting in a very high accuracy with errors that remain lower than 1 smoothing length h. Secondly, results from the coupled model are compared to those from two experimental set-ups: one with a fixed OWC device and another one with a floating box. The results show agreement with errors remaining below or close to the smoothing length h. The coupling methodology has the following generic benefits:

- The computation time can be significantly smaller since only a part of the full wave propagation domain is simulated in the wave-structure interaction solver (here, SPH). In the performed tests, the coupled model has at least 2 to 4 times less particles to simulate, which directly results into faster computation times;

- Alternatively, for the same computation time as a stand-alone SPH simula-

tion, there is the possibility of simulating more particles for a higher accuracy.

- Almost no overhead time is lost, since the SPH computation step is by far the largest part of a complete cycle;
- The MPI protocol ensures an efficient and practical way of transferring data from one model to another, since it minimizes the necessary source code alterations in each model;

However, there are a number of limitations to this two-way coupling methodology. Firstly, the generation and absorption of waves in the coupled model is implemented by horizontally moving boundary blocks. This means the vertical orbital velocities and surface elevation are not coupled and need to be generated within DualSPHysics. This inevitably leads to lower accuracy. Next, the horizontally moving boundaries slowly drift away from each other, limiting the simulation time. Additionally, only the surface elevation is coupled back to the wave propagation model. A stronger coupling would be obtained when the velocity field can be coupled back as well. This would ensure that both the velocity field and surface elevation are exactly the same in OceanWave3D and DualSPHysics, within the coupling domain. The difficulty however lies within integrating the noisy DualSPHysics velocities to a non-linear wave potential field for OceanWave3D. Lastly, only 2-D vertical simulations are supported.

In the next chapter, the two-way coupled model will be adapted to overcome these limitations and expanded with the following features:

- The moving boundary blocks will be replaced by buffer zones with inlet and outlet boundary conditions (Tafuni et al., 2018). This will result in automatic creation and removal of water particles at the boundaries;
- The model will be extended to a 3-D domain;

Logically, the upgraded methodology will be thoroughly tested and compared to theoretical solutions and experimental datasets.

Chapter 6

Non-Linear Coupling Methodology with Open Boundaries

In this sixth chapter of the thesis, the previously presented coupling methodology is extended to apply open boundaries instead of moving boundaries at the coupling interface. This new methodology proves to have excellent accuracy in propagating non-linear waves and is validated with theoretical and experimental results. The research presented is based on the following articles:

submitted for publication as:
Verbrugghe, T., Domìnguez, J. M., Altomare, C., Tafuni, A., Vacondio, R., Troch, P. and Kortenhaus, A. (2018). Non-linear wave generation and absorption using open boundaries within DualSPHysics. *Computer Physics Communications*, submitted for publication on 12/07/2018.

submitted for publication as:
Verbrugghe, T., Domìnguez, J. M., Altomare, C., Tafuni, A., Troch, P. and Kortenhaus, A. (2018). Application of open boundaries within a two-way coupled SPH model to simulate non-linear wave-structure interactions. In Proceedings of the 36th International Conference on Coastal Engineering, presented on 02/08/2018.

6.1 Introduction

SPH methods typically are computationally very intensive. However, recent advances using HPC and GPU have strongly contributed to significant gains in computational effort (Gotoh and Khayyer, 2018). Despite the use of HPC and GPUs, it is still challenging to model real engineering problems, which are usually multi-scale problems. An alternative to optimizing SPH for powerful computing hardware, is to study possible reduction of the computational domain. Importantly, this requires

accurate and stable boundary conditions, which is one of the SPHERIC Grand Challenges (spheric-sph.org/grand-challenges). This research focuses on applying open boundary conditions for wave generation and wave absorption of non-linear regular and irregular waves, with a high accuracy within a small computational domain. These open boundaries are then implemented in a 2-way coupling methodology between OceanWave3D and DualSPHysics. A detailed state-of-the art literature overview of wave generation and wave absorption techniques within SPH is presented in Section 2.3 of this manuscript.

Typically, SPH domains for wave propagation modelling are at least 3-4 wavelengths long (Altomare et al., 2016a). Combined with a required small particle size to accurately reproduce the surface elevation, this leads to computationally intensive simulations. This research is aimed at reducing the necessary fluid domain to a length of only one wavelength, and provide accurate boundary conditions capable of active wave generation and absorption. In this manner, real open sea conditions can be simulated where waves enter at the left-hand-side of the fluid domain and exit freely at the right-hand-side. The WCSPH model DualSPHysics will be used to demonstrate these new wave generation and wave absorption techniques, using the recently developed open boundaries (Tafuni et al., 2016, 2017, 2018). The applied open boundary formulation is based on the use of buffer layers adjacent to the fluid domain. Buffer particles are used to enforce certain conditions in the presence of fluid inlets and outlets. Particularly, the physical information of buffer particles is either assigned *a priori* or extrapolated from the fluid domain using a first order consistent procedure. The major benefits of this method are:

- Using open boundaries for wave generation and absorption is meant to cover those cases where classical wave generation techniques can fail or are very computationally expensive, for example open sea states, simulating floating devices, wave breaking conditions.
- The buffer zones in the open boundaries accept physical information from any source: for example linear wave theory, non-linear wave theories, external numerical models such as CFD models, or even measurement data.

In Section 6.2 of this Chapter, the open boundaries will be used to generate, propagate and absorb non-linear waves within DualSPHysics. Next, in Section 6.3, the 2-way coupling methodology introduced in Chapter 5 will be redesigned, now applying the open boundaries at the coupling interface instead of moving boundaries.

6.2 Open Boundaries Within DualSPHysics

6.2.1 Description of Open Boundaries

Within this research, open boundaries are applied to generate and absorb waves. The implementation of open boundaries in DualSPHysics is discussed in detail in Tafuni et al. (2018). Inflow and outflow buffers can be defined near the inlets and

outlets of the computational domain. Flow properties can be either imposed or extrapolated from the fluid domain bulk using ghost nodes.

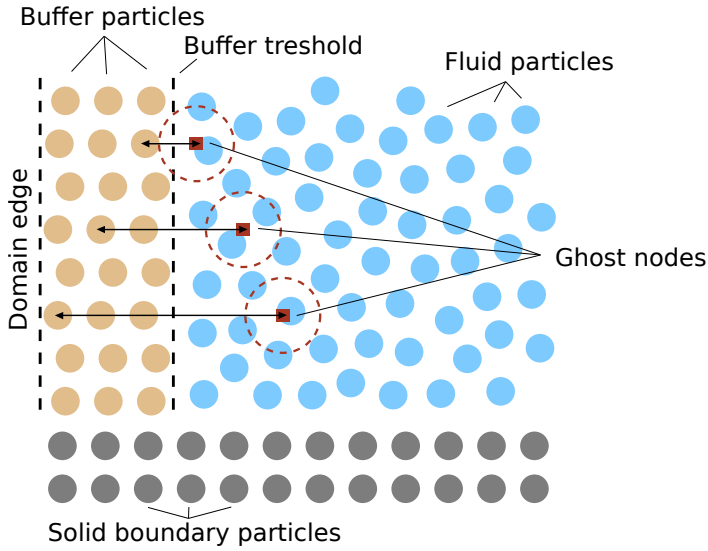

Figure 6.1: Sketch of the implemented open boundary model, adapted from Tafuni et al. (2018).

A sketch of the implemented boundary condition model is shown in Figure 6.1 in the generic case of a fluid flowing near a buffer area identifying an open boundary. The buffer zone is situated in between the domain edge and the buffer threshold boundary, i.e. the fluid-buffer interface. The zone is filled with layers of SPH buffer particles used to enforce certain boundary conditions. The buffer size should be at least equal to or exceed the kernel radius. This is necessary to have full kernel support for the fluid particles near an inlet or outlet. In the present research, the buffer width is chosen as $8 \cdot d_p$ in the direction normal to the open boundary, where d_p is the particle size adopted in DualSPHysics. Providing the information to an open boundary is possible using two methods: physical quantities are either assigned a priori or extrapolated from the fluid domain to the buffer zones (inflow and outflow) using ghost nodes. As illustrated in Figure 6.1, the positions of the ghost nodes are calculated by mirroring the buffer particles into the fluid along a direction normal to the open boundary. When calculating fluid quantities at the ghost nodes, a standard particle interpolation would not be consistent due to the proximity to an open boundary, which translates into a truncated kernel. The method proposed by Liu and Liu (2006) is thereby adopted to retrieve first order kernel and particle consistency. The multi-dimensional first-order Taylor series approximation of the field function $f(\mathbf{x})$ multiplied by the kernel function evaluated

at particle k, $W_k(\mathbf{x})$, and its first order derivatives, $W_{k,\beta}(\mathbf{x})$, are given by:

$$\int f(\mathbf{x})W_k(\mathbf{x})d\mathbf{x} = f_k \int W_k(\mathbf{x})d\mathbf{x} + f_{k,\beta} \int (\mathbf{x}-\mathbf{x}_k)W_k(\mathbf{x})d\mathbf{x} \tag{6.1}$$

$$\int f(\mathbf{x})W_{k,\beta}(\mathbf{x})d\mathbf{x} = f_k \int W_{k,\beta}(\mathbf{x})d\mathbf{x} + f_{k,\beta} \int (\mathbf{x}-\mathbf{x}_{k,\beta})W_{k,\beta}(\mathbf{x})d\mathbf{x} \tag{6.2}$$

Here, β is an index ranging from 1 to d, the number of dimensions. Equations 6.1 and 6.2 form a system of $d+1$ equations in $d+1$ unknowns, f_k and $f_{k,\beta}$. Using the particle notation, the system solution is found as:

$$f_k = \frac{\begin{vmatrix} \sum_i f_i W_{ki}\Delta V_i & \sum_i (\mathbf{x}_i-\mathbf{x}_k)W_{ki}\Delta V_i \\ \sum_i f_i W_{ki,\beta}\Delta V_i & \sum_i (\mathbf{x}_i-\mathbf{x}_k)W_{ki,\beta}\Delta V_i \end{vmatrix}}{\begin{vmatrix} \sum_i f(\mathbf{x}) W_{ki}\Delta V_i & \sum_i (\mathbf{x}_i-\mathbf{x}_k)W_{ki}\Delta V_i \\ \sum_i f(\mathbf{x}) W_{ki,\beta}\Delta V_i & \sum_i (\mathbf{x}_i-\mathbf{x}_k)W_{ki,\beta}\Delta V_i \end{vmatrix}} \tag{6.3}$$

$$f_{k,\beta} = \frac{\begin{vmatrix} \sum_i W_{ki}\Delta V_i & \sum_i f_i W_{ki}\Delta V_i \\ \sum_i W_{ki,\beta}\Delta V_i & \sum_i f_i W_{ki,\beta}\Delta V_i \end{vmatrix}}{\begin{vmatrix} \sum_i W_{ki}\Delta V_i & \sum_i (\mathbf{x}_i-\mathbf{x}_k)W_{ki}\Delta V_i \\ \sum_i W_{ki,\beta}\Delta V_i & \sum_i (\mathbf{x}_i-\mathbf{x}_k)W_{ki,\beta}\Delta V_i \end{vmatrix}} \tag{6.4}$$

These have been employed to find the value of f_o at the open boundary given the corrected values of f_k and $f_{k,\beta}$ at the ghost nodes:

$$f_o = f_k + (\mathbf{r}_o - \mathbf{r}_k) \cdot \widetilde{\nabla} f_k \tag{6.5}$$

where $\widetilde{\nabla} f_k$ is the corrected gradient calculated at the ghost nodes.

The open boundary algorithm introduces several new features that make SPH more applicable to real engineering problems. The first one is the possibility of using buffer areas to impose unsteady velocity and pressure profiles, as well as pressure and velocity gradients along a chosen direction. Next, a variable free-surface elevation can be imposed, which is an essential prerequisite in free-surface flow problems where waves can enter and exit the computational domain. Finally, the buffer areas are characterised by a dual behaviour, allowing both inward and outward flows, making flow reversion possible. Consequently, when flow velocities are extrapolated from the fluid domain, mixed velocity fields are possible where part of the buffer area contains fluid particles entering the domain, and another part contains fluid particles leaving the domain. This can be specifically important when flow problems with strong rotations or oscillations need to be modeled. This flexibility is an important distinctive feature. Since the open boundary algorithm is available on both the parallel CPU and GPU versions of DualSPHysics, considerable speed-ups can be achieved when running the code on high-end GPUs or large CPU clusters. This is particularly necessary when simulating real engineering problems where a large number of particles is necessary to study high-resolution flow problems with complicated geometries, while maintaining a reasonable computation time.

6.2.2 Wave Propagation with Open Boundaries

In this research, generation and absorption of non-linear regular and irregular waves is performed within the Weakly Compressible SPH (WCSPH) solver DualSPHysics, by applying the open boundary formulation from Tafuni et al. (2018), as described in Section 6.2.1. The open boundaries are implemented as a zone of buffer particles. The imposed physical quantities can originate from any source: linear or non-linear wave theories, external numerical models or even measurement data. When buffer particles cross the domain edge, they are removed from the domain. Buffer particles entering the fluid domain are transformed into a fluid particle, and fluid particles entering the buffer zone become buffer particles. In the specific case an inflow buffer particle crosses the buffer-fluid interface, it becomes a fluid particle and a new buffer particle is created at the inflow boundary. This generation method is similar to what was presented by Ni et al. (2018), but there are some key differences making the here-used formulation more flexible. Firstly, flow reversion problems can not be simulated with the method by Ni et al. (2018). Secondly, there is no possibility to extrapolate flow quantities using ghost nodes. Thirdly, the method to impose free surface elevation is different. Fourthly, the applied velocity profiles and corrections are depth-averaged. Lastly, only 2^{nd} order wave generation is possible, where the method introduced here is compatible with up to 5^{th} order generation.

Here, a fluid domain with a length of 1 wave length is chosen, with an inlet at the left-hand-side of the domain and an outlet at the right-hand-side of the domain (see Figure 6.2). Each buffer zone consists of 8 layers of buffer particles. A sensitivity analysis illustrated in Figure 6.3 has shown that wave propagation results are accurate for buffer zones with at least 8 layers. The dimensionless amplitude K_D is shown in function of the normalized position x/L_{wav} for a Stokes third-order wave. The number of layers n_l is varied from 1 to 16 and is doubled each iteration.

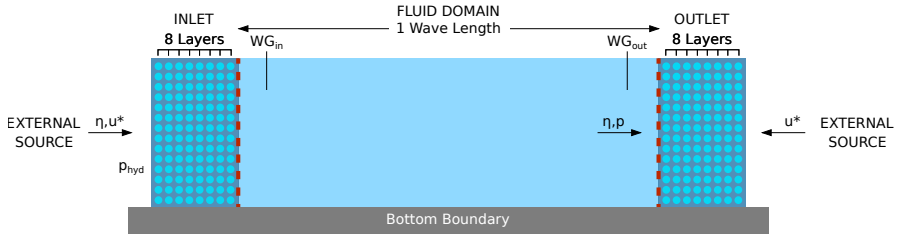

Figure 6.2: General sketch of numerical domain set-up to illustrate the generation/absorption methodology.

The imposed physical quantities originate from non-linear wave theory, detailed in Section 6.2.2.4. At the inlet, theoretical horizontal orbital velocities and surface elevation are imposed on the buffer particles, while the pressure is set to be hydrostatic. At the outlet, only the horizontal orbital velocities are imposed, the surface elevation and pressure are extrapolated from the fluid domain. No vertical orbital velocities are applied, analysis has proven that there is no accuracy benefit

Table 6.1: Imposed and extrapolated quantities for inlet and outlet buffer particles (Imp=imposed, Ext=extrapolated, Hyd=hydrostatic).

Quantity	u	w	η	p
inlet	Imp	0	Imp	Hyd
outlet	Imp	0	Ext	Ext

by imposing vertical velocities, but there is a negative impact on particle spacing.

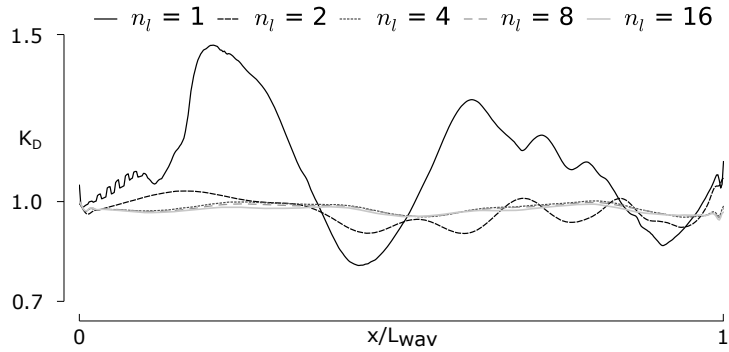

Figure 6.3: Sensitivity analysis on the number of buffer particle layers n_l necessary for accurate wave propagation.

By imposing horizontal velocities on both the inlet and outlet, the hydrodynamic problem becomes over-constrained, which can result in unwanted reflections in the fluid domain. Additionally, when a floating or fixed structure is positioned in the fluid domain, waves will reflect on the structure and transform around it. The open boundaries should be able to compensate for the reflected waves and the outlet needs to absorb the transformed wave effectively. In this research, this is done by applying velocity corrections at the inlet and the outlet, based on the measured free surface close the buffer interface, specifically at a distance of $8 \cdot d_p$. This distance has been selected based on a sensitivity analysis, illustrated in Figure 6.4. The same Stokes third-order wave was simulated, each time varying the wave measurement distance from $1 \cdot d_p$ to $16 \cdot d_p$. At a distance of $8 \cdot d_p$, the wave measurement location is close enough to the buffer zone to have a minimal phase difference, but far enough to avoid inaccuracies due to transitional effects between the buffer zone and the fluid domain. In Figure 6.2, these measuring locations are denoted as WG_{in} (Wave Gauge) and WG_{out}. The applied velocity correction is a shallow water wave correction based on the measured reflection (Dean and Dalrymple, 1991a), but is implemented differently depending on the inlet or the outlet.

6.2.2.1 Inlet Velocity Correction

At the inlet, the objective is to always generate the required incident wave. The surface elevation is measured directly outside of the inlet, and the velocity is cor-

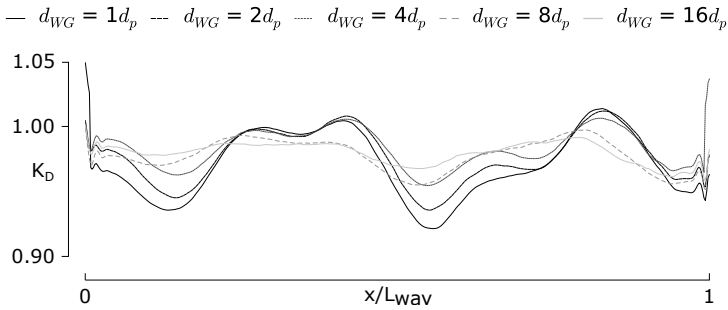

Figure 6.4: Sensitivity analysis on distance d_{WG} to the inlet/outlet interface of the active wave absorption wave gauges, necessary for accurate wave propagation.

rected to ensure that the generated surface elevation matches the theoretical one. In case a higher surface elevation is measured than what was imposed, the corrected velocity should be lower than the originally imposed profile, in order to compensate the excess of velocity, since that profile leads to reflections in the fluid domain. Within the code, this correction is implemented as follows:

$$u_{in}(z,t) = u_{theory}(z,t) - [\eta_{WG,in} - \eta_{theory}] \cdot \sqrt{\frac{g}{d}} \tag{6.6}$$

Here, u_{in} is the horizontal velocity at the inlet, u_{theory} is the imposed horizontal velocity, $\eta_{WG,in}$ is the measured free surface elevation near the inlet, η_{theory} is the imposed free surface, g is the earth's acceleration and d is the water depth. This correction is similar to the active wave absorption applied in Altomare et al. (2017), although there it was used to correct the displacement of a piston-type wavemaker formed by moving boundary particles.

6.2.2.2 Outlet Velocity Correction

At the outlet, the objective is to absorb any wave propagating towards the outlet. Technically, the applied open boundaries do not absorb the wave, but rather try to match the velocity field present in the fluid domain as close as possible, creating an 'open door' for the propagating wave. The surface elevation is measured directly outside of the outlet, and the velocity is corrected to ensure that the imposed velocities match the measured ones. In case a higher surface elevation is measured than what was imposed, the corrected velocity should be higher than the originally imposed profile, in order to prevent discontinuities in the velocity field, which would induce unwanted reflected waves into the domain:

$$u_{out}(z,t) = u_{theory}(z,t) - [\eta_{theory} - \eta_{WG,out}] \cdot \sqrt{\frac{g}{d}} \tag{6.7}$$

6.2.2.3 Implementation Into DualSPHysics

The methodology described above is implemented into the DualSPHysics source code, as illustrated in Figure 6.5. In the main simulation script `JSphGpuSingle.cpp`,

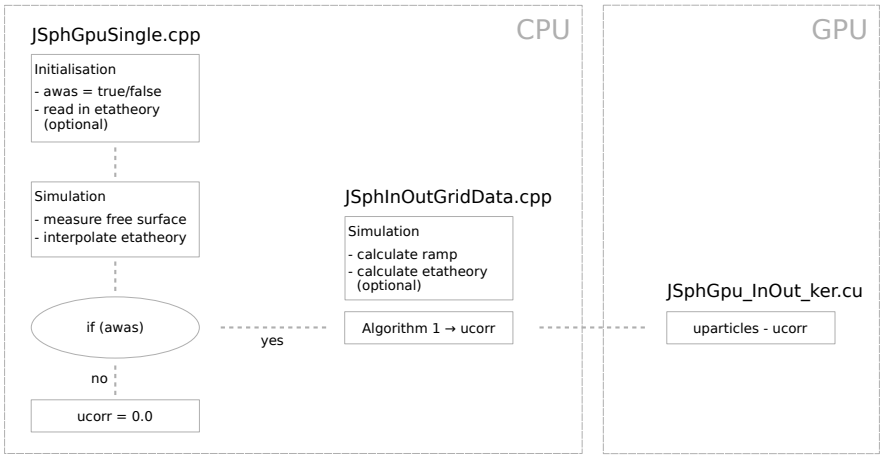

Figure 6.5: Implementation of velocity correction in DualSPHysics source code.

some minor modifications are made. At initialisation, a boolean `awas` is created to specify if active wave absorption is required or not.

if *zone* = *inlet* **then**
  if *time* < *ramptime* **then**
    ramp = time/ramptime;
  else
    ramp = 1.0;
  etainlet = etatheory*ramp;
  ucorr = (etameasured-etainlet)*sqrt(g/depth);
else zone = outlet
  if *time* < *ramptime* **then**
    ramp = time/ramptime;
  else
    ramp = 1.0;
  etaoutlet = etatheory*ramp;
  ucorr = (etaoutlet-etameasured)*sqrt(g/depth);
call inletoutletvelocity(other input,ucorr);

Algorithm 1: Implementation of active wave absorption in `JSphInOutGridData.cpp`.

Additionally, it is possible to read in the theoretical surface elevations needed to calculate the velocity correction from a text file. Alternatively, these theoretical values are calculated within the DualSPHysics code itself by using newly created Stokes fifth-order functions. During the simulation, the surface elevation at WG_{in} and WG_{out} are measured and put into global variables. The theoretical surface elevations are read in from a file at discrete time intervals, and thus need to be interpolated to the current DualSPHysics timestep. If `awas` is true, the velocity correction is activated in the script `JSphInOutGridData.cpp`. Optionally, the theoretical surface elevations are calculated here. The velocity correction `ucorr` is calculated as detailed in Algorithm 1 below. There, a distinction is made between an inlet and an outlet, since the velocity correction is calculated differently. A ramp function is used to smoothly introduce the velocity correction over a certain ramp time. Next, the velocity correction is calculated as discussed in equations 6.6 and 6.7. Lastly, the particle velocities are then corrected with `ucorr` on the GPU, in the file `JSphGpu_InOut_ker.cu`.

6.2.2.4 Applied Non-linear Wave Theory

Both the wave generation and absorption applied in this work are based on imposing free surface and horizontal orbital velocities.

6.2.2.4a Regular Waves For regular waves, the imposed quantities are calculated with the 5^{th} order solution to the Stokes Theory, given by Fenton (1985):

$$k\eta(x,t) = \sum_{i=1}^{5} \epsilon^i \sum_{j=1}^{i} B_{ij} \cos[jk(x - ct + \frac{\theta}{k})] \tag{6.8}$$

$$\epsilon = ka \tag{6.9}$$

$$c = \bar{U}_c + \bar{U} \tag{6.10}$$

$$\bar{U}\sqrt{\frac{k}{g}} = C_0 + \epsilon^2 C_2 + \epsilon^4 C_4 \tag{6.11}$$

$$u(x,z,t) = \bar{U}_c + C_0\sqrt{\frac{g}{k^3}} \sum_{i=1}^{5} \epsilon^i \sum_{j=1}^{i} A_{ij} \cosh(jkz) jk \cos[jk(x - ct + \frac{\theta}{k})] \tag{6.12}$$

Here, η is the surface elevation, k is the wave number (defined as $k = 2\pi/L$, with L the wavelength), a is the wave amplitude, g is the earth acceleration, c is the wave velocity, $\bar{U}_c$ is the mean current velocity, $\bar{U}$ is the mean horizontal velocity, θ is the phase constant. The wave period T can be calculated based on the wave number k and the wave celerity c, $T = 2\pi/(kc)$. The constants A_{ij} B_{ij} and C_i are theory-specific and can be found in Appendix B. The z-axis has its origin at the sea bed.

6.2.2.4b Irregular Waves For irregular waves, the surface elevation is calculated based on linear wave theory with a second-order correction, including both

sub-harmonic (bound long waves) and super-harmonic components. This is done based on a Joint North Sea Wave Observation Project (JONSWAP) wave spectrum, of which N wave components are uniformly distributed. N is chosen to be 200 to ensure an acceptable accuracy of the discretised spectrum. A phase seed is also used to obtain different time series of irregular waves assigning randomly a value for the initial phase to each wave component. Changing the phase seed allows generating different irregular wave time series with the same significant wave height (H_s) and peak period (T_p). From this spectrum, the irregular surface elevations are calculated and the corresponding orbital velocities are approximated by applying the shallow water wave theory and are thus considered constant over the water depth:

$$u(x,t) = \eta(x,t) \cdot \sqrt{\frac{g}{d}} \tag{6.13}$$

6.2.3 Test Program

The application of open boundaries in DualSPHysics is hereby validated with theoretical results and scientific results from the literature. Firstly, a stable non-linear standing wave is simulated by considering the outlet as a fixed wall. Secondly, simple wave propagation of regular and irregular waves is studied. Thirdly, a number of tests is performed to investigate the correct reproduction of wave transmission and wave reflection.

6.2.3.1 Standing Wave Test

First, a non-linear standing wave is simulated. A $2-D$ fluid domain with a water depth d and a length of 1 wavelength L_{wav} is used. An inlet is used for wave generation, while a wall is placed at the other end of the domain. If the inlet functions correctly, the applied velocity correction should ensure a stable standing wave in the fluid. This should result in visible nodes and antinodes in the surface elevation, as well as in the orbital velocities.

6.2.3.2 Wave Propagation Tests

A series of propagating waves is simulated. A $2-D$ fluid domain with a water depth d and a length of 1 wavelength L_{wav} is used. An inlet is used for wave generation, while an outlet handles the wave absorption (see Figure 6.2). The waves are selected based on their linear or non-linear characteristics, as described by the diagram of Le Méhauté (1969), adapted in Figure 6.6. A selection of 5 wave types is chosen, including 4 regular waves and 1 irregular wave. The specific characteristics such as wave height $H_{(s)}$, wave period $T_{(m)}$, water depth d and particle size d_p are listed in Table 6.2. The particle size is selected based on the recommendation that $d_p \leq H/10$, as demonstrated in Altomare et al. (2017) and Roselli et al. (2018). The validity of the regular wave theories is illustrated in Figure 6.6. The accuracy of the wave propagation is assessed by comparing surface elevation, orbital velocities and dynamic pressures with theoretical results.

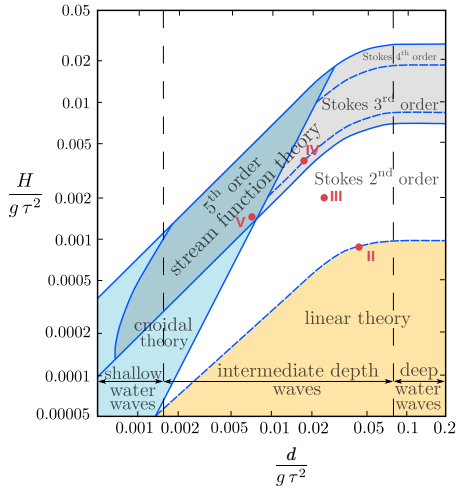

Figure 6.6: Selection of waves tested with the open boundary conditions. Tests II-V are indicated on the graph (adapted from Le Méhauté (1969)). $\frac{d}{g\tau^2}$ is the normalized water depth while $\frac{H}{g\tau^2}$ is the normalized wave height.

6.2.3.3 Wave Transmission Tests

Next, a combination of wave reflection and wave transformation is studied by simulating wave propagation over a submerged breakwater with a smooth impermeable slope (see Figure 6.7). Part of the wave will reflect on the breakwater, while part of the wave will be transmitted over the breakwater. A fluid domain with a water depth of d and length of $2 \cdot L_{wav}$ is selected. An inlet is used for wave generation, while an outlet handles the wave absorption. The submerged breakwater is positioned midway along the length, has a height of h_{bw} and a slope of $1/1.5$. The ratio d/h_{bw} is equal to 1.2. Validation of this test case is obtained by comparing the transmission coefficient $C_T = \frac{H_t}{H_i}$ with results from Seelig (1980).

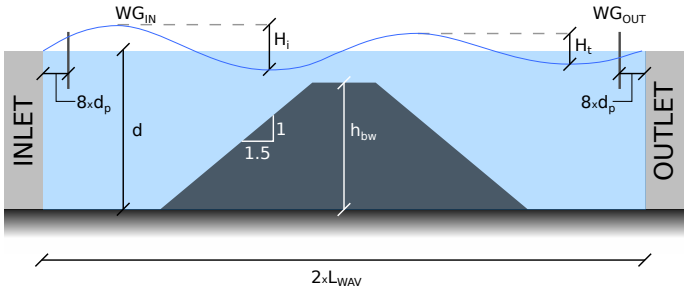

Figure 6.7: Set-up of wave transmission tests with submerged breakwaters and smooth impermeable slopes.

Table 6.2: Wave Propagation Tests: Wave Conditions.

Test Number	Wave Theory	Wave Height $H_{(s)}$ [m]	Wave Period $T_{(m)}$ [s]	Water Depth d [m]	Wave Length L [m]	Particle Size d_p [m]
I	Standing	0.15	2.0	0.7	4.62	0.020
II	Linear	0.02	1.5	1.0	3.35	0.002
III	Stokes 2^{nd}	0.08	2.0	1.0	5.22	0.010
IV	Stokes 3^{rd}	0.15	2.0	0.7	4.62	0.010
V	Stream Function	0.06	2.0	0.3	3.26	0.005
VI	Irregular Wave	0.15	2.0	1.0	/	0.010

6.2.3.4 Wave Reflection Tests

Lastly, wave reflection tests are carried out by propagating irregular waves on smooth impermeable breakwaters with varying slopes (see Figure 6.8). The domain consists of a fluid section with a water depth d and a length of 1 wavelength L_{wav}. A smooth impermeable breakwater with slope angle α is installed at the right side of the domain. Validation of the test case is achieved by calculating the reflection coefficient C_R with WaveLab, and comparing the result to the formula of Seelig (1983):

$$C_R = \frac{a\xi}{b+\xi^2} \qquad \xi = \frac{\tan\alpha}{\sqrt{\frac{2\pi H}{gT^2}}} \tag{6.14}$$

Equation (6.14) is valid for values of ξ ranging from 2.0 to 6.0. For the wave conditions used in this test case, this results in slope angles between 20° and 45°.

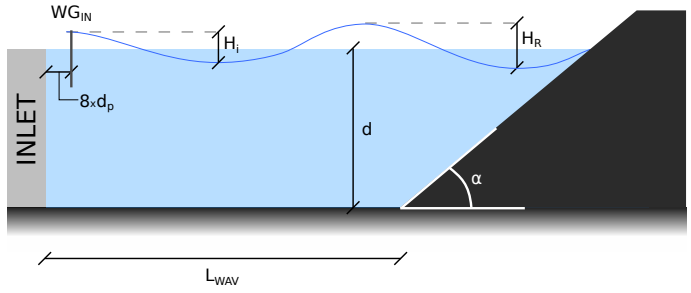

Figure 6.8: Set-up of wave reflection tests on breakwaters with a smooth impermeable slope.

6.2.4 Validation

6.2.4.1 DualSPHysics Parameters

The efficiency and accuracy of DualSPHysics was investigated in Altomare et al. (2015b) for wave propagation and absorption showing good agreement between numerical results and experimental data. Accordingly, similar SPH options used for that work will be used here to perform the numerical simulations. The solver options used in this section are summarized in Table 6.3.

Table 6.3: SPH formulation and parameters.

Time Integration Scheme	Verlet
Time Step	Variable (including CFL and viscosity)
Kernel	Wendland
Smoothing Length	$2.0 \cdot d_p$
Viscosity Treatment	Artificial ($\alpha = 0.01$)
Equation of State	Tait equation
Boundary Conditions	Open Boundary Conditions
δ-SPH	Yes (δ-SPH $= 0.1$)

6.2.4.2 Standing Wave Test

The accuracy of wave propagation with open boundaries is assessed by comparing SPH surface elevation and orbital velocities with the corresponding theoretical results, as illustrated in Figure 6.9. The first graph shows the comparison of the surface elevation, the second graph the horizontal orbital velocities and the third graph the vertical orbital velocities. The theoretical standing wave was calculated as a Stokes second-order standing wave. For a perfectly linear standing wave pattern, the free-surface elevation should be zero at the nodes and twice the amplitude of the incident waves at the antinodes. As visible in Figure 6.9, a perfect pattern is not achieved. Nevertheless, the amplitudes at the nodes are very small (maximum 2 cm) as predicted by the second-order solution, and the amplitudes at the antinodes are close to their maximum. Both the horizontal and vertical orbital velocities show good agreement with the theoretical result. The calculated errors are summarized in Table 6.4. The RMSE error on the surface elevation at both the node and antinode remain below $0.26h$. The maximum (L_∞) errors remain below $0.5h$. For the orbital velocities, the RMSE values for the orbital velocities range from 0.13 to 0.41 times the maximum calculated velocity. The maximum errors are higher and reach up to 1.16 times the maximum vertical velocity at the node.

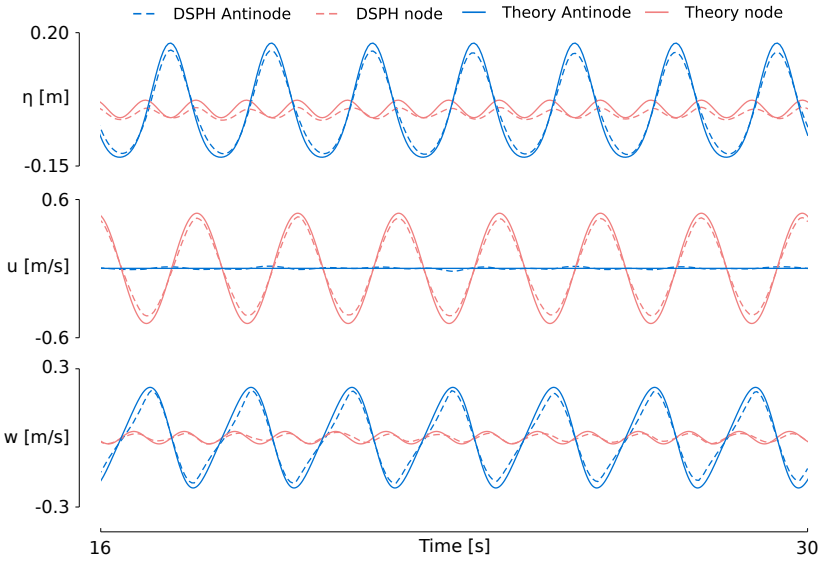

Figure 6.9: Comparison of surface elevation η (top), horizontal orbital velocity u (middle) and vertical orbital velocity w (bottom) in nodes and antinodes for a non-linear standing wave.

Table 6.4: Error values of surface elevation, horizontal and vertical orbital velocities at nodes (N) and antinodes (A) for the standing wave test. The RMSE error and L_∞ error are normalized with the smoothing length for the surface elevations and with the maximum velocity for the orbital velocities.

Error	η_N	η_A	u_N	u_A	w_N	w_A
RMSE [-]	0.26	0.25	0.13	0.41	0.40	0.13
L_∞ [-]	0.49	0.50	0.21	1.00	1.16	0.24
t_∞ [s]	24.8	23.5	20.9	22.5	19.1	27.7

6.2.4.3 Wave Propagation Tests

The accuracy of wave propagation with open boundaries is now assessed by comparing SPH surface elevation, orbital velocities and dynamic pressures with the corresponding theoretical results.

6.2.4.3a Surface Elevations The surface elevation for the regular waves, measured at the center of the domain is compared to the theoretical surface elevation in Figure 6.10. It is clear that the surface elevation is simulated with a very high accuracy. Both the wave crest and wave through are reproduced excellently. Additionally, the asymmetry of the non-linear wave types is present as well. In order

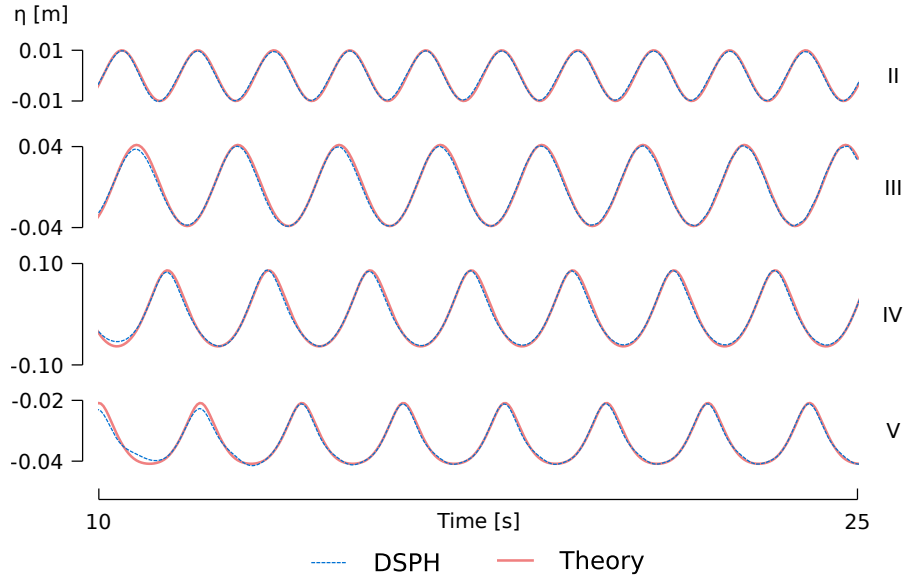

Figure 6.10: Surface elevations of wave tests II-V, measured in the center of the fluid domain $x = L_{wav}/2$.

to quantify the accuracy, RMSE values are calculated as follows:

$$RMSE = \frac{\sqrt{\frac{1}{n}\sum_{i=1}^{n}(\eta_{\mathrm{SPH}} - \eta_{theory})^2}}{h_{\mathrm{SPH}}} \qquad h_{\mathrm{SPH}} = 2.0 \cdot d_p \cdot \sqrt{2} \tag{6.15}$$

This is a specific RMSE calculation for SPH simulations, where the error is non-dimensional with respect to the smoothing length h_{SPH}. Results are considered acceptable when the RMSE value is lower than one. In Table 6.5, the RMSE values for the surface elevation of the propagating wave tests are given. The calculated errors are low and range from 13.9% for wave V to 17.5% for wave III, proving that the applied wave generation and absorption technique is capable of accurately reproducing the surface elevation of linear and non-linear waves.

Table 6.5: RMSE values for surface elevations of wave types II-V.

Wave Test	II	III	IV	V
RMSE	0.169	0.175	0.172	0.139

Additionally, the dimensionless amplitude K_D is calculated as follows:

$$K_D = \sqrt{\frac{8 \cdot \sum_{i=0}^{n_t} \eta_i^2}{H^2 \cdot n_t}} \tag{6.16}$$

Here, n_t is the number of time steps. The K_D value is calculated for waves II-V

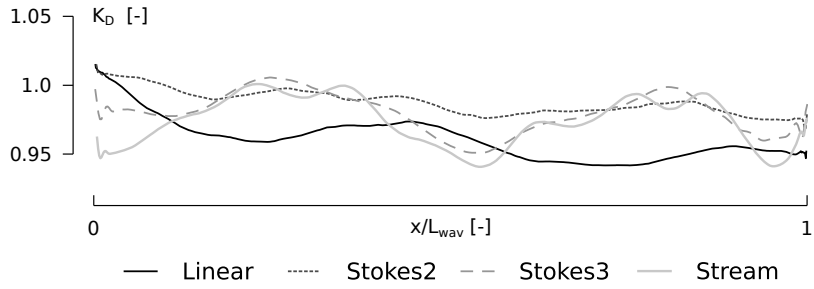

Figure 6.11: Dimensionless amplitude K_D for wave tests II-V.

and plotted as a function of the domain length in Figure 6.11. It is clear that the reflections in the domain are minimal, with K_D values ranging from 0.95 to 1.02.

Lastly, the propagation of an irregular wave with $H_s = 0.15$ m and $T_m = 2.0$ s was simulated. The accuracy of the simulation is determined by performing a reflection analysis with WaveLab on an irregular wave train of 500 waves. The analysis is based on the N-gauge extension of the 3-gauge Mansard and Funke method, as presented in Zelt and Skjelbreia (1992). The result is illustrated in Figure 6.12, where the incident spectrum $S_{incident}$, the reflected spectrum $S_{reflected}$, and the reflection coefficient C_R are given. Around the peak frequency of $0.39Hz$, reflection is very low with C_R ranging from 8% to 11%. Towards the higher frequencies, C_R rises up to 26%. However, the spectral density from these high-frequency components is very low, and the impact on the accuracy of the surface elevation is minimal.

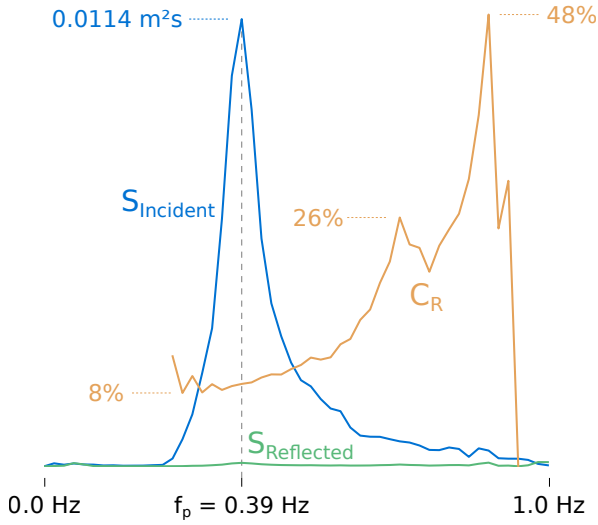

Figure 6.12: Reflection analysis of irregular wave (Test VI).

Next to a frequency analysis, the surface elevation can be compared in the time domain. A visual representation of the comparison of the surface elevation between the theoretical and numerical results is visible in Figure 6.13. It is clear that DualSPHysics with the current open boundary formulation can propagate non-linear irregular waves.

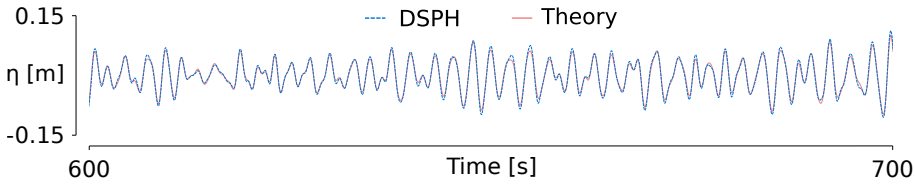

Figure 6.13: Surface elevation comparison of the irregular wave (test VI) between theoretical and numerical result, measured in the middle of the domain.

6.2.4.3b Orbital Velocities A propagating wave is not only characterized by its surface elevation, but also by the orbital velocities in the horizontal and vertical directions. In Figure 6.14, the horizontal orbital velocities under a wave crest are compared to theoretical results, while the vertical orbital velocities are compared in Figure 6.15. DualSPHysics is capable of accurately reproducing the horizontal and vertical orbital velocities. In order to quantify the accuracy, RMSE and L_∞ values are calculated as follows:

$$RMSE = \frac{\sqrt{\frac{1}{n}\sum_{i=1}^{n}(u_{SPH} - u_{theory})^2}}{max(u_{theory})} \tag{6.17}$$

$$L_\infty = \frac{\max|u_{SPH} - u_{theory}|}{max(u_{theory})} \tag{6.18}$$

The results for each Wave Test are summarized in Table 6.6. The RMSE values range from 1.5% to 4.3%, proving the high accuracy of wave generation, propagation and absorption. Also the maximum errors (L_∞) remain low, ranging from 2.9% to 7.2%. The location of the maximum error varies from case to case and can be located anywhere from the sea bottom until the free surface.

6.2.4.3c Pressure Herein the pressure distribution obtained with SPH is compared to the corresponding pressure profile from theory. The results are shown in Figure 6.16, where the mean total pressure, $\overline{p}(z)$, and its standard deviation are plotted as a function of the vertical position, z, at a certain time, t_i, and at the middle section $x_s = L_{wav}/2$. The solid line represents the value of $\overline{p}(z)$ while the shaded area is indicative of the standard deviation, calculated as:

$$\overline{p}(z) = \frac{1}{n_t}\sum_{t_i=0}^{t_{sim}} p(x_s, z, t_i) \tag{6.19}$$

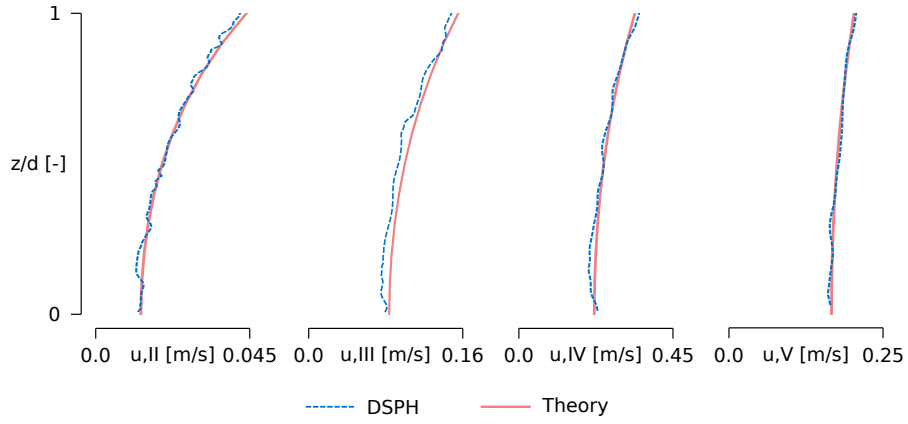

Figure 6.14: Comparison of horizontal orbital velocities of simulated waves to non-linear wave theory.

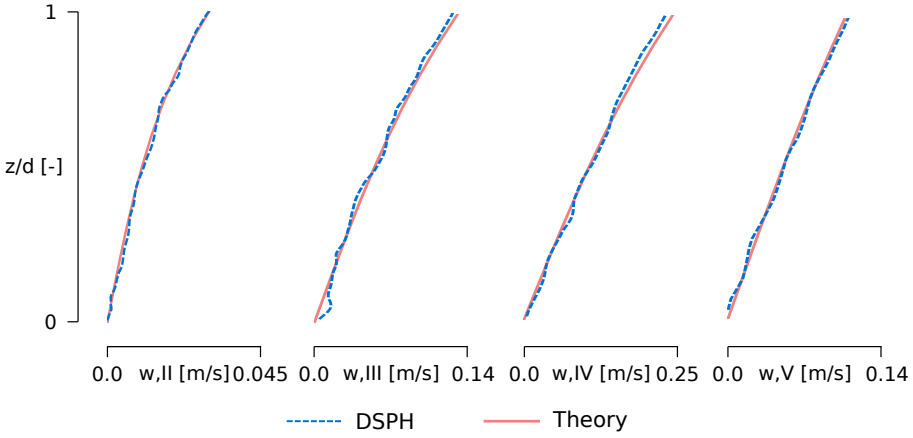

Figure 6.15: Comparison of vertical orbital velocities of simulated waves to non-linear wave theory.

Table 6.6: RMSE values for orbital velocities of wave types II-V.

Wave Test	II	III	IV	V
$\mathbf{RMSE}_u$	0.023	0.043	0.027	0.015
$\mathbf{L}_{\infty,u}$	0.043	0.072	0.053	0.030
$\mathbf{z/d}_{\infty,u}$	1.0	0.6	0.2	0.3
$\mathbf{RMSE}_w$	0.021	0.024	0.026	0.018
$\mathbf{L}_{\infty,w}$	0.036	0.040	0.049	0.029
$\mathbf{z/d}_{\infty,w}$	0.8	0.0	1.0	0.6

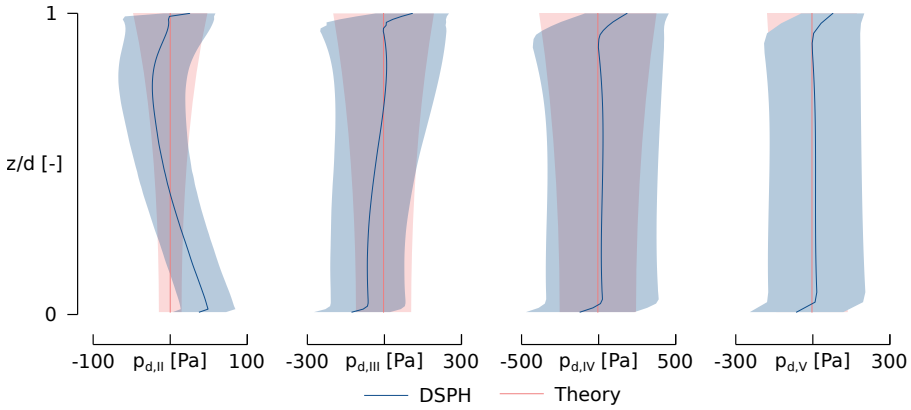

Figure 6.16: Comparison of dynamic pressure of tested waves. Solid lines represent the mean total pressure while the shaded areas represent the standard deviation of the time-varying pressure and are thus directly linked to the dynamic pressure.

$$\sigma_p(z) = \sqrt{\frac{1}{n_t}\sum_{t_i=0}^{t_{sim}} \left(p(x_s, z, t_i) - \overline{p}(z)\right)^2} \tag{6.20}$$

Here, p is the total pressure at a certain point (x_s, z) at a certain time t_i. The standard deviation is directly related to the added dynamic pressure due to the wave action. Good results are obtained. The wave tests III, IV and V have excellent agreement, while wave test II has a slightly curved pressure distribution. Wave test IV has the highest wave height of $0.15m$, leading to higher pressure fluctuations and higher velocities of the buffer particles. Again, the RMSE values are calculated for the mean total pressure as $RMSE_p = \sqrt{\frac{1}{n}\sum_{i=1}^{n}(p_{sim} - p_{theory})^2}/max(p_{theory})$, see Table 6.7. The RMSE values for all 4 waves are low, ranging from 0.002 to 0.008, with the best performance for wave type II and the worst performance for wave type V. It is remarked that the RMSE values are low because the total pressure is considered here rather than the dynamic pressure. This is preferred for simplicity as RMSE calculation on the dynamic pressure is more cumbersome.

Table 6.7: RMSE values for mean total pressure of wave types II-V.

Wave Test	II	III	IV	V
RMSE$_p$	0.002	0.004	0.006	0.008

6.2.4.3d Computational Speed-up One of the main benefits of applying open boundaries is to have a relatively small domain for open sea states where waves need to freely propagate through the domain without any reflections. While classic wave propagation simulations in SPH require a domain length of 3-4 wavelengths (Altomare et al., 2016a), the domain here can be only 1 wavelength long. This leads to a significant reduction in computational effort and cost. In order to quantify the achievable computational speed-up, the number of particles and the simulation runtime are compared between the new open boundary method and a classic wave propagation simulation with a flume length of 4 wavelengths. Based on this recommendation, the classic simulations are run and compared to new method in Table 6.8. The comparison between the number of particles results in a theoretical speed-up. However, the runtime comparison indicates that there can be a difference between theoretical speed-up and effective computational speed-up. Nevertheless, it is clear that a significant computational speed-up is possible by using open boundaries and a reduced domain size. The effective computational speed-up ranges from 146% to 727%. This is comparable to results obtained by Omidvar et al. (2013), where variable particle mass was used to speed up the simulation rather than coupling. There, depending on the studied particle refinement ratios, speed-ups ranging from 133% to 600% were observed.

Table 6.8: Computational speed-up for wave propagation tests.

	Time [hr]			**# Particles**		
Wave Test	**Classic Method**	**New Method**	**Computational Speed-up**	**Classic Method**	**New Method**	**Theoretical Speed-up**
II	39.33	14.38	273%	2442k	1512k	162%
III	3.74	0.51	727%	434k	89k	487%
IV	0.83	0.42	197%	260k	66k	396%
V	1.30	0.89	146%	301k	144k	209%

6.2.4.4 Wave Transmission Tests

A number of regular waves are hereby propagating towards a submerged breakwater with a smooth, impermeable slope of $1/1.5$. Part of the waves reflects on the structure, while another part of the wave energy is transmitted over the breakwater. This results in a reduction of the wave height behind the breakwater. The accuracy of the simulations is quantified by comparing the calculated transmission coefficient, C_T, with the theoretical values published in Seelig (1980). The comparison is illustrated in Figure 6.17. Since there are some fluctuations in the measured wave height in the lee of the submerged breakwater, the average transmission co-

efficient is calculated and plotted together with the measured standard deviation. In the left graph, the theoretical relation between the dimensionless wave height H/gT^2 and the transmission coefficient C_T is compared to the simulated data. Simulations were performed with 4 wave heights, ranging from $0.035m$ to $0.18m$. Lower wave heights would result in a too small particle size and thus a too long computation time. The accuracy is good with errors on C_T ranging from 1% to 4%. The right graph illustrates this by comparing the measured and theoretical transmission coefficient directly.

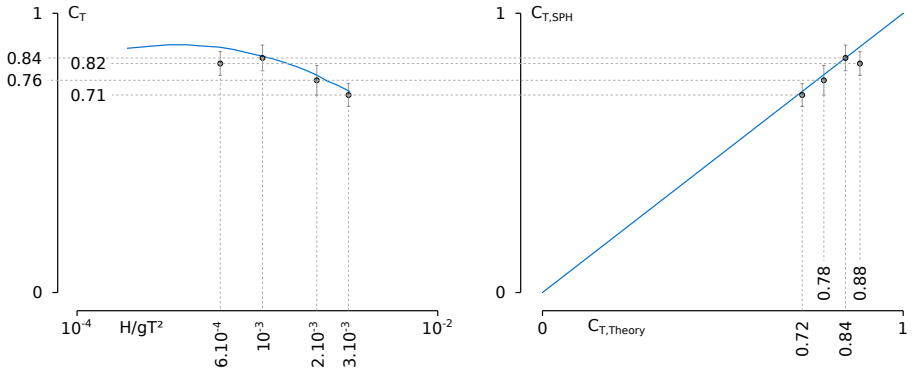

Figure 6.17: Comparison of simulated transmission coefficient $C_{T,SPH}$ and theoretical transmission coefficient $C_{T,Theory}$.

6.2.4.5 Wave Reflection Tests

An irregular wave train of 500 waves is propagated towards a breakwater with a smooth, impermeable slope. Part of the waves reflects on the structure, while another part of the wave energy dissipates due to breaking and run-up. The accuracy of the simulations is quantified by comparing the calculated reflection coefficient C_R, with the theoretical values published in Seelig (1983). The comparison is illustrated in Figure 6.18. In the left graph, the theoretical relation between the slope angle α and the reflection coefficient C_R is compared to the simulated data. Simulations were performed with 6 slope angles, ranging from 20° to 45° with a step of 5°. The accuracy is good with errors on C_R ranging from 1.2% to 6.8%. The right graph illustrates this by comparing the measured and theoretical reflection coefficient directly.

6.2.5 Discussion

A novel wave generation and absorption method using open boundaries was introduced. A fluid domain of one wavelength long was selected, with an inlet and outlet composed of 8 buffer particle layers at both sides. At the inlet, theoretical horizontal velocity and surface elevation were imposed to the buffer particles, while the pressure was extrapolated from ghost nodes placed in the fluid domain. At the outlet, only theoretical horizontal velocity was imposed, while pressure and surface

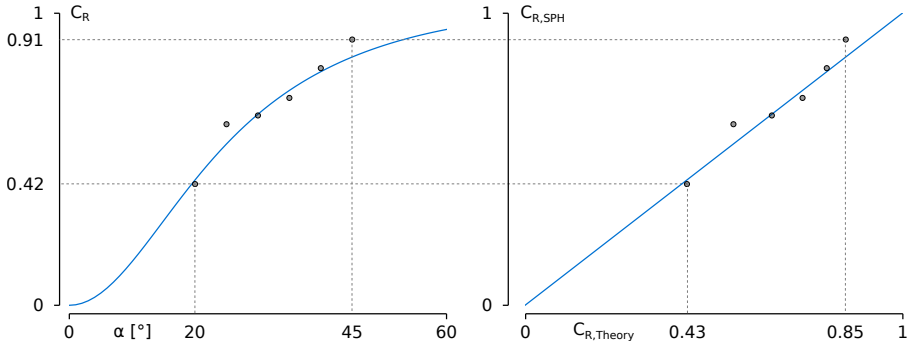

Figure 6.18: Comparison of simulated reflection coefficient $C_{R,SPH}$ and theoretical reflection coefficient $C_{R,Theory}$.

elevation were extrapolated from the fluid domain. At both the inlet and outlet, a custom velocity correction algorithm was applied, based on measuring the reflected wave and calculating the corrected velocity based on shallow water wave theory. The accuracy of the methodology was tested by comparing simulation results to theoretical results and results from literature. Generally, wave generation/absorption with open boundaries has the following benefits:

- The computation time can be significantly smaller for open sea simulations where no reflections are present since a fluid domain of only one wavelength long is sufficient for accurate wave propagation. Cases where this is of high interest are, for example, simulations of floating structures/devices such as Wave Energy Converters, offshore floating wind platforms, etc. Alternatively, for the same computation time as a typical SPH simulation with moving boundaries and a domain length of 3-4 wavelengths, there is the possibility of simulating more particles for a higher accuracy (see also Table 6.8).
- The quantities imposed on the buffer particles can come from any type of external source: linear or non-linear wave theories, other numerical models such as CFD models, potential flow models, Boussinesq models, and even measurement data could be imposed.
- Due to the automatic insertion and removal of buffer particles through the boundary lines, there are no issues with preserving mass conservation due to Stokes drift.

It is clear that this wave generation/absorption method is superior to the method with moving boundaries described in Chapter 5. This indicates that the open boundary formulation is ideal to allow DualSPHysics to be coupled to other wave propagation models, such as OceanWave3D.

6.3 Coupling Methodology with Open Boundaries

It has been shown that the newly developed open boundaries are well suited for wave generation, propagation and absorption. Additionally, they do not have the disadvantages of the moving boundary wave generation, used in Chapter 5. Firstly, there is no drift of the boundaries possible, since they remain at their initial position throughout the simulation. Secondly, significantly less coding is needed to apply wave generation with open boundaries than with moving boundaries. Lastly, since no dynamic boundary particles are used within the open boundaries, there are no pressure peaks, resulting in a significantly smoother pressure and velocity field.

6.3.1 Description of Coupling Methodology

The main principle of the coupling methodology and the coupling algorithm of Chapter 5 remains the same. However, the implementation is extended and slightly changed, as illustrated in Figure 6.19. The detailed wave-structure interactions are still calculated with the latest version of DualSPHysics (v4.2.030). As mentioned in Section 6.2.2, velocity corrections need to be applied for accurate representation of the free-surface elevation and the wave kinematics. For this reason, a two-way online coupling is realised between a Python program and DualSPHysics. Socket programming is used for the data transfer. At the start of the simulation, a dedicated port 50007 is opened to allow online communication. At the start of each time step, Python sends both the inlet and outlet velocities and the inlet surface elevation to DualSPHysics. At the end of the time step, DualSPHyics sends back the measured surface elevation near the inlet and outlet. In Python, the velocity corrections are calculated and applied to the originally imposed orbital velocities.

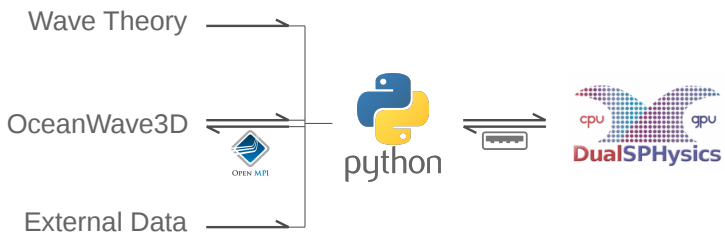

Figure 6.19: Redesigned coupling implementation

The previously applied coupling methodology (see Chapter 5) only allowed wave generation through coupling with the FNPF solver OceanWave3D. With the extended coupling methodology, any data can be used to impose velocities and surface elevation to the inlet and outlet zones. Wave theory solutions are an excellent method to provide the model with accurate orbital velocities. Currently, linear, Stokes second-order and Stokes fifth-order wave theories are supported. The previously applied two-way coupling with OceanWave3D is still available, and again uses the MPI protocol for data transfer. Here, socket programming was not possible due to compatibility issues with the OceanWave3D Fortran code.

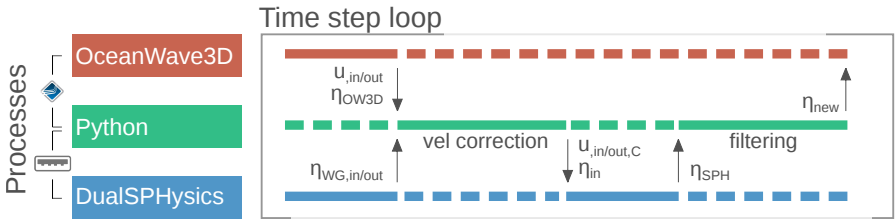

Figure 6.20: Redesigned coupling algorithm

Apart from the redesigned implementation, the coupling algorithm has slightly changed as well (see Figure 6.20 for a schematic representation of the algorithm during one coupling time step). The most complex coupling is discussed, being the two-way coupling with OceanWave3D. The coupling communication still occurs at the beginning and at the end of an OceanWave3D timestep, which we will call the communication time step. At the beginning of a time step, the horizontal orbital velocities at the inlet and outlet locations, $u_{in/out}$, are calculated in OceanWave3D, as well as the surface elevation of the complete OceanWave3D domain η_{OW3D}, and sent to the Python programming using the MPI protocol. Simultaneously, Python receives the measured surface elevation from DualSPHysics near the inlet and outlet $\eta_{WG,in/out}$. The velocity correction is calculated and the corrected orbital velocities $u_{in/out,C}$ are sent back to DualSPHysics, together with the surface elevation at the inlet η_{in}. The quantities are imposed within the inlet and outlet and the DualSPHysics simulation continues until the communication time step is finished. The surface elevation from DualSPHysics is sent to Python, where the signal is filtered as previously done in Section 5.3.3 and sent back to OceanWave3D as η_{new} to overwrite the original result.

6.3.2 Code Implementations

The redesigned coupling implementation from Figure 6.19 requires source code changes in OceanWave3D, DualSPHysics and the creation of new Python scripts. All the code is available through the GitHub respository `https://github.ugent.be/tverbrug/OW3D-DSPH`. This section summarizes the code alterations for each software package.

6.3.2.1 OceanWave3D Code Changes

In order to enable an online two-way coupling with OceanWave3D, a number of code changes need to be made. The following files were adapted to allow the coupling methodology to work:

1. Input file `OW3D.inp`;
   An extra line was added to the input file, indicating coupling should be applied, and specifying the coordinates of the coupling zone.

2. file `globalvariables.f90`;
   Global variables are created for the coupling file, coupling zone coordinates and indices and the received SPH free surface.

3. file `ReadinputFileParameters.f90`;
   The extra line added to the input file is read into its corresponding global variables, to be used by the coupling routine.

4. file `OceanWave3DTakeATimeStep.f90`;
   At every time step, the coupling routine is called, after a check if coupling is enabled.

5. file `CoupleRoutine.f90`;
   This subroutine initializes the MPI communication, calculates the indices for the coupling interface locations and calculates the horizontal orbital velocities from the wave potential. It sends the velocities and the surface elevation to the Python script, and receives the filtered SPH surface elevation, which it uses to overwrite the original surface elevations.

The full code can be found in Appendix E.1.

6.3.2.2 Python Code

Python is used to connect the different coupling pieces together. Although a direct coupling between OceanWave3D and DualSPHysics is technically possible, using Python as an intermediate station allows for a much higher flexibility and allows the user to perform easy accuracy checks and simplifies the debugging process. The following files have been developed:

1. set-up file `simsetup.py`;
   This file contains all the simulation variables: the wave conditions, OceanWave3D parameters and DualSPHysics parameters. It calculates the inlet and outlet conditions based on the selected parameters.

2. main file `WaveGen_socket.py`;
   This file loads in the set-up parameters, writes away the input files for OceanWave3D and DualSPHysics, and executes the simulations. For a one-way simulation, the Python script `comm_socket.py` is executed. For a two-way simulation, an MPI-run is started where the OceanWave3D simulation is assigned to the first process and the script `comm_socket_2way.py` is assigned to the second process.

3. communication file `comm_socket.py`;
   In a one-way simulation, this file manages the communication between Python and DualSPHysics, using the socket protocol. The inlet and outlet conditions are sent to DualSPHysics, while the surface elevations necessary for the velocity corrections are received.

4. communication file `comm_socket_2way.py`;
   This file is very similar to the previous one, but manages the two-way communication. In addition to the code of `comm_socket.py`, there are several MPI commands to receive and send data from and to OceanWave3D.

5. functions file `functions.py`;
   This file contains functions for calculating the theoretical orbital velocities, to apply the relaxation functions, to create the input files and to post-process the results.

The full code can be found in Appendix E.2.

6.3.2.3 DualSPHysics Code Changes

A number of code changes and additions are performed on the DualSPHysics source code. The following files were altered:

1. main file `JSphGpuSingle.cpp`;
   This is the main simulation file for a GPU run. Here, extra global variables are added for the communication with Python. Function are made for socket initialization, socket sending, socket receiving and closing the connection. During the time-stepping, values received from Python are stored in the global variables, while the free surface elevation is calculated and sent back to Python.

2. file `JSphInOutGridData.cpp`;
   This file is normally used to impose external quantities, arranged on a grid, on to the inlet and outlet particles. Here, the horizontal orbital velocities received from Python, are interpolated in time, and copied to the GPU memory, together with the necessary velocity correction.

3. file `JSphGpu_InOut_ker.cu`;
   Here, the GPU calculations for the inlet and outlet points are performed. Only minor changes are made here. In the interpolation functions, the corrected velocity is added as an extra function variable, and in the function is subtracted from the imposed velocities.

4. file `JSphInOut.cpp`;
   Here, the function updating the surface elevation in the inlet zone is modified. The surface elevation received from Python is interpolated in time and copied to the GPU memory.

5. file `JSphGpu_ker.cu`;
   Here, the motion of floating objects can be restricted to a specific degree of freedom, for example the heave motion.

The full code can be found in Appendix E.3.

6.3.3 2-D Validation

First, the coupling methodology is validated in 2-D. This section will focus on the 2-way coupling with OceanWave3D (middle section of Figure 6.19), since the coupling with wave theory already has been validated in Section 6.2.4. For the validation of the 2-way coupling with OceanWave3D, the coupled model is applied to compare the response of a floating box to experimental data, as described in Ren et al. (2015). The experimental and numerical test set-up is illustrated in Figure 6.21. The full wave propagation domain has a length of $20.0\ m$. The floating box is positioned at $x = 5.5\ m$ and has the dimensions $0.3\ m$ x $0.2\ m$ (length x height) with a draft of $0.1\ m$. The water depth is $0.4\ m$, while the DualSPHysics domain is $6.12\ m$ wide (3 wave lengths) and starts at $x = 4.0\ m$. A regular wave with wave height $H = 0.1\ m$ and wave period $T = 1.2\ s$ is generated, characterised as a Stokes third-order wave. A particle size of $d_p = 0.01\ m$ is used. The SPH domain is chosen to be larger than one wavelength L, since the box is freely floating and will drift in the x-direction over time.

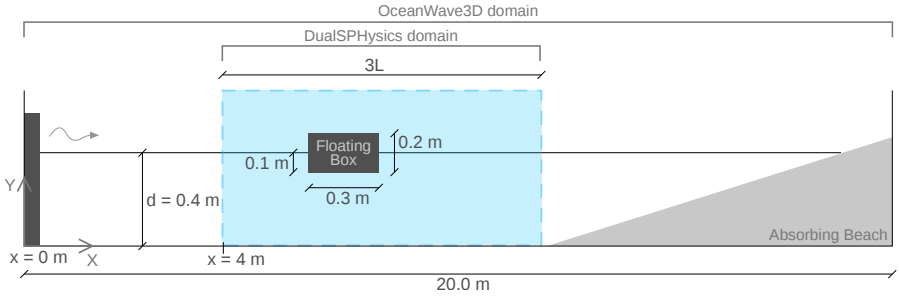

Figure 6.21: Experimental and numerical test set-up for simulation of the response of a floating box to a custom wave signal. The DualSPHysics domain and OceanWave3D domain are indicated. L is the wavelength.

6.3.3.1 DualSPHysics Parameters

The SPH options used in this section are summarised in Table 6.9. The parameters are equal to the ones used in Section 5.5.3, with the exception of the boundary conditions.

6.3.3.2 Results and discussion

Both a one way coupling and two-way coupling are compared to the experimental data, and the corresponding errors are illustrated in Figure 6.22. In the one-way coupling, OceanWave3D only provides the horizontal orbital velocities to the inlet and outlet zone, and the surface elevations for the inlet and the calculation of the velocity corrections. For the two-way coupling, the surface elevations from the DualSPHysics domain are transferred back to the OceanWave3D domain, where the original solution is overwritten. The zone close around the floating box is not coupled back, since the 'measured' SPH free surface elevations are not physical

Table 6.9: SPH formulation and parameters.

Time Integration Scheme	Verlet
Time Step	Variable (including CFL and viscosity)
Kernel	Wendland
Smoothing Length	$2.0 \cdot d_p$
Viscosity Treatment	Artificial ($\alpha = 0.01$)
Equation of State	Tait equation
Boundary Conditions	Open Boundary Conditions
δ-SPH	Yes (δ-SPH = 0.1)

there. A good correspondence between the numerical and experimental results is shown. Specifically the heave and pitch motions are accurately reproduced. The error on the heave motions remains well below the smoothing length $h = 0.017\ m$ while the pitch error stays below 3.5 degrees. Although the cyclic surge path is also visible in the numerical results, the net drift in the x-direction is less accurately modelled. Logically, the error on the surge motion becomes larger in time.

Additionally, the surface elevation profile at $t = 15\ s$ of DualSPHysics and OceanWave3D is compared in Figure 6.23. Three wave profiles are plotted. For the two-way coupling methodology, both the OceanWave3D and DualSPHysics profile are plotted. Normally, these lines are expected to be exactly the same, since the original OceanWave3D surface elevation is overwritten. However, as described in 5.3.3, relaxation functions are applied to ensure a smooth transition between the OceanWave3D solution and the DualSPHysics solution. In Figure 6.23, this is visible where only close to the masked out zone both solutions match perfectly. Behind the masked out zone, both solutions remain the same until they slightly differ again at the boundary of the SPH zone. As a reference, the OceanWave3D solution for a one-way coupling is shown as well. Here, there is no influence from the DualSPHysics solution, and OceanWave3D propagates waves as if there is no floating box present. Nevertheless, this does not impact the accuracy of the results significantly, as proven in Figure 6.22. Again, it can be concluded that the 2-way coupling methodology should only be applied when there is a significant wave transformation effect around the structure, present in the SPH domain.

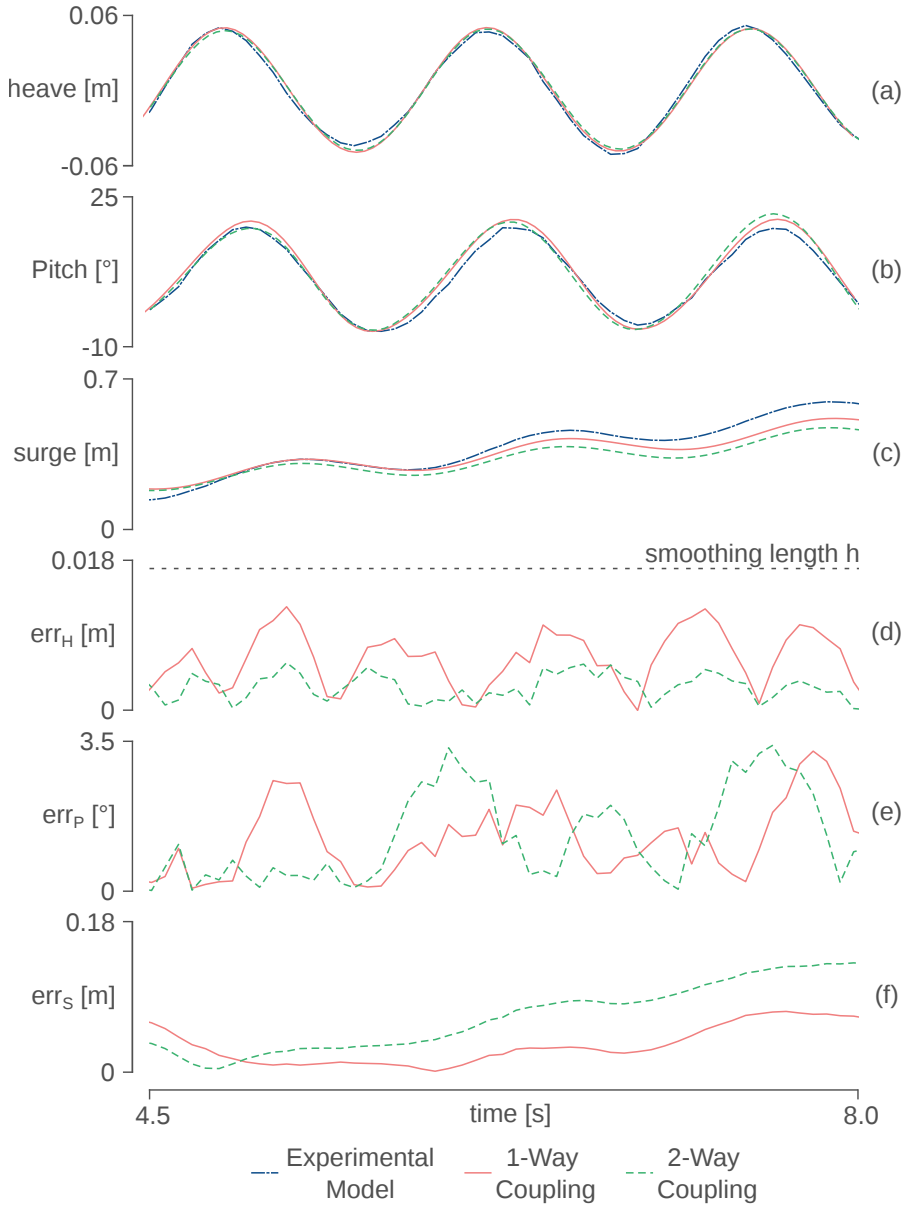

Figure 6.22: Comparison of time series and error between numerical and experimental results of the 3 degrees of freedom of the box with heave, pitch and surge motions.

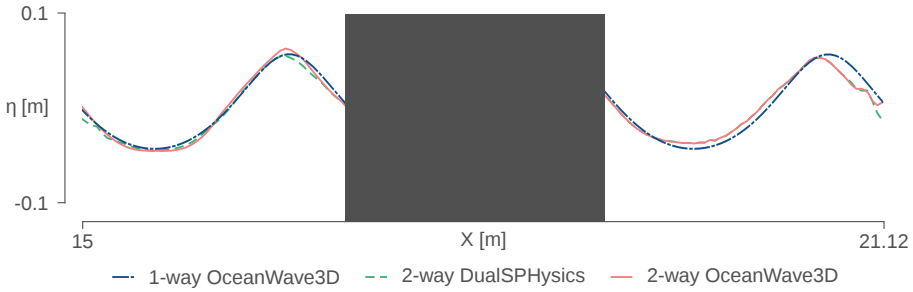

Figure 6.23: Comparison of wave profile between one-way and two-way coupling results of OceanWave3D and DualSPHysics. The gray masked out zone is the region around the floating box, omitted from the coupling.

6.3.4 3-D Proof-of-concept

In this Section, the introduced coupling methodology is extended to a 3-D domain. A one-way coupling with a fifth-order Stokes wave theory is applied. The buffer zones are stretched in the y-direction and the imposed quantities are constant in that direction. This means 3-D simulations are restricted to long-crested waves. This means the coupling methodology can be used to model wave flume type experiments where significant 3-D effects are present. To demonstrate this, a heaving disk is simulated, impacted by steep non-linear waves. This results in non-linear wave surge forces and overtopping.

6.3.4.1 DualSPHysics Parameters

The SPH options used in this section are summarised in Table 6.10.

Table 6.10: SPH formulation and parameters.

Time Integration Scheme	Verlet
Time Step	Variable (including CFL and viscosity)
Kernel	Wendland
Smoothing Length	$2.0 \cdot d_p$
Viscosity Treatment	Artificial ($\alpha = 0.01$)
Equation of State	Tait equation
Boundary Conditions	Open Boundary Conditions
δ-SPH	Yes (δ-SPH $= 0.1$)

6.3.4.2 Experimental set-up

Experimental tests have been performed in the large wave flume of Ghent University (see Figure 6.24). The flume is 30 m long and 1 m wide. A cylindrical WEC with a diameter of 0.5 m is positioned at 10.6 m from the wave paddle. Its motion is restricted to heave by a vertical rod over which it is sliding. Friction losses are minimized by using two sets of PTFE bearings: one on the top and one on the bottom of the cylinder. The WEC consists of 10 glued plastic disks and is waterproofed with a black, MS polymer coating. Absorption material is installed at the end of the flume to ensure minimal reflections. Active wave absorption is applied using two wave gauges about 3 m away from the paddle. 7 wave gauges are installed to measure the free surface elevation. The WEC has a diameter of $D = 0.5\ m$ and a draft of $T_{WEC} = 0.113\ m$. The motion of the WEC is captured by video tracking using a GoPro Hero 5, filming in Full HD at 120 fps. The fisheye effect was corrected using the video processing software Adobe After Effects. The horizontal surge force is measured by 2 force transducers, installed in a rigid rod behind the WEC to which it is connected. The incident wave has a wave height of $H = 0.12\ m$, a wave period of $T = 1.2\ s$ in a water depth of $d = 0.7\ m$. This results in a Stokes third-order wave with a wave length of $L_{wav} = 2.17\ m$.

6.3.4.3 Numerical set-up

The numerical set-up is illustrated in Figure 6.25 and summarized in Table 6.11. It is chosen to keep set the length of the fluid domain to twice the wave length $2 \cdot L_{wav} = 4.34\ m$. This is around $1/7$ of the total flume length. The particle size is chosen to be $d_p = \ 0.01\ m$, which is smaller than $H/10$. The Stokes fifth-order wave theory is applied. Since there is always a gap of 1.5 times the smoothing length h between fluid particles and boundary particles, the top of the floating disk is lowered with a value of $1.5 \cdot h = 3.0\ d_p$, in order to get the correct overtopping height. A 3-D inlet zone and outlet zone are configured, with each 8 planes of buffer particles. All other boundaries are wall conditions with an option to extrapolate the pressure from the fluid domain, in order to avoid local pressure peaks. The WEC is positioned in the center of the domain and is restricted to allow only the heave motion.

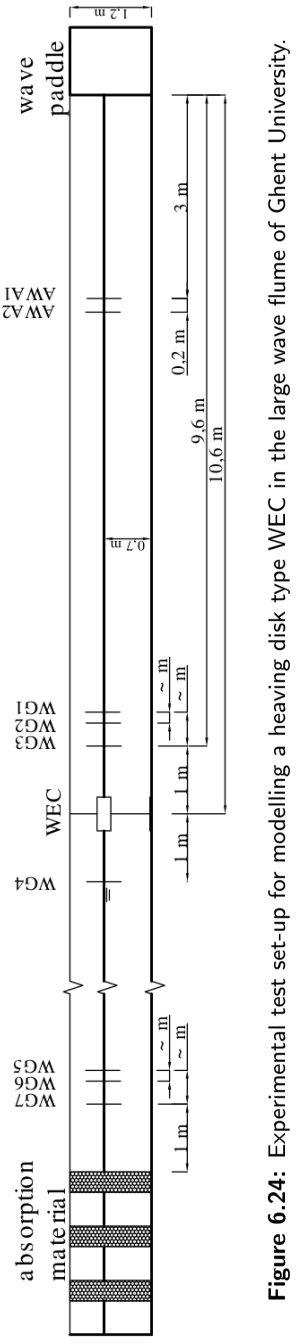

Figure 6.24: Experimental test set-up for modelling a heaving disk type WEC in the large wave flume of Ghent University.

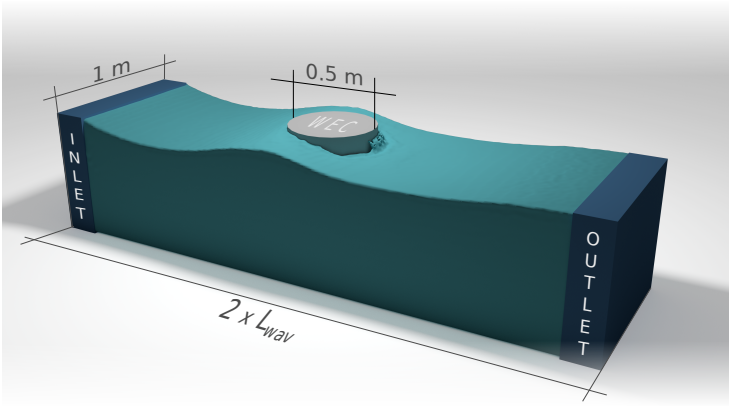

Figure 6.25: Numerical test set-up for 3-D modelling of a heaving cylindrical WEC in a numerical wave flume.

6.3.4.4 Results and discussion

First, the model surface elevations are compared with the experimental results. The signals from WG3 and WG4 (see Figure 6.24) are compared to the numerical result. WG3 is positioned 1 m in front of the WEC, WG4 1 m behind the WEC. The comparison with the data from WG3 is shown in plot (a) of Figure 6.26, while plot (b) shows the WG4 data. The surface elevation in front of the WEC is accurately reproduced. There is some initialisation time, but after a while the wave signal is steady and matches the experimental data very well. The error remains well below the smoothing length $h = 0.017\ m$. Behind the WEC the numerical results are less accurate. The coupled 3-D model predicts lower wave heights behind the WEC than what was registered in real life. The measured free surface also has a steeper non-linear profile than what was calculated numerically. This could be due to the shortened SPH domain with respect to the full experimental flume length. However, the error is still acceptable since the maximum error lies around the smoothing length h.

Second, the horizontal surge force is calculated and compared to the experimental data in plot (c) of Figure 6.26. Here, it is clear that there is a very good match between the numerical and experimental results. Although both signals have some noise, the overall trend of the data matches very well.

Third, the comparison of the heave motion of the WEC to the experimental data is shown in plot (d) of Figure 6.26. Again, after initialisation of the surface elevation in the flume, a steady regime is obtained in which the calculated WEC motion and measured motion show an excellent agreement, with a maximum error of $0.4h$.

Table 6.11: Simulation parameters for 3-D modelling of a heaving cylindrical WEC

Wave Height H [m]	0.12
Wave Period T [s]	1.2
Water Depth d [m]	0.7
Wave Length L_{wav} [m]	2.17
Particle Size d_p [m]	0.01
Domain Length L [m]	4.34
Domain Width W [m]	1.0
WEC Diameter D [m]	0.5
WEC Draft T_{WEC} [m]	0.113
Wave Theory	Stokes 5^{th}

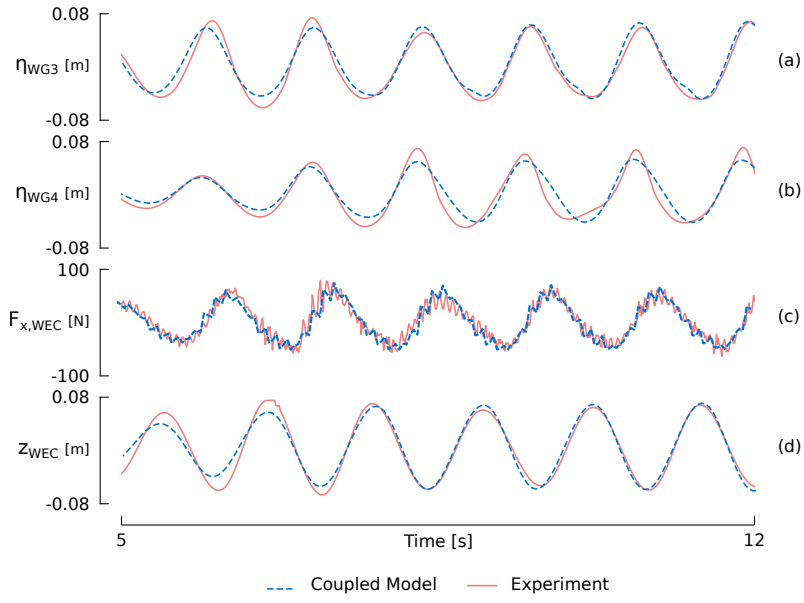

Figure 6.26: Comparison of 3-D proof-of-concept with experimental data of a heaving cylinder in overtopping non-linear waves. Plot (a) shows the surface elevation 1 m in front of the WEC, (b) the surface elevation 1 m behind the WEC, (c) the horizontal surge force acting on the WEC and (d) the heave motion of the WEC

6.3.4.5 Computational Speed-up

As already demonstrated in Section 6.2.4.3d, the coupling methodology with open boundaries leads to significant performance gains with respect to typical SPH simulations. In this section, an estimation of the computational speed-up is made, comparing the presented model with a numerical model, describing the complete experimental set-up. The latter is thus an SPH simulation where the full wave flume is modelled, including the wave paddle motion and the floating disk, installed at $x = 10.6\ m$. The comparison is summarized in Table 6.12. In the coupled model, the domain length was set at twice the wave length, resulting in a total length of 4.34 m. This is about $1/7$ of the wave flume length, which explains the number of fluid particles in the full model, which is about 718 % more than in the coupled model. The difference in total number of particles is lower, at only 508 %. This is due to the thickness of the bottom boundary in the coupled model, which is thicker to allow for accurate pressure extrapolation. The difference in GPU memory is similar at 505 %, with an absolute value of 3941 MB for the full model. Although our GPU card has 8106 MB of memory available, this simulation is incredibly demanding. Computational performance is not only dependent on GPU memory, since the number of CUDA cores and their clock rate are much more indicative of simulation time. Additionally, the GPU occupancy also has an effect on the simulation time (Mokos et al., 2015). The estimated runtime, which is calculated at the start of the simulation, is significantly longer for the full model than for the coupled model. However, the difference of 411 % is slightly lower than the difference in particles. The real runtime of the coupled model was 91 hours. This remarkable difference in estimated runtime and real runtime can be explained by inaccurate estimations at the beginning of the simulation, in combination with performing other tasks on the computer, slowing down the simulation. It is chosen to not run the full model completely, since the computer becomes unusable during the simulation and it could take up to 375 hours or almost 16 days to finish if the same performance as the coupled model is assumed. It is safe to assume that a speed-up of around 400 % can be achieved, by applying the coupling methodology. This is line with the results from Section 6.2.4.3d.

Table 6.12: Computational speed-up for 3-D proof-of-concept

	Coupled Model	Full Model	Difference
# Particles	5 010 954	25 473 152	508 %
# Fluid Particles	2 949 433	21 165 100	718 %
GPU Memory [MB]	780	3941	505 %
Estimated Runtime [hr]	35	144	411 %
Real Runtime [hr]	91	375	411 %

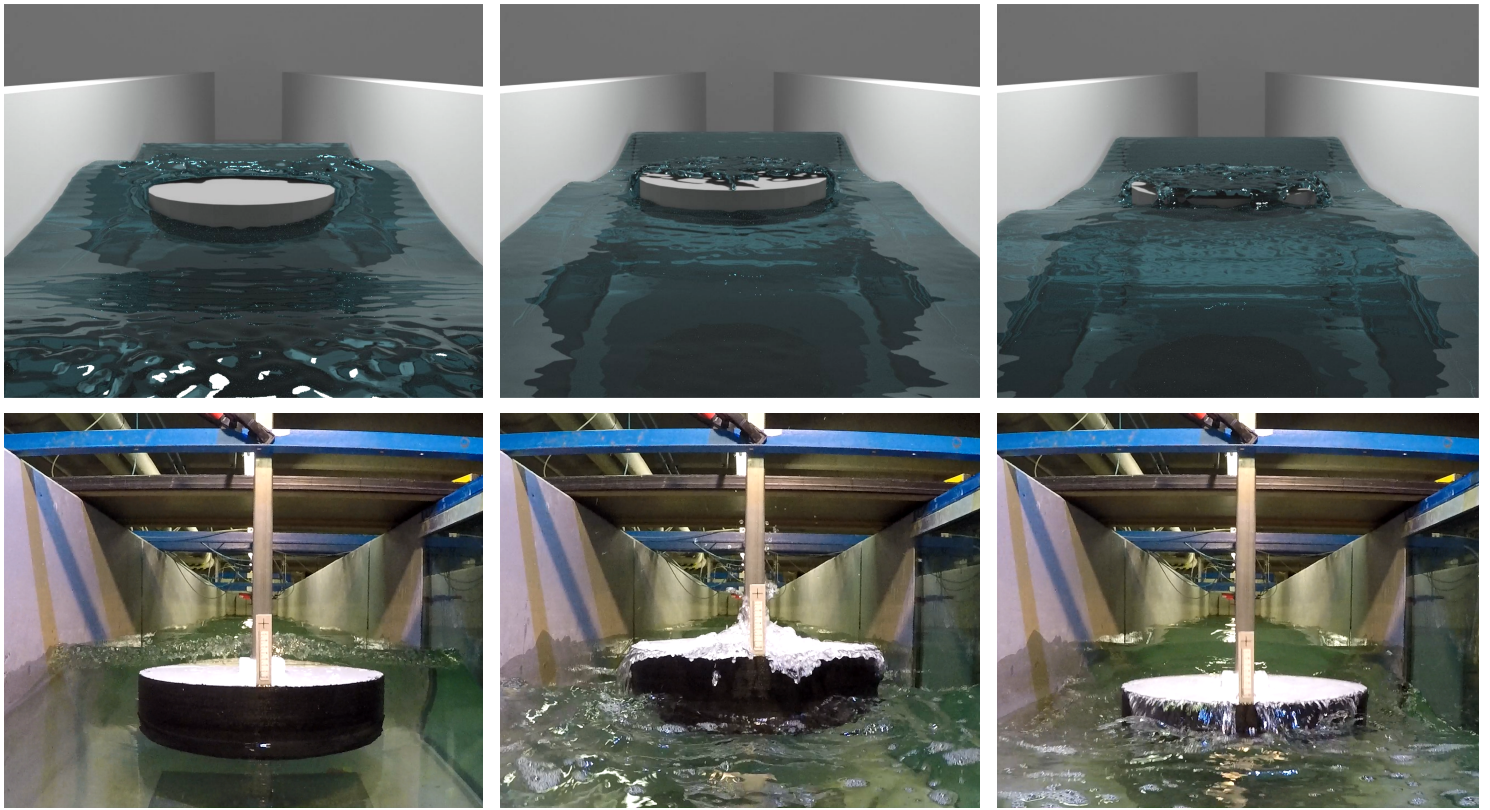

Figure 6.27: Visual comparison of overtopping waves between the 3-D proof-of-concept with experimental data of a heaving cylinder in overtopping non-linear waves. The plot shows a time progression of the wave, from left to right with a time difference of 0.4 s between each frame

6.3.4.6 Visual Comparison of overtopping

During the experiments, the steep non-linear waves are overtopping the cylindrical WEC. However, no overtopping rates or thickness of the overtopping layer were measured, so a real validation is impossible. For this reason, only a visual comparison of an overtopping event between the experiment and the numerical model is performed. In Figure 6.27, a time progression of an overtopping wave is shown. Here, the wave height was set at $H = 0.15\ m$ and the wave period was $T = 1.0\ s$. This resulted in steep, highly non-linear waves with significant overtopping. Also, for this test case, video images were available to perform a visual comparison. In the left plot, the wave is just about to hit the cylindrical WEC. In the middle plot, 0.4 seconds later, the overtopping wave is on top of the WEC, and in the final plot, the overtopped volume is flowing from the top back into the flume. Visually, the correspondence between the numerical model and the experimental images is very good, apart from the splash of the water against the rod, since it is not present in the numerical model.

6.4 Application range of coupling methodology

It has been demonstrated that open boundaries can be applied within 1-way and 2-way coupling methodologies. Here, the focus was put on non-linear propagating waves, but any type of non-linear free surface flow could be imposed on the open boundaries. This section introduces an application range for the introduced 1-way and 2-way coupling methodologies.

6.4.1 1-way Coupling

Within this work, 1-way coupling has been applied by imposing the orbital velocities and surface elevations based on a non-linear wave theory, or based on the results of an external wave propagation model. The validity of this 1-way coupling method has been tested for a wide range of wave conditions, illustrated in Figure 6.28. The range includes shallow water waves as well as deep water waves, weakly non-linear and highly non-linear waves. For the stream function waves, OceanWave3D was used as input, while the other tests were performed using the fifth-order Stokes Theory. No breaking waves were tested since neither the applied wave theory nor OceanWave3D are capable of calculating flow velocities and surface elevations of breaking waves. This is an important range of wave conditions which needs to be tested in future work.

6.4.2 2-way Coupling

More caution is needed when coupling DualSPHysics to external wave propagation models, specifically when a 2-way coupling is selected. Compatibility of the coupled variables is advised. Here, the fully non-linear potential flow solver OceanWave3D was used. This model is capable of accurately calculating the flow field and surface elevation of non-breaking waves. This flow field is free of viscous effects. A 2-way

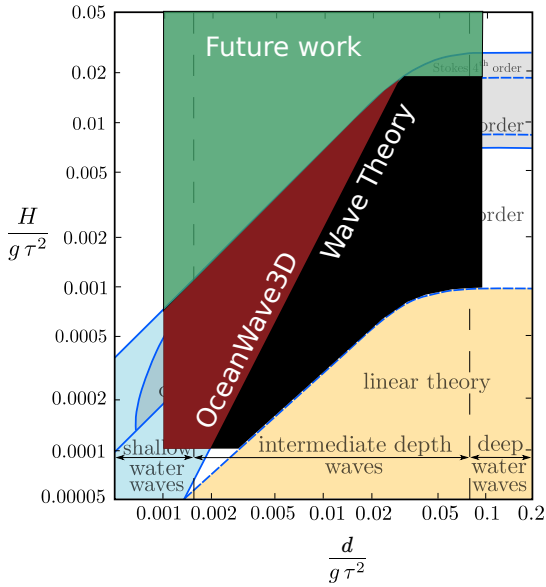

Figure 6.28: Tested validity range of the one-way coupled model. $\frac{d}{g\tau^2}$ is the normalized water depth while $\frac{H}{g\tau^2}$ is the normalized wave height. Adapted from Le Méhauté (1969).

coupling where the original surface elevation is overwritten, is thus only possible when the SPH surface elevation is originating from a non-breaking, non-viscous flow condition. Overwriting the OceanWave3D free surface with a breaking wave is impossible since a breaking wave cannot be characterised by one surface elevation value, and the overwritten surface elevation would not obey the physical limitations of OceanWave3D, rendering the simulation unstable.

6.5 Conclusions

In this Chapter, the two-way coupling methodology introduced in Chapter 5, was improved and extended. First, the recently introduced open boundaries were applied to accurately generate, propagate and absorb waves within DualSPHysics. A 2-way coupling between Python and DualSPHysics was realised to apply velocity corrections to the inlet and outlet buffer zones, to avoid reflections inside the fluid domain. This resulted in accurate surface elevations and wave kinematics, which was proven by calculation of error values. Next, the coupling methodology was extended to accept theoretical solutions as a wave input, as well as the original 2-way coupling with OceanWave3D. The coupling is implemented using two data communication protocols. The 2-way Python-DualSPHysics coupling is established with socket programming, while the 2-way OceanWave3D-Python coupling uses the MPI protocol. These developments fills the fourth and fifth knowledge gap, defined in Section 2.4.

The wave propagation with open boundaries was validated in 2-D by comparing the surface elevation, orbital velocities and pressures of a set of regular and irregular waves to non-linear theoretical solutions. Additionally, results from wave transmissions tests with regular waves and wave reflection tests with irregular waves on sloping beaches were compared to experimental results from literature. Next, the 2-way coupling methodology with OceanWave3D was validated in 2-D by comparing the motions of a floating box to experimental data. Finally, a 3-D proof-of-concept was introduced where steep non-linear waves interact with and overtop a heaving cylindrical WEC. The results all show a good agreement with the theoretical solutions or experimental data. The coupling methodology has the following benefits:

- The computation time can be significantly smaller since only a part of the full wave propagation domain is simulated in DualSPHysics. In the performed tests, the coupled model has at least 2 to 4 times less particles to simulate, which directly results into faster computation times;
- Alternatively, for the same computation time as a stand-alone SPH simulation, there is the possibility of simulating more particles for a higher accuracy.
- Due to the application of open boundaries, there are no issues with Stokes drift, and the velocity and pressure field are significantly smoother than those calculated with the coupling methodology applying moving boundaries.

However, there are still a number of limitations to this revised coupling methodology. Firstly, only quasi-3-D simulations are possible. The buffer zones do not allow non-uniform velocities or surface elevations along the y-directions. This means the 3-D simulations are limited to long-crested waves. However, this can already be very meaningful to simulate typical wave flume experiments, or real engineering problems where there is not much variability in the y-direction. The numerical stability in 3-D simulations needs to improve. The open boundaries still have some compatibility issues with the periodic boundary conditions within DualSPHysics and with the boundary pressure extrapolation algorithm. Although good results are obtained, there is a certain loss of particles during the simulations. This will however be solved within future releases of the source code.

Chapter 7

Comparison and Applicability of Coupling Methodologies

In this seventh chapter of the thesis, a short comparison of the previously presented coupling methodologies is provided. Additionally, advice is given on the applicability of each methodology, based on their specific advantages and disadvantages.

7.1 Comparison of linear and non-linear coupling methodology

The non-linear coupling methodology is compared to the linear-coupling methodology by using the final test case presented in Section 6.3.4 of Chapter 6. For the convenience of the reader, the test set-up is repeated.

7.1.1 Experimental set-up

Experimental tests have been performed in the large wave flume of Ghent University (see Figure 6.24). The flume is 30 m long and 1 m wide. A cylindrical WEC with a diameter of 0.5 m is positioned at 10.6 m from the wave paddle. Absorption material is installed at the end of the flume to ensure minimal reflections. Active wave absorption is applied using two wave gauges about 3 m away from the paddle. 7 wave gauges are installed to measure the free surface elevation. The WEC has a diameter of $D = 0.5\ m$ and a draft of $T_{WEC} = 0.113\ m$. The motion of the WEC is captured by video tracking using a GoPro Hero 5, filming in Full HD at 120 fps. The horizontal surge force is measured by 2 force transducers, installed in a rigid rod behind the WEC to which it is connected. The incident wave has a wave height of $H = 0.12\ m$, a wave period of $T = 1.2\ s$ in a water depth of $d = 0.7\ m$. This results in a Stokes 3^{rd} order wave with a wave length of $L_{wav} = 2.17\ m$.

7.1.2 Numerical set-up

The numerical set-up for the linear coupling consists of a wave flume, measuring 30 m $\times$ 1 m. The incident waves are calculated with OceanWave3D, while the radiated and diffracted waves are calculated with Nemoh. The coupling radius is set to $10d_x = 1m$.

The numerical set-up for the non-linear coupling is illustrated in Figure 7.1. It is chosen to keep set the length of the fluid domain to twice the wave length $2 \cdot L_{wav} = 4.34\ m$. This is around $1/7$ of the total flume length. A 3-D inlet zone and outlet zone are configured, with each 8 planes of buffer particles. All other boundaries are wall conditions with an option to extrapolate the pressure from the fluid domain, in order to avoid local pressure peaks. The WEC is positioned in the center of the domain and is restricted to allow only the heave motion.

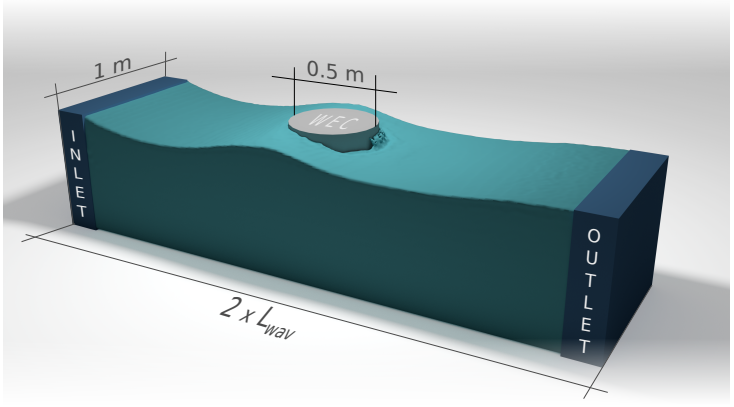

Figure 7.1: Numerical test set-up for 3-D modelling of a heaving cylindrical WEC in a numerical wave flume.

7.1.3 Results and discussion

The comparison between the two coupling methodologies is shown in Figure 7.2. Again, the surface elevation 1 m in front of the WEC and 1 m behind the WEC are compared, as well as the horizontal surge force and the WEC heave motion. Looking at plot (a), it can be noticed that the non-linear method is significantly better at calculating the surface elevation. The linear method cannot capture the elevated wave troughs present in non-linear waves. The wave crests are also underestimated. Behind the WEC, none of the models are capable of accurately predicting the free surface. This could be due to the shortened SPH domain with respect to the full experimental flume length. However, the non-linear method gives more acceptable results than the linear method. Looking at the horizontal surge force, the non-linear calculation almost perfectly matches the experimental data. Here, the linear result also shows a good correspondence, only slightly underestimating the total surge force. Finally, looking at the WEC heave motion, it is visible that the linear coupling overestimates the heave motion, while the non-linear coupling shows

accurate results. This is a typical result, where linear models overestimate the response of floating point absorber WECs near the resonance period, since these models do not take into account non-linear effects such as vorticity and viscosity.

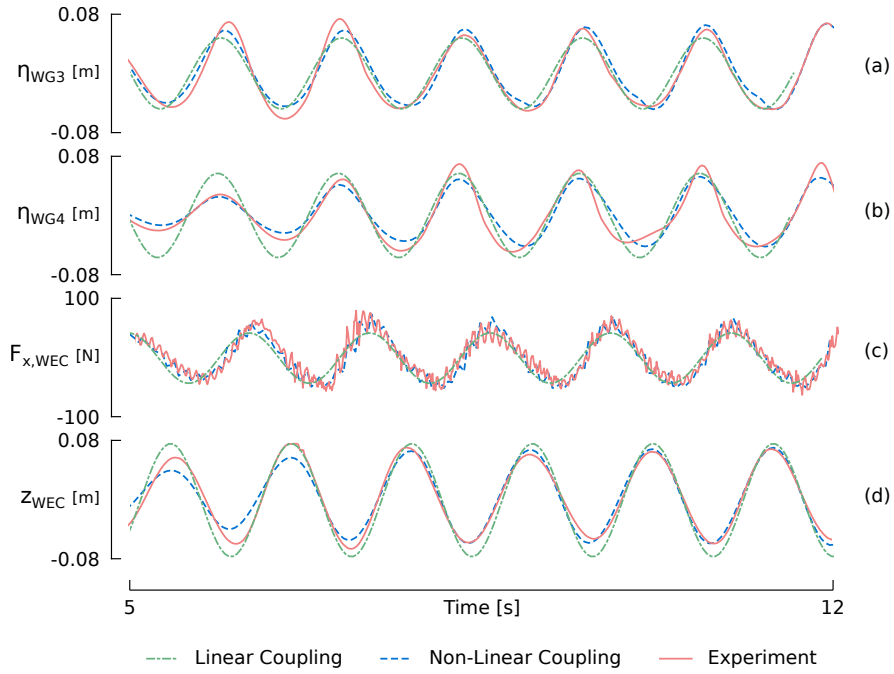

Figure 7.2: Comparison between the presented linear coupling methodology, non-linear coupling methodology and experimental data for non-linear waves interacting with a heaving cylindrical WEC. Plot (a) shows the surface elevation 1 m in front of the WEC, (b) the surface elevation 1 m behind the WEC, (c) the horizontal surge force acting on the WEC and (d) the heave motion of the WEC

It is possible to quantify the accuracy of the results by calculating RMSE values of both coupling methodologies with respect to experimental data. For the surface elevations and heave motion, the RMSE is normalized with the wave height. For the surge force, the RMSE is normalized with the hydrostatic force. The results are provided in Table 7.1. Here, it is clear that the non-linear coupling is capable of producing significantly more accurate results than the linear coupling. The RMSE values on surface elevation and heave motion stay below 10 %, while this is not the case for the linear coupling. For the non-linear coupling, these results are very satisfactory, since the absolute error remains well below the smoothing length h. The RMSE values for the horizontal force are higher, because they are normalized with the hydrostatic force, which is lower than the maximum values measured in the numerical and experimental results.

Table 7.1: RMSE values for comparison of linear coupling and non-linear coupling with the experimental test results.

RMSE	Linear Coupling	Non-Linear Coupling
η_{WG3}	14,8 %	7,9 %
η_{WG4}	15,8 %	9,8 %
$F_{x,WEC}$	40,8 %	23,3 %
z_{WEC}	10,5 %	7,7 %

Nevertheless, it is noted that the linear coupling methodology is capable of predicting surface elevations, surge forces and WEC motions with a reasonable accuracy. All the results are within the same order of magnitude as the experimental data. Logically, the linear coupled model was also not capable of simulating the wave overtopping over the WEC, while this was the case for the non-linear coupled model. However, since the linear coupling methodology is very computationally cheap, it is an excellent tool for preliminary design and preparatory tests for an accurate, non-linear model. Caution is needed when waves become strongly non-linear. Here, a Stokes 3^{rd} order wave was applied, which can be classified as rather weakly non-linear. The linear model will fall completely apart when very steep waves are modelled, or when waves are breaking on the device.

The largest benefit of the linear coupling methodology is the fast computation time. Table 7.2 illustrates the difference in computational effort between the non-linear coupling and the linear coupling. The linear coupling is more than 1000 times faster than the non-linear coupling, due to a combination of a significantly smaller number of cells, a larger simulation time step and easier equations to solve.

Table 7.2: Comparison of computational effort between linear coupling and non-linear coupling methodology for the 3-D proof-of-concept

	Linear Coupling	Non-Linear Coupling	Difference
# Particles/Cells	60 000	5 010 954	83
Memory [MB]	150	780	5,2
Runtime [hr]	0,09	91	1011

7.2 Distinctive features

It is important to provide an overview of what can be achieved by applying the developed coupling methodologies, that was not possible before. Tables 7.3 and 7.4 list the distinctive features of the linear OceanWave3D-Nemoh coupling (LC) and the non-linear OceanWave3D-DualSPHysics coupling (NLC), defining what their advantages and disadvantages with respect to more traditional methods are.

Table 7.3: Advantages of OceanWave3D-Nemoh (LC) and OceanWave3D-DualSPHysics (NLC) with respect to more traditional methods.

>	**BEM**	**Wave Propagation Solver**	**Stand-Alone SPH**	**CFD**
LC	Variable bathymetry far-field effects irregular waves	Radiated waves detailed WEC geometry multiple DOF	faster large domain	faster large domain
NLC	non-linear waves wave breaking wave overtopping vorticity	non-linear waves wave breaking wave overtopping vorticity	faster smaller domain	smaller domain implementation of floating devices meshless

Table 7.4: Disadvantages of OceanWave3D-Nemoh (LC) and OceanWave3D-DualSPHysics with respect to more traditional methods.

<	**BEM**	**Wave Propagation Solver**	**Stand-Alone SPH**	**CFD**
LC	slower	complex implementation	less accurate	less accurate
NLC	slower	slower complex implementation	complex implementation	no adaptivity slower on CPU no air phase

7.3 Decision models

In the following section, a number of decision models are presented, to provide guidance to the user of the coupling methodologies. Three flowcharts are created, based on the following starting options:

- The number of WECs
- The wave conditions
- Purpose of the study

The combination of all three flowcharts, leads to an advice to use the linear OceanWave3D-Nemoh coupling methodology (LC OW3D-Nemoh) or the non-linear OceanWave3D-DualSPHysics coupling methodology (NLC OW3D-DSPH). The reader should take into account these flowcharts need to be interpreted as guidelines, not as a protocol. It is of course allowed to for example use the non-linear coupling methodology to investigate energy production of a WEC, but it is advised to use the linear coupling since operational conditions mostly consist of mild sea conditions which can be accurately modeled with the linear coupling methodology.

7.3.1 Number of WECs

A first choice for applying a certain coupling methodology can be made, based on the number of WECs that need to be modelled (see Figure 7.3). When a complete WEC farm needs to be modeled, it is advised to use the linear coupling methodology. Typical GPU hardware is not yet capable of simulating very large domains with high accuracy. Only a dedicated multi-GPU set-up could deliver the necessary performance. Additionally, modelling complete WEC farms is mostly done to investigate the wave transformations in operational conditions, which makes the linear coupling methodology more suitable. The choice between coupling methodologies becomes less clear when modeling small WEC clusters, or single WEC devices. The latter can easily be modeled with the non-linear coupling methodology, but the user needs to make that decision based on the objective of the study, and the incident wave conditions. The choice for the case with small WEC clusters, also depends on the study objective and wave conditions, but equally important on the available processing power. A standard desktop GPU is not capable of modeling clusters of WECs with satisfying accuracy.

7.3.2 Wave Conditions

Another starting point to decide between the coupling methodologies is the incident wave conditions (see Figure 7.4). Firstly, a distinction can be made between regular and irregular waves. When irregular waves are studied, distinction is made between short-crested and long-crested waves. The current non-linear coupling methodology does not allow simulation of short-crested waves, thus only the linear coupling can be used here. However, when the incident waves are long-crested, both options

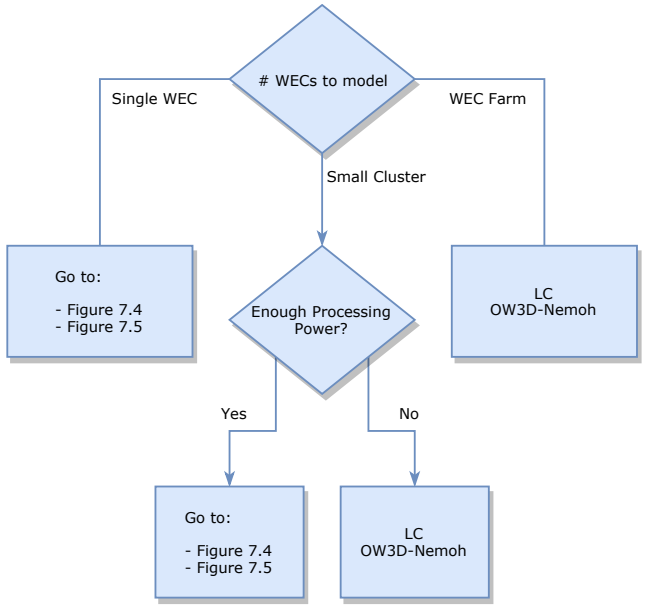

Figure 7.3: Decision model for selection of coupling methodology based on the number of WECs to be modelled simultaneously.

are still available and the decision is made based on the governing wave theory. Secondly, when the incident waves are regular, the advised coupling is also selected based on the wave theory. Only when the incident waves are non-linear, it is strongly advised to use the non-linear coupling. The linear coupling applies the superposition principle, which is only valid when the waves are linear. However, the linear coupling can produce meaningful results for weakly non-linear waves. For both linear and non-linear waves, it is thus advised to choose the coupling methodology based on the objective of the study.

7.3.3 Objective of Study

The objective of the study plays an important role in deciding which coupling methodology to use (see Figure 7.5). Firstly, it is advised to apply the linear coupling methodology for the following study objectives:

- Energy Production;
  When studying the energy production of a WEC farm or a single WEC, mostly operational conditions are simulated in which incident waves are linear, weakly non-linear or short-crested.

- Wake Effects;
  Studying wake effects of WEC farms require large simulation domains, and wave conditions are mostly moderate.

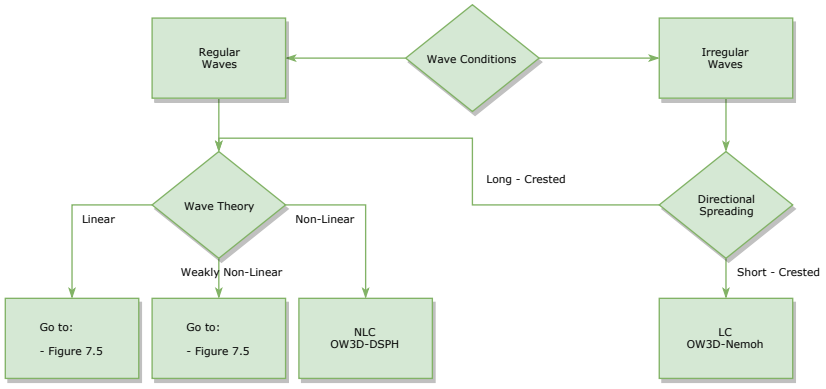

Figure 7.4: Decision model for selection of coupling methodology based on the wave conditions and the governing wave theory.

- Coastal Impact;
  In order to study the coastal impact of a WEC farm, it is necessary to simulate very large domains. Here, the added accuracy of a non-linear wave-structure interaction model would only have a limited effect on the wave condition far away from the WEC farm.

- Farm Optimization;
  When the layout of a WEC farm needs to be optimized, mostly operational conditions are modelled, making it unnecessary to use the computationally expensive non-linear coupling.

Secondly, applying the non-linear coupling methodology is more useful in the following cases:

- Survivability;
  Studying the survivability of a WEC devices or WEC farm requires modelling of strongly non-linear wave conditions, including wave impacts, overtopping and viscous effects. Accurate results can only be achieved with the non-linear coupling methodology.

- Complex mooring;
  Modelling freely floating devices with complex mooring can only be accurately done with the non-linear coupling methodology. Specifically, coupling with MoorDyn or Project Chrono can be applied to achieve maximum accuracy.

- PTO mechanics;
  The response of a floating WEC can significantly change when a PTO system is exerting forces on the body. In most cases, complex tuning strategies are used resulting in non-linear PTO forces and a complex motion response. This behaviour can only be captured with a non-linear model, specifically coupled to Project Chrono to include the PTO physics.

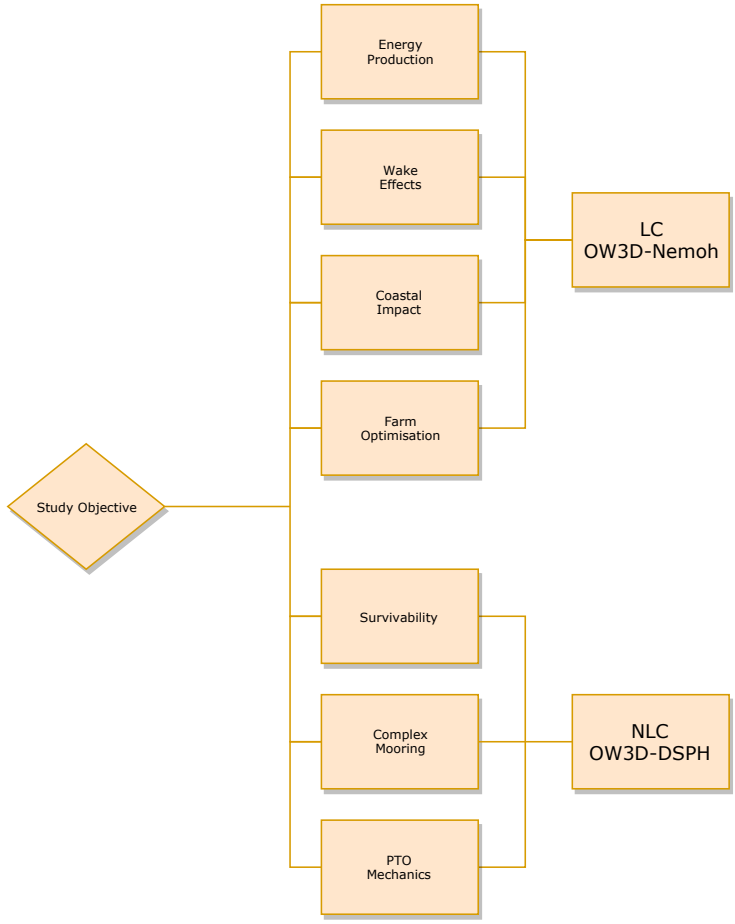

Figure 7.5: Decision model for selection of coupling methodology based on the purpose of the study.

7.4 Case Examples

7.4.1 Case 1: Energy production of a WEC farm

An engineering company is hired to perform a study on the economic viability of installing a WEC farm in front of the northern coast of Spain (see Figure 7.6). This implies that the average annual energy production of the complete WEC farm, consisting of several clusters of WEC arrays, should be calculated. A relatively simple 1-D WEC model could be used to estimate the energy production of a single WEC device. However, the company realises that simply multiplying the energy production of a single WEC with the total number of devices in the farm, could lead to a significant overestimation of the total energy yield. Consequently, the company decides to try to include near-field and far-field effects in their numerical study. Since the northern coastline of Spain is characterised by steep gradients, it is important to take into account the local bathymetry into the numerical model. Assuming the engineer assigned for this task, has a copy of this manuscript on his/her desk, he/she can use the decision models to decide on a numerical modelling method for this specific problem. Starting from Figure 7.3, the flowchart immediately leads to the advise of using the linear coupling methodology. When consulting the decision model in Figure 7.4, the advise depends on the selected wave conditions. Considering the annual energy production needs to be estimated, irregular waves should be modelled, and preferably short-crested waves. Again, the flowchart advises to use the linear coupling methodology. Finally, consulting Figure 7.5, the flowchart points in the direction of the linear coupling as well.

The company can now apply the OceanWave3D-Nemoh coupling, or apply the coupling methodology to the software packages of their choice. The annual wave conditions are divided into a set of wave bins, representing the total wave climate. Each bin contains an irregular sea state, characterised by a directional wave spectrum, which needs to be discretised in a number of wave frequencies and a number of wave directions. Assuming 20 frequencies and 20 direction are selected, each sea state requires 400 simulation runs of the linear coupling to model the wave transformations in and around the WEC farm. Assuming similar CPU performance

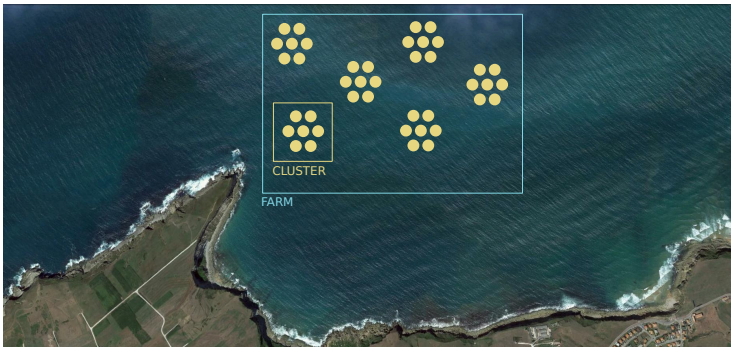

Figure 7.6: Concept sketch of WEC farm concept for Case 1

as in this research (see Table 7.2), a complete sea state could be modelled in around 40 hours. This needs to be repeated for every wave bin to achieve an estimate for the total annual energy production. Logically, the computation time can be significantly lowered when a multi-core high-performance computing system is available.

7.4.2 Case 2: Survivability of a floating WEC

A start-up WEC developer has engineered a novel WEC concept, with promising energy yield at a competitive price. Before starting the construction of a full scale prototype, the company wants to know how their design will respond in storm conditions, and what impact forces they can expect (see Figure 7.7). Although the company has several powerful desktop computers, they do not have access to a supercomputer with a large number of CPUs. It is thus necessary to make the numerical model as efficient as possible, which can be achieved by applying a coupled model.

Figure 7.7: Artist impression of WEC concept for Case 2

First consulting the decision model in Figure 7.3, it is advised to decide which program to use based on the wave conditions and the purpose of the study. The flowchart of Figure 7.4 directs us towards a non-linear wave theory, and thus the non-linear OceanWave3D-DualSPHysics coupling is advised. A quick look at Figure 7.5 indicates that survivability studies are best performed with the non-linear coupling.

The OceanWave3D-DualSPHysics coupling can be applied. OceanWave3D is used to model the local wave climate: regular or irregular storm waves. A 3D SPH domain is set up around the floating WEC, with open boundaries in front and behind the device. At the interface, the orbital velocities and surface elevations from OceanWave3D are imposed onto the buffer particles. The storm wave is replicated in the SPH domain and impacts the floating WEC. Post-processing the results provides the company with accurate estimates for the response of the WEC, the impact force on the device as well as an indication of overtopping and possible

spray. A wave train of 10 waves can be modelled on a desktop PC equipped with a GPU card in 1-4 days, based on the model of the GPU. This methodology is the most time-efficient, since modelling with stand-alone SPH would lead to a computation time at least 4 times as long. Alternatively, opting for a more traditional mesh-based CFD model like openFOAM would be another possibility. However, implementing a full 6DOF motion solver comes less naturally than in SPH, since sliding meshes or over-set mesh interpolation would be necessary.

7.5 Scaling to prototype conditions

The validation cases performed in this research were all conducted at laboratory scale. It is important to mention that scaling up the SPH simulations to a prototype scale can lead to a different accuracy, since not all numerical parameters can be scaled up according to Froude's similarity law. Specifically, artificial viscosity and diffusion schemes cannot be scaled up accordingly and thus scaling effects depend on the model resolution. Additionally, GPU calculations start to suffer from precision problems when very large domains are simulated. Calculations need be performed with double precision in order to avoid loss of accuracy.

In order to check the scalability of wave propagation with open boundaries, a comparison is performed between the surface elevation results of a laboratory-scale wave and a full-scale wave. Both wave conditions are defined in Table 7.5 and obey Froude's similarity law with a scale factor of 5.

Table 7.5: Wave conditions for a full-scale and a laboratory-scale wave to study scale effects on surface elevation.

Scale	$H\ [m]$	$T\ [s]$	$d\ [m]$	$d_p\ [m]$
Full	1	8	5	0.1
Laboratory	0.2	3.59	1	0.02

The comparison of the surface elevation between the two waves is illustrated in Figure 7.8. The first graph shows a comparison of the surface elevation of the laboratory-scale wave with a second-order Stokes solution. Accuracy is good with an RMSE error of $0.16h$ and a maximum error of $0.39h$. The second graph shows the comparison of the surface elevation of the full-scale wave with a second-order Stokes solution. Again, good accuracy is obtained with an RMSE error of $0.18h$ and a maximum error of $0.37h$. In comparison to theoretical solutions, both waves thus offer a very comparable accuracy of the surface elevation. In the third graph, the laboratory-scale wave is scaled up using Froude's similarity law and the surface elevation is directly compared to the full-scale wave. The surface elevation is reproduced accurately with an RMSE error of $0.09h$ and a maximum error of $0.54h$. Looking closely at the full-scale solution, it is clear that there are some irregularities in the free surface in the wave trough. This can be explained by the numerical diffusion and viscosity not scaling up properly. This can be investigated in more detail by looking at pressure profiles for both waves.

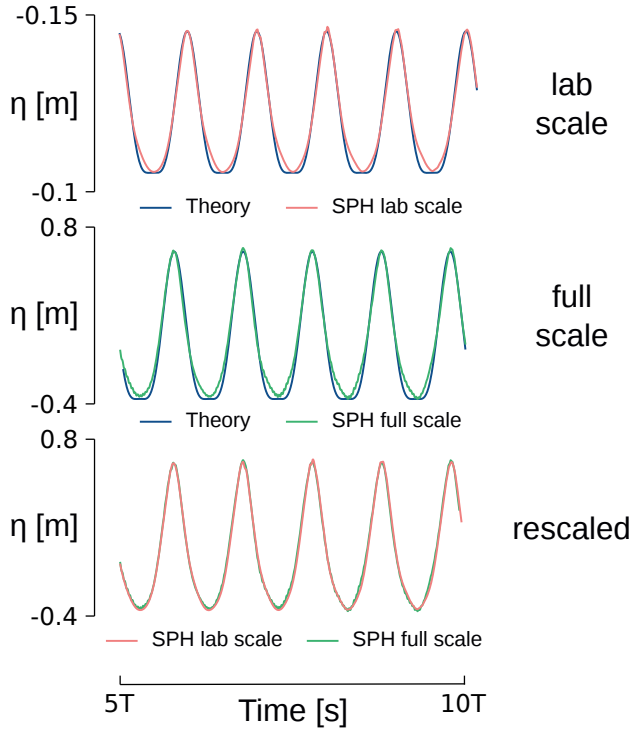

Figure 7.8: Comparison of surface elevation between laboratory-scale wave and full-scale wave. The first graph compares the laboratory-scale wave to a theoretical solution, the second graph compares the full-scale wave to a theoretical solution and the third graph compares an upscaled version of the laboratory-scale wave to the full-scale wave.

Although the surface elevation scales up according to Froud's similarity law, the pressure profiles need to be investigated to identify scaling effects due to incorrect scaling of numerical diffusion and artificial viscosity. For this reason, the full-scale pressure profile is compared to a scaled up pressure profile of the laboratory-scale wave in Figure 7.9. On the left graph, the upscaled pressure field of the laboratory-scale wave is given. A smooth pressure field is shown, with a maximum pressure at the sea bottom, under the wave crest, of around 52.8 kPa. This pressure has an error of 1.9 kPa with respect to the theoretical Stokes solution of 54.7 kPa. On the right side, the pressure field of the full-scale wave is provided. Here, it is noticed that the maximum pressure exceeds the theoretical solution with 10.5 kPa, resulting in a total maximum pressure of 66.2 kPa. The pressure field of the full-scale is thus less accurate than the laboratory-scale wave. This is an important result, which indicates the need to tune the numerical diffusion and artificial viscosity when performing full-scale simulations rather than laboratory-scale simulations.

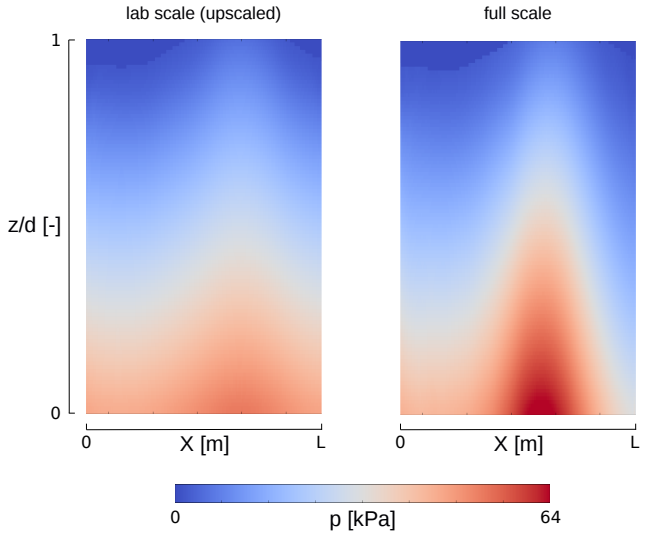

Figure 7.9: Comparison of pressure between upscaled laboratory-scale wave and full-scale wave. The first graph shows the upscaled laboratory-scale wave pressure, while the second graph shows the full-scale wave pressure. Both pressure fields are calculated after a simulation time of 5 times the wave period and are plotted over the full domain length, which is 1 wavelength long.

Chapter 8

Conclusions and Further Work

8.1 Summary of the key findings

In this work, coupling methodologies have been introduced to model floating WECs and WEC arrays. The first part of the manuscript focused on the development of a linear coupling methodology, resulting in a tool capable of modelling near-field and far-field effects around WEC arrays, over a variable bathymetry. The second part focused on non-linear wave structure interactions, where two coupling methodologies were introduced: one which applied moving boundaries at the interface and one which applied open boundaries at the interface.

A linear coupling methodology between the wave-structure interaction solver Nemoh and the wave propagation model OceanWave3D was introduced. Nemoh is a BEM solver, able to calculated the diffracted and radiated wavefield in a local zone around a floating WEC device, where the bathymetry is constant. By imposing the perturbed wavefield (radiated + diffracted) on a circular zone inside a large OceanWave3D domain, it can propagate further away from the WEC, over a variable bathymetry. Since linear theory is applicable, the superposition principle is valid. Like this, the incident wavefield, calculated over the variable bathymetry in OceanWave3D, can be superposed on top of the perturbed wavefield, resulting in the total wavefield, reproducing both the near-field and far-field effects. The coupling methodology has been validated by comparing results of a number of tests with several WEC array layouts and different bathymetries to results from another numerical model as well as by comparing results to the experimental WECwakes dataset.

The linear coupling between Nemoh and OceanWave3D (OW3D) logically only allows linear wave modelling. This is acceptable when studying WEC devices or WEC arrays in their operational conditions, in mild sea states. However, WEC devices and arrays often have to endure severe wave conditions. It is important to be able to accurately model the response of WECs in heavy sea states to study their

survivability. For that reason, a new coupling methodology was developed, focusing on non-linear wave-structure interactions. Here, the SPH solver DualSPHysics (DSPH) was coupled to the wave propagation model OW3D. OW3D was used to model wave propagation over a large domain, in which a small DSPH domain is nested. At the model interfaces, horizontal orbital velocities from OW3D are transferred to a set of moving boundary particles in DSPH, reproducing the exact same wave. Within the nested SPH domain, accurate and complex non-linear wave-structure interactions can be modelled. The effect of these interactions on the free surface can be further propagated in the OW3D domain due to the 2-way coupling where surface elevations from DSPH are sent back to OW3D. The online information transfer between both models was realised with the MPI protocol, to which an additional python process was connected to control the data flow. The model proved to provide accurate results after validation with theoretical solutions and experimental data. However, the moving boundary particles had the tendency to drift away in time, and significant pressure peaks were noticed, originating near the moving boundary particles.

In order to mitigate the disadvantages of applying moving boundaries in the coupling methodology between OW3D and DSPH, a second version of the non-linear coupling methodology was developed applying the newly-developed open boundaries. First, the open boundaries were applied to accurately model wave generation, propagation and absorption in DSPH. This as an alternative to typical wave paddle generation or source generation. Open boundaries proved to generate and absorb waves with very high accuracy, when imposing horizontal orbital velocities at inlet and outlet, albeit with a correction applied, based on the shallow water theory. Additionally, the SPH domain could be reduced to as short as one wave length long, where traditional wave propagation simulations in DSPH required a domain of three to four wave lengths long. The new wave generation and absorption technique was validated with theoretical solutions and experimental data. Subsequently, it was introduced into the coupling methodology, replacing the moving boundary formulation, solving the drift problem and smoothing out the pressure peaks. The coupling implementation was extended, allowing 2-way communication through socket programming instead of using the MPI protocol, creating an interface to connect any external model to DSPH. This revised coupling methodology was validated in 2-D with experimental data and a 3-D proof-of-concept was shown, simulating steep overtopping waves over a heaving cylindrical WEC.

8.2 Recommendations for future research

The developed coupling methodologies have extended the possibilities for WEC and WEC array modelling, and have significantly reduced the necessary computational effort to perform accurate wave-structure interaction simulations. However, the methodologies certainly contain much more potential, which can be unlocked in future research.

The development of the linear coupling methodology is still ongoing, as shown by Verao Fernandez et al. (2017) and Balitsky et al. (2017a). The methodology

has been applied to model large WEC farms in variable bathymetry, subjected to short-crested irregular waves consisting of more than 20 frequency components. Additionally, it has been applied to model several WEC arrays, located near each other, to study the effect of one WEC array on the other (Balitsky et al., 2017b). However, there is still growing potential in the methodology, as described in these recommendations:

1. Direct simulation of irregular waves;
   Currently, simulation of short-crested irregular waves is done by superposing several regular waves, each with a certain wave direction and wave frequency. To obtain an accurate result, this means a lot of separate simulations are needed, consuming a lot of computation time. Allowing to model the total wave field of short-crested waves with a WEC array in one coupling iteration, would lead to a significant performance gain.

2. Variable bathymetry within the WEC array;
   Currently, the bathymetry within the WEC array needs to be constant to get an accurate perturbed wavefield. However, in practice, there is the possibility of having different water depths within one WEC array.

3. Coupling radius around individual WECs;
   Instead of coupling the perturbed wave field of a full WEC array, modelled in Nemoh, it could be valuable to consider individual coupling zones around each WEC. This could specifically prove to be necessary in solving the previous recommendation.

4. Simulating multiple degrees of freedom of floating WECs;
   Up to now, only floating WECs with one degree of freedom (DOF) have been modelled, for example heaving point absorbers or pitching flap-type WECs. Since Nemoh allows full 6DOF modelling, this could be easily implemented into the coupling methodology.

The non-linear coupling methodology can be improved and extended as well, based on the following recommendations::

1. Extended research in 3-D coupling methodology;
   In this manuscript, only a 3-D proof-of-concept was provided instead of a full validation. This is mainly because the open boundary formulation was not ready yet to be included in the full release of DualSPHysics. There are still some issues with applying open boundaries in 3-D, in combination with pressure extrapolation at the boundaries and/or periodic boundaries. Although this will be fixed in the near future, it will not be ready before the submission of this manuscript.

2. Investigate coupling of other wave propagation models;
   In this work, OceanWave3D was used as an external wave propagation model. This mainly because the accurate propagation of non-linear waves and the vertical sigma-layers. In the future, other wave propagation models (for example SWASH as in Altomare et al. (2016a)) could be coupled to DualSPHysics using the open boundaries.

3. Detailed analysis of communication costs;
   When two separate codes are coupled, and data has to be transferred from one to another, there is a certain computational effort necessary to perform these communication steps. In this work, this was only treated in a basic manner considering all extra necessary commands as overhead. A more detailed profiling needs to be performed, applied for several particle resolutions, in order to obtain a sufficient insight into the additionally required computational effort when coupling is applied.

4. Implement wave-current interactions;
   The open boundaries could be ideal to study wave-current interactions, since there are no drift issues. This is something that could be easily implemented, since a steady current can be imposed on top of the oscillating horizontal orbital velocities.

5. Coupling interface after wave breaking;
   Since OceanWave3D does not accurately model wave breaking, the coupling interface was always located before the breaking location. However, it is worth investigating if the open boundaries are capable of accepting velocity information from a broken wave, for example modelled in SWASH, and accurately propagating this broken wave towards a coastal structure. This would result in huge computational performance gains.

6. Circular open boundaries;
   Once the open boundaries are fully validated in 3-D, it is worthwhile to investigate the possibility of a circular inlet/outlet zone, where quantities are imposed along the normal to the curvature of the buffer zone. This could simplify the generation/absorption of short-crested non-linear waves and ultimately lead to a coupling methodology where several nested DualSPHysics zones containing WEC devices are positioned inside a large wave propagation domain, as originally suggested in Section 5.3.

7. Coupling with project Chrono;
   In an upcoming release of DualSPHysics, coupling with the Chrono physics engine will be supported (Canelas et al., 2018). This will allow the modelling of physical joints within WEC devices and modelling of their PTO system as well. Inclusion of these extra physics would result in a fully non-linear simulation tool for complete WEC devices, including the effect of a non-linear PTO system on the WEC's response.

Appendix A

OpenWEC: a free, easy-to-use wave energy converter simulation tool.

A.1 Introduction

The success of a renewable energy resource depends strongly on the final electricity cost for the end user. For this reason, it is important to be able to make quick assessments of the energy production of renewable energy devices, without performing a detailed design and accurate numerical modelling study. That is why openWEC was created, specifically aimed at floating wave energy converters. It is an open-source tool to simulate the hydrodynamic behaviour and predict the energy production from single body wave energy converters (WECs), and visualize diffracted and radiated wave fields for WEC arrays. It is an ideal tool for WEC start-ups who want to quickly predict the energy production of a certain device at a certain location, and can be used in academic institutes for teaching or preparatory work for more detailed simulations. It is based on the linear wave theory and

assumes potential flow. Three software packages are coupled:

- Frequency domain solver Nemoh (Babarit and Delhommeau, 2015), developed by Ecole Centrale de Nantes
- Time domain solver, developed by the author of this manuscript
- MoorDyn (Hall and Goupee, 2015), an open-source dynamic mooring line model, developed by Matt Hall

Additional to these 2 solvers, a preprocessing meshing tool and a post-processing visualisation tool are part of the package.

A.2 Installation

There are two ways to run openWEC on your computer. You can choose to run the python source code directly, or install a compiled Windows/Linux/MacOS executable. Both the source code and executables are accessible through the projects webpage and github page: `https://github.com/tverbrug/openWEC` and `http://users.ugent.be/~tverbrug/` In order to run the source code directly, the following prerequisites are needed:

- Python 2.7
- Numpy
- Scipy
- Matplotlib
- PyQt bindings for QT 4
- (py)VTK (only when importing .stl meshes)

If the users prefers to run the source code directly, it is advised to install complete python packages such as Anaconda, Enthought Canopy or pythonxy. When you choose to install the pre-compiled executable for Windows, download the setup_openWEC.exe file and follow the installation instructions. Make sure your firewall allows the program to be executed. Note that it is necessary to have administrator privileges over the computer u are using.

A.3 Getting Started

When running the program, you can select the type of WEC simulator you want to use. There are three typical WEC types available, with limited but easy-to-understand functionality, ideal for learning to use the program or for teaching purposes:

- Point-Absorber Simulator: a heaving hemispherical buoy floating in the water.

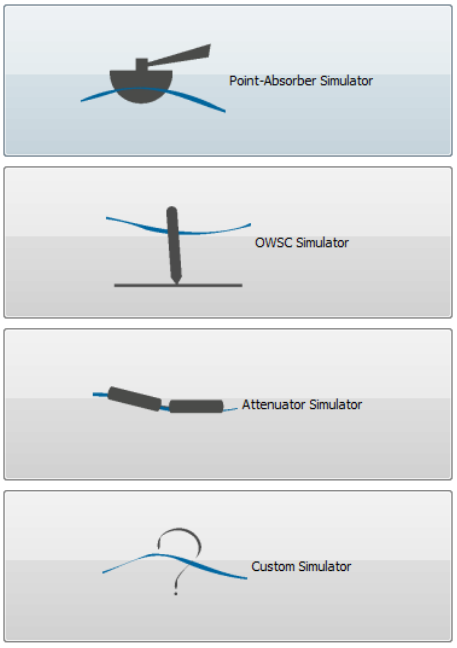

Figure A.1: OpenWEC Start Screen

- OWSC Simulator: a pitching flap-type device, anchored to the sea bottom
- Attenuator Simulator: a pitching floating snake-type device, consisting of two rigid body elements

Additionally, a custom simulator is provided, in which all functionality is available and a custom floater mesh can be created or imported.

A.4 Pre-Processing

A.4.1 Mesh Tool

First, a mesh needs to be created. This is done with the Mesh Tool. In the first 3 simulators, you only need to fill in the dimensions of the device, the water depth, the density and the approximate number of meshing panels you want the mesh tool to create. In the Custom Simulator, the options are far more diverse, with 4 mesh creation options:

1. **Generate a new mesh**, based on pre-described shapes: for example a floating buoy with a conical or spherical bottom, and a cylindrical top.
2. **Import a Nemoh mesh** from a previous simulation.

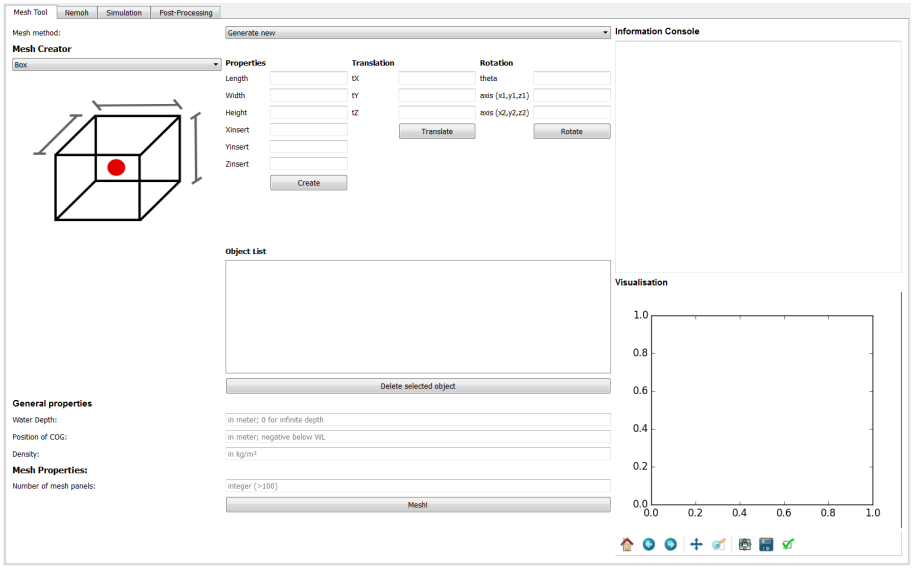

Figure A.2: OpenWEC Mesh Tool

3. **Import an .stl mesh** you have created with other software for example MeshLab.

Depending on what option you have selected, you must fill in some of the parameters below the WEC shapes. If you have selected anything else than 'Generate new', the information console will display what options need to be filled. When selecting 'Generate new', you can create a new Mesh with the Mesh Tool. You can add the following basic shapes to the mesh project:

- Box
- Cylinder
- Cone
- Sphere
- Pyramid
- Wedge
- Hemisphere
- Hemicylinder
- Torus

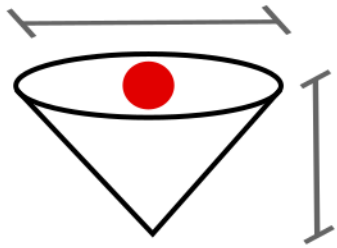

Figure A.3: Cone shape in OpenWEC Mesh Tool

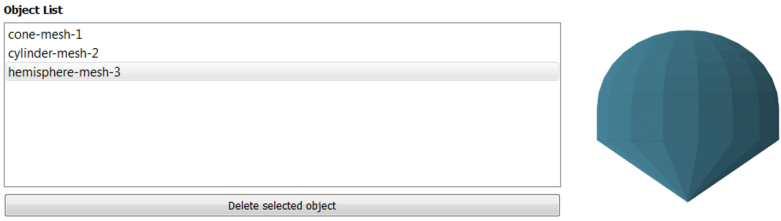

Figure A.4: Object list in OpenWEC Mesh Tool

The GUI will show the geometry of the selected object, together with a red dot explaining what the point of insertion will be. For example for the cone, the insertion point is at the center of the base circle, and the cone tip is pointed downwards.

Several mesh elements can be added to the project, and will be added to the Object List. All elements in the list are subject to the following manipulations:

- Translation
- Rotation
- Delete

When the complete mesh object is assembled. The general properties should be filled in:

- **Water Depth**: positive values for a finite depth, negative or zero for infinite depth
- **Position of COG**: relative to the water surface, important for rotational movements
- **Water Density**: salt/fresh/... water
- **Number of mesh panels**: refinement of the mesh

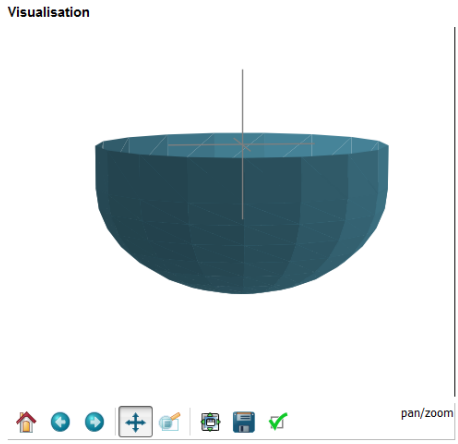

Figure A.5: Meshed hemisphere in OpenWEC Mesh Tool

Once every required option is filled, the refined mesh is created by pressing the 'Mesh!' button. In the shell window you will see the code is running. Once finished, the created mesh is displayed in the plotting window. When creating a mesh from a .stl file, make sure you visually check the mesh for inconsistencies. The .stl mesh must be correctly created to result in a good Nemoh mesh!

If the meshing tool crashes or returns an error, please go through this checklist:

- Are your mesh units in meters?
- Have you correctly meshed the underwater part of the device: Z-coordinates must be below zero!
- Are all panel normals pointing outwards?
- In case of importing an .stl file, is should be ASCII formatted, not binary.

The result files of the mesh are found in the './Calculation/mesh' folder in the main program directory.

A.4.2 Loading previous configurations

openWEC is able to save your set-up and parameters, to be reloaded at a later time. It is as simple as clicking file-save to save your configuration and file-open to reload a configuration.

A.5 Frequency-domain modelling with Nemoh

The frequency domain modelling is performed with the Nemoh BEM Solver. It is based on the linear wave theory and thus assumes potential flow. For each panel of a mesh, the hydrodynamic parameters are calculated for a certain frequency range.

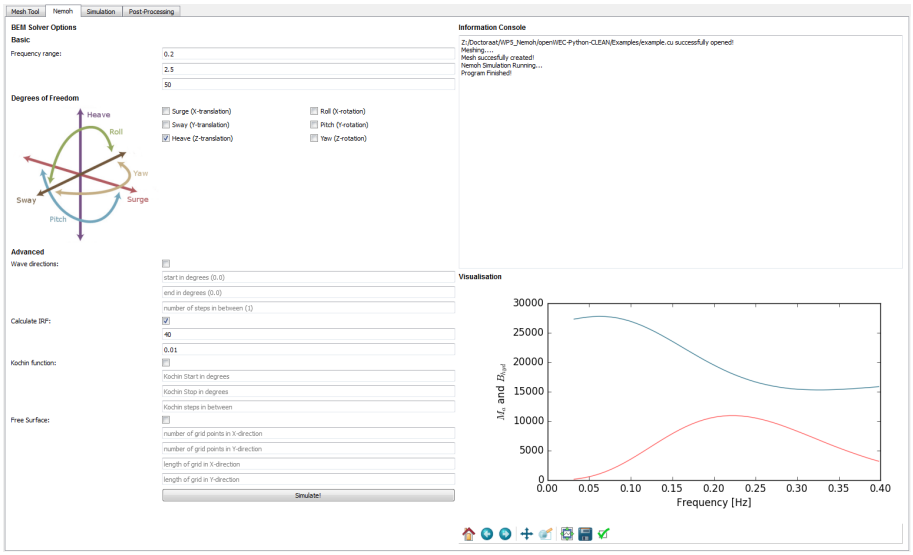

Figure A.6: OpenWEC Nemoh frequency-domain modelling

A.5.1 Nemoh

Next, the BEM solver can be run to calculate the hydrodynamic parameters. The solver can be run with only the basic options, or you can choose to include several advanced options. Within the basic options you are required to give a frequency range for the calculations by entering three values:

- The starting frequency in rad/s (for example 0.2 rad/s)
- The ending frequency in rad/s (for example 2.5 rad/s)
- The number of frequency steps (preferably ¿50)

The degrees of freedom can be selected. All combinations are possible.

The advanced functions can be enabled or disabled with the different check boxes:

- Wave directions: only applicable for non-axisymmetric shapes, otherwise you will get the same results for every wave direction.
- Calculate IRF: When selected, the impulse response function is calculated. This option is needed if you want to use irregular waves in the time-domain.
- Kochin function: calculates the kochin function for each solved problem
- Free Surface: calculates the free surface elevation around the WEC for all solved problems, for a given grid.

The calculation will start when pressing the 'Simulate!' button. In the shell window you can follow the calculations. Once finished the Added Mass and Hydrodynamic damping will be plotted in the visualisation window.

A.6 Time-domain modelling

Once the frequency domain modelling is finished, the time-domain solver can be used. Here the WEC heaving response and energy absorption is calculated for regular or irregular waves.

A.6.1 Simulation

The time-domain solver can be accessed through the tab 'Simulation'. Options are split up into three sections: wave climate, PTO properties and Simulation. All option boxes need to be filled in to be able to simulate.

- Wave Type: select between irregular or regular waves. When irregular waves are chosen, you have the option to apply a custom wave spectrum.
- Wave Height: enter the wave height in meters
- Wave Period: enter the wave period in seconds
- Damping type: set the damping type, choosing between two options:
  - Linear: set fixed PTO parameters resulting in forces proportional to the device's acceleration (Mpto), velocity (Bpto), or position (Cpto)
  - Coulomb: set a fixed PTO forces which is fully applied when the device has a positive velocity
- Mooring: you have the option to couple the time domain solver with the mooring line simulation package MoorDyn. The configure button needs to be pushed to edit the mooring line parameters.
- Time: simulation duration
- Time Step: time step for each iteration

A.7 Post-Processing

The final tab allows the user to postprocess the results. In the plotting tool, you have two visualisation windows at your disposal. For each plot you can select a variable to plot on the x-axis and one on the y-axis. The options for the Y-axis variable will automatically change according to the selected x-axis variable. Both frequency-domain parameters and time-domain parameters can be plotted. When radiation/diffraction calculations have been made, it is also possible to plot the radiation and diffraction surface elevations. The quantities are plotted in interactive plot windows, where the user can zoom in, select a region to plot, and save the figure in several common formats (for example png, jpeg, svg, pdf).

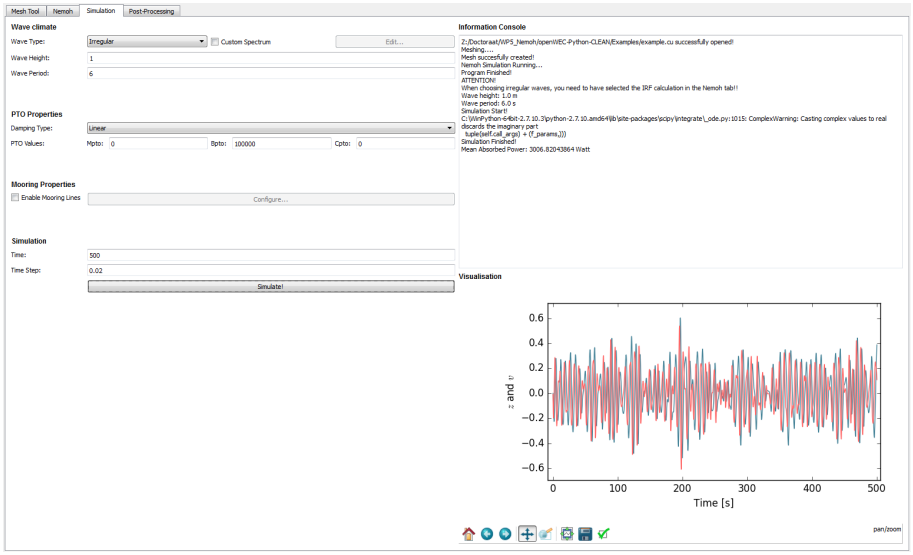

Figure A.7: OpenWEC time-domain modelling

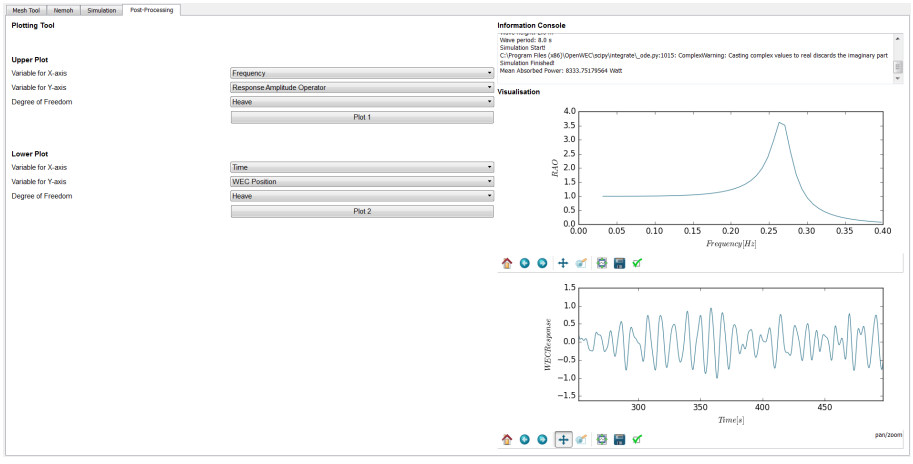

Figure A.8: OpenWEC post-processing module

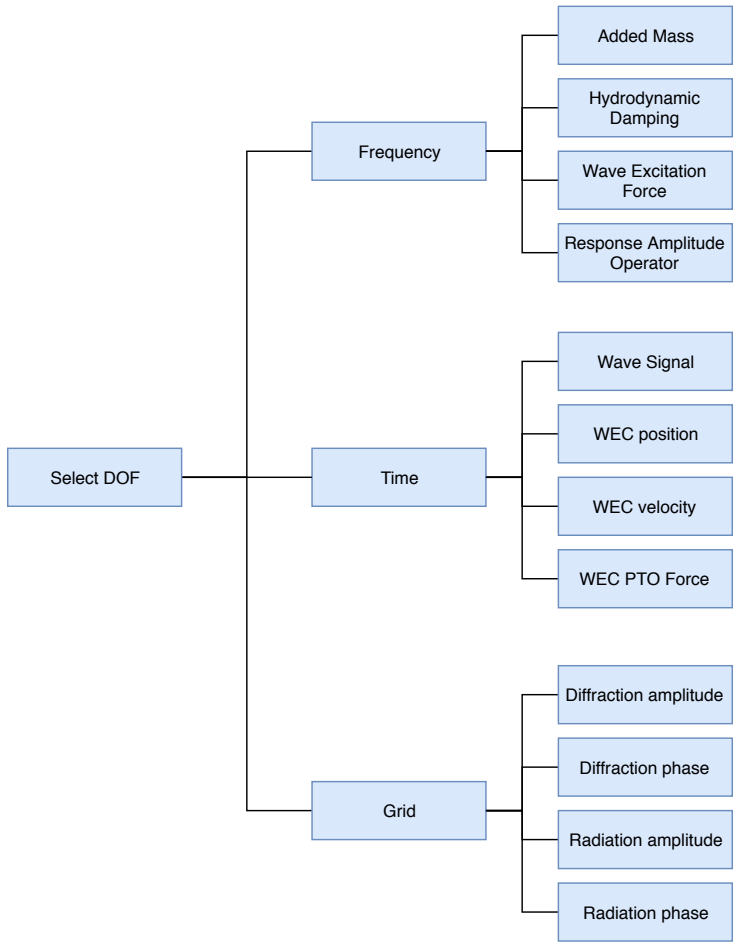

Figure A.9: OpenWEC post-processing options

Appendix B

Stokes Fifth-Order Wave Theory

For regular waves, the imposed quantities are calculated with the 5^{th} order solution to the Stokes Theory, given by Fenton (1985):

$$k\eta(x,t) = \sum_{i=1}^{5} \epsilon^i \sum_{j=1}^{i} B_{ij} \cos[jk(x - ct + \frac{\theta}{k})] \tag{B.1}$$

$$\epsilon = ka \tag{B.2}$$

$$c = \bar{U}_c + \bar{U} \tag{B.3}$$

$$\bar{U}\sqrt{\frac{k}{g}} = C_0 + \epsilon^2 C_2 + \epsilon^4 C_4 \tag{B.4}$$

$$v_x(x,z,t) = \bar{U}_c + C_0\sqrt{\frac{g}{k^3}} \sum_{i=1}^{5} \epsilon^i \sum_{j=1}^{i} A_{ij} \cosh(jkz) jk \cos[jk(x - ct + \frac{\theta}{k})] \tag{B.5}$$

Here, η is the surface elevation, k is the wave number (defined as $k = 2\pi/L$, with L the wavelength), a is the wave amplitude, g is the earth acceleration, c is the wave velocity, $\bar{U}_c$ is the mean current velocity, $\bar{U}$ is the mean horizontal velocity, θ is the phase constant. The wave period T can be calculated based on the wave number k and the wave celerity c, $T = 2\pi/(kc)$. The constants A_{ij} B_{ij} and C_i are theory-specific and are given below. The z-axis has its origin at the sea bed.

$$
\begin{aligned}
S &= \frac{\cosh 2kD}{\sinh 2kD} \\
A_{11} &= 1/\sinh(kD) \\
A_{22} &= 3S^2/[2(1-S)^2] \\
A_{31} &= (-4-20S+10S^2-13S^3)/[8\sinh(kD)(1-S)^3] \\
A_{33} &= (-2S^2+11S^3)/[8\sinh(kD)(1-S)^3] \\
A_{42} &= (12S-14S^2-264S^3-45S^4-13S^5)/[24(1-S)^5] \\
A_{44} &= (10S^3-174S^4+291S^5+278S^6)/[48(3+2S)(1-S)^5] \\
A_{51} &= (-1184+32S+13232S^2+21712S^3+20940S^4+12554S^5 \\
&\quad -500S^6-3341S^7-670S^8) \\
&\quad /[64\sinh(kD)(3+2S)(4+S)(1-S)^6] \\
A_{53} &= (4S+105S^2+198S^3-1376S^4-1302S^5-117S^6+58S^7) \\
&\quad /[32\sinh(kD)(3+2S)(1-S)^6] \\
A_{55} &= (-6S^3+272S^4-1552S^5+852S^6+2029S^7+430S^8) \\
&\quad /[64\sinh(kD)(3+2S)(4+S)(1-S)^6] \\
B_{11} &= 1 \\
B_{22} &= \coth(kD)(1+2S)/[2(1-S)] \\
B_{31} &= -3(1+3S+3S^2+2S^3)/[8(1-S)^3] \\
B_{33} &= -B_{31} \\
B_{42} &= \coth(kD)\left(6-26S-182S^2-204S^3-25S^4+26S^5\right) \\
&\quad /[6(3+2S)(1-S)^4] \\
B_{44} &= \coth(kD)\left(24+92S+122S^2+66S^3+67S^4+34S^5\right) \\
&\quad /[24(3+2S)(1-S)^4] \\
B_{51} &= -(B_{53}+B_{55}) \\
B_{53} &= 9(132+17S-2216S^2-5897S^3-6292S^4-2687S^5 \\
&\quad +194S^6+467S^7+82S^8) \\
&\quad /[128(3+2S)(4+S)(1-S)^6] \\
B_{55} &= 5(300+1579S+3176S^2+2949S^3+1188S^4+675S^5 \\
&\quad +1326S^6+827S^7+130S^8) \\
&\quad /[384(3+2S)(4+S)(1-S)^6] \\
C_0 &= \sqrt{\tanh(kD)} \\
C_2 &= C_0(2+7S^2)/[4(1-S)^2] \\
C_4 &= C_0(4+32S-116S^2-400S^3-71S^4+146S^5)/[32(1-S)^5]
\end{aligned}
$$

Appendix C

Comparison between OceanWave3D-Nemoh and MILDwave-Nemoh

C.1 Test Matrix

Table C.1: Test program for the comparison of the linear coupling methodology. (H = Wave Height, T = Wave Period, d = Water Depth, L_{W-W} = WEC-WEC distance)

Test Number #	Wave Type	H (m)	T (s)	d (m)	Layout	L_{W-W} (m)
1	REG	0.5	8	50		-
2	REG	0.5	8	25		-
3	REG	0.5	8	25		3D
4	REG	0.5	8	25		3D
5	REG	0.5	8	25		3D
6	REG	0.5	8	25		3D
7	REG	0.5	8	Beach_1		3D
8	REG	0.5	8	Beach_2		3D
9	REG	0.5	8	Sea Bottom		3D
10	IRR	0.5	8	Sea Bottom		3D

C.2 Test 1

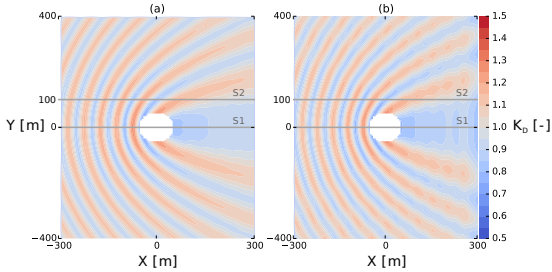

Figure C.1: Contour plots of K_D results for the coupled models: (**a**) MILDwave-Nemoh and (**b**) OceanWave3D-Nemoh.

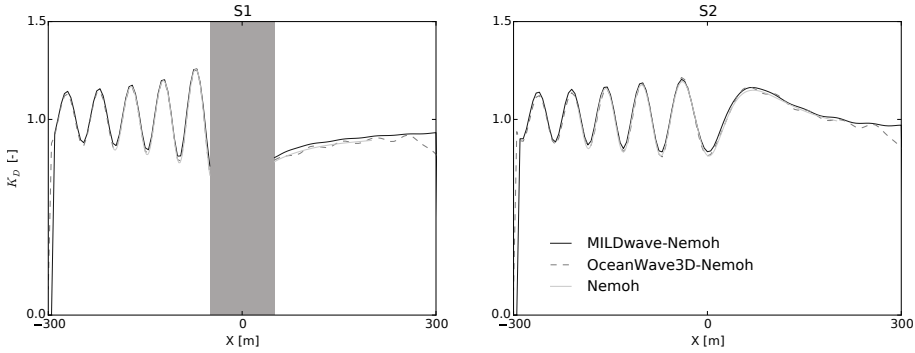

Figure C.2: K_D results along the two longitudinal sections indicated in Figure C.1 (Section 1 (S1): left; S2: right) for MILDwave-Nemoh, OceanWave3D-Nemoh and Nemoh.

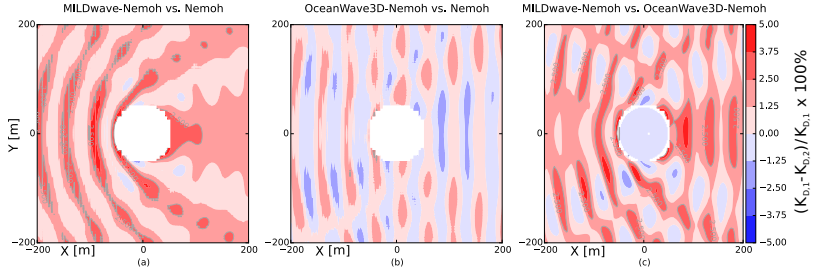

Figure C.3: Contour plots of relative K_D errors comparing: (**a**) MILDwave-Nemoh and Nemoh; (**b**) OceanWave3D-Nemoh and Nemoh; (**c**) MILDwave-Nemoh and OceanWave3D-Nemoh.

C.3 Test 2

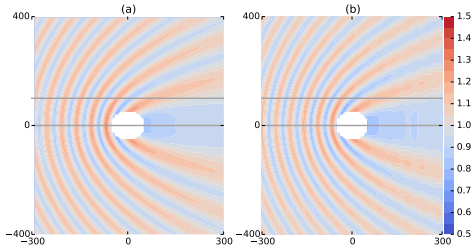

Figure C.4: Contour plots of K_D results for the coupled models: (**a**) MILDwave-Nemoh and (**b**) OceanWave3D-Nemoh.

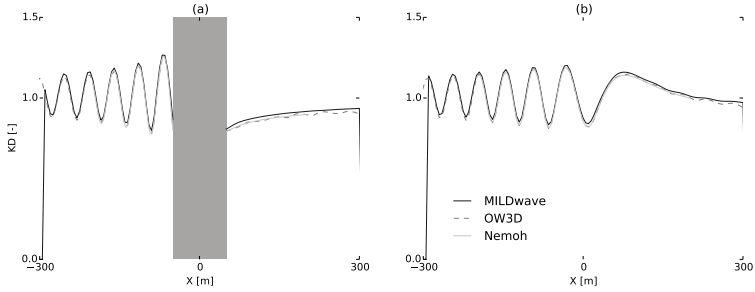

Figure C.5: K_D results along the two longitudinal sections indicated in Figure C.4 (Section 1 (S1): left; S2: right) for MILDwave-Nemoh, OceanWave3D-Nemoh and Nemoh.

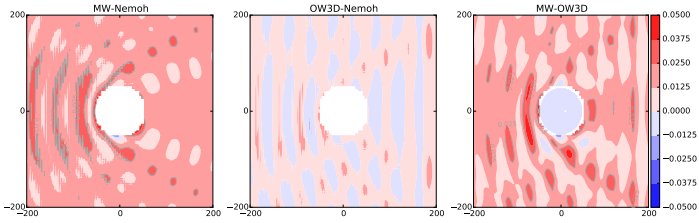

Figure C.6: Contour plots of relative K_D errors comparing: (**a**) MILDwave-Nemoh and Nemoh; (**b**) OceanWave3D-Nemoh and Nemoh; (**c**) MILDwave-Nemoh and OceanWave3D-Nemoh.

C.4 Test 3

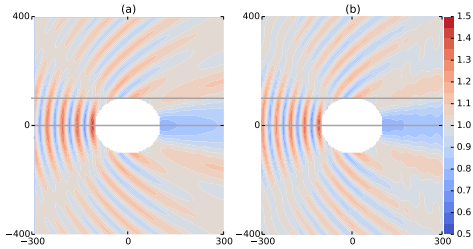

Figure C.7: Contour plots of K_D results for the coupled models: (**a**) MILDwave-Nemoh and (**b**) OceanWave3D-Nemoh.

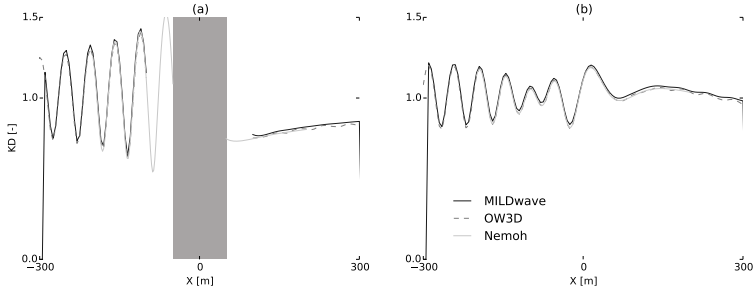

Figure C.8: K_D results along the two longitudinal sections indicated in Figure C.7 (Section 1 (S1): left; S2: right) for MILDwave-Nemoh, OceanWave3D-Nemoh and Nemoh.

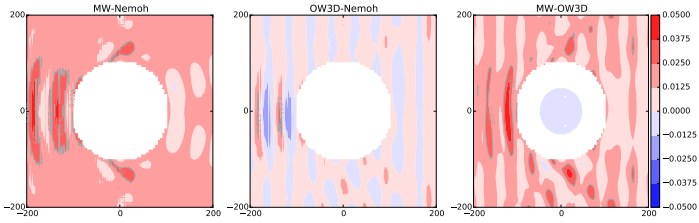

Figure C.9: Contour plots of relative K_D errors comparing: (**a**) MILDwave-Nemoh and Nemoh; (**b**) OceanWave3D-Nemoh and Nemoh; (**c**) MILDwave-Nemoh and OceanWave3D-Nemoh.

C.5 Test 4

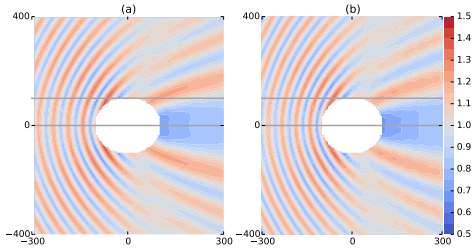

Figure C.10: Contour plots of K_D results for the coupled models: (**a**) MILDwave-Nemoh and (**b**) OceanWave3D-Nemoh.

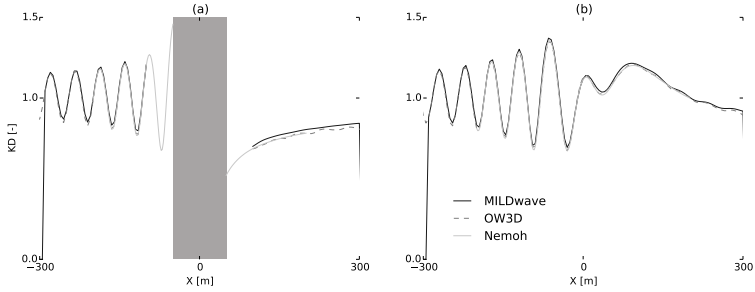

Figure C.11: K_D results along the two longitudinal sections indicated in Figure C.10 (Section 1 (S1): left; S2: right) for MILDwave-Nemoh, OceanWave3D-Nemoh and Nemoh.

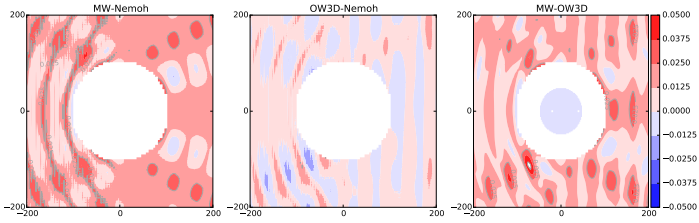

Figure C.12: Contour plots of relative K_D errors comparing: (**a**) MILDwave-Nemoh and Nemoh; (**b**) OceanWave3D-Nemoh and Nemoh; (**c**) MILDwave-Nemoh and OceanWave3D-Nemoh.

C.6 Test 5

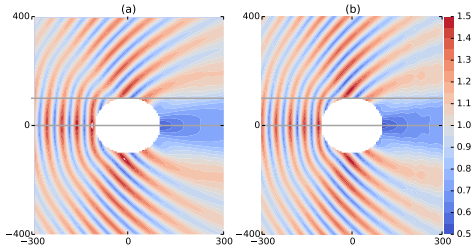

Figure C.13: Contour plots of K_D results for the coupled models: (**a**) MILDwave-Nemoh and (**b**) OceanWave3D-Nemoh.

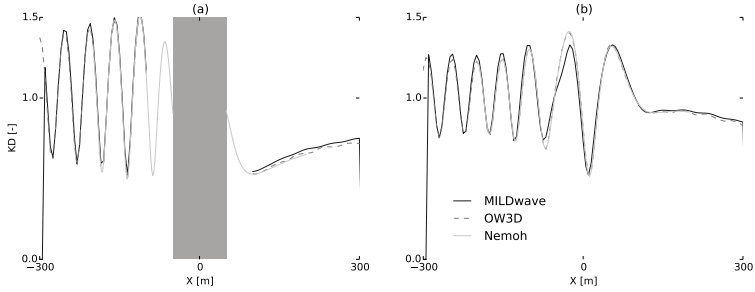

Figure C.14: K_D results along the two longitudinal sections indicated in Figure C.13 (Section 1 (S1): left; S2: right) for MILDwave-Nemoh, OceanWave3D-Nemoh and Nemoh.

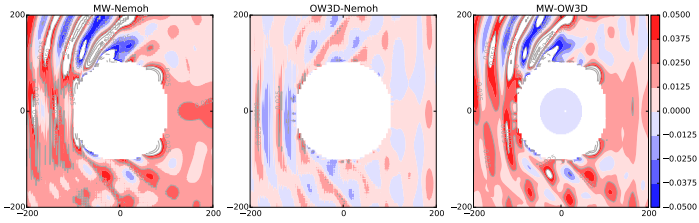

Figure C.15: Contour plots of relative K_D errors comparing: (**a**) MILDwave-Nemoh and Nemoh; (**b**) OceanWave3D-Nemoh and Nemoh; (**c**) MILDwave-Nemoh and OceanWave3D-Nemoh.

C.7 Test 6

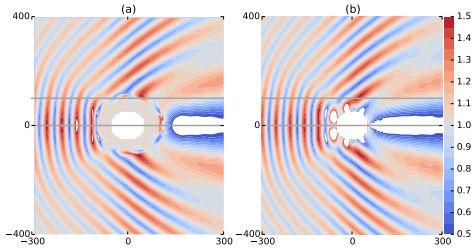

Figure C.16: Contour plots of K_D results for the coupled models: (**a**) MILDwave-Nemoh and (**b**) OceanWave3D-Nemoh.

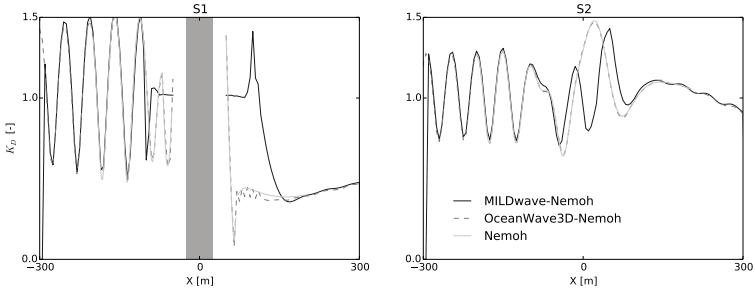

Figure C.17: K_D results along the two longitudinal sections indicated in Figure C.16 (Section 1 (S1): left; S2: right) for MILDwave-Nemoh, OceanWave3D-Nemoh and Nemoh.

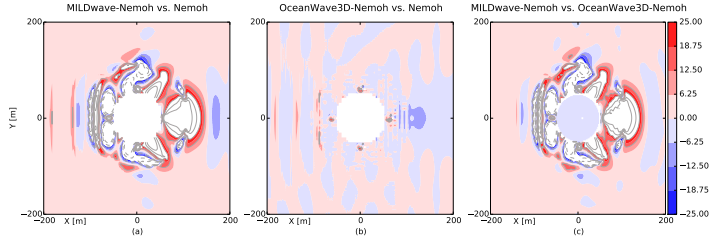

Figure C.18: Contour plots of relative K_D errors comparing: (**a**) MILDwave-Nemoh and Nemoh; (**b**) OceanWave3D-Nemoh and Nemoh; (**c**) MILDwave-Nemoh and OceanWave3D-Nemoh.

C.8 Test 7

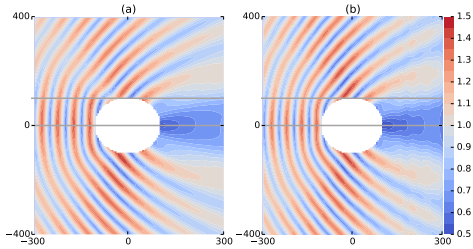

Figure C.19: Contour plots of K_D results for the coupled models: (**a**) MILDwave-Nemoh and (**b**) OceanWave3D-Nemoh.

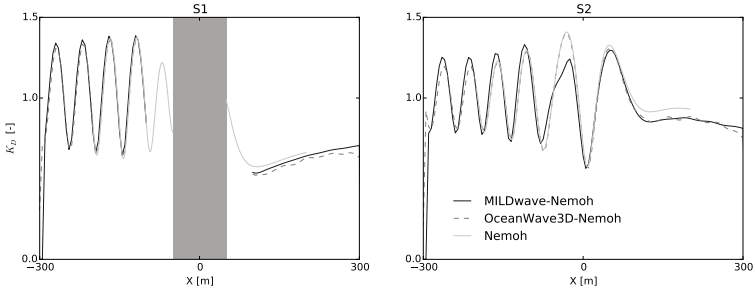

Figure C.20: K_D results along the two longitudinal sections indicated in Figure C.19 (Section 1 (S1): left; S2: right) for MILDwave-Nemoh, OceanWave3D-Nemoh and Nemoh.

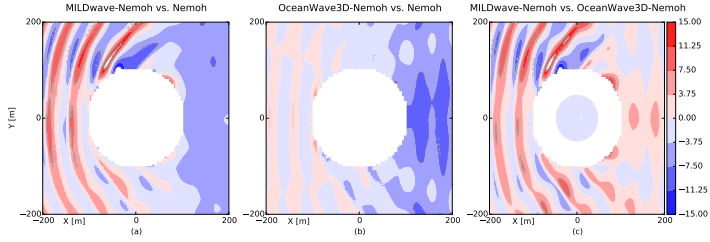

Figure C.21: Contour plots of relative K_D errors comparing: (**a**) MILDwave-Nemoh and Nemoh; (**b**) OceanWave3D-Nemoh and Nemoh; (**c**) MILDwave-Nemoh and OceanWave3D-Nemoh.

C.9 Test 8

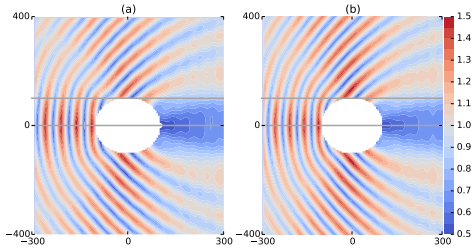

Figure C.22: Contour plots of K_D results for the coupled models: (**a**) MILDwave-Nemoh and (**b**) OceanWave3D-Nemoh.

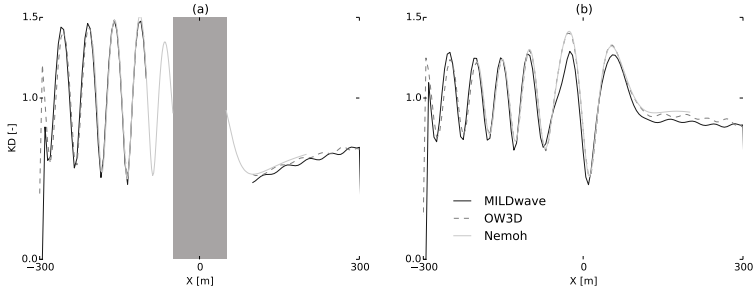

Figure C.23: K_D results along the two longitudinal sections indicated in Figure C.22 (Section 1 (S1): left; S2: right) for MILDwave-Nemoh, OceanWave3D-Nemoh and Nemoh.

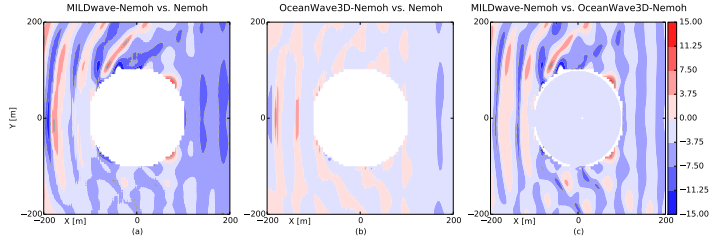

Figure C.24: Contour plots of relative K_D errors comparing: (**a**) MILDwave-Nemoh and Nemoh; (**b**) OceanWave3D-Nemoh and Nemoh; (**c**) MILDwave-Nemoh and OceanWave3D-Nemoh.

C.10 Test 9

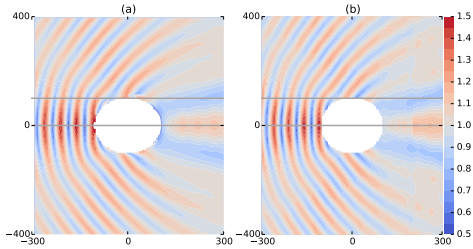

Figure C.25: Contour plots of K_D results for the coupled models: (**a**) MILDwave-Nemoh and (**b**) OceanWave3D-Nemoh.

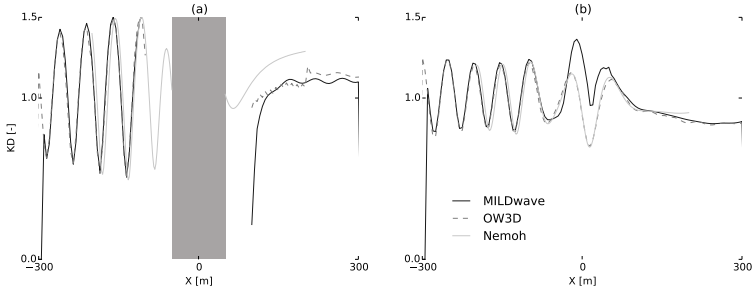

Figure C.26: K_D results along the two longitudinal sections indicated in Figure C.25 (Section 1 (S1): left; S2: right) for MILDwave-Nemoh, OceanWave3D-Nemoh and Nemoh.

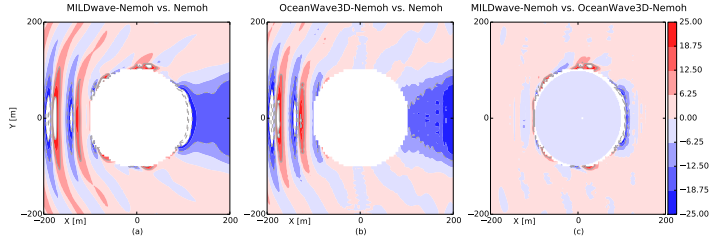

Figure C.27: Contour plots of relative K_D errors comparing: (**a**) MILDwave-Nemoh and Nemoh; (**b**) OceanWave3D-Nemoh and Nemoh; (**c**) MILDwave-Nemoh and OceanWave3D-Nemoh.

C.11 Test 10

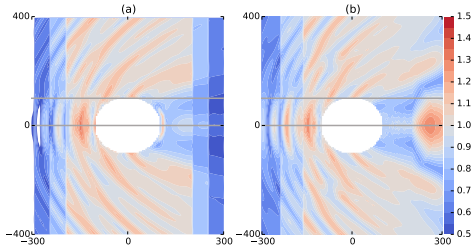

Figure C.28: Contour plots of K_D results for the coupled models: (**a**) MILDwave-Nemoh and (**b**) OceanWave3D-Nemoh.

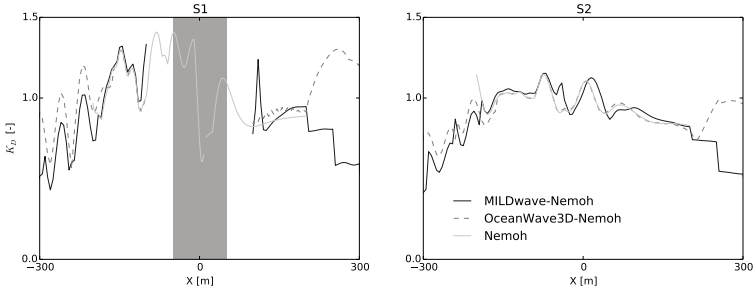

Figure C.29: K_D results along the two longitudinal sections indicated in Figure C.28 (Section 1 (S1): left; S2: right) for MILDwave-Nemoh, OceanWave3D-Nemoh and Nemoh.

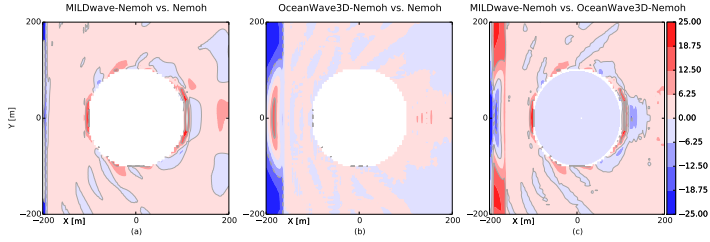

Figure C.30: Contour plots of relative K_D errors comparing: (**a**) MILDwave-Nemoh and Nemoh; (**b**) OceanWave3D-Nemoh and Nemoh; (**c**) MILDwave-Nemoh and OceanWave3D-Nemoh.

Appendix D

Comparison between OceanWave3D-Nemoh and WECwakes experiments

D.1 Test Matrix

Table D.1: Test program for the comparison of the linear coupling methodology with WECwakes data. (H = Wave Height, T = Wave Period, Δx = WEC x-spacing, Δy = WEC y-spacing)

Test Number	H (m)	T (s)	# Rows	# Columns	Δx (m)	Δy (m)
123	0.074	1.18	1	1	1.575	1.575
124	0.074	1.26	1	1	1.575	1.575
167	0.074	1.18	1	2	1.575	1.575
168	0.074	1.26	1	2	1.575	1.575
342	0.074	1.18	2	1	1.575	1.575
343	0.074	1.26	2	1	1.575	1.575
202	0.074	1.18	5	1	1.575	1.575
203	0.074	1.26	5	1	1.575	1.575
223	0.074	1.18	5	2	1.575	6.3
224	0.074	1.26	5	2	1.575	6.3
246	0.074	1.18	5	5	1.575	1.575
247	0.074	1.26	5	5	1.575	1.575

D.2 Wave Gauge Layout

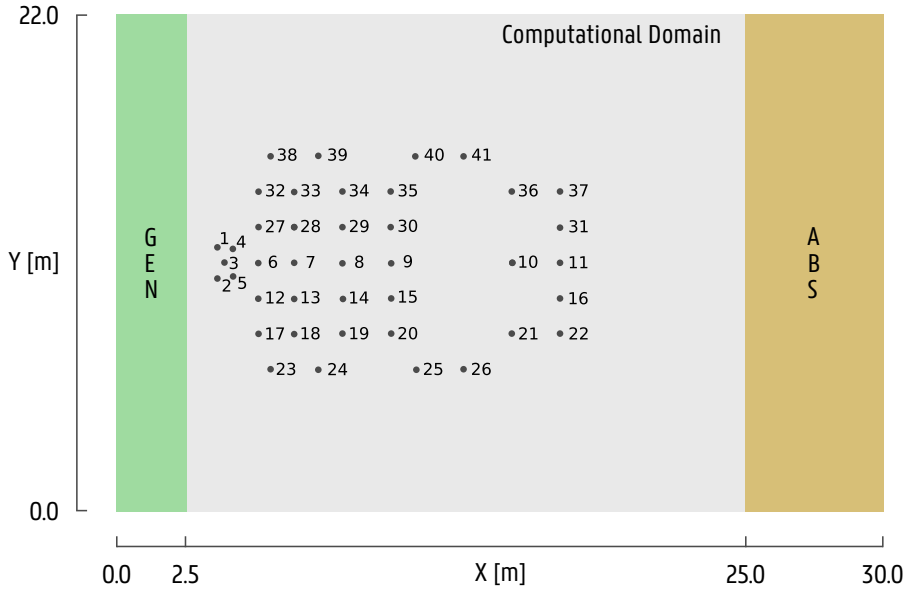

Figure D.1: Wave gauge distribution (•) used for the comparison with experimental tests. The code numbers of the used wave gauges are also shown.

D.3 Test 123

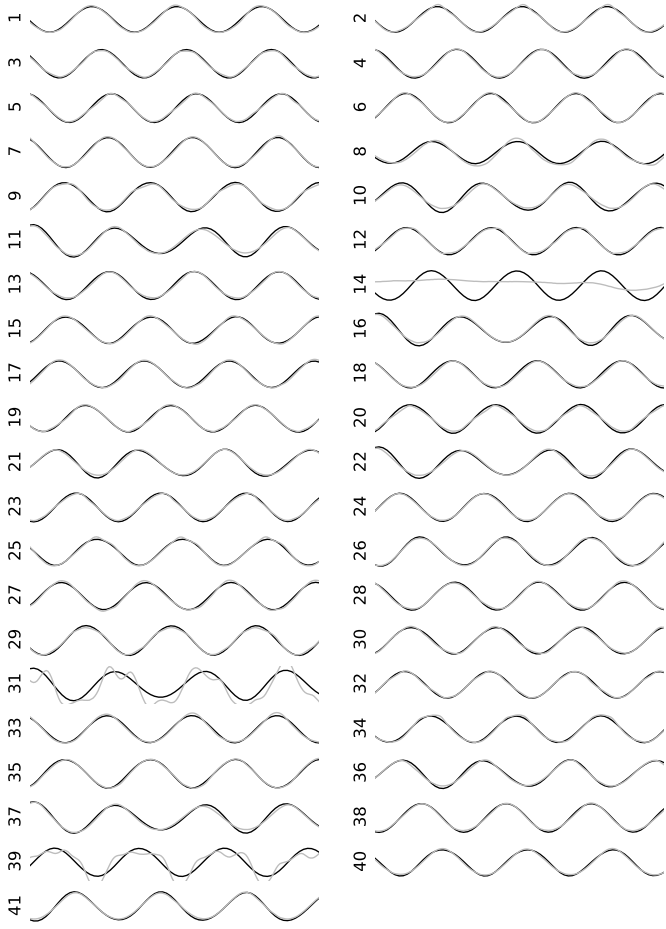

Figure D.2: Comparison of the wave signal between the OceanWave3D-Nemoh model (black line) and the experimental data (gray line) for all 19 wave gauges in the experimental dataset. The WG number (see Figure D.1) is indicated at the left of each wave signal.

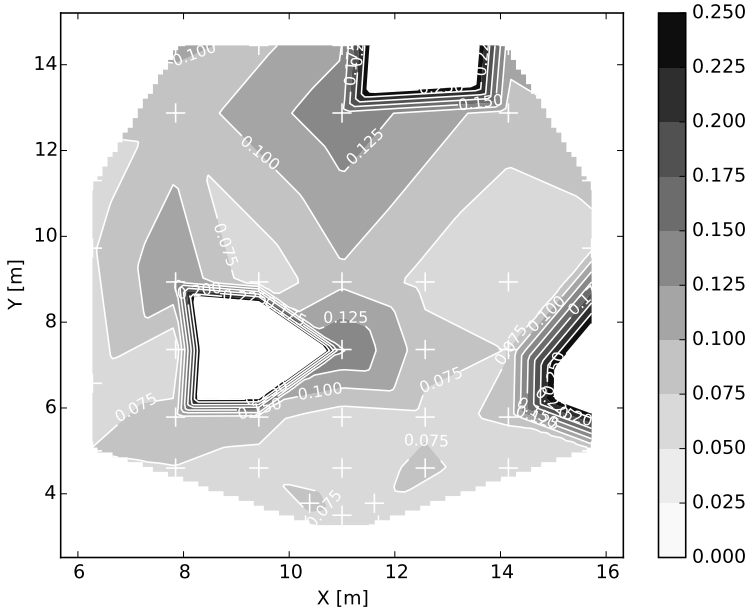

Figure D.3: Scatter plot of the error on the wave signal between the OceanWave3D-Nemoh model and the experimental data for all 19 wave gauges in the experimental dataset.

D.4 Test 124

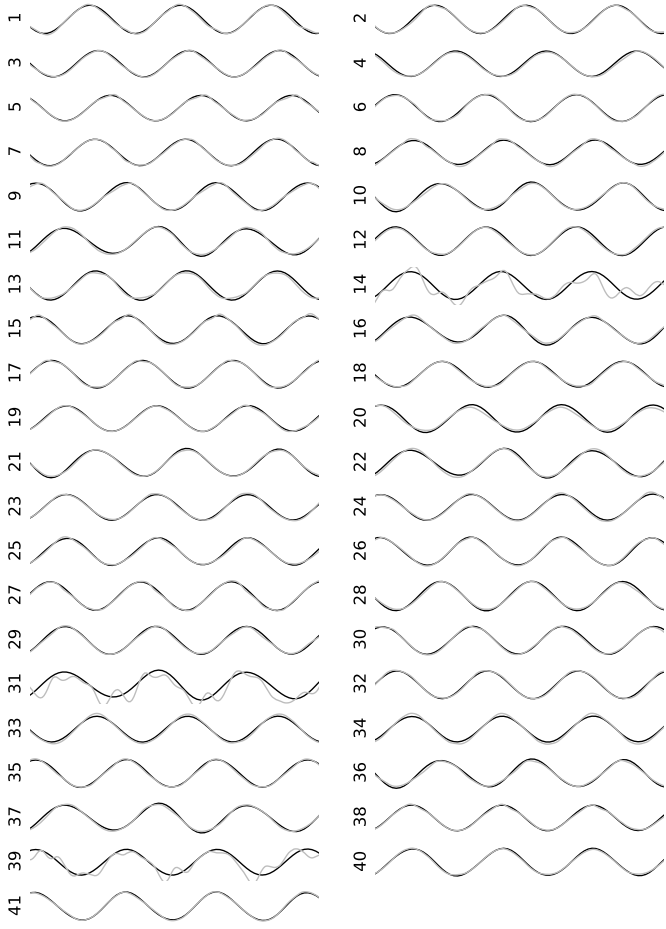

Figure D.4: Comparison of the wave signal between the OceanWave3D-Nemoh model (black line) and the experimental data (gray line) for all 19 wave gauges in the experimental dataset. The WG number (see Figure D.1) is indicated at the left of each wave signal.

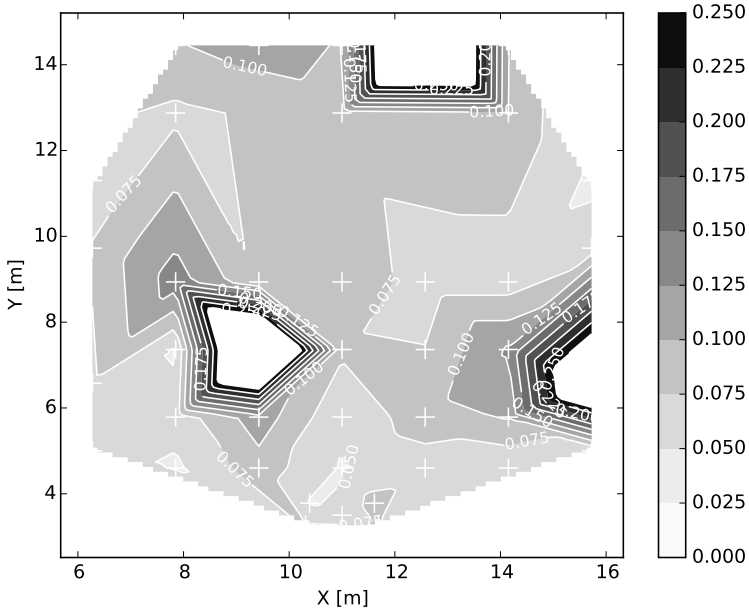

Figure D.5: Scatter plot of the error on the wave signal between the OceanWave3D-Nemoh model and the experimental data for all 19 wave gauges in the experimental dataset.

D.5 Test 167

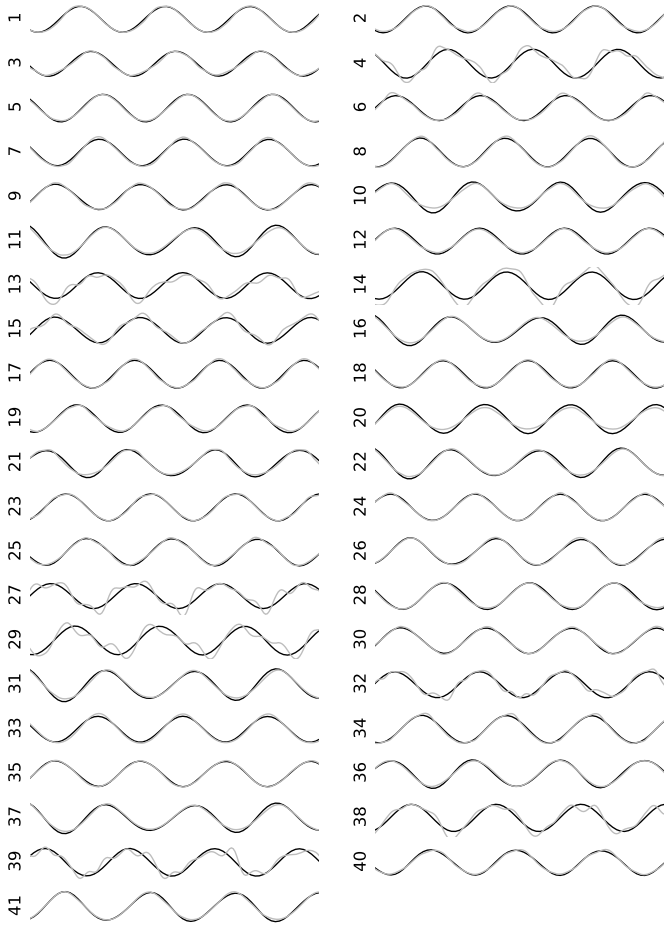

Figure D.6: Comparison of the wave signal between the OceanWave3D-Nemoh model (black line) and the experimental data (gray line) for all 19 wave gauges in the experimental dataset. The WG number (see Figure D.1) is indicated at the left of each wave signal.

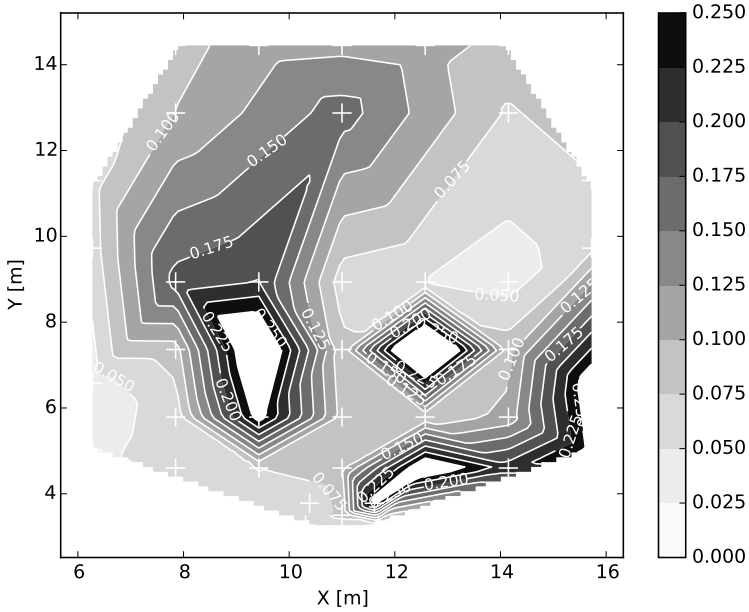

Figure D.7: Scatter plot of the error on the wave signal between the OceanWave3D-Nemoh model and the experimental data for all 19 wave gauges in the experimental dataset.

D.6 Test 168

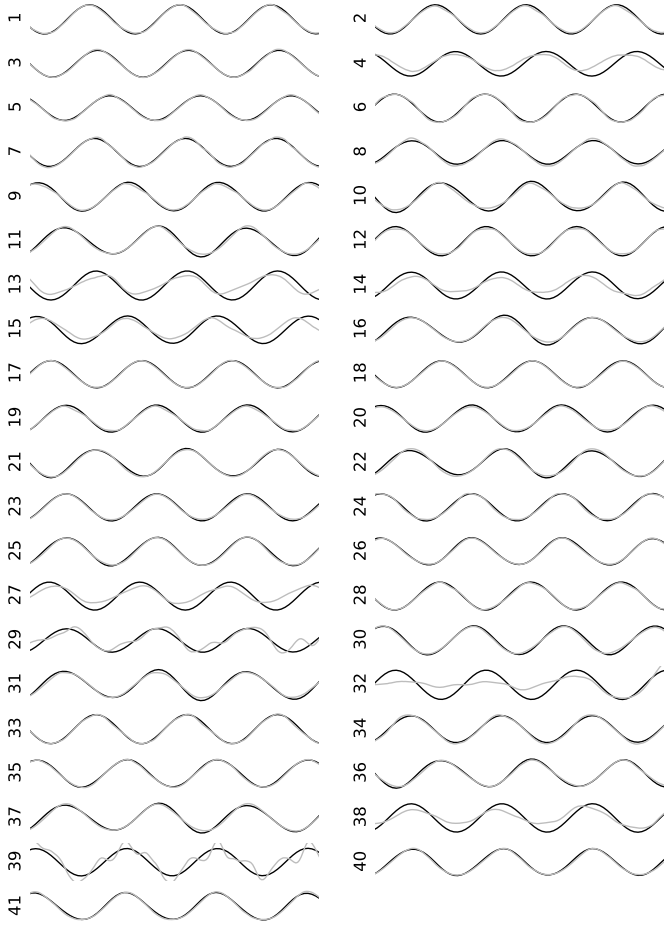

Figure D.8: Comparison of the wave signal between the OceanWave3D-Nemoh model (black line) and the experimental data (gray line) for all 19 wave gauges in the experimental dataset. The WG number (see Figure D.1) is indicated at the left of each wave signal.

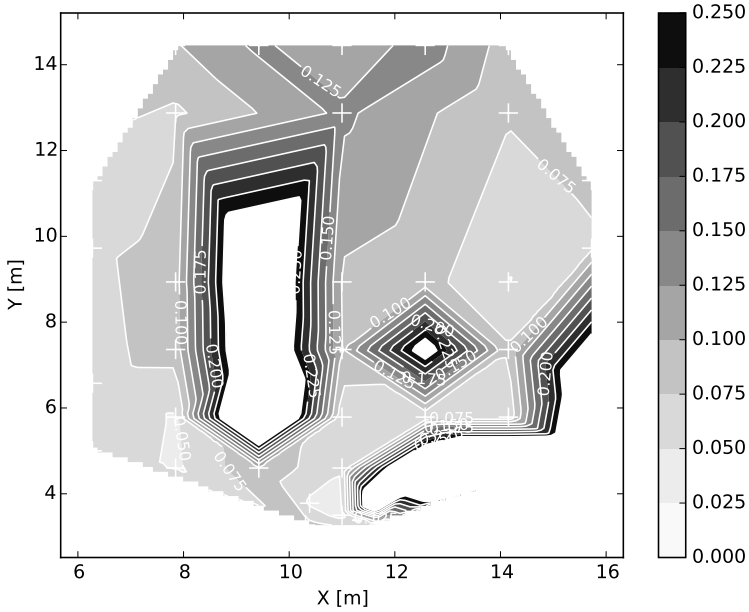

Figure D.9: Scatter plot of the error on the wave signal between the OceanWave3D-Nemoh model and the experimental data for all 19 wave gauges in the experimental dataset.

D.7 Test 342

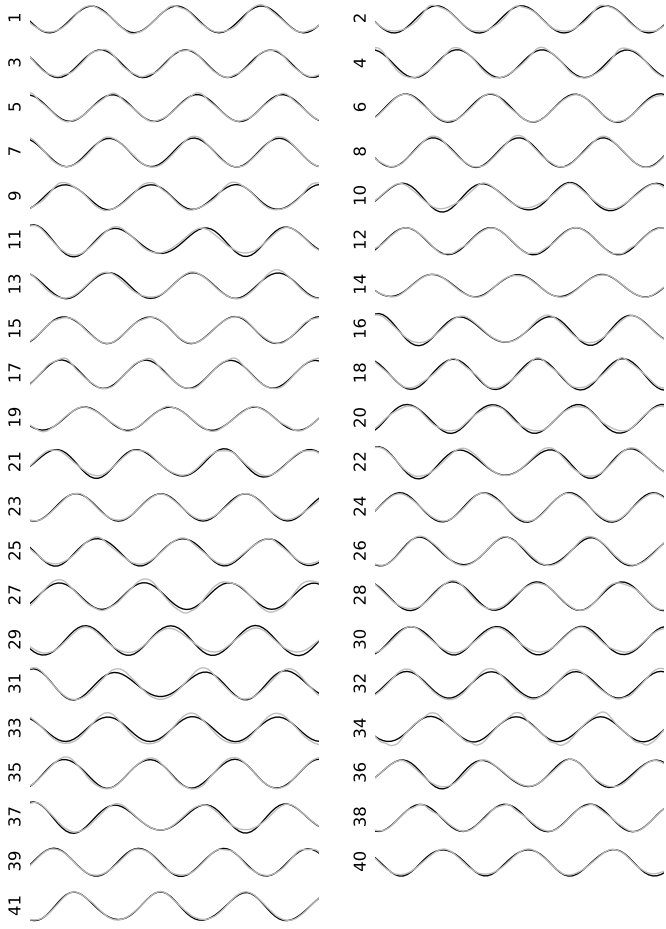

Figure D.10: Comparison of the wave signal between the OceanWave3D-Nemoh model (black line) and the experimental data (gray line) for all 19 wave gauges in the experimental dataset. The WG number (see Figure D.1) is indicated at the left of each wave signal.

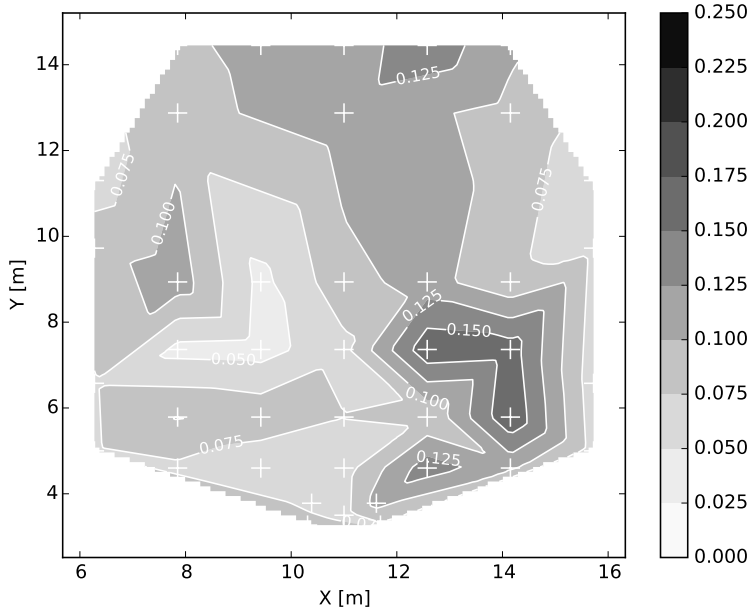

Figure D.11: Scatter plot of the error on the wave signal between the OceanWave3D-Nemoh model and the experimental data for all 19 wave gauges in the experimental dataset.

D.8 Test 343

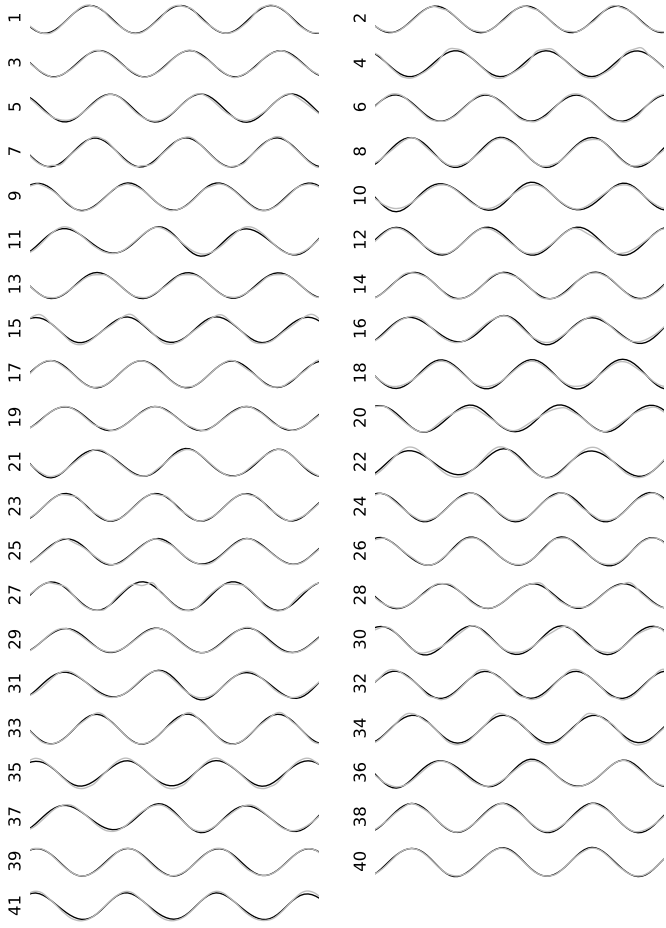

Figure D.12: Comparison of the wave signal between the OceanWave3D-Nemoh model (black line) and the experimental data (gray line) for all 19 wave gauges in the experimental dataset. The WG number (see Figure D.1) is indicated at the left of each wave signal.

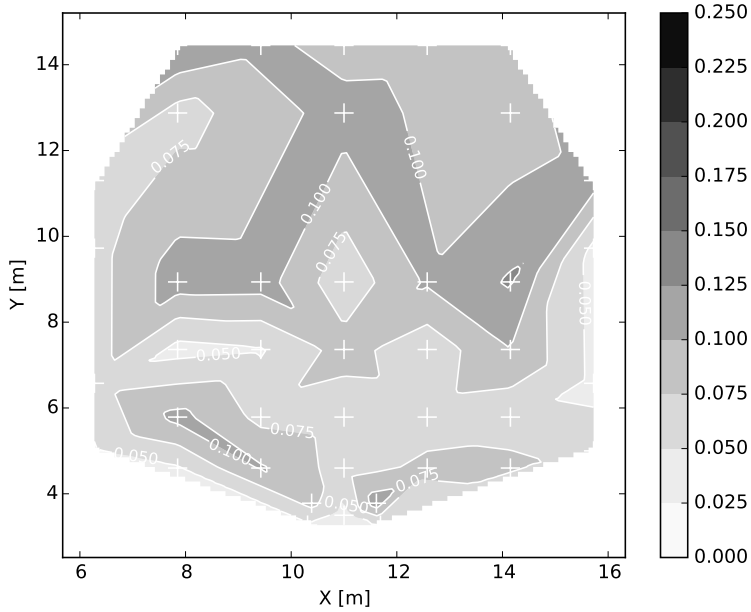

Figure D.13: Scatter plot of the error on the wave signal between the OceanWave3D-Nemoh model and the experimental data for all 19 wave gauges in the experimental dataset.

D.9 Test 202

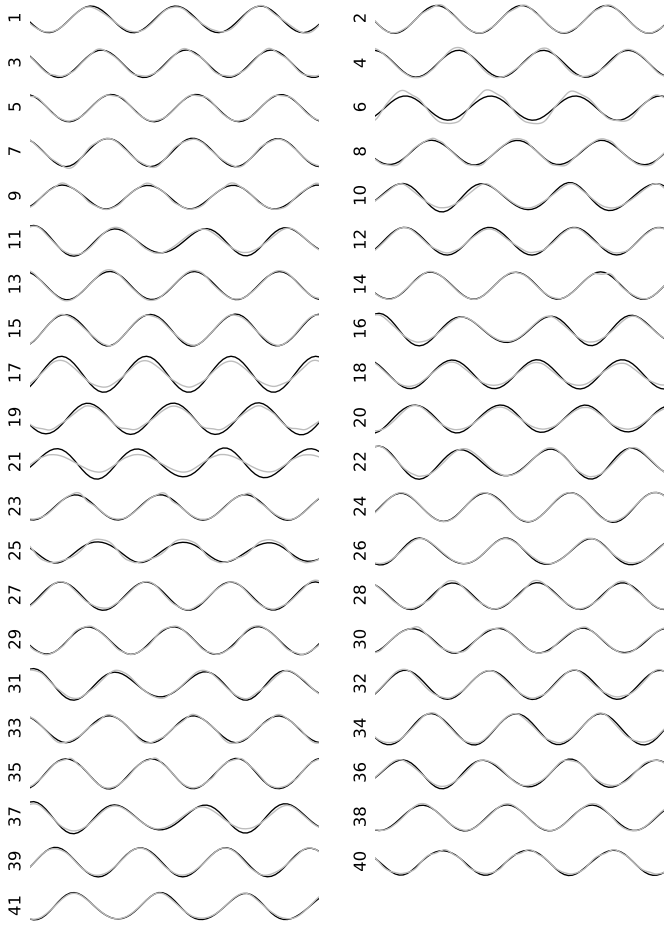

Figure D.14: Comparison of the wave signal between the OceanWave3D-Nemoh model (black line) and the experimental data (gray line) for all 19 wave gauges in the experimental dataset. The WG number (see Figure D.1) is indicated at the left of each wave signal.

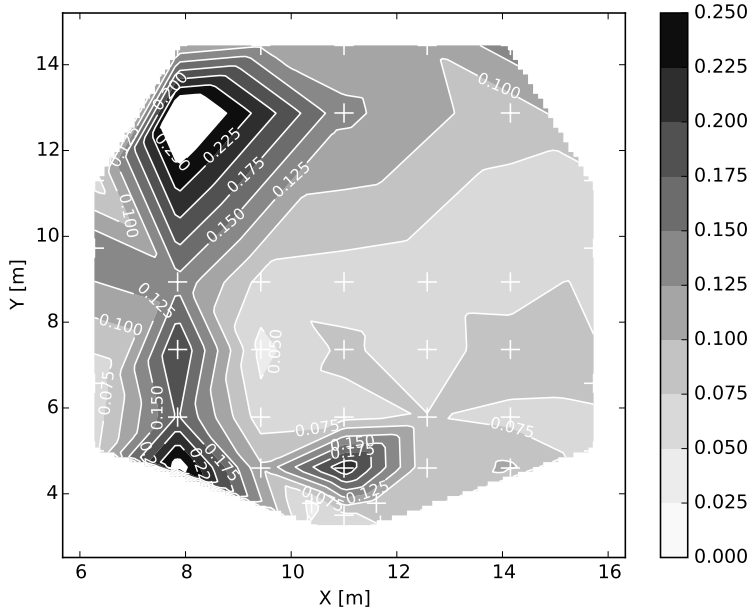

Figure D.15: Scatter plot of the error on the wave signal between the OceanWave3D-Nemoh model and the experimental data for all 19 wave gauges in the experimental dataset.

D.10 Test 203

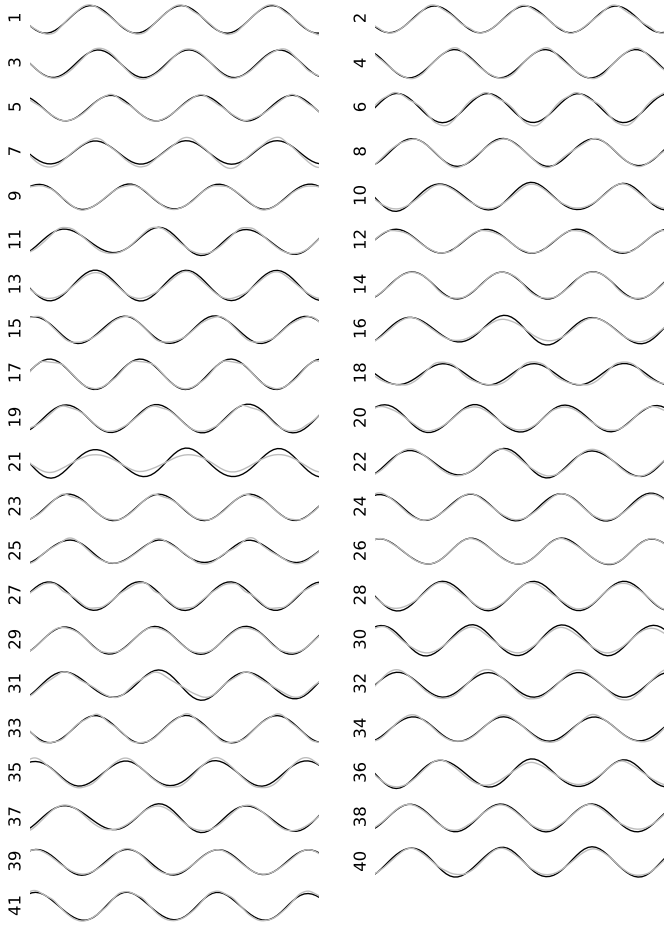

Figure D.16: Comparison of the wave signal between the OceanWave3D-Nemoh model (black line) and the experimental data (gray line) for all 19 wave gauges in the experimental dataset. The WG number (see Figure D.1) is indicated at the left of each wave signal.

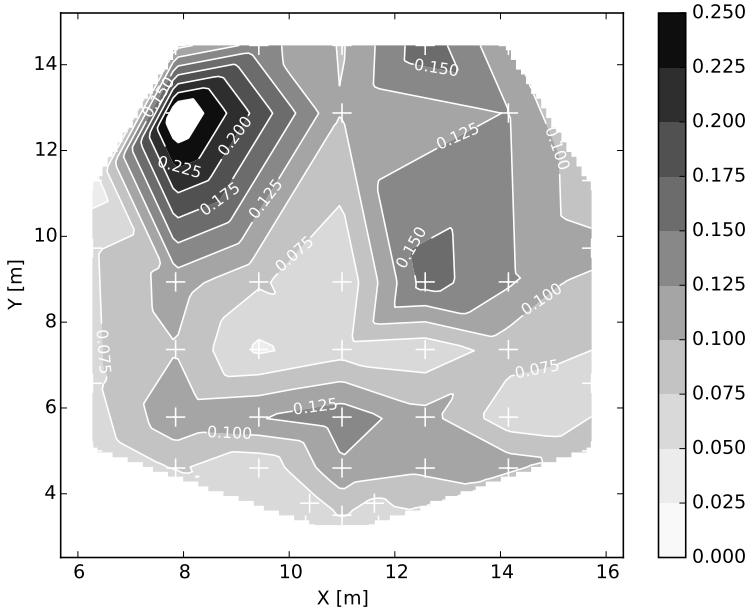

Figure D.17: Scatter plot of the error on the wave signal between the OceanWave3D-Nemoh model and the experimental data for all 19 wave gauges in the experimental dataset.

D.11 Test 223

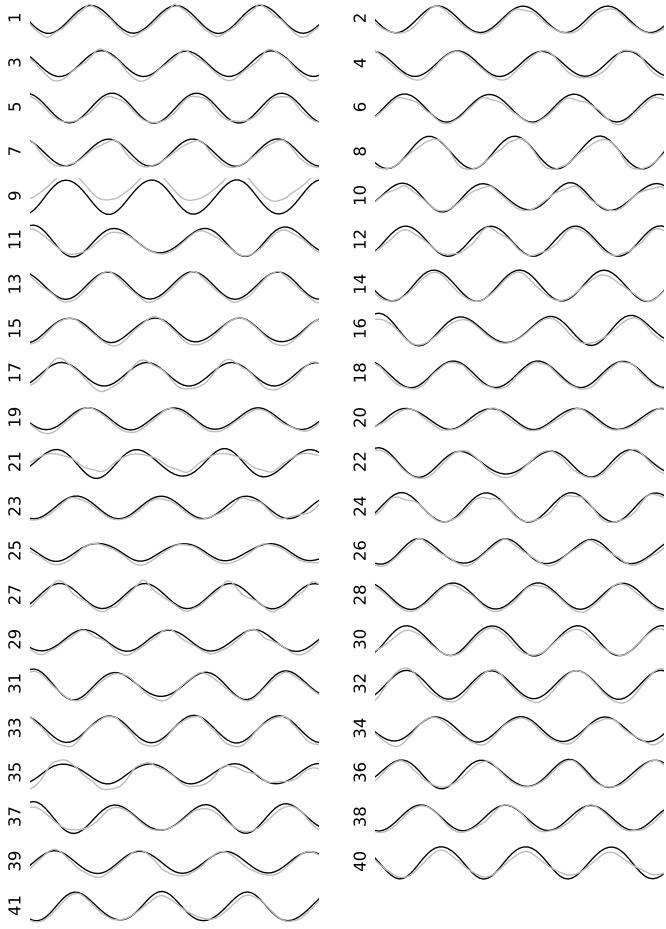

Figure D.18: Comparison of the wave signal between the OceanWave3D-Nemoh model (black line) and the experimental data (gray line) for all 19 wave gauges in the experimental dataset. The WG number (see Figure D.1) is indicated at the left of each wave signal.

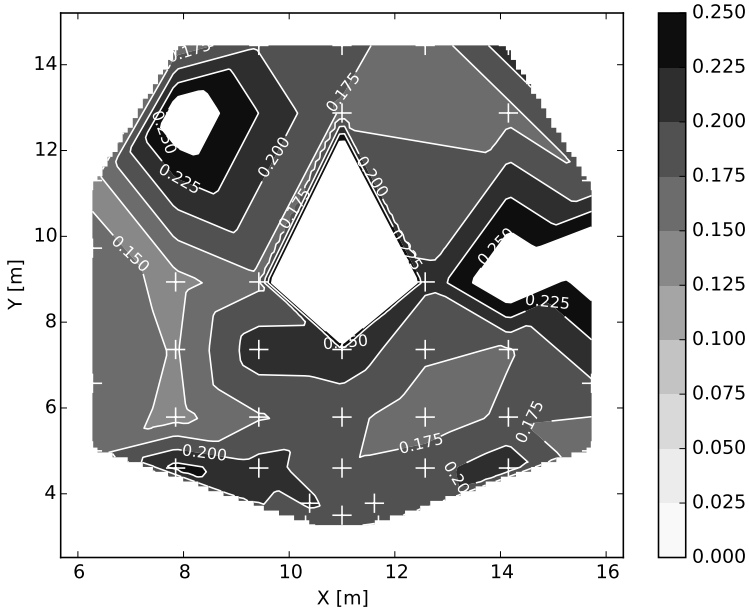

Figure D.19: Scatter plot of the error on the wave signal between the OceanWave3D-Nemoh model and the experimental data for all 19 wave gauges in the experimental dataset.

D.12 Test 224

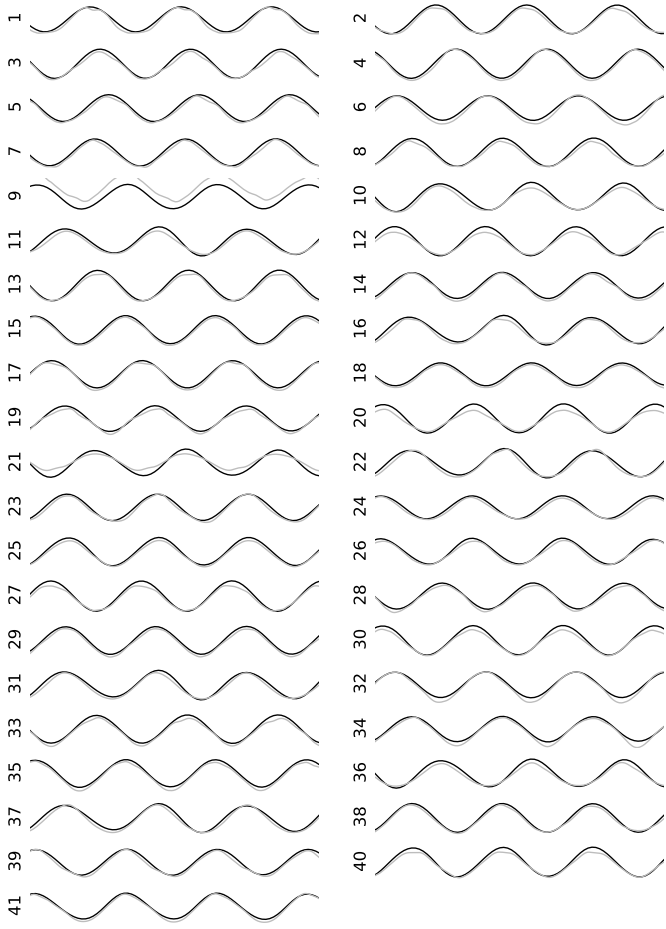

Figure D.20: Comparison of the wave signal between the OceanWave3D-Nemoh model (black line) and the experimental data (gray line) for all 19 wave gauges in the experimental dataset. The WG number (see Figure D.1) is indicated at the left of each wave signal.

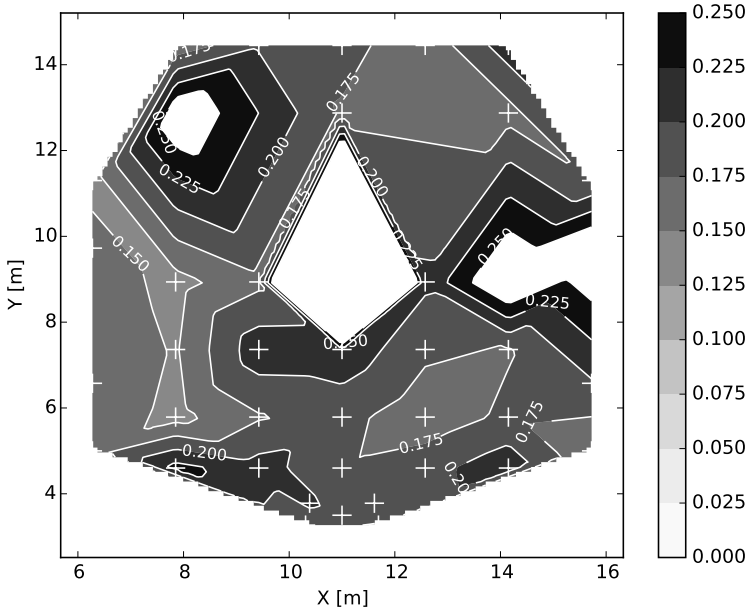

Figure D.21: Scatter plot of the error on the wave signal between the OceanWave3D-Nemoh model and the experimental data for all 19 wave gauges in the experimental dataset.

D.13 Test 246

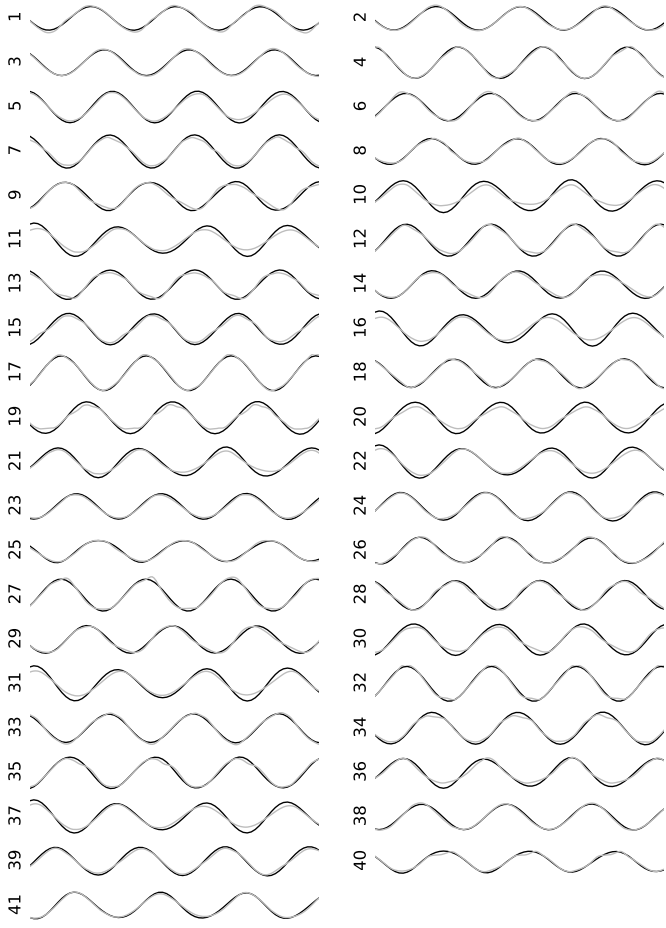

Figure D.22: Comparison of the wave signal between the OceanWave3D-Nemoh model (black line) and the experimental data (gray line) for all 19 wave gauges in the experimental dataset. The WG number (see Figure D.1) is indicated at the left of each wave signal.

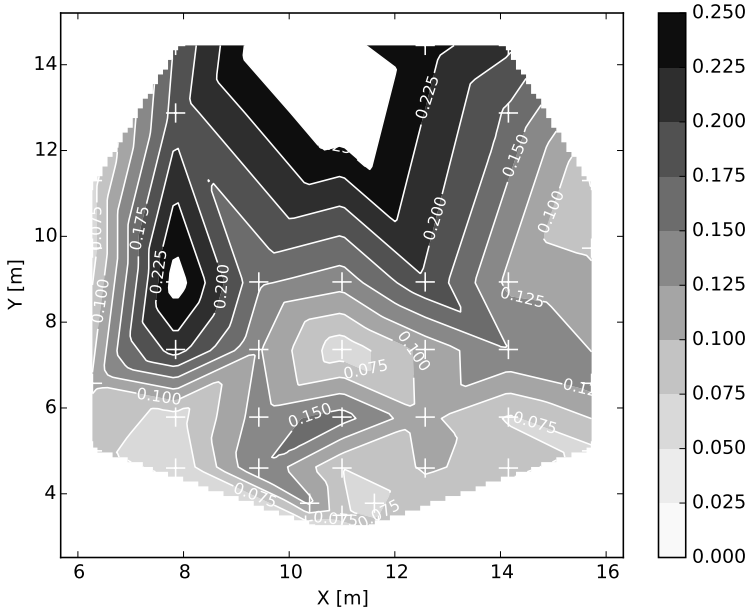

Figure D.23: Scatter plot of the error on the wave signal between the OceanWave3D-Nemoh model and the experimental data for all 19 wave gauges in the experimental dataset.

D.14 Test 247

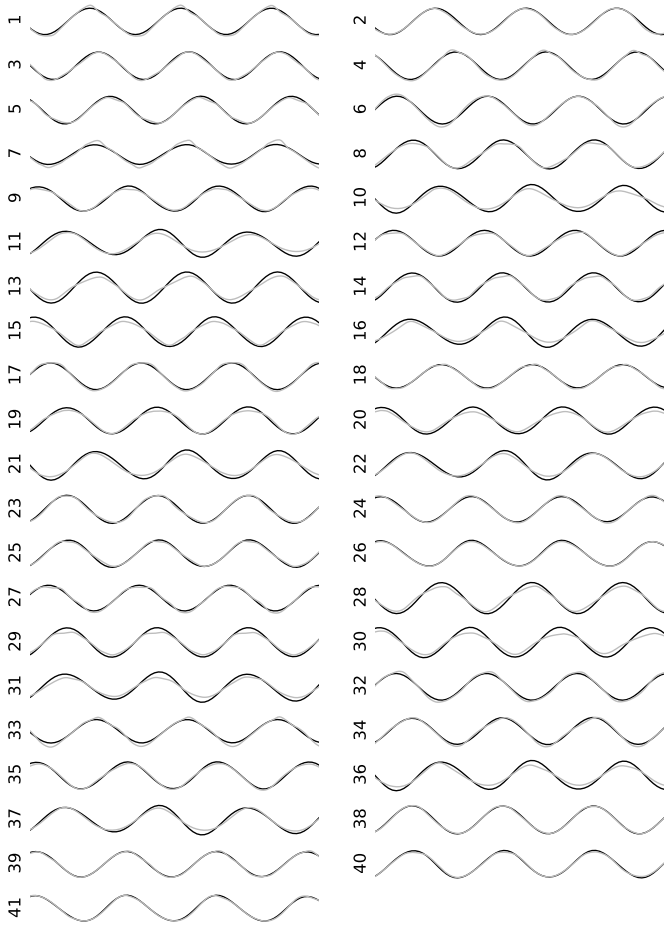

Figure D.24: Comparison of the wave signal between the OceanWave3D-Nemoh model (black line) and the experimental data (gray line) for all 19 wave gauges in the experimental dataset. The WG number (see Figure D.1) is indicated at the left of each wave signal.

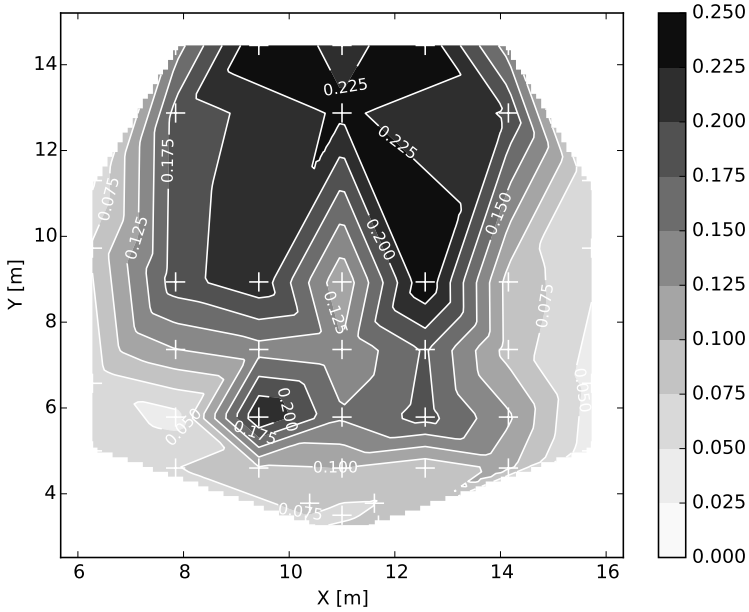

Figure D.25: Scatter plot of the error on the wave signal between the OceanWave3D-Nemoh model and the experimental data for all 19 wave gauges in the experimental dataset.

Appendix E

Source Code of the non-linear Coupling Methodology

This chapter provides the reader with all the code changes and newly created code, which is also available on GitHub: `https://github.ugent.be/tverbrug/OW3D-DSPH`.

E.1 OceanWave3D Code Changes

E.1.1 Changes to `OW3D.inp`

An extra final line is added to a standard OceanWave3D input file:

```
1 15.000000 21.120000 <- Coupling Yes/No, xInlet, xOutlet
```

The first number is a flag to indicate if coupling should be enabled or not, the second value is the x-location of the inlet and the third value is the x-location of the outlet.

E.1.2 Changes to `globalvariables.f90`

Global variables are created for the coupling file, coupling zone coordinates and indices and the received SPH free surface.
line 43-48:

```
! VARIABLES for coupling with SPH
INTEGER :: couplingFlag
CHARACTER(LEN=40) :: couplingFile
REAL :: xSPH1, xSPH2
REAL(KIND=long), DIMENSION(:),    ALLOCATABLE :: etaCP
INTEGER, DIMENSION(:), ALLOCATABLE :: iCP, jCP
```

E.1.3 Changes to `ReadinputFileParameters.f90`

The extra line added to the input file is read into its corresponding global variables, to be used by the coupling routine.
line 463-464

```
! Read in SPH Coupling Info
READ(FILEIP(1),*) couplingFlag, xSPH1, xSPH2
```

E.1.4 Changes to `OceanWave3DTakeATimeStep.f90`

At every time step, the coupling routine is called, after a check if coupling is enabled.
line 153-155:

```
IF(couplingFlag.EQ.1) THEN
    CALL CoupleModel
ENDIF
```

E.1.5 New routine `CoupleRoutine.f90`

This subroutine initializes the MPI communication, calculates the indices for the coupling interface locations and calculates the horizontal orbital velocities from the wave potential. It sends the velocities and the surface elevation to the Python script, and receives the filtered SPH surface elevation, which it uses to overwrite the original surface elevations:

```
subroutine CoupleModel()

USE GlobalVariables
USE MPI
IMPLICIT NONE

CHARACTER(LEN=10):: astring
INTEGER :: comm, rank, size, mpierr
INTEGER :: status(MPI_Status_size)
! Local variables
INTEGER :: Nx, Ny, Nz, io, it, iXSPH1, iXSPH2
INTEGER ::  i, j, k, i0, i1, is, j0, j1, js, nxSPH
REAL(KIND=long), DIMENSION(:,:), POINTER :: x, y, h, &
                                            hx, hy, eta, &
                                            etax, etay
REAL(KIND=long), DIMENSION(:), POINTER    :: z
REAL(KIND=long), DIMENSION(:), ALLOCATABLE :: wlev, &
                                              xreq, etaSPH
! Automatic work space
REAL(KIND=long) :: &
```

```
U(FineGrid%Nz+GhostGridZ,FineGrid%Nx+2*GhostGridX, &
FineGrid%Ny+2*GhostGridY), &
V(FineGrid%Nz+GhostGridZ,FineGrid%Nx+2*GhostGridX, &
FineGrid%Ny+2*GhostGridY), &
W(FineGrid%Nz+GhostGridZ,FineGrid%Nx+2*GhostGridX, &
FineGrid%Ny+2*GhostGridY), &
d(FineGrid%Nx+2*GhostGridX,FineGrid%Ny+2*GhostGridY), &
dummy, bndLoc(4), xIn, xOut, etaIn, etaOut, dxSPH

! Assign local pointers
x => FineGrid%x; y => FineGrid%y; z => FineGrid%z; &
h => FineGrid%h; hx => FineGrid%hx; hy => FineGrid%hy; &
eta => WaveField%E; etax => WaveField%Ex; &
etay => WaveField%Ey

Nx = FineGrid%Nx+2*GhostGridX
Ny = FineGrid%Ny+2*GhostGridY
Nz = FineGrid%Nz+GhostGridZ

! Initialize MPI on first timestep
IF(tstep .LT. 2) THEN
  CALL MPI_INIT(mpierr)
  CALL MPI_Comm_size(MPI_COMM_WORLD, size, mpierr)
  print *, 'SIZE ', size
  CALL MPI_Comm_rank(MPI_COMM_WORLD, rank, mpierr)
  print *, 'RANK ', rank
  CALL MPI_SEND(U(:,iXSPH1,1), Nz, MPI_DOUBLE_PRECISION, &
                1, 23, MPI_COMM_WORLD, mpierr)
  CALL MPI_SEND(U(:,iXSPH2,1), Nz, MPI_DOUBLE_PRECISION, &
                1, 24, MPI_COMM_WORLD, mpierr)
  CALL MPI_SEND(eta(:,1), Nx, MPI_DOUBLE_PRECISION, &
                1, 25, MPI_COMM_WORLD, mpierr)
ENDIF

! Find index of coupling location
DO i=1,Nx
  IF (abs(x(i,1)-xSPH1) .LT. 0.001) THEN
    iXSPH1 = i
    EXIT
  ENDIF
ENDDO
DO i=1,Nx
  If (abs(x(i,1)-xSPH2) .LT. 0.001) THEN
    iXSPH2 = i
    EXIT
  ENDIF
```

```
ENDDO

! The fluid thickness d=h+eta
DO j=1,Ny
  DO i=1,Nx
    d(i,j)=h(i,j)+eta(i,j)
  ENDDO
ENDDO

! Calculate velocity field
IF (FineGrid%Nx>1) THEN
  ! Compute dphi/dx
  CALL DiffXEven(phi,U,1,FineGrid%Nx+2*GhostGridX, &
                 FineGrid%Ny+2*GhostGridY,  &
                 FineGrid%Nz+GhostGridZ, &
                 FineGrid%DiffStencils,alpha)
  IF ( LinearOnOff /= 0) THEN
    ! Add in the chain rule contribution
    DO j=1,Ny
      DO i=1,Nx
        DO k=1,Nz
          U(k,i,j) = U(k,i,j) + &
          ((1-z(k))/d(i,j)*hx(i,j) - &
          z(k)/d(i,j)*etax(i,j))*W(k,i,j)
        ENDDO
      ENDDO
    ENDDO
  ENDIF
ELSE
  U=zero
ENDIF

! Send time step to python
CALL MPI_SEND(time, 1, MPI_DOUBLE_PRECISION, 1, 22, &
              MPI_COMM_WORLD, mpierr)

! Send velocity and surface elevation OW3D->python->SPH
CALL MPI_SEND(U(:,iXSPH1,1), Nz, MPI_DOUBLE_PRECISION, &
              1, 23, MPI_COMM_WORLD, mpierr)
CALL MPI_SEND(U(:,iXSPH2,1), Nz, MPI_DOUBLE_PRECISION, &
              1, 24, MPI_COMM_WORLD, mpierr)
CALL MPI_SEND(eta(:,1), Nx, MPI_DOUBLE_PRECISION, &
              1, 25, MPI_COMM_WORLD, mpierr)

! Receive surface elevation SPH->python->OW3D
CALL MPI_RECV(xIn, 1, MPI_DOUBLE_PRECISION, &
```

```
                1, 40, MPI_COMM_WORLD, status, mpierr)
CALL MPI_RECV(dummy, 1, MPI_DOUBLE_PRECISION, &
                1, 41, MPI_COMM_WORLD, status, mpierr)
nxSPH = INT(dummy)
ALLOCATE(etaSPH(INT(dummy)))
CALL MPI_RECV(dxSPH, 1, MPI_DOUBLE_PRECISION, &
                1, 42, MPI_COMM_WORLD, status, mpierr)
CALL MPI_RECV(etaSPH, nxSPH, MPI_DOUBLE_PRECISION, &
                1, 43, MPI_COMM_WORLD, status, mpierr)

! Overwrite original surface elevation
DO i=1,nxSPH
  WHERE (ABS(x-(xIn+(i-1)*dxSPH)).LT.0.02) &
   Wavefield%E = etaSPH(i)
END DO

IF(tstep .EQ. Nsteps) THEN
  CALL MPI_FINALIZE(mpierr)
ENDIF

end subroutine coupleModel
```

E.2 Python Code

E.2.1 Set-up file `simsetup.py`

This file contains all the simulation variables: the wave conditions, OceanWave3D parameters and DualSPHysics parameters. It calculates the inlet and outlet conditions based on the selected parameters:

```
import functions as f

#-~-~-~-~-~-~-~-~-~-~-~-~-~-~-~-~-~-~-~-~-~-~-~-~-~-~-~-~-~-~-~-~-~-~-~-
#                          THEORY INPUT
#-~-~-~-~-~-~-~-~-~-~-~-~-~-~-~-~-~-~-~-~-~-~-~-~-~-~-~-~-~-~-~-~-~-~-~-

# Wave Conditions
H = 0.01                                    # Wave Height
T = 1.0                                     # Wave Period
d = 0.7                                     # Water Depth
genType = 'T'
# 'T' = Regular, 'O' = OceanWave3D, 'I' = Irregular
dim = 3                                     # 2-D or 3-D
Lwav = f.wavlen(H,T,d)
dp = 0.01                                   # Particle Size
```

```
#-~-~-~
```

```
import subprocess
import numpy as np
import matplotlib.pyplot as plt
import os
import functions as f
from cleanup import *
from simsetup import *

#-~-~-~-~-~-~-~-~-~-~-~-~-~-~-~-~-~-~-~-~-~-~-~-~-~-~-~-~-~-~-~-~-~-~-~-
#                        PRE PROCESSING
#-~-~-~-~-~-~-~-~-~-~-~-~-~-~-~-~-~-~-~-~-~-~-~-~-~-~-~-~-~-~-~-~-~-~-~-

# Write SPH input file
f.writeXml(dp,H,T,d,tsim,dtOut,nLayers,xIn,xOut,nIO=nIO,
           dim=dim,width=width)
# Request z and vel output locations
f.setGauges([xIn,xOut],dp,d,H,dim=dim,width=width)

#-~-~-~-~-~-~-~-~-~-~-~-~-~-~-~-~-~-~-~-~-~-~-~-~-~-~-~-~-~-~-~-~-~-~-~-
#                        Start MPI run
#-~-~-~-~-~-~-~-~-~-~-~-~-~-~-~-~-~-~-~-~-~-~-~-~-~-~-~-~-~-~-~-~-~-~-~-

# Set environment
os.environ['LD_LIBRARY_PATH'] = '/home/tverbrug/\
          OW3D_SPH/SPH_src/DSPH-socket2/EXECS_LINUX/'
os.system('export LD_LIBRARY_PATH=$LD_LIBRARY_PATH:
          /home/tverbrug/OW3D_SPH/SPH_src/
          DSPH-socket2/EXECS_LINUX/')

# Run GenCase
os.system('/home/tverbrug/OW3D_SPH/SPH_src/DSPH-socket2/
          EXECS_LINUX/GenCase4_linux64 WaveGen
          WaveGen_out/WaveGen -save:all -debug:-1')

# Start DualSPHysics Run
subprocess.Popen(["/home/tverbrug/OW3D_SPH/SPH_src/
                  DSPH-socket2/EXECS_LINUX/
                  DualSPHysicsInletSocket_linux64",
                  "WaveGen_out/WaveGen","WaveGen_out",
                  "-svres","-gpu:1"])

# Start communication
if (genType=='O' and nCouple==2):
  os.system('mpirun -n 1 OceanWave2D_SPH OW3D.inp :
  -n 1 python comm_socket_2way.py')
else:
```

```
os.system('python comm_socket.py')
```

E.2.3 Communication file `comm_socket.py`

In a one-way simulation, this file manages the communication between Python and DualSPHysics, using the socket protocol. The inlet and outlet conditions are sent to DualSPHysics, while the surface elevations necessary for the velocity corrections are received:

```
import socket
import numpy as np
from simsetup import *

#-~-~-~-~-~-~-~-~-~-~-~-~-~-~-~-~-~-~-~-~-~-~-~-~-~-~-~-~-~-~-~-~-~-~-~-
#                    SOCKET INITIALIZATION
#-~-~-~-~-~-~-~-~-~-~-~-~-~-~-~-~-~-~-~-~-~-~-~-~-~-~-~-~-~-~-~-~-~-~-~-

# Socket init
HOST, PORT = "localhost", 50007
s = socket.socket(socket.AF_INET, socket.SOCK_STREAM)
s.connect((HOST, PORT))

# Data init
etaIP = np.copy(time)*0.0
etaIPin = np.copy(time)*0.0
etaIPout = np.copy(time)*0.0
for iT in range(len(time)):
    etaIP[iT] = np.interp(xIn,x,eta[iT,:])
    etaIPin[iT] = np.interp(xIn+8.0*dp,x,eta[iT,:])
    etaIPout[iT] = np.interp(xOut-8.0*dp,x,eta[iT,:])

# Ramp function
cel = f.wavlen(H,T,d)/T
celdt = (xOut-xIn)/cel
nt = len(time)
ramp = np.ones(nt)
ramp2 = np.ones(nt)
nt = int(tsim/dt)
ramp[0:200] = np.linspace(0,1.0,200)  # Inlet ramp
ramp2[0:0+int(celdt/dt)] = 0.0        # Outlet ramp
ramp2[0+int(celdt/dt):200+int(celdt/dt)] = \
      np.linspace(0,1.0,200)

#-~-~-~-~-~-~-~-~-~-~-~-~-~-~-~-~-~-~-~-~-~-~-~-~-~-~-~-~-~-~-~-~-~-~-~-
#                  SEND INITIAL DATA TO DSPH
#-~-~-~-~-~-~-~-~-~-~-~-~-~-~-~-~-~-~-~-~-~-~-~-~-~-~-~-~-~-~-~-~-~-~-~-
```

```
# Send water depth and dt for communication
data = '{:f}'.format(d)
s.send(data.encode())
data = s.recv(1000)
data = '{:f}'.format(dt)
s.send(data.encode())
for iZ in range(11):
    uln1 = np.interp(dt,time,inlet[:,iZ+1])
    data = s.recv(1000)
    data = '{:f}'.format(uln1)
    s.send(data.encode())
    uOut1 = np.interp(dt,time,outlet[:,iZ+1])
    data = s.recv(1000)
    data = '{:f}'.format(uOut1)
    s.send(data.encode())
# Send zsurf
data = s.recv(1000)
zsurf = np.interp(dt,time,etaIP)*0.0 + d
data = '{:f}'.format(zsurf)
s.send(data.encode())
# Send nCouple
data = s.recv(1000)
data = '{:f}'.format(nCouple)
s.send(data.encode())

#-~-~-~-~-~-~-~-~-~-~-~-~-~-~-~-~-~-~-~-~-~-~-~-~-~-~-~-~-~-~-~-~-~-~-~-
#                TIME STEPPING & COMMUNICATION
#-~-~-~-~-~-~-~-~-~-~-~-~-~-~-~-~-~-~-~-~-~-~-~-~-~-~-~-~-~-~-~-~-~-~-~-

WGin = []
WGout = []
ucO = []
ucI = []
eI = []
eO = []
tm = []

t = 0.0
count = 0

while (t<tsim-dt/2.0):

    #------------------- Receive from DSPH -------------------
    # receive time
    data = s.recv(1000)
```

```
t = float(data)
print('tSPH = ' + str(t))
tm.append(t)
data = '{:f}'.format(1.0)
s.send(data.encode())
# receive etaWGIn
data = str(s.recv(1000))
etaWGin = float(data)-d
WGin.append(float(data))
data = '{:f}'.format(1.0)
s.send(data.encode())
# receive etaWGOut
data = str(s.recv(1000))
etaWGout = float(data)-d
WGout.append(float(data))

# ------------------ Calculate uCorrIn ------------------
rampIn = np.interp(t,time,ramp[:])
etaIn = np.interp(t,time,etaIPin)*rampIn
el.append(etaIn)
if t > celdt:
    uCorrIn = (etaWGin-etaIn)*np.sqrt(9.81/d)
else:
    uCorrIn = 0.0
ucI.append(uCorrIn)
data = '{:f}'.format(uCorrIn)
s.send(data.encode())
data = s.recv(1000)

# ------------------ Calculate uCorrOut ------------------
rampOut = np.interp(t,time,ramp2[:])
etaOut = np.interp(t,time,etaIPout)*rampOut
eO.append(etaOut)
if t > celdt:
    uCorrOut = (etaOut-etaWGout)*np.sqrt(9.81/d)
else:
    uCorrOut = 0.0
ucO.append(uCorrOut)
data = '{:f}'.format(uCorrOut)
s.send(data.encode())

# ------------------ Send Velocities ------------------
for iZ in range(11):
    data = s.recv(1000)
    uIn0 = np.interp(t,time,inlet[:,iZ+1])
    data = '{:f}'.format(uIn0)
```

```
            s.send(data.encode())
            data = s.recv(1000)
            uIn1 = np.interp(t+dt,time,inlet[:,iZ+1])
            data = '{:f}'.format(uIn1)
            s.send(data.encode())
            data = s.recv(1000)
            uOut0 = np.interp(t,time,outlet[:,iZ+1])
            data = '{:f}'.format(uOut0)
            s.send(data.encode())
            data = s.recv(1000)
            uOut1 = np.interp(t,time+dt,outlet[:,iZ+1])
            data = '{:f}'.format(uOut1)
            s.send(data.encode())

        #------------------ Send Zsurf ------------------------
        data = s.recv(1000)
        zsurf0 = np.interp(t,time,etaIP)*rampIn+d
        data = '{:f}'.format(zsurf0)
        s.send(data.encode())
        data = s.recv(1000)
        zsurf1 = np.interp(t+dt,time,etaIP)*rampIn+d
        data = '{:f}'.format(zsurf1)
        s.send(data.encode())

        count += 1

s.close()
```

E.2.4 Communication file `comm_socket_2way.py`

This file is very similar to the previous one, but manages the two-way communication. In addition to the code of `comm_socket.py`, there are several MPI commands to receive and send data from and to OceanWave3D:

```
from mpi4py import MPI
import socket
import numpy as np
from simsetup import *

#-~-~-~-~-~-~-~-~-~-~-~-~-~-~-~-~-~-~-~-~-~-~-~-~-~-~-~-~-~-~-
#                       MPI INITIALIZATION
#-~-~-~-~-~-~-~-~-~-~-~-~-~-~-~-~-~-~-~-~-~-~-~-~-~-~-~-~-~-~-

# Check if MPI is initialized
comm = MPI.COMM_WORLD
rank = comm.Get_rank()
```

```
print("Python rank = " + str(rank))

#-~-~-~
```

```
comm.Recv([data, MPI.DOUBLE], source=0, tag=25)
etaOW3D = data[:]

for iZ in range(11):
    uIn1 = np.interp(z[iZ]+d,ZO,uInOW3D)
    data = s.recv(1000)
    data = '{:f}'.format(uIn1)
    s.send(data.encode())
    uOut1 = np.interp(z[iZ]+d,ZO,uOutOW3D)
    data = s.recv(1000)
    data = '{:f}'.format(uOut1)
    s.send(data.encode())

# Send zsurf
data = s.recv(1000)
zsurf = np.interp(xIn,XO,etaOW3D+d)
data = '{:f}'.format(zsurf)
s.send(data.encode())

# Send nCouple
data = s.recv(1000)
data = '{:f}'.format(nCouple)
s.send(data.encode())

# Send xIn
data = s.recv(1000)
data = '{:f}'.format(xIn)
s.send(data.encode())

# Send dx
data = s.recv(1000)
data = '{:f}'.format(dx)
s.send(data.encode())

# Send nx
data = s.recv(1000)
data = '{:f}'.format(np.ceil((xOut-xIn)/dx))
s.send(data.encode())

# Data storage
uInOW3D_old = np.copy(uInOW3D)
uOutOW3D_old = np.copy(uOutOW3D)
etaOW3D_old = np.copy(etaOW3D)
xOW3D = np.arange(xIn,xOut-dx/2.0,dx)
etaAll = np.copy(xOW3D)*0.0
```

```
#-~-~-~-~-~-~-~-~-~-~-~-~-~-~-~-~-~-~-~-~-~-~-~-~-~-~-~-~-~-~-~-~-~-~-~-~-~-~-
#                    TIME STEPPING & COMMUNICATION
#-~-~-~-~-~-~-~-~-~-~-~-~-~-~-~-~-~-~-~-~-~-~-~-~-~-~-~-~-~-~-~-~-~-~-~-~-~-~-

WGin = []
WGout = []
ucO = []
ucI = []
eI = []
eO = []
eOW3D = []
tm = []

t = 0.0
count = 0

while (t<tsim-dt/2.0):

    #------------------- Receive from OW2D -------------------
    if (genType=='O' and nCouple==2):
        # Create an MPI status object
        status = MPI.Status()
        # Wait for a message without receiving it
        comm.Probe(source=0, tag=22, status=status)
        # Allocate a big enough data array of characters
        data = np.zeros(1, dtype=np.float64)
        # Receive time
        comm.Recv([data, MPI.DOUBLE], source=0, tag=22)
        tOW3D = data[0]
        print('tOW3D = ' + str(tOW3D))
        # Receive inlet velocity
        data = np.zeros(nzO, dtype=np.float64)
        comm.Recv([data, MPI.DOUBLE], source=0, tag=23)
        uInOW3D = data[:]
        # Receive outlet velocity
        data = np.zeros(nzO, dtype=np.float64)
        comm.Recv([data, MPI.DOUBLE], source=0, tag=24)
        uOutOW3D = data[:]
        # Receive eta
        data = np.zeros(nxO, dtype=np.float64)
        comm.Recv([data, MPI.DOUBLE], source=0, tag=25)
        etaOW3D = data[:]

    #------------------- Receive from DSPH -------------------
    # receive time
    data = s.recv(1000)
```

```
t = float(data)
print('tSPH = ' + str(t))
tm.append(t)
data = '{:f}'.format(1.0)
s.send(data.encode())
# receive etaWGIn
data = str(s.recv(1000))
etaWGin = float(data)-d
WGin.append(float(data))
data = '{:f}'.format(1.0)
s.send(data.encode())
# receive etaWGOut
data = str(s.recv(1000))
etaWGout = float(data)-d
WGout.append(float(data))

#------------------ Calculate uCorrIn ------------------
etaIn = np.interp(xIn+8.0*dp,XO,etaOW3D)
print('etaIn = ' + str(etaIn))
el.append(etaIn)
if t > celdt:
    uCorrIn = (etaWGin-etaIn)*np.sqrt(9.81/d)
else:
    uCorrIn = 0.0
ucl.append(uCorrIn)
data = '{:f}'.format(uCorrIn)
s.send(data.encode())
data = s.recv(1000)

#------------------ Calculate uCorrOut ------------------
etaOut = np.interp(xOut-8.0*dp,XO,etaOW3D)
print('etaOut = ' + str(etaOut))
eO.append(etaOut)
if t > celdt:
    uCorrOut = (etaOut-etaWGout)*np.sqrt(9.81/d)
else:
    uCorrOut = 0.0
ucO.append(uCorrOut)
data = '{:f}'.format(uCorrOut)
s.send(data.encode())

#------------------ Send Velocities ------------------
for iZ in range(11):
    data = s.recv(1000)
    uIn0 = np.interp(z[iZ]+d,ZO,uInOW3D_old)
    data = '{:f}'.format(uIn0)
```

```
        s.send(data.encode())
        data = s.recv(1000)
        uIn1 = np.interp(z[iZ]+d,ZO,uInOW3D)
        data = '{:f}'.format(uIn1)
        s.send(data.encode())
        data = s.recv(1000)
        uOut0 = np.interp(z[iZ]+d,ZO,uOutOW3D_old)
        data = '{:f}'.format(uOut0)
        s.send(data.encode())
        data = s.recv(1000)
        uOut1 = np.interp(z[iZ]+d,ZO,uOutOW3D)
        data = '{:f}'.format(uOut1)
        s.send(data.encode())

    # ------------------ Receive Eta ------------------------
    for iX in range(int(np.ceil((xOut-xIn)/dx))):
        data = s.recv(1000)
        etaAll[iX] = float(data)-d
        s.send(data.encode())
    eOW3D.append(etaAll)

    # ------------------ Send Zsurf -------------------------
    data = s.recv(1000)
    print("etaAll = " + data)
    zsurf0 = np.interp(xIn,XO,etaOW3D_old+d)
    data = '{:f}'.format(zsurf0)
    s.send(data.encode())
    data = s.recv(1000)
    zsurf1 = np.interp(xIn,XO,etaOW3D+d)
    data = '{:f}'.format(zsurf1)
    s.send(data.encode())

    # ------------------ Send Zsurf to OW3D ------------------
    # Relaxation zones
    etaCouple = f.relaxZones([xIn,xOut],XO,etaOW3D,d,
                             xOW3D,etaAll)

    data = np.zeros(1, dtype=np.float64) + float(xIn)
    comm.Send([data,MPI.DOUBLE],dest=0, tag=40)
    data = np.zeros(1, dtype=np.float64) + \
           float(np.ceil((xOut-xIn)/dx))
    comm.Send([data,MPI.DOUBLE],dest=0, tag=41)
    data = np.zeros(1, dtype=np.float64) + float(dx)
    comm.Send([data,MPI.DOUBLE],dest=0, tag=42)
    data = np.zeros(int(np.ceil((xOut-xIn)/dx)),
           dtype=np.float64) + etaAll
```

```
        comm.Send([data,MPI.DOUBLE],dest=0, tag=43)

        uInOW3D_old = np.copy(uInOW3D)
        uOutOW3D_old = np.copy(uOutOW3D)
        etaOW3D_old = np.copy(etaOW3D)
        count += 1

        np.save('etaSPH.npy',etaAll)
        np.save('etaOWD.npy',etaOW3D)
        np.save('xO.npy',XO)

s.close()
```

E.2.5 Functions file `functions.py`

This file contains functions for calculating the theoretical orbital velocities, to apply the relaxation functions, to create the input files and to post-process the results. However, this files contains 1300 lines of code, which is too much to include into this manuscript. The file is however available from the Github repository.

E.3 DualSPHysics Code Changes

E.3.1 Main file `JSphGpuSingle.cpp`

This is the main simulation file for a GPU run. Here, extra global variables are added for the communication with Python. Function are made for socket initialization, socket sending, socket receiving and closing the connection. During the time-stepping, values received from Python are stored in the global variables, while the free surface elevation is calculated and sent back to Python.
Line 37-49:

```
#include <iostream>
#include <sstream>
#include <sys/types.h>
#include <sys/socket.h>
#include <netinet/in.h>
#include <netdb.h>
#include <unistd.h>
#include <string>
#include <arpa/inet.h>
#include <string.h>
#include <stdio.h>
```

Line 54-72:

```
#define SERVER_PORT htons(50007)
```

```
int clientSock = 0;
int serverSock = 0;
double dwav = 0.0;
double ucorrIn = 0.0;
double ucorrOut = 0.0;
double zawasin = 0.0;
double zawasout = 0.0;
double facT = 0.0;
float* velIn;
float* velOut;
float* ZsurfS;
double velIn0[11] = {};
double velOut0[11] = {};
double velIn1[11] = {};
double velOut1[11] = {};
double ZsurfS0 = 0.0;
double ZsurfS1 = 0.0;
```

Line 641-662:

```
//~~~~~~~~~~~~~~~~~~~~~~~~~~~~~~~~~~~~~~~~~~~~~~~~~~~~~~~~~~~~~~~~
///                    Socket Init
//~~~~~~~~~~~~~~~~~~~~~~~~~~~~~~~~~~~~~~~~~~~~~~~~~~~~~~~~~~~~~~~~
void JSphGpuSingle::SocketInit(){

  // Start socket
  serverSock = socket(AF_INET, SOCK_STREAM, 0);

  sockaddr_in serverAddr;
  serverAddr.sin_family = AF_INET;
  serverAddr.sin_port = SERVER_PORT;
  serverAddr.sin_addr.s_addr = INADDR_ANY;

  // bind (this socket, local address, address length)
  bind(serverSock, (struct sockaddr*)&serverAddr,
       sizeof(struct sockaddr));

  // wait for a client
  cout << "Listening..." << endl;
  listen(serverSock,1);

  sockaddr_in clientAddr;
  socklen_t sin_size = sizeof(struct sockaddr_in);
  clientSock = accept(serverSock,
              (struct sockaddr*)&clientAddr, &sin_size);
  cout << "Connection Established!" << endl;
}
```

Line 666-675:

```
//_~_~_~_~_~_~_~_~_~_~_~_~_~_~_~_~_~_~_~_~_~_~_~_~_~_~_~_~_~_~_~_~_~_~_~_~_~_~_
///                    Socket Read
//_~_~_~_~_~_~_~_~_~_~_~_~_~_~_~_~_~_~_~_~_~_~_~_~_~_~_~_~_~_~_~_~_~_~_~_~_~_~_

double JSphGpuSingle::SocketRead(int clientSock,
                                 int serverSock){
  char buffer[1000];
  int n;

  bzero(buffer, 1000);
  n = read(clientSock, buffer, 500);
  double test = atof(buffer);

  return(test);
}
```

Line 680-691:

```
//_~_~_~_~_~_~_~_~_~_~_~_~_~_~_~_~_~_~_~_~_~_~_~_~_~_~_~_~_~_~_~_~_~_~_~_~_~_~_
///                   Socket Send
//_~_~_~_~_~_~_~_~_~_~_~_~_~_~_~_~_~_~_~_~_~_~_~_~_~_~_~_~_~_~_~_~_~_~_~_~_~_~_

void JSphGpuSingle::SocketSend(int clientSock,
                               int serverSock,
                               double test){
  char buffer[1000];
  char c[10];
  int n;

  bzero(buffer, 1000);

  sprintf(c, "%lf", test);

  strcpy(buffer, c);
  n = write(clientSock, buffer, strlen(buffer));
}
```

Line 696-703:

```
//_~_~_~_~_~_~_~_~_~_~_~_~_~_~_~_~_~_~_~_~_~_~_~_~_~_~_~_~_~_~_~_~_~_~_~_~_~_~_
///                   Socket close
//_~_~_~_~_~_~_~_~_~_~_~_~_~_~_~_~_~_~_~_~_~_~_~_~_~_~_~_~_~_~_~_~_~_~_~_~_~_~_
void JSphGpuSingle::SocketClose(int serverSock){

  close(serverSock);
  cout << "Server Closed!" << endl;
```

```
}
```

Line 741-778:

```
//-~-~-~-~-~-~-~-~-~-~-~-~-~-~-~-~-~-~-~-~-~-~-~-~-~-~-~-~-~-~-~-~-~-~-~-~-~-~-
///                        First Timestep
//-~-~-~-~-~-~-~-~-~-~-~-~-~-~-~-~-~-~-~-~-~-~-~-~-~-~-~-~-~-~-~-~-~-~-~-~-~-~-

  SocketInit();
  dwav = SocketRead(clientSock,serverSock);
  SocketSend(clientSock,serverSock,0.0);
  dtCom = SocketRead(clientSock,serverSock);
  dtComOrig = dtCom;
  velIn = new float[11];
  velOut = new float[11];
  for (size_t i = 0; i < 11; i++) {
    SocketSend(clientSock,serverSock,0.0);
    velIn1[i] = SocketRead(clientSock,serverSock);
    SocketSend(clientSock,serverSock,0.0);
    velOut1[i] = SocketRead(clientSock,serverSock);
  }
  SocketSend(clientSock,serverSock,0.0);
  ZsurfS1 = SocketRead(clientSock,serverSock);
  SocketSend(clientSock,serverSock,0.0);
  int nCouple = (int) SocketRead(clientSock,serverSock);
  std::cout << "nCouple = " << nCouple << '\n';
  char gaugeName[50];
  int nn;
  int nxG;
  if (nCouple > 1) {
    SocketSend(clientSock,serverSock,0.0);
    double xStart = SocketRead(clientSock,serverSock);
    SocketSend(clientSock,serverSock,0.0);
    double dxG = SocketRead(clientSock,serverSock);
    SocketSend(clientSock,serverSock,0.0);
    nxG = (int) SocketRead(clientSock,serverSock);
    // Define gauges for OW3D
    JGaugeSwl* gauge;
    for (int i = 0; i < nxG; i++) {
      nn = sprintf (gaugeName, "gauge_%d", i);
      gauge = GaugeSystem->AddGaugeSwl(gaugeName,0,
              DBL_MAX,0,TDouble3(xStart+i*dxG,1.0,0),
              TDouble3(xStart+i*dxG,1.0,1.17),
              GaugeSystem->GetDp()*0.25);
    }
  }
```

Line 810-862:

```
//_~_~_~_~_~_~_~_~_~_~_~_~_~_~_~_~_~_~_~_~_~_~_~_~_~_~_~_~_~_~_~_~_~_~_~_~_~_~_
///                    At Every Timestep
//_~_~_~_~_~_~_~_~_~_~_~_~_~_~_~_~_~_~_~_~_~_~_~_~_~_~_~_~_~_~_~_~_~_~_~_~_~_~_

  facT = (TimeStep-dtCom)/dtComOrig;

  // Read in new values
  if(TimeStep>=dtCom){

    // Measure Free Surface at inlet & outlet
    unsigned gid=GaugeSystem->GetGaugeIdx("MyGauge");
    JGaugeSwl* gswl=(JGaugeSwl*)GaugeSystem->GetGauge(gid);
    double lasttime=gswl->GetResult().timestep;
    SocketSend(clientSock,serverSock,lasttime);
    dummy = SocketRead(clientSock,serverSock);
    tfloat3 lastpointswl=gswl->GetResult().posswl;
    zawasout = lastpointswl.z;
    gid=GaugeSystem->GetGaugeIdx("MyGauge2");
    JGaugeSwl* gswl2=(JGaugeSwl*)GaugeSystem->GetGauge(gid);
    lasttime=gswl2->GetResult().timestep;
    lastpointswl=gswl2->GetResult().posswl;
    zawasin = lastpointswl.z;

    // Perform Communications
    SocketSend(clientSock,serverSock,zawasin);
    dummy = SocketRead(clientSock,serverSock);
    SocketSend(clientSock,serverSock,zawasout);
    ucorrIn = SocketRead(clientSock,serverSock);
    SocketSend(clientSock,serverSock,0.0);
    ucorrOut = SocketRead(clientSock,serverSock);

    for (size_t i = 0; i < 11; i++) {
      SocketSend(clientSock,serverSock,0.0);
      velIn0[i] = SocketRead(clientSock,serverSock);
      SocketSend(clientSock,serverSock,0.0);
      velIn1[i] = SocketRead(clientSock,serverSock);
      SocketSend(clientSock,serverSock,0.0);
      velOut0[i] = SocketRead(clientSock,serverSock);
      SocketSend(clientSock,serverSock,0.0);
      velOut1[i] = SocketRead(clientSock,serverSock);
    }

    if (nCouple > 1) {
      // Wave gauge measurements to send back
      for (int i = 0; i < nxG; i++) {
        nn = sprintf (gaugeName, "gauge_%d", i);
```

```
        gid = GaugeSystem->GetGaugeIdx(gaugeName);
        gswl2 = (JGaugeSwl*)GaugeSystem->GetGauge(gid);
        lastpointswl = gswl2->GetResult().posswl;
        etaAll = lastpointswl.z;
        SocketSend(clientSock,serverSock,etaAll);
        dummy = SocketRead(clientSock,serverSock);
      }
    }

    SocketSend(clientSock,serverSock,0.0);
    ZsurfS0 = SocketRead(clientSock,serverSock);
    SocketSend(clientSock,serverSock,0.0);
    ZsurfS1 = SocketRead(clientSock,serverSock);
    dtCom += dtComOrig;
  }
```

Line 884:

```
//_~_~_~_~_~_~_~_~_~_~_~_~_~_~_~_~_~_~_~_~_~_~_~_~_~_~_~_~_~_~_~_~_~_~_~_
///                    At Final Timestep
//_~_~_~_~_~_~_~_~_~_~_~_~_~_~_~_~_~_~_~_~_~_~_~_~_~_~_~_~_~_~_~_~_~_~_~_

  SocketClose(serverSock);
```

E.3.2 Inlet-Outlet file `JSphInOutGridData.cpp`

This file is normally used to impose external quantities, arranged on a grid, on to the inlet and outlet particles. Here, the horizontal orbital velocities received from Python, are interpolated in time, and copied to the GPU memory, together with the necessary velocity correction.
Line 39-47:

```
extern double ucorrIn;
extern double ucorrOut;
extern double facT;
extern float* velIn;
extern float* velOut;
extern double velIn0[11];
extern double velOut0[11];
extern double velIn1[11];
extern double velOut1[11];
```

Line 540-566:

```
//_~_~_~_~_~_~_~_~_~_~_~_~_~_~_~_~_~_~_~_~_~_~_~_~_~_~_~_~_~_~_~_~_~_~_~_
/// Interpolate velocity in time and Z-position
//_~_~_~_~_~_~_~_~_~_~_~_~_~_~_~_~_~_~_~_~_~_~_~_~_~_~_~_~_~_~_~_~_~_~_~_
```

```
void JSphInOutGridData::InterpolateZVelGpu(double time,
  unsigned izone,unsigned np,const int *plist,
  const double2 *posxyg,const double *poszg,
  const typecode *codeg,const unsigned *idpg,
  float4 *velrhopg){

  ComputeTimeGpu(time);
  // Interpolate velocities TVE
  for (size_t i = 0; i < 11; i++) {
    velIn[i] = velIn0[i] + facT*(velIn1[i]-velIn0[i]);
    velOut[i] = velOut0[i] + facT*(velOut1[i]-velOut0[i]);
  }
  double ucorr = 0.0;
  if (velrhopg){
    if (izone == 1){
      ucorr = ucorrOut;
      //SelVelxg = VelOut coming through socket
      cudaMemcpy(SelVelxg,velOut,sizeof(float)*Npt,
                 cudaMemcpyHostToDevice); //inlet
    } else {
      ucorr = ucorrIn;
      cudaMemcpy(SelVelxg,velIn,sizeof(float)*Npt,
                 cudaMemcpyHostToDevice); //outlet
  }
}

cusphinout::InOutInterpolateZVel(izone,PosMin.z,Dpz,Nz-1,
                                 SelVelxg,SelVelzg,np,
                                 plist,poszg,codeg,
                                 velrhopg,ucorr);
}

#endif
```

E.3.3 Inlet-Outlet GPU file `JSphGpu_InOut_ker.cu`

Here, the GPU calculations for the inlet and outlet points are performed. Only minor changes are made here. In the interpolation functions, the corrected velocity is added as an extra funciton variable, and in the funciton is subtracted from the imposed velocities.
1168-1195:

```
//~~~~~~~~~~~~~~~~~~~~~~~~~~~~~~~~~~~~~~~~~~~~~~~~~~~~~~~~
/// Interpolate velocity in time and Z-position.
//~~~~~~~~~~~~~~~~~~~~~~~~~~~~~~~~~~~~~~~~~~~~~~~~~~~~~~~~
__global__ void KerInOutInterpolateZVel(unsigned izone,
```

```
  double posminz,double dpz,int nz1,
  const float *velx,const float *velz,
  unsigned np,const int *plist,const double *posz,
  const typecode *code,float4 *velrhop, double ucorr)
{
  const unsigned cp=blockIdx.y*gridDim.x*blockDim.x +
                    blockIdx.x*blockDim.x + threadIdx.x;
                    //-Number of particle.
  if(cp<np){
    const unsigned p=plist[cp];

    if(izone==CODE_GetIzoneFluidInout(code[p])){
      const double pz=posz[p]-posminz;
      int cz=int(pz/dpz);
      cz=max(cz,0);
      cz=min(cz,nz1);
      const double fz=(pz/dpz-cz);

      //-Interpolation in Z.
      const unsigned cp=cz;
      const float v00=velx[cp];
      const float v01=(cz<nz1? velx[cp+1]: v00);
      const float v=float(fz*(v01-v00)+v00);
      velrhop[p]=make_float4(v-ucorr,0,0,velrhop[p].w);

      if(velz!=NULL){
        const float v00=velz[cp];
        const float v01=(cz<nz1? velz[cp+1]:     v00);
        const float v=float(fz*(v01-v00)+v00);
        velrhop[p].z=v;
      }
    }
  }
}
```

Line 1200-1209:

```
//-~-~-~-~-~-~-~-~-~-~-~-~-~-~-~-~-~-~-~-~-~-~-~-~-~-~-~-~-~-~-
/// Interpolate velocity in time and Z-position.
//-~-~-~-~-~-~-~-~-~-~-~-~-~-~-~-~-~-~-~-~-~-~-~-~-~-~-~-~-~-~-
void InOutInterpolateZVel(unsigned izone,
  double posminz,double dpz,int nz1,
  const float *velx,const float *velz,
  unsigned np,const int *plist,const double *posz,
  const typecode *code,float4 *velrhop, double ucorr)
{
  if(np){
```

```
    dim3 sgrid=cusph::GetGridSize(np,SPHBSIZE);
    KerInOutInterpolateZVel <<<sgrid,SPHBSIZE>>>(izone,
      posminz,dpz,nz1,velx,velz,np,plist,posz,code,
      velrhop,ucorr);
  }
}
```

E.3.4 Inlet-Outlet GPU file `JSphInOut.cpp`

Here, the function updating the surface elevation in the inlet zone is modified. The surface elevation received from Python is interpolated in time and copied to the GPU memory.
Line 48-50:

```
extern double ZsurfS0;
extern double ZsurfS1;
extern double facT;
```

Line 1411-1424:

```
//-~-~-~-~-~-~-~-~-~-~-~-~-~-~-~-~-~-~-~-~-~-~-~-~-~-~-~-~-~-~-
/// Updates zsurf according timestep.
/// Returns true when the data was changed.
//-~-~-~-~-~-~-~-~-~-~-~-~-~-~-~-~-~-~-~-~-~-~-~-~-~-~-~-~-~-~-
bool JSphInOut::UpdateZsurf(double timestep,bool full){
  const char met[]="UpdateZsurf";
  bool modified=full;

  for(unsigned ci=0;ci<ListSize;ci++)if(full ||
      List[ci]->GetVariableZsurf() ||
      List[ci]->GetCalculatedZsurf()){
        modified|=List[ci]->UpdateZsurf(timestep,
                                        full,Zsurf[ci]);
  }

  #ifdef _WITHGPU
  Zsurf[0] = (float)(ZsurfS0 + facT*(ZsurfS1-ZsurfS0));
  if(modified && !Cpu)cudaMemcpy(Zsurfg,Zsurf,
                                 sizeof(float)*ListSize,
                                 cudaMemcpyHostToDevice);
  #endif

  return(modified);
}
```

E.3.5 Inlet-Outlet GPU file `JSphGpu_ker.cu`

Here, the motion of floating objects can be restricted to a specific degree of freedom, for example the heave motion.
Line 2330-2334:

```
face.x *= 0.0;
face.y *= 0.0;
fomegaace.x *= 0.0;
fomegaace.y *= 0.0;
fomegaace.z *= 0.0;
```

References

Abas, N., Kalair, A., and Khan, N. (2015). Review of fossil fuels and future energy technologies. *Futures*, 69:31 – 49.

Agamloh, E. B., Wallace, A. K., and von Jouanne, A. (2008). Application of fluid-structure interaction simulation of an ocean wave energy extraction device. *Renewable Energy*, 33(4):748–757.

Airy, G. B. (1841). Tides and waves.

Alexandre, A., Stallard, T., and Stansby, P. K. (2009). Transformation of Wave Spectra across a Line of Wave Devices. *Power*, (Proceedings of the 8th European Wave and Tidal Energy Conference, Uppsala, Sweden):1–9.

Altomare, C., Crespo, A. J., Domínguez, J. M., Gómez-Gesteira, M., Suzuki, T., and Verwaest, T. (2015a). Applicability of Smoothed Particle Hydrodynamics for estimation of sea wave impact on coastal structures. *Coastal Engineering*, 96:1–12.

Altomare, C., Crespo, A. J., Rogers, B., Domínguez, J., Gironella, X., and Gómez-Gesteira, M. (2014). Numerical modelling of armour block sea breakwater with smoothed particle hydrodynamics. *Computers & Structures*, 130:34–45.

Altomare, C., Domínguez, J., Crespo, A., González-Cao, J., Suzuki, T., Gómez-Gesteira, M., and Troch, P. (2017). Long-crested wave generation and absorption for sph-based dualsphysics model. *Coastal Engineering*, 127:37–54.

Altomare, C., Domínguez, J. M., Crespo, A. J. C., Suzuki, T., Caceres, I., and Gómez-Gesteira, M. (2016a). Hybridisation of the wave propagation model SWASH and the meshfree particle method SPH for real coastal applications. *Coastal Engineering Journal*, 57(4):1–34.

Altomare, C., Suzuki, T., Crespo, A., Domínguez, J., Barreiro, A., González-Cao, J., and Gómez-Gesteira, M. (2016b). Sph model to simulate oscillating water column wave energy converter. In *11th International Spheric workshop 2016*, pages 1–8.

Altomare, C., Suzuki, T., Domínguez, J., Barreiro, A., Crespo, A., and Gómez-Gesteira, M. (2015b). Numerical wave dynamics using lagrangian approach:

wave generation and passive & active wave absorption. In *Proceedings of the 10th SPHERIC International Workshop, Parma, Italy*.

Altomare, C., Tagliafierro, B., Domínguez, J., Suzuki, T., and Viccione, G. (2018a). Improved relaxation zone method in sph-based model for coastal engineering applications. *Applied Ocean Research*, 81:15 – 33.

Altomare, C., Tagliafierro, B., Suzuki, T., Domínguez, J. M., Crespo, A. J., Briganti, R., et al. (2018b). Relaxation zone method in sph-based model applied to wave-structure interaction. In *The 28th International Ocean and Polar Engineering Conference*. International Society of Offshore and Polar Engineers.

Alves, M. (2016). Frequency-Domain Models. In *Numerical Modelling of Wave Energy Converters*, pages 11–30. Elsevier.

Antuono, M., Colagrossi, A., and Marrone, S. (2012). Numerical diffusive terms in weakly-compressible sph schemes. *Computer Physics Communications*, 183(12):2570 – 2580.

Aqwa, A. (2018). Hydrodynamics Simulation and Diffraction Analysis.

Babarit, A. (2015). A database of capture width ratio of wave energy converters. *Renewable Energy*, 80:610–628.

Babarit, A. and Delhommeau, G. (2015). Theoretical and numerical aspects of the open source BEM solver NEMOH. In *Proceedings of the 11th European Wave and Tidal Energy Conference.*, pages 1–12, Nantes.

Babarit, A., Folley, M., Charrayre, F., Peyrard, C., and Benoit, M. (2013). On the modelling of WECs in wave models using far field coefficients. *European Wave and Tidal Energy Conference, EWTEC*, pages 1—-9.

Balitsky, P., Fernandez, G. V., Stratigaki, V., and Troch, P. (2017a). Coupling methodology for modelling the near-field and far-field effects of a wave energy converter. In *ASME 2017 36th International Conference on Ocean, Offshore and Arctic Engineering*, pages V010T09A029–V010T09A029. American Society of Mechanical Engineers.

Balitsky, P., Verao Fernandez, G., Stratigaki, V., and Troch, P. (2017b). Assessing the impact on power production of wec array separation distance in a wave farm using one-way coupling of a bem solver and a wave propagation model. In *Proceedings of the 12th wave and tidal energy conference*, pages 1176–1186.

Batchelor, G. K. (2000). *An introduction to fluid dynamics*. Cambridge university press.

Beels, C. (2009). *Optimization of the lay-out of a farm of wave energy converters in the North Sea: analysis of wave power resources, wake effects, production and cost*.

Beels, C., De Backer, G., and Mathys, P. (2008). Wave energy conversion in a sheltered sea. *SEA TECHNOLOGY*, 49(9):21–24.

Beels, C., Troch, P., De Backer, G., Vantorre, M., and De Rouck, J. (2010). Numerical implementation and sensitivity analysis of a wave energy converter in a time-dependent mild-slope equation model. *Coastal Engineering*, 57(5):471–492.

Beels, C., Troch, P., Kofoed, J. P., Frigaard, P., Kringelum, J. V., Kromann, P. C., Donovan, M. H., De Rouck, J., and De Backer, G. (2011). A methodology for production and cost assessment of a farm of wave energy converters. *RENEWABLE ENERGY*, 36(12):3402–3416.

Bellew, S. and Stallard, T. (2010). Linear modelling of wave device arrays and comparison to experimental and second order models. In *Proc. Int. Workshop for Water Waves and Floating Bodies*, pages 1–4.

Bellew, S., Stallard, T., and Stansby, P. (2009). Optimisation of a heterogeneous array of heaving bodies. In *Proceedings of the 8th European Wave and Tidal Energy Conference*, pages 519–527.

Biausser, B., Fraunié, P., Grilli, S. T., Marcer, R., et al. (2004). Numerical analysis of the internal kinematics and dynamics of 3-d breaking waves on slopes. *International Journal of Offshore and Polar Engineering*, 14(04).

Bouscasse, B., Colagrossi, A., Marrone, S., and Antuono, M. (2013a). Nonlinear water wave interaction with floating bodies in sph. *Journal of Fluids and Structures*, 42:112–129.

Bouscasse, B., Marrone, S., Colagrossi, A., and Di Mascio, A. (2013b). Multipurpose interfaces for coupling SPH with other solvers. In *Proceedings of the 8th International SPHERIC Workshop*, Trondheim.

Brorsen, M. and Helm-Petersen, J. (1999). On the reflection of short-crested waves in numerical models. *Coastal Engineering 1998*.

Budal, K. (1977). Theory for absorption of wave power by a system of interacting bodies. *Journal of Ship Research*.

Canelas, R., Brito, M., Feal, O., Domínguez, J., and Crespo, A. (2018). Extending dualsphysics with a differential variational inequality: modeling fluid-mechanism interaction. *Applied Ocean Research*, 76:88 – 97.

Canelas, R. B., Domínguez, J. M., Crespo, A. J., Gómez-Gesteira, M., and Ferreira, R. M. (2015). A smooth particle hydrodynamics discretization for the modelling of free surface flows and rigid body dynamics. *International Journal for Numerical Methods in Fluids*, 78(9):581–593.

Carballo, R. and Iglesias, G. (2013). Wave farm impact based on realistic wave-WEC interaction. *Energy*, 51:216–229.

Chang, K.-H., Sheu, T. W.-H., and Chang, T.-J. (2018). A 1d–2d coupled sph-swe model applied to open channel flow simulations in complicated geometries. *Advances in Water Resources*, 115:185 – 197.

Charrayre, F., Benoit, M., Peyrard, C., Babarit, A., Edf, H. S.-V., and Paristech, P. (2014a). Modeling of interactions in a farm of wave energy converters taking into account the bathymetry. *14eme Journées de l'Hydrodynamique*, pages 1–12.

Charrayre, F., Peyrard, C., Benoit, M., and Babarit, A. (2014b). A coupled methodology for wave-body interactions at the scale of a farm of wave energy converters including irregular bathymetry. In *ASME 2014 33rd International Conference on Ocean, Offshore and Arctic Engineering*, pages V08AT06A043–V08AT06A043. American Society of Mechanical Engineers.

Chen, D.-W., Tzang, S.-Y., Hsieh, C.-M., Chow, Y.-C., Chen, J.-H., Lin, C.-C., and Hwang, R. R.-J. (2014). Numerical modeling of wave-induced rotations of a bottom-hinged flapper with a sph model. *Journal of Marine Science and Technology*, 22(3):372–380.

Chicheportiche, J., Hergault, V., Yates, M., Raoult, C., Leroy, A., Joly, A., and Violeau, D. (2016). Coupling SPH with a potential Eulerian model for wave propagation problems. In *Proceedings of the 11th SPHERIC International Workshop*, number 1, pages 246–252, Munich.

Child, B. (2016). Semi-analytical Array Models. In *Numerical Modelling of Wave Energy Converters*, pages 165–190. Elsevier.

Colicchio, G., Greco, M., and Faltinsen, O. (2006). A bem-level set domain-decomposition strategy for non-linear and fragmented interfacial flows. *International journal for numerical methods in engineering*, 67(10):1385–1419.

Crespo, A., Altomare, C., Domínguez, J., González-Cao, J., and Gómez-Gesteira, M. (2017). Towards simulating floating offshore oscillating water column converters with Smoothed Particle Hydrodynamics. *Coastal Engineering*, 126:11–26.

Crespo, A., Domínguez, J., Gómez-Gesteira, M., Barreiro, A., and Rogers, B. (2018a). User guide for dualsphysics code. *University of Vigo. The University of Manchester and Johns Hopkins University*.

Crespo, A., Domínguez, J., Gómez-Gesteira, M., Hall, M., Altomare, C., Wu, M., Verbrugghe, T., Stratigaki, V., Troch, P., Kisacik, D., Simonetti, I., Cappietti, L., Canelas, R., Ferreira, R., and Stansby, P. (2018b). Survivability of floating moored offshore structures studied with dualsphysics. In *Proceedings of the 13th International SPHERIC Workshop*.

Crespo, A., Domínguez, J., Rogers, B., Gómez-Gesteira, M., Longshaw, S., Canelas, R., Vacondio, R., Barreiro, A., and García-Feal, O. (2015). DualSPHysics: Open-source parallel CFD solver based on Smoothed Particle Hydrodynamics (SPH). *Computer Physics Communications*, 187:204–216.

Crespo, A., Gómez-Gesteira, M., and Dalrymple, R. A. (2007). Boundary conditions generated by dynamic particles in sph methods. *CMC-TECH SCIENCE PRESS-*, 5(3):173.

Dalrymple, R. and Rogers, B. (2006). Numerical modeling of water waves with the sph method. *Coastal engineering*, 53(2):141–147.

De Backer, G. (2009). *Hydrodynamic Design Optimization of Wave Energy Converters Consisting of Heaving Point Absorbers*. PhD thesis, University Of Ghent.

Dean and Dalrymple (1991a). *Wavemaker Theory*, pages 170–186. WORLD SCIENTIFIC.

Dean, R. G. and Dalrymple, R. A. (1991b). *Water wave mechanics for engineers and scientists*, volume 2. world scientific publishing Co Inc.

Delhommeau, G. (1987). *Les problemes de diffraction-radiation et de resistance de vagues : etude theorique et resolution numerique par la methode des singularites*. PhD thesis.

Delhommeau, G. (1989). Amélioration des performances des codes de calcul de diffraction-radiation au premier ordre. *Proc. Deuxièmes Journées de l'Hydrodynamique*.

Devolder, B. (2018). *Hydrodynamic Modelling of Wave Energy Converter Arrays*. PhD thesis, PhD thesis, Ghent University and KU Leuven.

Devolder, B., Rauwoens, P., and Troch, P. (2016). Numerical simulation of a single Floating Point Absorber Wave Energy Converter using OpenFOAM®. In *2nd International Conference on Renewable Energies Offshore*, number 5, pages 1–2.

Didier, E., Neves, D., Teixeira, P. R. F., Neves, M. G., Viegas, M., and Soares, H. (2013). Coupling of FLUINCO mesh-based and SPH mesh-free numerical codes for the modeling of wave overtopping over a porous breakwater. In *International Short Course on Applied Coastal Research*, Lisbon.

Didier, E. and Neves, M. (2012). A semi-infinite numerical wave flume using smoothed particle hydrodynamics. 22:193–199.

Domínguez, J., Crespo, A., Fourtakas, G., Rogers, B., Cercós-Pita, J., and Vacondio, R. (2015). Evaluation of reliability and efficiency of different boundary conditions in an sph code. In *Proceedings of the 10th SPHERIC International Workshop, Parma, Italy*.

Domínguez, J. M., Crespo, A. J., and Gómez-Gesteira, M. (2013). Optimization strategies for cpu and gpu implementations of a smoothed particle hydrodynamics method. *Computer Physics Communications*, 184(3):617–627.

Engsig-Karup, A. P., Bingham, H. B., and Lindberg, O. (2009). An efficient flexible-order model for 3D nonlinear water waves. *Journal of Computational Physics*, 228(6):2100–2118.

Engsig-Karup, A. P., Glimberg, S. L., Nielsen, A. S., and Lindberg, O. (2013). Fast hydrodynamics on heterogeneous many-core hardware. *Designing Scientific Applications on GPUs*, pages 251–294.

Evans, D. (1980). Some analytic results for two and three dimensional wave-energy absorbers. *Power from sea waves*.

Falnes, J. (1980). Radiation impedance matrix and optimum power absorption for interacting oscillators in surface waves. *Applied Ocean Research*, 2(2):75–80.

Fenton, J. D. (1985). A fifth-order stokes theory for steady waves. *Journal of waterway, port, coastal, and ocean engineering*, 111(2):216–234.

Finnegan, W. and Goggins, J. (2012). Numerical simulation of linear water waves and wave–structure interaction. *Ocean Engineering*, 43:23–31.

Fitzgerald, C. (2016). Nonlinear Potential Flow Models. In *Numerical Modelling of Wave Energy Converters*, pages 83–104. Elsevier.

Folley, M. (2016a). *Numerical Modelling of Wave Energy Converters: State-of-the-Art Techniques for Single Devices and Arrays*. Academic Press.

Folley, M. (2016b). Spectral-Domain Models. In *Numerical Modelling of Wave Energy Converters*, pages 67–80. Elsevier.

Folley, M., Babarit, A., Child, B., Forehand, D., O'Boyle, L., Silverthorne, K., Spinneken, J., Stratigaki, V., and Troch, P. (2012). A review of numerical modelling of wave energy converter arrays. In *ASME 2012 31st International Conference on Ocean, Offshore and Arctic Engineering*, pages 535–545. American Society of Mechanical Engineers.

Fourtakas, G., Stansby, P., Rogers, B., and Lind, S. (2018). An Eulerian-Lagrangian incompressible SPH formulation (ELI-SPH) connected with a sharp interface. *Comput. Methods Appl. Mech. Engrg. Comput. Methods Appl. Mech. Engrg*, 329(329):532–552.

Fourtakas, G., Stansby, P. K., Rogers, B. D., Lind, S. J., Yan, S., Ma, Q. W., et al. (2017). On the coupling of incompressible sph with a finite element potential flow solver for nonlinear free surface flows. In *The 27th International Ocean and Polar Engineering Conference*. International Society of Offshore and Polar Engineers.

Frigaard, P. and Andersen, T. L. (2014). Analysis of waves: Technical documentation for wavelab 3. Technical report, Department of Civil Engineering, Aalborg University.

Frigaard, P. and Christensen, M. (1995). An absorbing wave-maker based on digital filters. In *Coastal Engineering 1994*, pages 168–180.

Gomez-Gesteira, M., Rogers, B. D., Crespo, A. J., Dalrymple, R. A., Narayanaswamy, M., and Domínguez, J. M. (2012). Sphysics–development of a free-surface fluid solver–part 1: Theory and formulations. *Computers & Geosciences*, 48:289–299.

Gotoh, H. and Khayyer, A. (2018). On the state-of-the-art of particle methods for coastal and ocean engineering. *Coastal Engineering Journal*, 0(0):1–25.

Gu, H., Stansby, P., Stallard, T., and Moreno, E. C. (2018). Drag, added mass and radiation damping of oscillating vertical cylindrical bodies in heave and surge in still water. *Journal of Fluids and Structures*, 82:343–356.

Gunn, K. and Stock-Williams, C. (2012). Quantifying the global wave power resource. *Renewable Energy*, 44:296–304.

Guo, L.-d., Sun, D.-p., and Hao, W. (2012). A new numerical wave flume combining the 0–1 type bem and the vof method. *Journal of Hydrodynamics, Ser. B*, 24(4):506–517.

Hadžić, I., Hennig, J., Perić, M., and Xing-Kaeding, Y. (2005). Computation of flow-induced motion of floating bodies. *Applied mathematical modelling*, 29(12):1196–1210.

Hall, M. and Goupee, A. (2015). Validation of a lumped-mass mooring line model with DeepCwind semisubmersible model test data. *Ocean Engineering*, 104:590–603.

Hildebrandt, A., Sriram, V., Schlurmann, T., et al. (2013). Simulation of focusing waves and local line forces due to wave impacts on a tripod structure. In *The Twenty-third International Offshore and Polar Engineering Conference*. International Society of Offshore and Polar Engineers.

Hill, C. (2018). Wamit R User Manual.

IEA, I. E. A. (2017). Key world energy statistics.

Ito, S. (2018). STUDY OF THE TRANSIENT HEAVE OSCILLATION OF A FLOATING CYLINDER.

Iturrioz, A., Guanche, R., Armesto, J., Alves, M., Vidal, C., and Losada, I. (2014). Time-domain modeling of a fixed detached oscillating water column towards a floating multi-chamber device. *Ocean Engineering*, 76:65 – 74.

Janssen, C. F., Krafczyk, M., Grilli, S., et al. (2010). Modeling of wave breaking andwave-structure interactions by coupling of fully nonlinear potential flow and lattice-boltzmann models. In *The Twentieth International Offshore and Polar Engineering Conference*. International Society of Offshore and Polar Engineers.

Kassiotis, C., Ferrand, M., Violeau, D., Rogers, B., Stansby, P., Benoit, M., Rogers, B. D., and Stansby, P. K. (2011). Coupling SPH with a 1-D Boussinesq-type wave model. In *6th International SPHERIC Workshop*, pages 241–247, Hamburg.

Kim, S.-H., Yamashiro, M., and Yoshida, A. (2010). A simple two-way coupling method of bem and vof model for random wave calculations. *Coastal Engineering*, 57(11):1018–1028.

Kumar, P., Yang, Q., Jones, V., and Mccue-Weil, L. (2015). Coupled SPH-FVM simulation within the OpenFOAM framework. *Procedia IUTAM*, 18:76–84.

Lachaume, C., Biausser, B., Fraunié, P., Grilli, S. T., Guignard, S., et al. (2003). Modeling of breaking and post-breaking waves on slopes by coupling of bem and vof methods. In *The Thirteenth International Offshore and Polar Engineering Conference*. International Society of Offshore and Polar Engineers.

Larsen, J. and Dancy, H. (1983). Open boundaries in short wave simulations — A new approach. *Coastal Engineering*, 7(3):285–297.

Le Crom, I., Brito-Melo, A., and Sarmento, A. (2008). Maritime portuguese pilot zone for wave energy conversion: Modelling analysis of the impact on surfing conditions. In *Proc. 2nd International Conference on Ocean Energy*.

Le Méhauté, B. (1969). An introduction to hydrodynamics and water waves. *Oceanic Fronts in Coastal Processes*, page 114.

Lee, E.-S., Violeau, D., Issa, R., and Ploix, S. (2010). Application of weakly compressible and truly incompressible SPH to 3-D water collapse in waterworks. *Journal of Hydraulic Research*, 48(sup1):50–60.

Leimkuhler, B. J., Reich, S., and Skeel, R. D. (1996). Integration methods for molecular dynamics. *IMA Volumes in Mathematics and its Applications*, 82:161–186.

Li, G., Weiss, G., Mueller, M., Townley, S., and Belmont, M. R. (2012). Wave energy converter control by wave prediction and dynamic programming. *Renewable Energy*, 48:392–403.

Lin, P. and Liu, P. L.-F. (1999). Internal wave-maker for navier-stokes equations models. *Journal of waterway, port, coastal, and ocean engineering*, 125(4):207–215.

Lind, S., Xu, R., Stansby, P., and Rogers, B. (2012). Incompressible smoothed particle hydrodynamics for free-surface flows: A generalised diffusion-based algorithm for stability and validations for impulsive flows and propagating waves. *Journal of Computational Physics*, 231:1499–1523.

Liu, M. and Liu, G. (2006). Restoring particle consistency in smoothed particle hydrodynamics. *Applied Numerical Mathematics*, 56(1):19 – 36.

López, I., Andreu, J., Ceballos, S., Martínez De Alegría, I., and Kortabarria, I. (2013). Review of wave energy technologies and the necessary power-equipment. *Renewable and Sustainable Energy Reviews*, 27:413–434.

Manenti, S., Panizzo, A., Ruol, P., and Martinelli, L. (2008). Sph simulation of a floating body forced by regular waves. In *Proceedings of 3rd SPHERIC Workshop*, pages 38–41.

Marrone, S., Di Mascio, A., and Le Touzé, D. (2016). Coupling of smoothed particle hydrodynamics with finite volume method for free-surface flows. *Journal of Computational Physics*, 310:161–180.

Mccallum, P. D. (2017). *Numerical methods for modelling the viscous effects on the interactions between multiple wave energy converters*. University of Edinburgh, Edinburgh.

Mendes, L., Palha, A., Fortes, C. J., Sarmento, A., et al. (2008). Analysis of the impact of a pilot zone for wave energy conversion offshore portugal. In *The Eighteenth International Offshore and Polar Engineering Conference*. International Society of Offshore and Polar Engineers.

Meringolo, D. D., Aristodemo, F., and Veltri, P. (2015). Sph numerical modeling of wave–perforated breakwater interaction. *Coastal Engineering*, 101:48–68.

Meringolo, D. D., Colagrossi, A., Marrone, S., and Aristodemo, F. (2017). On the filtering of acoustic components in weakly-compressible SPH simulations.

Millar, D. L., Smith, H. C. M., and Reeve, D. E. (2007). Modelling analysis of the sensitivity of shoreline change to a wave farm. *Ocean Engineering*, 34(5-6):884–901.

Mokos, A., Rogers, B. D., Stansby, P. K., and Domínguez, J. M. (2015). Multi-phase sph modelling of violent hydrodynamics on gpus. *Computer Physics Communications*, 196:304 – 316.

Molteni, D. and Colagrossi, A. (2009). A simple procedure to improve the pressure evaluation in hydrodynamic context using the sph. *Computer Physics Communications*, 180(6):861 – 872.

Monaghan, J. and Kos, A. (1999). Solitary waves on a cretan beach. *Journal of waterway, port, coastal, and ocean engineering*, 125(3):145–155.

Monaghan, J., Kos, A., and Issa, N. (2003). Fluid motion generated by impact. *Journal of Waterway, Port, Coastal, and Ocean Engineering*, 129(6):250–259.

Monaghan, J. J. (1992). Smoothed particle hydrodynamics. *Annual review of astronomy and astrophysics*, 30(1):543–574.

Monaghan, J. J. (1994). Simulating free surface flows with sph. *Journal of computational physics*, 110(2):399–406.

Monaghan, J. J. (2005). Smoothed particle hydrodynamics. *Reports on progress in physics*, 68(8):1703.

Moreno, E. C. (2015). *Wave energy conversion based on multi-mode line absorbing systems*. PhD thesis, The University of Manchester.

Napoli, E., De Marchis, M., Gianguzzi, C., Milici, B., and Monteleone, A. (2016). A coupled finite volume–smoothed particle hydrodynamics method for incompressible flows. *Computer Methods in Applied Mechanics and Engineering*, 310:674–693.

Narayanaswamy, M., Crespo, A. J. C., Gómez-Gesteira, M., and Dalrymple, R. A. (2010). Sphysics-funwave hybrid model for coastal wave propagation. *Journal of Hydraulic Research*, 48(S1):85–93.

Ni, X., Feng, W., Huang, S., Zhang, Y., and Feng, X. (2018). A sph numerical wave flume with non-reflective open boundary conditions. *Ocean Engineering*, 163:483 – 501.

Ni, X., Feng, W., and Wu, D. (2014). Numerical simulations of wave interactions with vertical wave barriers using the sph method. *International Journal for Numerical Methods in Fluids*, 76(4):223–245.

Ni, X. Y. and Feng, W. B. (2013). Numerical Simulation of Wave Overtopping Based on DualSPHysics. *Applied Mechanics and Materials*, 405-408:1463–1471.

of Engineers, U. A. C. (2002). *Coastal Engineering Manual, Chapter II-1. Engineer Manual 1110-2-1110*. U.s. Army Corps of Engineers, Washington, D.C.

Omidvar, P., Stansby, P. K., and Rogers, B. D. (2012). Wave body interaction in 2d using smoothed particle hydrodynamics (sph) with variable particle mass. *International Journal for Numerical Methods in Fluids*, 68(6):686–705.

Omidvar, P., Stansby, P. K., and Rogers, B. D. (2013). Sph for 3d floating bodies using variable mass particle distribution. *International Journal for Numerical Methods in Fluids*, 72(4):427–452.

Padova, D. D., Dalrymple, R. A., and Mossa, M. (2014). Analysis of the artificial viscosity in the smoothed particle hydrodynamics modelling of regular waves. *Journal of Hydraulic Research*, 52(6):836–848.

Pelc, R. and Fujita, R. M. (2002). Renewable energy from the ocean. *Marine Policy*, 26(6):471 – 479.

Penalba, M., Giorgi, G., and Ringwood, J. V. (2017). Mathematical modelling of wave energy converters: A review of nonlinear approaches. *Renewable and Sustainable Energy Reviews*, 78:1188–1207.

Radder, A. and Dingemans, M. (1985). Canonical equations for almost periodic, weakly nonlinear gravity waves. *Wave Motion*, 7(5):473–485.

Rahmati, M. and Aggidis, G. (2016). Numerical and experimental analysis of the power output of a point absorber wave energy converter in irregular waves. *Ocean Engineering*, 111:483–492.

Ren, B., He, M., Dong, P., and Wen, H. (2015). Nonlinear simulations of wave - induced motions of a freely floating body using WCSPH method. *Applied Ocean Research*, 50:1–12.

Ricci, P. (2016). Time-Domain Models. In *Numerical Modelling of Wave Energy Converters*, pages 31–66. Elsevier.

Richardson, L. F. (1911). The approximate arithmetical solution by finite differences of physical problems involving differential equations, with an application to the stresses in a masonry dam. *Philosophical Transactions of the Royal Society of London. Series A, Containing Papers of a Mathematical or Physical Character*, 210:307–357.

Richardson, L. F. and Gaunt, J. A. (1927). The deferred approach to the limit. part i. single lattice. part ii. interpenetrating lattices. *Philosophical Transactions of the Royal Society of London. Series A, containing papers of a mathematical or physical character*, 226:299–361.

Rogers, B. D. and Dalrymple, R. A. (2008). Sph modeling of tsunami waves. *Advances in Coastal and Ocean Engineering*, 10:75–100.

Roselli, R. A. R., Vernengo, G., Altomare, C., Brizzolara, S., Bonfiglio, L., and Guercio, R. (2018). Ensuring numerical stability of wave propagation by tuning model parameters using genetic algorithms and response surface methods. *Environmental Modelling & Software*, 103:62–73.

Salter, S. H. (1981). Absorbing wave makers and wide tanks. Proceedings of the Conference on Directional Wave Applications.

Savitzky, A. and Golay, M. J. (1964). Smoothing and differentiation of data by simplified least squares procedures. *Analytical chemistry*, 36(8):1627–1639.

Schäffer, H. A. and Klopman, G. (2000). Review of multidirectional active wave absorption methods. *Journal of waterway, port, coastal, and ocean engineering*, 126(2):88–97.

Seelig, W. (1983). Wave reflection from coastal structures. In *Proceedings of coastal structures 1983 Conference*, pages 961–973, Arlington, USA, ASCE, New York.

Seelig, W. N. (1980). Estimation of wave transmission coefficients for overtopping of impermeable breakwaters. Technical report, COASTAL ENGINEERING RESEARCH CENTER FORT BELVOIR VA.

Simscale (2018). Free Heave Motion of a Floating Cylinder.

Sriram, V., Ma, Q., and Schlurmann, T. (2014). A hybrid method for modelling two dimensional non-breaking and breaking waves. *Journal of computational physics*, 272:429–454.

Stratigaki, V., Troch, P., Stallard, T., Forehand, D., Kofoed, J., Folley, M., Benoit, M., Babarit, A., and Kirkegaard, J. (2014a). Modelling of wave attenuation induced by multi-purpose floating structures used for power supply and coastal protection. *Proceedings of the Coastal Engineering Conference*, 2014-January.

Stratigaki, V., Troch, P., Stallard, T., Forehand, D., Kofoed, J. P., Folley, M., Benoit, M., Babarit, A., and Kirkegaard, J. (2014b). Wave basin experiments with large wave energy converter arrays to study interactions between the converters and effects on other users in the sea and the coastal area. *Energies*, 7(2):701–734.

Stratigaki, V., Vanneste, D., Troch, P., Gysens, S., and Willems, M. (2011). Numerical modeling of wave penetration in ostend harbour. *Coastal Engineering Proceedings*, 1(32):42.

Tafuni, A., Domínguez, J., Vacondio, R., and Crespo, A. (2018). A versatile algorithm for the treatment of open boundary conditions in smoothed particle hydrodynamics gpu models. *Computer Methods in Applied Mechanics and Engineering*, 342(1):604–624.

Tafuni, A., Domínguez, J., Vacondio, R., Sahin, I., and Crespo, A. (2016). Open boundary conditions for large-scale sph simulations. In *Proceedings of the 11th SPHERIC International Workshop*.

Tafuni, A., Domínguez, J. M., Vacondio, R., and Crespo, A. (2017). Accurate and efficient SPH open boundary conditions for real 3-D engineering problems. In *12th International SPHERIC Workshop*, pages 1–12, Ourense.

Thomas, S., Weller, S., and Stallard, T. (2008). Float response within an array: Numerical and experimental comparison. In *Proceedings of the 2nd International Conference on Ocean Energy (ICOE), Brest, France*, volume 1517.

Todalshaug, J. H. (2013). Practical limits to the power that can be captured from ocean waves by oscillating bodies. *International Journal of Marine Energy*, 3-4.

Tomey-Bozo, N., Murphy, J., Lewis, T., Troch, P., Babarit, A., and Thomas, G. (2016). The modelling of a flap type wave energy converter in a time-dependent mild-slope equation model. In *Progress in Renewable Energies Offshore: Proceedings of the 2nd International Conference on Renewable Energies Offshore (RENEW2016), Lisbon, Portugal, 24-26 October 2016*, page 277. CRC Press.

Troch, P. (1998). A numerical model for propagation & transformation of linear water waves. Technical report, Department of Civil Engineering, Ghent University.

Troch, P., Beels, C., De Rouck, J., and De Backer, G. (2010). Wake effects behind a farm of wave energy converters for irregular long-crested and short-crested waves. In *32nd International conference on Coastal Engineering (ICCE 2010)*, volume 32, pages 1–15. Engineering Foundation. Council on Wave Research.

Troch, P. and Stratigaki, V. (2016). Phase-resolving wave propagation array models. In Foley, M., editor, *Numerical modelling of wave energy converters : state-of-the-art techniques for single devices and arrays*, pages 191–216. Elsevier.

Venugopal, V. and Smith, G. H. (2007). Wave climate investigation for an array of wave power devices. *7th European Wave and Tidal Energy Conference*, pages 1–10.

Verao Fernandez, G., Balitsky, P., Stratigaki, V., and Troch, P. (2018). Validation of a coupling methodology for numerical modelling of near and far field effects of wave energy converter arrays using the mildwave and nemoh models, based on the wecwakes experimental database. In *VLIZ Marine Scientists Day, Book of Abstracts*, pages 124–125.

Verao Fernandez, G., Balitsky, P., Tomey Bozo, N., Stratigaki, V., and Troch, P. (2017). Far-field effects by arrays of oscillating wave surge converters and heaving point absorbers : a comparative study. In *Proceedings of the 12th wave and tidal energy conference*, pages 1030–1039.

Verbrugghe, T., Devolder, B., Domínguez, J., Kortenhaus, A., and Troch, P. (2017a). Feasibility study of applying sph in a coupled simulation tool for wave energy converter arrays. In *Proceedings of the 12th wave and tidal energy conference*, pages 679–689.

Verbrugghe, T., Stratigaki, V., Troch, P., Rabussier, R., and Kortenhaus, A. (2017b). A Comparison Study of a Generic Coupling Methodology for Modeling Wake Effects of Wave Energy Converter Arrays. *Energies*, 10(1697):1–25.

Verbrugghe, T., Troch, P., Kortenhaus, A., and Stratigaki, V. (2016). Development of a numerical modelling tool for combined near field and far field wave transformations using a coupling of potential flow solvers. In *Conference: 2nd International Conference on Renewable energies Offshore*, pages 61–68.

Vidal, C., Méndez Fernando, J., Díaz, G., and Legaz, R. (2007). Impact of santoña wec installation on the littoral processes. In *Proceedings of the 7th European wave and tidal energy conference, Porto, Portugal*, pages 11–14.

Wamit (2016). Wamit User Manual.

Wen, H., Ren, B., Dong, P., and Wang, Y. (2016). A sph numerical wave basin for modeling wave-structure interactions. *Applied Ocean Research*, 59:366–377.

Wendland, H. (1995). Piecewise polynomial, positive definite and compactly supported radial functions of minimal degree. *Advances in computational Mathematics*, 4(1):389–396.

Windt, C., Davidson, J., Akram, B., and Ringwood, J. V. (2018). Performance assessment of the overset grid method for numerical wave tank experiments in the OpenFOAM environment. In *Proceedings of the ASME 2018 37th International Conference on Ocean, Offshore and Arctic Engineering (OMAE2018)*, pages 1–10.

Wolgamot, H., Taylor, R., and Taylor, P. (2015). Effects of second-order hydrodynamics on efficiency of a wave energy array. *Proceedings of the 11th European Wave and Tidal Energy Conference*, pages 1–10.

Yu, Y. and Li, Y. (2013). Reynolds-Averaged Navier–Stokes simulation of the heave performance of a two-body floating-point absorber wave energy system. *Computers & Fluids*.

Zelt, J. and Skjelbreia, J. E. (1992). *Estimating Incident and Reflected Wave Fields Using an Arbitrary Number of Wave Gauges*.